UNIVERSITY OF CAPE TOWN
IYUNIVESITHI YASEKAPA • UNIVERSITEIT VAN KAAPSTAD

University of Cape Town

Building a Hybrid Compton Camera System for Improving Medical Imaging Applications

Supervisor:
Prof. Steve Peterson
Co-Supervisors:
Dr. Pete Jones
Assoc. Prof. Luna Pellegri

Candidate:
Shanyn-Dee Hart

A dissertation submitted to the Department of Physics, University of Cape Town, in fulfilment of the requirements for the degree of Doctor of Philosophy.

2022-2024

University of Cape Town

The copyright of this thesis vests in the author. No quotation from it or information derived from it is to be published without full acknowledgement of the source. The thesis is to be used for private study or non-commercial research purposes only.

Published by the University of Cape Town (UCT) in terms of the non-exclusive license granted to UCT by the author.

University of Cape Town

DECLARATION

I, Shanyn-Dee Hart, hereby confirm that this dissertation is my original, independent work. It is submitted in fulfillment of the requirements for the Degree of Doctor of Philosophy at the University of Cape Town, South Africa. This work has not been submitted for any other degree or examination at any institution.

Signed by candidate

(Shanyn-Dee Hart)

January 2025 at iThemba LABS, South Africa.

Abstract

Compton cameras present a powerful advancement in gamma-ray imaging, offering enhanced resolution and efficiency over conventional imaging methods for medical applications such as proton therapy and other targeted radiotherapies. Unlike mechanically collimated imaging systems, a two-stage Compton camera uses a combination of scatterer and absorber detectors to reconstruct gamma-ray paths through Compton scattering events, allowing for greater flexibility in capturing images from uncollimated gamma rays. This study investigated the development, optimisation, and performance of three novel two-stage Compton camera prototypes designed to advance gamma-ray detection specifically for medical imaging applications. The prototypes — referred to as CC1, CC2, and CC3 — each featured unique configurations of scatterer and absorber detectors, tailored to explore and maximise imaging capabilities.

The CC1 design integrated a hybrid setup, combining a commercial Polaris-J CZT detector as the scatterer layer with a $2'' \times 2''$ $LaBr_3$:Ce detector as the absorber. CC2 and CC3 incorporated novel MacroPixel LB-14x25c-SiPM-T scintillation detector assemblies using a variety of different physical configurations. CC2 was evaluated for three distinct geometries, utilising a 4×1 matrix of detector assemblies in both the scatterer and absorber layers. Meanwhile, CC3 employed a 6×1 matrix in the scatterer layer with a $2'' \times 2''$ $LaBr_3$:Ce detector as the absorber.

To ensure optimal performance, each detector system — including the $2'' \times 2''$ $LaBr_3$:Ce, $LaBr_3$:Ce and SrI_2:Eu MacroPixel LB-14x25c-SiPM-T, and Polaris-J CZT detector — was characterised for energy resolution, detection efficiency, and timing precision prior to their use as Compton camera imaging detectors. A digital data acquisition system was used to optimise the energy resolution through signal shaping, achieving measurements of 4.07(9)% for the $2'' \times 2''$ $LaBr_3$:Ce detector, 3.41(20)% and 3.82(18)% for the $LaBr_3$:Ce and SrI_2:Eu detector assemblies, respectively, and 1.38(25)% for the CZT detector at 662 keV. The fast timing capabilities of the $2'' \times 2''$ $LaBr_3$:Ce detector produced an excellent timing resolution of 218.08(11) ps. Characterisation indicated that the SrI_2:Eu detector, while promising in terms of energy resolution, experienced significant pile-up effects at close source-to-detector distance, rendering it unsuitable for Compton camera applications.

The detection performance of each prototype was evaluated through TOPAS Monte Carlo simulations, validated by experimental measurements with gamma-ray sources and proton beam tests conducted at iThemba LABS in Cape Town, South Africa. The simulations were well validated in terms of full-energy peak detection efficiency and energy resolution, although charge build-up effects led to minor discrepancies for the CZT and SrI_2:Eu detectors.

Key figures of merit were chosen to be image resolution, angular resolution, and double-scatter Compton event efficiency, used to assess each Compton camera design. Image resolution determines the system's ability to produce clear, spatially accurate images, essential for pinpointing gamma-ray sources in medical imaging. Angular resolution, assessed by compar-

ing the angle derived from the kinematics of the Compton scattering equation with the angle reconstructed from the geometrical positions of interactions, reflects the system's ability to distinguish between gamma-ray paths and accurately resolve closely spaced sources. Lower values of angular resolution translate to sharper images with less ambiguity, enhancing diagnostic clarity. Efficiency, defined as the fraction of detected gamma rays that contribute to image formation, influences both imaging speed and quality. An iterative three-dimensional filtered back projection method was chosen as the optimal method of image reconstruction, a technique that calculates likely gamma-ray paths and reconstructs an image by refining these projections.

The results showed that CC1 achieved reasonable performance for each figure of merit; however, timing synchronisation issues limited its clinical viability. The setup of the CC1 layers included a Polaris-J CZT detector with an onboard data acquisition system, which was configured to send synchronisation pulses to the absorber's data acquisition system. Microsecond timing delays were encountered and were corrected extensively using background subtraction, time-walk correction, and synchronisation techniques for the data acquisition systems of CC1. Ultimately, it was not possible to track double scatter Compton camera events across CC1. Although CC2 and CC3 were assessed through simulation, their figures of merit demonstrated potential for superior imaging capabilities when compared to the other designs, primarily due to their innovative configurations and timing resolution.

The 4×2 matrix of $LaBr_3$:Ce MacroPixel LB-14x25c-SiPM-T detector assemblies in CC2 design exhibited the greatest promise for clinical application, balancing the benefits of low-voltage operation, modular scalability and Compton camera performance. In summary, while CC1 performed strongly in simulation, CC2's optimised geometry and modular design make it a suitable candidate for further development as a high-resolution gamma-ray imaging system, particularly in advanced medical diagnostics.

Keywords: compton camera, proton therapy, prompt gamma-ray imaging, particle therapy, imaging system, medical imaging

Acknowledgements

There is no way to achieve personal accomplishments without the support, kindness, and understanding of a village. I am profoundly privileged to have been supported and encouraged by friends, family, neighbours, and colleagues. There are a few people I would like to thank explicitly.

Above all, I extend my heartfelt gratitude to my supervisors. I owe massive thanks to Dr. Pete Jones for his invaluable guidance, the learning opportunities he provided throughout my PhD and for being the greatest teacher. You made this journey an incredibly enjoyable one and ignited a lasting passion for instrumentation along the way. My thanks also go to Dr. Luna Pellegri for her constructive comments and insightful recommendations throughout my work, and to Prof. Steve Peterson for making this project possible. Your roles in overseeing my work and providing feedback have been essential to this process.

A special thank-you goes to my best friend, Peter, for his seemingly inexhaustible ability to hear me talk about my project and for the never-ending cups of tea. Your support has known no bounds, and I could never have done this without you.

I would like to thank the security staff member Mark Wyngaard at the lab for his unique ability to express genuine excitement for the life journey of others. Starting the days by enthusiastically being called "Dr. Hart" (despite my protests at the title) was heartwarming and uplifting. The world needs more kind people like you.

To everyone at S-block, I wish to thank you all; you have made it a great pleasure to work at the lab. It is a privilege to work with such lovely people.

Finally, I would like to express my appreciation to the Southern African Institute for Nuclear Technology and Sciences (SAINTS) for the scholarships that made both my MSc and PhD degrees possible, and for providing the resources necessary for me to present my work internationally. *The financial assistance of the National Research Foundation (ITHEMBA LABS) towards this research is hereby acknowledged. Opinions expressed and conclusions arrived at, are those of the author and are not necessarily to be attributed to National Research Foundation (ITHEMBA LABS).*

CONTENTS

NOMENCLATURE

ADC Analogue-to-Digital Converter

ARM Angular Resolution Measurement

BP Bragg Peak

BSE Backward-Scattering Events

CC Compton Camera

CFD Constant-Fraction Discriminator

CLF Compton Line Filtering

CSDA Continuously Slowing Down Approximation

CT Computed Tomography

CZT Cadmium Zinc Telluride

DAQ Data Acquisition System

DA Detector Assembly

DCA Distance of Closest Approach

DCR Dark Count Rate

DOI Depth of Interaction

DPP Digital Pulse Processing

EC Electron Capture

FEPE Full-Energy Peak Efficiency

FOV Field of View

FPGA Field Programmable Gate Array

FSE Forward-Scattering Event

FWHM Full Width at Half Maximum

GUI Graphical User Interface

HV High Voltage

LV Low Voltage

MCS Multiple Coulomb Scattering

MC Monte Carlo

MLEM Maximum Likelihood Expectation Maximisation

MWD Moving-Window Deconvolution

PCA Point of Closest Approach

PCI Peripheral Component Interconnect

PDE Photon Detection Efficiency

PG Prompt Gamma-Ray

PMT Photomultiplier Tube

PT Proton Therapy

QDC Charge-to-Digital Converter

RF Radiofrequency

SiPM Silicon Photomultiplier

SPAD Single Photon Avalanche Diode

STM Synchronisation-Timing Module

TOF Time-of-Flight

TOPAS TOol for PArticle Simulation [1]

UPS Uninterrupted Power Supply

UV Ultraviolet Light

ZCP Zero-Crossing Point

LIST OF FIGURES

LIST OF TABLES

1 INTRODUCTION

1.1 PROTON THERAPY

In 2018, cancer was the second leading cause of death globally, responsible for approximately 17% of all deaths, despite significant advances in treatment [2]. While surgery remains the most effective treatment for solid cancers, successful strategies often combine multiple approaches [3].

Radiation therapy plays a key role, covering over 50% of solid tumours. Among the options, Proton Therapy (PT) is a cutting-edge method for treating deep-seated tumours. Proposed over 70 years ago by physicist Robert Wilson, PT was first used in 1954 at the Lawrence Berkeley National Laboratory, USA [4]. Wilson's idea, based on Hans Bethe's work on proton energy loss and Ernest Lawrence's cyclotron developments, highlighted the benefits of ion beams over X-rays. Although heavier ions have greater biological effectiveness, PT has become the primary form of ion beam radiotherapy due to the relatively lower cost of proton cyclotrons.

PT works similarly to traditional radiotherapy by inducing damage in targeted cells, but it offers a unique advantage in how protons interact with matter. The dose, measured in Grays (Gy), is more concentrated in PT, minimising damage to healthy tissues while delivering higher doses to tumours. This is due to the distinctive Bragg peak (BP) (see Section 2.1.3.1 for more detailed information), where the proton energy deposition peaks just before the beam stops, enabling precise targeting of the tumour [5].

Proton beams in PT typically range from 70.0–250.0 MeV, with higher energies used for deeper tumours. The flexibility of dose distribution shaping, due to the BP, allows oncologists to precisely control the treatment area. Fig. 1.1.1(a) shows the clear difference in dose deposition. By modulating the beam energy, the beam range can be tailored to deliver the peak dose to the tumour while sparing surrounding tissues.

However, one major challenge remains: the lack of real-time methods to monitor proton depth-dose characteristics during treatment. This can lead to inaccurate beam targeting, either under dosing the tumour or overdosing healthy tissues. Uncertainties such as computed tomography (CT) artefacts, tumour shrinkage, and patient positioning necessitate safety margins in treatment plans, which can diminish the clinical advantages of PT [5].

These margins, typically 2.5–3% of the proton range or 2–3 mm [6], can extend up to 1 cm for deep-seated tumours. A method for accurately monitoring the proton beam's distal edge during treatment would reduce these margins, improving the dose precision and min-

imising damage to healthy tissues beyond the tumour. This would also allow the use of more challenging gantry angles in treatment, further enhancing PT's effectiveness [6].

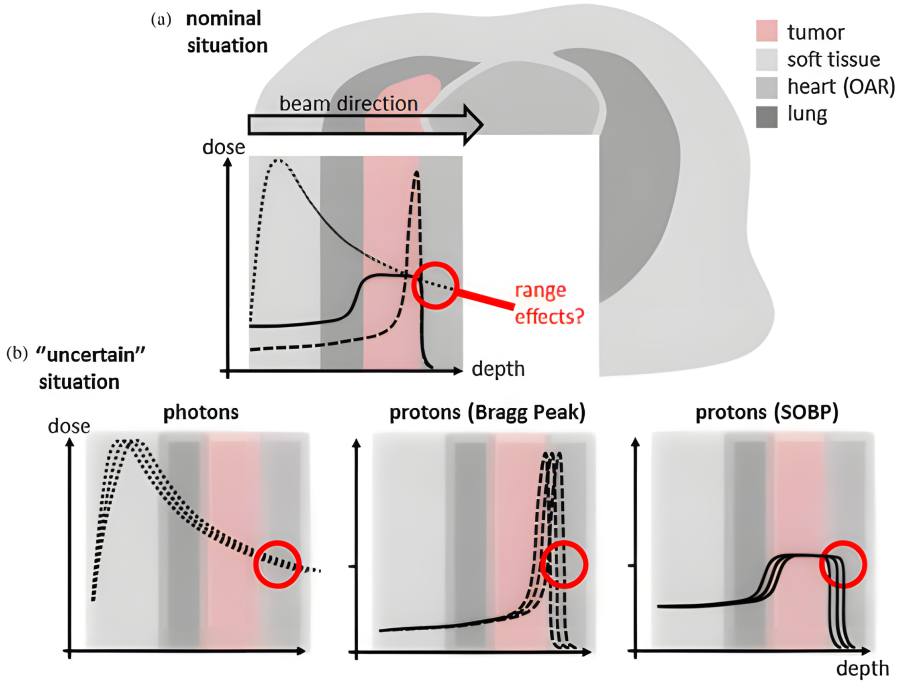

Figure 1.1.1: The potential dose advantage of proton therapy compared to photon therapy is illustrated in: (a) the dotted line showing the photon depth-dose curve, the dashed line representing the depth-dose curve for mono-energetic protons, and the solid line depicting the spread-out Bragg peak (SOBP) used to cover the entire tumor; and (b) the impact of uncertainties on the depth-dose curves for the three treatment modalities described in (a) [7].

1.1.1 Range Uncertainty

One promising strategy to mitigate range uncertainty in PT is the use of advanced imaging systems, such as CCs. These devices offer real-time monitoring by detecting secondary gamma rays emitted when protons interact with atomic nuclei in the patient's body. By reconstructing the spatial origin of these prompt gamma emissions, CCs enable indirect imaging of the proton beam path and range, allowing clinicians to confirm that the BP lies within the tumour volume.

Compared to conventional collimated gamma detectors, CCs provide superior detection efficiency and a wider field of view. Mechanical collimators, while effective at spatially filtering incoming photons, inherently block a large portion of the emitted gamma rays, limiting sensitivity and reducing count rates—especially problematic for the low-yield prompt gamma signal in PT. In contrast, Compton cameras employ electronic collimation based on Compton scattering kinematics, eliminating the need for heavy shielding and enabling a significantly larger solid angle of detection. This results in more compact, flexible systems that are better suited for clinical integration.

Additionally, while collimated detectors typically offer only one-dimensional or limited-angle projections, CCs allow full 3D reconstruction of gamma-ray emission distributions. This capability is critical for accurate, real-time range verification in complex or heterogeneous anatomical regions.

Recent advances in CC design—particularly the integration of high-resolution scintillators and silicon photomultipliers (SiPMs)—have further improved angular and energy resolution [8, 9]. These improvements enhance the precision of gamma-ray tracking and thus the accuracy of the inferred proton range. By incorporating Compton imaging into the PT workflow, it becomes possible to reduce the reliance on conservative safety margins, enabling more conformal treatment plans while maintaining patient safety. This makes CCs a compelling option for image-guided PT, especially in cases involving deep-seated tumours or proximity to critical structures.

1.2 RECENT DEVELOPMENTS IN COMPTON CAMERA IMAGING

Recent developments in scintillator-based CCs have made significant progress due to their advantages of high detection efficiency, lower cost, and ability to operate at room temperature. However, one of the main limitations of scintillator-based CCs compared to semiconductor-based counterparts lies in their relatively lower angular resolution, attributed to poorer energy and position resolution. Various scintillators have been commonly employed in CC systems, including thallium-doped sodium iodide (NaI:Tl), thallium-doped caesium iodide (CsI:Tl), sodium-doped caesium iodide (CsI:Na), cerium-doped gadolinium aluminium gallium garnet (GAGG:Ce), and cerium-doped lanthanum bromide ($LaBr_3$:Ce) [10, 11, 12, 13].

Scintillators are often paired with photomultiplier tubes (PMTs) or silicon photodiodes, but recent advances in multipixel photon counters (MPPCs), a form of SiPMs, have allowed for more effective integration of scintillators into CC designs. This development is particularly important for improving position sensitivity, a critical feature for advanced imaging techniques. Scintillators work by undergoing a scintillation process in which incident radiation excites electrons, transferring energy to ionised electrons, and ultimately leading to the emission of fluorescence.

Historically, NaI(Tl) was the first widely adopted scintillator after being discovered by Hofstadter et al. in 1948 [14]. Although highly sensitive, NaI(Tl) and CsI(Tl) suffer from limited energy resolution, especially in the lower energy range, which makes them less suitable for medical imaging applications, where typical radiopharmaceuticals emit gamma rays with energies below 250.0 keV (e.g., ^{99m}Tc at 141.0 keV, ^{123}I at 159.0 keV) [11, 12, 13]. This limitation prompted the exploration of alternative scintillators for CCs.

Among the alternatives, GAGG:Ce has emerged as a leading choice due to its superior properties. GAGG:Ce scintillators possess a high density, high light output, fast decay time, low self-radiation, and good energy resolution [15]. They are also non-hygroscopic and have

high stopping power. GAGG:Ce became especially valuable after the 2011 Fukushima nuclear disaster in Japan, where it was deployed for remote sensing of radioactive materials. Researchers such as Kishimoto et al. developed a portable CC using GAGG:Ce scintillators coupled with MPPCs, which also featured depth-of-interaction (DOI) capability [16]. This prototype demonstrated an angular resolution of less than 10° and was initially used for the detection of radioactive elements [17].

In recent years, developments in this field have continued, with research groups focusing on specialised applications. The work of Ogane et al. introduced a hybrid Compton-PET camera utilising GAGG:Ce scintillators for simultaneous imaging of different radioactive sources, such as ^{131}I and ^{18}F [18]. This setup involved two GAGG:Ce-based CCs placed opposite each other, designed for advanced imaging in particle therapy applications. While the study confirmed the system's ability to obtain accurate Compton and PET images simultaneously, allowing for prognosis prediction and treatment evaluation, further research is needed using phantom models that simulate complex anatomical structures to verify the feasibility of simultaneous imaging in real-world clinical scenarios.

Further contribution to this progress was in work done by Takahashi et al. by designing an omnidirectional Compton imager using stacked GAGG scintillators for rapid radioactive fallout detection, such as during nuclear accidents [19]. These innovations highlight the increasing role of GAGG:Ce and other scintillators in diverse fields, from medical imaging to environmental monitoring. The three-dimensional position resolution of these systems has been a particular focus, demonstrating improvements in spatial resolution and efficiency. However, further work is needed to optimise detection algorithms, reduce system complexity, and enhance sensitivity to low-energy gamma rays to expand their practical applications.

In addition to the CCs discussed, recent developments have introduced innovative designs utilising both semiconductor detectors and scintillators. To address the limitations of low sensitivity and high costs in silicon-based CCs, Katagiri et al. have pioneered a new approach with a europium-doped calcium fluoride (CaF_2:Eu) scintillator-based omnidirectional CC [20]. This system is tailored for monitoring environmental radiation in nuclear medicine settings and is effective for detecting gamma-ray sources with energies under 250.0 keV. The camera features four CaF_2:Eu crystals, each 2.54 cm in diameter, arranged in a tetrahedral pattern, serving as both scatterer and absorber. This configuration has demonstrated the capability to minimise "ghost" images and achieve a notable 12° angular resolution for ^{57}Co gamma rays, alongside improved detection efficiency. The term "ghost" images refers to artificial patterns that appear in reconstructed gamma-ray images when there are limitations in the detector's design. Specifically, in the context of the tetrahedral CaF_2:Eu scintillator-based omnidirectional CC, these patterns arise due to the small number of scintillation counters.

The work of Kasper et al. introduced a CC that integrates SiPMs with scintillation fibres [8]. This design utilises slender, high-density fibres made from inorganic scintillators such as LYSO:Ce, LuAG:Ce, and GAGG:Ce, coupled with SiPMs. Their research confirms that this setup is effective for proton beam monitoring, with the LYSO:Ce scintillator showing particularly promising results in this context.

In a similar vein, the work of Barrientos et al. focussed on advancing the development of the MACACO II, a CC featuring $LaBr_3$:Ce scintillators and SiPMs [21]. This updated model is optimised for proton beam monitoring, offering an energy resolution of 5.6% full width at half maximum (FWHM) at 511.0 keV and an angular resolution of 8°. The recent developments in the MACACO III CC have introduced significant enhancements compared to earlier versions [9]. The new version incorporates SiPM arrays with a 25 μm micro-pixel pitch, which reduces ASIC saturation and achieves a more linear response. This upgrade results in improved energy resolution, with values of 5.2% and 5.8% FWHM at 511.0 keV for the first and second detectors, respectively, which is better than the previous version's 5.6% and 6.6% FWHM. These results surpass other SiPM-based CCs used in applications such as hadron therapy and Compton-PET. Further, the CC showed a threefold reduction in temperature dependence compared to the 50 μm model, improving the energy resolution without requiring temperature stabilisation. This advancement enhances the detector's stability in varying environments. The MACACO III showed improved imaging performance, allowing for better resolution of complex structures. For instance, it can resolve sources in a ^{22}Na array with an average FWHM of 2.8 mm at 1274.5 keV, significantly better than previous measurements and other published results. The MACACO III achieved an angular resolution of 6.9° at 1274.5 keV, a 1.1° improvement over the previous version. Although this is still behind some solid-state detector systems, it represents a significant advancement over other scintillator-based cameras. The study suggested that integrating silicon or CZT detectors could improve angular resolution, and finer SiPM segmentation could enhance spatial resolution. Additionally, the use of neural networks for position determination might further optimise imaging capabilities.

Another notable innovation is the Polaris-J^{TM} CC, developed by H3D (Ann Arbor, MI USA). The work of McCleskey et al. evaluated this camera, which employs cadmium zinc telluride (CZT) detectors, known for their high gamma-ray interaction cross-sections, particularly for 6.0 MeV gamma rays [22] . The Polaris-J system includes four stages, each equipped with a ($20 \times 20 \times 15$) mm CZT detector arranged in an 11×11 pixel matrix. This system provides an energy resolution of 9.7 keV (FWHM) at 661.7 keV, as emitted by ^{137}Cs, and is being further refined for applications in PT.

Additionally, Brookhaven National Laboratory, in collaboration with NASA, is developing a CZT-based CC designed for astronomical studies [23]. This camera features an array of ($8 \times 8 \times 32$) mm position-sensitive virtual Frisch-grid CZT detectors configured as bars. Each unit is a 4×4 sub-array connected to an ASIC, delivering exceptional performance with less than 1% energy resolution at 1.0 MeV and sub-millimeter position accuracy. The camera is currently under evaluation, with future plans for deployment in high-altitude balloon flights for precise measurements.

As scintillator-based CCs continue to evolve, future advancements are expected to improve angular and spatial resolution further, potentially closing the gap between these systems and semiconductor-based alternatives while maintaining their operational advantages.

1.3 RESEARCH OBJECTIVES

- To assess the performance of various scintillator and semiconductor detectors for use in three distinct two-stage CC prototypes (CC1, CC2, and CC3) using a range of gamma-ray sources. Key metrics such as detection efficiency, energy resolution, and timing accuracy will be evaluated under various operational conditions.

- To create a TOPAS/Geant4 MC simulation of the performance of the CZT-$LaBr_3$:Ce hybrid system (CC1) and the detector assembly (DA) coupled CC designs (CC2 and CC3). The simulations will track the energy deposition and interaction positions of gamma rays to generate data for image reconstruction.

- To validate the performance of the Geant4/TOPAS simulations by benchmarking the results against experimental data.

- Implement and optimise image reconstruction algorithms, including the filtered back projection (FBP) method, to generate accurate images of gamma-ray sources using the simulated and experimental data from the Compton camera systems.

- To conduct experiments using different radioactive sources and proton beam measurements with the CC1 prototype to test the validity of the image reconstruction algorithms and to compare the results with Monte Carlo simulation results. This will allow for insight into the feasibility of using this CC design for PT imaging applications.

- To investigate the impact of different geometrical configurations of the scatterer and absorber layers on imaging performance. Optimise parameters such as source-to-detector distance and scatterer-to-absorber spacing to enhance image resolution and source localisation accuracy.

1.4 STRUCTURE OF THE THESIS

This thesis describes the work undertaken to develop a novel two-stage CC, with the aim of improving the imaging capabilities of PT. This work analyses the performance of three different CC detector systems that make use of a variety of solid-state and scintillation detectors in various geometrical configurations. The first CC, referred to in the thesis as CC1, comprises a hybrid design using a commercial CZT Polaris-J detector as the scatterer and a $2'' \times 2''$ $LaBr_3$:Ce detector as the absorber. The second CC, referred to as CC2, was a custom-built system that investigates using a state-of-the-art SiPM-readout detector, composed of 4 $LaBr_3$:Ce detector-SiPM assemblies in each of the scatterer layer and the absorber modules. The third CC, referred hereafter as CC3, investigates using 6 $LaBr_3$:Ce detector-SiPM assemblies in a matrix as the scatterer layer, with the $2'' \times 2''$ $LaBr_3$:Ce detector as the absorber.

The thesis is structured as follows:

- **Chapter 2:** This chapter provides a comprehensive overview of the theoretical principles underlying gamma-ray interactions with matter, including Compton scattering, photoelectric absorption, and pair production. Understanding these interactions is crucial for optimising CC design and operation.

- **Chapter 3:** This chapter details the design and methodology of CC1, which features a hybrid configuration with a CZT Polaris-J detector as the scatterer and a 2″ × 2″ $LaBr_3$:Ce detector as the absorber. The chapter covers the detector geometries, signal processing techniques, and experimental measurements used to characterise the performance of the detectors that make up the hybrid system.

- **Chapter 4:** This chapter focuses on CC2 and CC3, which employ advanced SiPM-readout detector assemblies. CC2 uses a 4×2 array of MacroPixel LB-14x25c-SiPM-T assemblies for both the scatterer and absorber layers, while CC3 integrates a 6×1 array of these assemblies as the scatterer with a 2″ × 2″ $LaBr_3$:Ce absorber. The chapter explores the design, operation, and characterisation of these systems, emphasising the benefits of high-performance SiPM electronics for modularity, low-voltage operation, and improved energy resolution and timing capability.

- **Chapter 5:** This chapter explores the use of TOPAS MC v3.6.1 for Monte Carlo simulations of the three Compton camera designs, investigating the impact of different detector configurations on imaging performance. It details the construction of realistic materials, selection of physics models, custom scoring techniques, and optimisation of image reconstruction algorithms to enhance simulation fidelity.

- **Chapter 6:** This chapter presents and analyses the results from both the simulations and experimental validations of the CC prototypes. Performance metrics such as timing accuracy, detection efficiency, angular resolution, and image resolution are evaluated. The chapter discusses the strengths and limitations of each CC design, providing insights into how well each prototype reconstructs source positions and performs under different conditions.

- **Chapter 7:** This chapter interprets the findings of Chapter 6, drawing conclusions about the effectiveness of each CC design. It offers a detailed analysis of how the different configurations impact overall performance and identifies key factors that contribute to the success or limitations of each system.

- **Chapter 8:** The final chapter summarises the key findings of the thesis, highlighting the most successful CC design based on the evaluated performance metrics. It also discusses potential improvements, future research directions, and the implications of the findings for advancing CC technology and its applications in medical imaging and other fields.

2 | THEORETICAL BACKGROUND

This chapter delves into the theoretical framework surrounding the interaction of radiation with matter, with a particular focus on gamma-ray interactions. These principles are foundational to the design and operation of CCs. Gamma-ray interactions, such as Compton scattering, photoelectric absorption, and pair production, determine how high-energy photons interact with different materials. A detailed understanding of these processes enables the accurate detection and reconstruction of gamma-ray paths, which is critical for optimising image quality and ensuring precise targeting in clinical settings such as PT. By enhancing the detection capabilities of CCs, it becomes possible to improve the accuracy of dose delivery, minimise exposure to healthy tissue, and ultimately ensure the safety and efficacy of treatments. Additionally, a thorough grasp of radiation interactions informs the selection of detector materials, geometry, and signal processing techniques, all of which play a pivotal role in refining the camera's performance.

2.1 INTERACTION OF RADIATION WITH MATTER

The interaction of radiation with matter can be broadly classified into two categories: electromagnetic interactions and nuclear interactions. Electromagnetic interactions include processes such as photoelectric absorption, Compton scattering, and pair production, while nuclear interactions include processes such as elastic scattering, inelastic scattering, and nuclear reactions. The interaction of radiation with matter is characterised by the energy of the radiation, the type of radiation, and the type of material.

Gamma rays are a type of electromagnetic radiation characterised by their short wavelength and high frequency. They are typically produced during the radioactive decay of atomic nuclei, which can involve processes such as alpha (α) decay, beta (β^+ and β^-) decay, or electron capture (EC). In the context of this project, the relevant energy range of gamma-ray interactions is between 0.0 and 7.0 MeV. At these energies, the dominant processes by which gamma rays interact with matter are photoelectric absorption, Compton scattering, and pair production.

The following section will further explore these key interaction mechanisms, forming the foundation for understanding the principles behind gamma-ray detection.

2.1.1 Gamma-Ray Interactions

2.1.1.1 *Photoelectric Absorption*

The photoelectric absorption process takes place when a gamma-ray photon collides with an atom that has an electron in a bound orbital. It is a dominant process for gamma-ray energies between 1.0–500.0 keV [24]. In this interaction, the photon's energy is completely absorbed by the atom, causing a shift in the atom's energy levels and leading to the ejection of an electron from one of its atomic shells, usually the K shell. This process is depicted schematically in Fig. 2.1.1, and Eq. 2.1.1 is the energy of the ejected electron.

$$E_{e^-} = E_0 - E_b, \tag{2.1.1}$$

where the incident energy of the gamma ray is given by E_0, and E_b is the binding energy of the electron to its orbital shell [24].

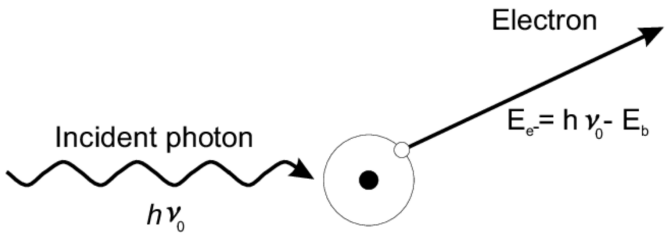

Figure 2.1.1: A diagram illustrating the photoelectric absorption process. The incoming gamma ray has an initial energy of E_0. Upon interacting with the atom, a bound electron is released from its orbital shell, carrying energy as described by Eq. 2.1.1 [25].

2.1.1.2 *Compton Scattering*

The Compton scattering process involves the interaction between an incoming gamma-ray photon and an electron, which is typically loosely bound within the atomic orbital. As depicted in Fig. 2.1.2, this interaction causes the gamma-ray photon, with an initial energy E_0, to scatter at an angle θ, resulting in a reduction of the photon's energy. The energy lost by the photon is transferred to the electron, which gains it as kinetic energy and becomes a recoil electron [24, 26].

The energy of the scattered photon, E_1, is determined by the scattering angle θ, as described by the Compton scattering Eq. 2.1.2. The Klein-Nishina formula accounts for relativistic effects and quantum electrodynamics, offering a more accurate representation of photon-electron interactions than the classical Thomson scattering formula [27]. For most energies, Compton scattering is not isotropic, which causes the Compton continuum to not be rectangular. Eq. 2.1.3 predicts the energy-dependent probability distribution for θ_1, seen in Fig. 2.1.3.

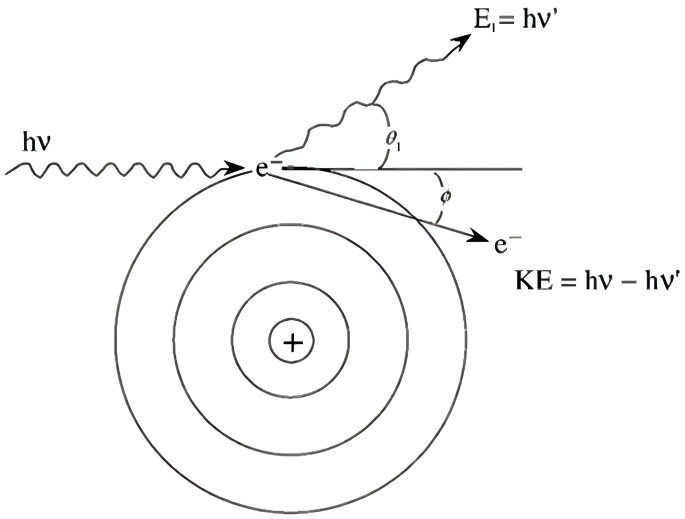

Figure 2.1.2: An illustration of the Compton scattering process. A gamma-ray photon with energy $E_0 = h\nu$ interacts with a loosely bound electron, resulting in scattering at an angle θ. The recoil electron is ejected at an angle ϕ with a kinetic energy of $E_0 - E_1$, while the scattered photon has energy given by equation 2.1.2 [26].

$$E_1 = \frac{E_0}{1 + \frac{E_0}{m_0 c^2}(1 - \cos\theta)} \tag{2.1.2}$$

$$\frac{d\sigma}{d\Omega} = \frac{r_0^2}{2}\left(\frac{E_1}{E_0}\right)^2\left(\frac{E_1}{E_0} + \frac{E_0}{E_1} - \sin^2\theta\right) \tag{2.1.3}$$

where r_0 is the classical electron radius, E_0 is the initial energy of the photon, E_1 is the energy of the scattered photon, and θ is the scattering angle. This formula is essential for accurately modeling Compton scattering in high-energy photon interactions [27].

When θ ranges from 0 to π, the energy of the scattered photon varies from a maximum (when $\theta = 0$) to a minimum (when $\theta = \pi$). This implies that the energy transferred to the electron can range from very little to nearly the entire energy of the incident photon, though it is impossible for the photon to transfer all its energy in a Compton interaction [28].

For gamma-ray energies between 0.5 and 10 MeV, Compton scattering dominates as the primary interaction mechanism. This energy range is common in radioactive sources and forms the basis of the principle of the CC, making the study of Compton scattering particularly relevant to this research.

In addition to the Compton scattering process, the relationships between the photopeak, backscatter peak, and Compton edge provide further insight into the behaviour of gamma-ray interactions, a labelled ^{137}Cs gamma-ray spectrum for which is shown in Fig. 2.1.4. Note that the 32 keV ^{138}Ba X-ray peak is labelled for completeness but it is not a Compton contribution. The Compton edge represents the maximum energy transfer to the electron, resulting in the highest kinetic energy that the recoil electron can acquire. This corresponds to the minimum

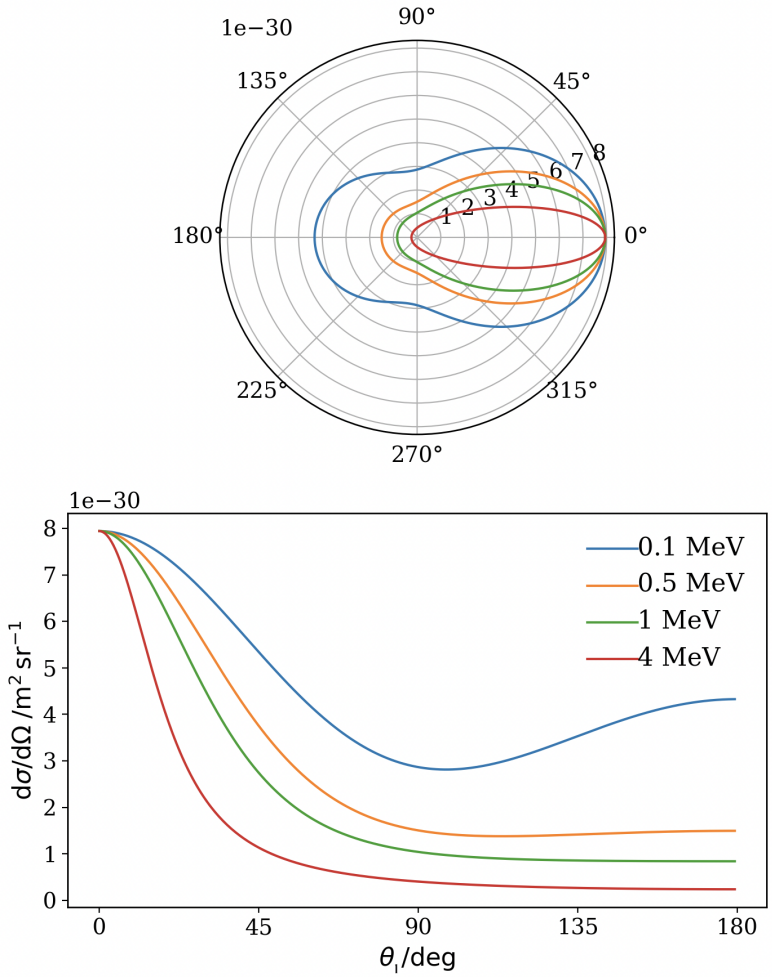

Figure 2.1.3: The Klein-Nishina formula behaviour, seen in the angular dependence of the differential cross-section at various incoming gamma-ray energies. Both forward and back-scattering dominate the low energy region as seen in the blue 0.1 MeV line; at higher gamma-ray energies, forward scattering dominates and the majority of energy transfer is to the electron, seen in the red 4.0 MeV line. This image was generated for energies in the range of interest using a custom Python code.

energy of the scattered photon and is seen as a sharp cut-off in the energy spectrum. The backscatter peak, on the other hand, arises when photons scatter at angles close to 180° and then re-enter the detector after interacting with surrounding materials. The backscatter peak and Compton edge are both lower in energy than the photopeak, which represents the full energy deposition by the incident photon. Referring to Fig. 2.1.4, note that the energy of the Compton peak (180 keV) combined with the energy of the Compton edge (482 keV) equals the energy of the photopeak (662 keV). The distribution of these features in the energy spectrum provides a comprehensive understanding of photon interactions within the detector, with the photopeak indicating full absorption and the Compton-related features revealing partial energy transfers.

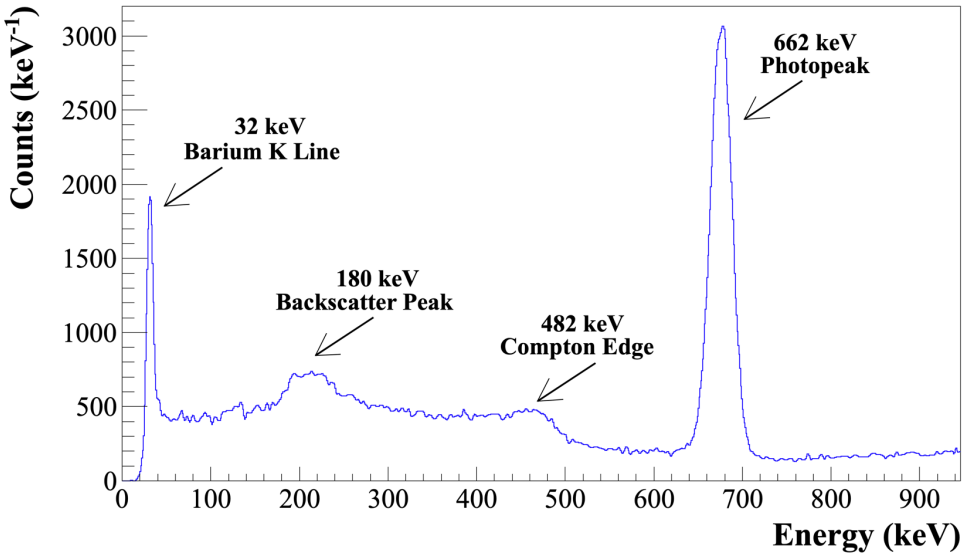

Figure 2.1.4: Annotated ^{137}Cs gamma-ray spectrum measured with a 2″ × 2″ $LaBr_3$:Ce detector for 10-minutes. The Compton contributions are labelled, seen as the Compton peak at 180 keV and the Compton edge at 482 keV, which sum to equal the photopeak at 662 keV.

2.1.1.3 Pair Production

Although it is not very relevant to the focus of this study, the process of pair production is included for the sake of thoroughness. Pair production occurs when a gamma ray interacts with an atomic nucleus, resulting in the creation of an electron-positron pair. This interaction requires the photon to possess a minimum energy of 1.02 MeV, which corresponds to the combined rest mass of the electron and positron. The positron produced in this process eventually interacts with an electron in the material, leading to mutual annihilation, generating two secondary photons as by-products. This is illustrated in Fig. 2.1.5.

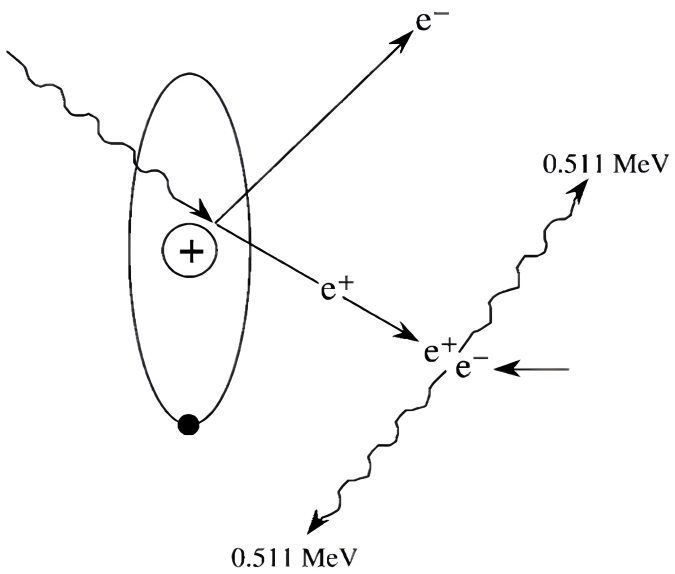

Figure 2.1.5: Schematic representation of pair production. An incoming photon with a minimum energy of 1.02 MeV interacts with the Coulomb field of an atomic nucleus, resulting in the creation of an electron-positron pair. The positron then annihilates, leading to the emission of two photons with energies of 511.0 keV each [26].

If pair production takes place within the detection material, both the kinetic energy of the produced electron-positron (e^+e^-) pair and any secondary annihilation photons (assuming they remain within the material) will be measured. Conversely, if pair production occurs outside the detection material, such as in the surrounding shielding, the kinetic energy of the e^+e^- pair will not be detected. Nonetheless, either of the secondary annihilation photons may still be detected if they traverse the detection material.

In radiation detection, the occurrence of this interaction can be deduced by analysing the energy spectrum. A single-escape peak is observed when one of the annihilation photons is detected while the other escapes the material. A double-escape peak, on the other hand, indicates that both annihilation photons have escaped the material without being detected.

It is important to note that although pair production can occur with an incident photon energy of 1.02 MeV, it becomes significantly more probable at energies exceeding 10.0 MeV.

2.1.1.4 Gamma-ray Interaction Mechanisms in Detector Materials

Figure 2.1.6 illustrates how gamma-ray interaction mechanisms vary with photon energy for different detector materials, highlighting their strong dependence on both photon energy and the Z of the material. At low photon energies (below ~100 keV), photoelectric absorption dominates. This process is highly favoured in materials with high atomic numbers, such as $LaBr_3$:Ce and CZT, due to its steep dependence on Z (approximately Z^4-Z^5) and inverse dependence on energy ($E^{-3.5}$). As photon energy increases into the intermediate range (100 keV – 2 MeV), Compton scattering becomes the dominant interaction. Unlike the photoelectric effect, Compton scattering scales roughly linearly with Z and inversely with photon energy, making it less sensitive to atomic number but ideal for directional gamma-ray detection, as exploited in Compton camera systems. At higher photon energies (>2 MeV), pair production begins to contribute significantly, especially in high-Z materials. Although it is not the focus for most Compton imaging applications, it is included in total attenuation and becomes increasingly relevant for high-energy gamma detection.

Figure 2.1.6 illustrates these trends by showing the mass attenuation cross-sections for three commonly used detector materials: $LaBr_3$:Ce, SrI_2:Eu, and CZT. The solid, dashed, and dotted lines represent the photoelectric, Compton, and total attenuation cross-sections, respectively. As seen in the figure, $LaBr_3$:Ce and CZT exhibit superior performance at low energies due to their high-Z constituents, while all three materials converge in behaviour in the Compton-dominated energy region. This cross-section behaviour underpins the material choices in Compton camera design, as it directly impacts the efficiency, resolution, and energy-dependence of gamma-ray detection.

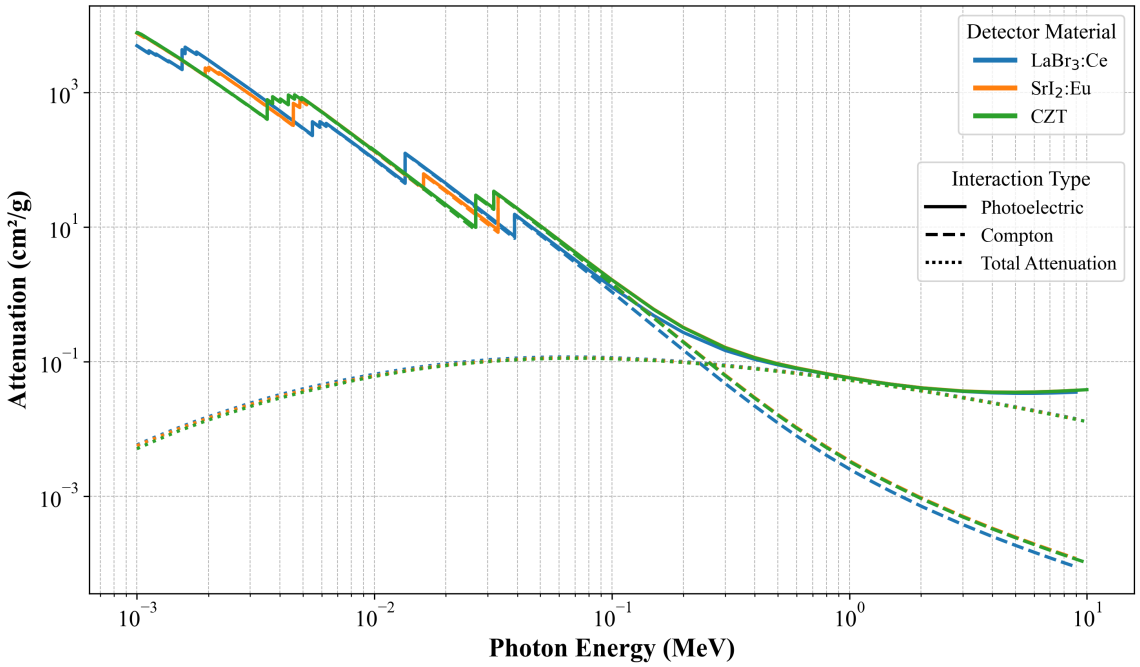

Figure 2.1.6: Mass attenuation cross-sections as a function of photon energy for three detector materials: $LaBr_3$:Ce (blue), SrI_2:Eu (orange), and CZT (green). Solid lines represent photoelectric absorption, dashed lines represent Compton scattering, and dotted lines represent total attenuation. Data spans photon energies from ~1 keV to 10 MeV, covering typical ranges used in nuclear imaging and spectroscopy. All data was obtained from the NIST XCOM database [29]

2.1.2 Radioactive Decay

Radioactive decay is a fundamental process that involves the transformation of an unstable atomic nucleus into a more stable configuration. Unlike photon interactions such as those listed above, radioactive decay is a spontaneous process governed by the principles of nuclear physics rather than electromagnetic interactions.

In general, radioactive decay can occur through several modes, including alpha decay, beta decay, and gamma decay. The decay process follows a probabilistic law described by an exponential decay function. The activity $A(t)$ of a radioactive substance at time t is given by:

$$A(t) = A_0 e^{-\lambda t} \tag{2.1.4}$$

where A_0 is the initial activity at $t = 0$, and λ is the decay constant, which is related to the half-life $T_{1/2}$ of the radioactive substance by:

$$\lambda = \frac{\ln(2)}{T_{1/2}} \tag{2.1.5}$$

The decay constant λ provides a measure of the rate at which the substance decays. The half-life $T_{1/2}$ is the time required for half of the radioactive nuclei in a sample to decay. This

relationship is crucial for understanding the behaviour of radioactive sources and their impact on radiation detection systems.

In the context of radiation detection and measurement, radioactive decay is used to determine the source strength and predict the number of decays that will occur over a given time period. It is also important in the calibration of detectors and in the interpretation of measurement data. The understanding of decay processes is fundamental for accurate dose calculations and for the effective use of radioactive materials in both research and clinical settings.

2.1.3 Proton Interactions

Protons interact with the matter in three distinct ways that are relevant to this work [30]:

1. **Scattering:** Protons experience angular deviation due to electromagnetic interactions with atomic nuclei, described by MCS. This stochastic process arises from numerous small-angle deflections caused by the Coulomb field of atomic nuclei, with occasional inelastic collisions contributing further. MCS broadens the beam profile and contributes $\sim 2\%$ to the BP width in water [31, 32].

2. **Nuclear Interaction:** Primary protons can interact directly with atomic nuclei through nuclear reactions, classified by timescale into:

   - *Compound reactions:* The projectile and target fuse to form a highly excited nucleus that decays via neutron, charged particle, or gamma-ray emission.
   - *Direct reactions:* Fast processes involving a few nucleons, without forming an intermediate nucleus; includes elastic, inelastic, or nucleon-transfer interactions.
   - *Pre-equilibrium reactions:* Intermediate-time-scale events where particle emission occurs before the nucleus reaches thermal equilibrium.

   These mechanisms often co-occur, and are described in more detail in Section 2.1.3.2. Nuclear reactions generate secondary particles (e.g., gamma rays, neutrons), and the resulting residual nuclei decay characteristically, reflecting properties such as spin, parity, and separation energy. Some short-lived radioisotopes produced may be exploited for in vivo range verification via proton-induced activation.

3. **Stopping:** Protons lose energy primarily via inelastic Coulomb interactions with orbital electrons, a process described by continuous slowing down. Due to the stochastic nature of these interactions, individual protons stop at slightly different depths—a phenomenon known as energy straggling. The rate of energy loss increases with penetration depth.

In a medium of density ρ, the energy loss per unit path length is quantified by the stopping power $S(E)$, given by the Bethe-Bloch equation for charged particles heavier than electrons [7]:

$$S(E) = 4\pi\rho\frac{Z}{A}N_A\left(\frac{e^2}{4\pi\epsilon_0}\right)^2\frac{z^2}{m_e v^2}\left\{\ln\left[\frac{2m_e c^2}{I}\right] + \ln[\beta^2] - \ln[1-\beta^2] - \beta^2 - \frac{C}{Z} - \frac{\delta}{2}\right\} \quad (2.1.6)$$

Here, Z and A are the atomic number and mass number of the target, z the projectile charge, and $\beta = v/c$ the normalized velocity. The formula separates dependencies on the projectile and target, enabling precise modeling of energy deposition.

- $\frac{S}{\rho} \propto \frac{z^2}{m_e v^2}$: The mass stopping power is proportional to the charge squared of the projectile and inversely proportional to its kinetic energy. When the particle stops, the maximum energy is released to the absorbing material.
- $\frac{S}{\rho} \propto \frac{Z}{A}N_A$: The projectile releases energy dependent on the characteristics of the target investigated.
- $\frac{S}{\rho} \propto \ln\left[\frac{2m_e c^2}{I}\right]$: The mass stopping power is also weakly dependent on its mean ionisation potential due to the logarithmic function.

The mass stopping power is related to the dose simply by a unit conversion:

$$D\ [\frac{J}{kg}] = \Phi\ [\frac{1}{cm^2}] \cdot \frac{S}{\rho}\ [\frac{J \cdot cm^2}{kg}] = 6.242 \cdot 10^9 \cdot \Phi\ [\frac{1}{cm^2}] \cdot \frac{S}{\rho}\ [\frac{MeV \cdot cm^2}{g}] \quad (2.1.7)$$

where Φ is the proton beam fluence.

The Bethe-Bloch equation, together with the statistical nature of MCS for protons, leads to the tell-tale depth-dose curve with its low entrance plateau and steep distal curve known as the BP.

2.1.3.1 *Bragg Peak*

Figure 2.1.7 illustrates the relationship between the depth-dose profile and the spatial distribution of secondary vertices from inelastic interactions of primary beams. As primary particles lose energy and penetrate deeper, interaction probability rises, correlating dose deposition with PG emission, peaking near the BP.

PT exploits the characteristic energy deposition pattern shown in Fig. 2.1.7, common to all charged particles regardless of ion species or medium. The curve can be divided into three regions:

1. **Plateau:** Near-constant dose in the beam entrance region due to high-energy stopping power, with low ionisation probability by primaries. Dose build-up occurs within the first few millimetres until nuclear equilibrium is reached, dominated by low-energy target fragments [34, 24].

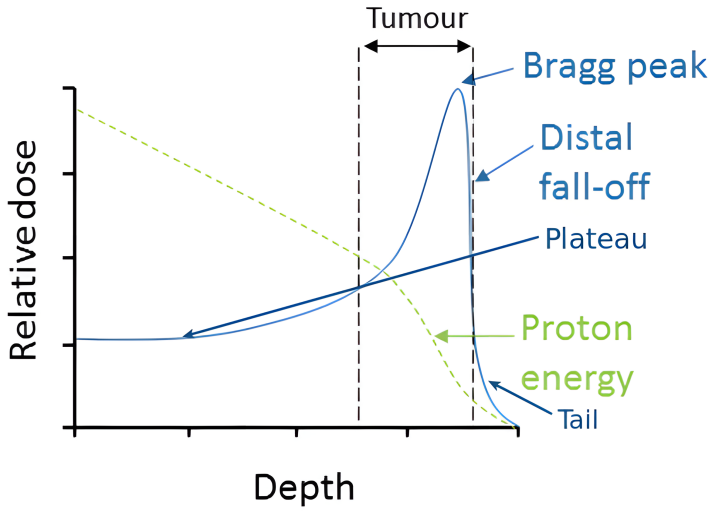

Figure 2.1.7: Schematic of proton percentage depth-dose regions at the BP, adapted from [33].

2. **Steep Distal Curve:** Nuclear interaction cross-sections increase near the BP, where the maximum dose is delivered at proton stopping. The BP's narrow width (few millimetres) results from range straggling of monoenergetic protons. The steep fall-off beyond the peak—the Distal Penumbra, defined by the difference between R_{80} and R_{20}—depends on beam spot size and MCS, which reduces central axis fluence and peak-to-plateau ratio.

3. **Tail:** Heavy ions (^{12}C, ^{16}O) produce secondary fragments through nuclear reactions, extending dose beyond the BP. These lighter fragments, having longer ranges due to lower mass stopping power proportional to Z_{eff}^2/β^2, contribute to the tail dose [35]. For protons, the tail dose is negligible as they do not undergo fragmentation [36].

2.1.3.2 Nuclear Interactions of Protons

Charged particles can undergo collision directly with the nuclei of the material they are passing through. Even if these interactions give only a small contribution to the total amount of energy loss compared to electromagnetic interactions, they can be very important to range verification. Nuclear interactions can take the form of elastic or inelastic collisions [24, 32]. In elastic collisions, kinetic energy is conserved, and the nucleus remains intact, and are thus not of interest here. This is similar to MCS, but due to the strong nuclear force as opposed to EM interactions. However, the nuclear reactions of interest between the incoming ions and the target nuclei are presented below.

- **Compound Nuclear Reaction:** When a low-energy proton (typically 10–20 MeV) interacts with a target nucleus, it can become fully absorbed, forming a highly excited intermediate state known as a compound nucleus. In this process, the proton's energy is redistributed among all nucleons, and the compound nucleus decays after a brief lifetime (~10^{-16}–10^{-18} s), emitting one or more particles. The reaction is approximately isotropic due to internal equilibration and is governed by statistical probabilities, largely independent of how the compound nucleus was formed. It can be expressed as:

$$a + X \rightarrow C^* \rightarrow Y + b \tag{2.1.8}$$

where a is the incident particle, X the target, C^* the compound nucleus, and b the emitted particle(s).

- **Direct Reactions:** At higher projectile energies (>20 MeV), direct reactions dominate. In these fast processes (on the order of 10^{-22} s), the incoming proton interacts with only a few nucleons in the target, often resulting in the emission of a particle and leaving the residual nucleus in a ground or excited state. The angular distribution of emitted particles is characteristic of the specific reaction mechanism.
- **Pre-equilibrium Reactions:** Pre-equilibrium reactions occur between the timescales of direct and compound reactions. Energy is partially shared among nucleons before equilibrium is reached, allowing the early emission of high-energy particles with distinct angular distributions. Toward the end of this stage, individual nucleons may evaporate from the excited nucleus, similar to molecules escaping from a hot liquid.

2.1.3.3 Overview of Gamma-Ray Decay

During PT, proton interactions with patient tissue produce a broad spectrum of secondary particles, including gamma rays, through nuclear reactions that often leave product nuclei in excited states. These states de-excite promptly (within nano to picoseconds) via gamma-ray emission [24, 32].

Gamma rays originate from transitions between nuclear energy levels, with energies defined by the difference between the initial and final states. Excited states are typically populated following the decay of a parent nuclide or from inelastic nuclear interactions. As shown in Fig. 2.1.8, ^{60}Co decays yield characteristic ^{60}Ni gamma-ray transitions, whose emission probabilities (branching ratios) inform the expected photon yield per disintegration.

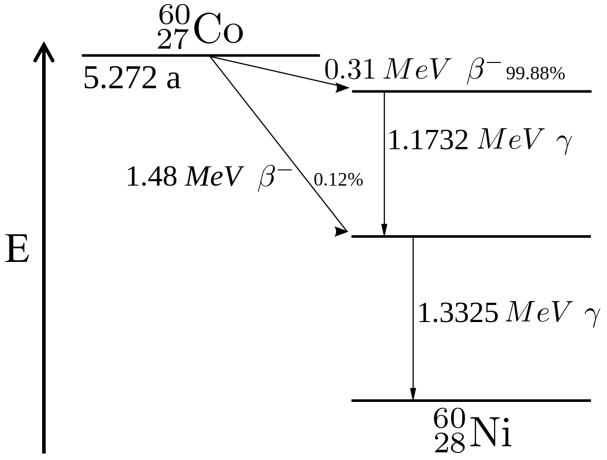

Figure 2.1.8: Decay scheme of ^{60}Co illustrating major gamma transitions and branching ratios [24].

Since nuclear states have well-defined energy levels, emitted gamma rays are nearly monoenergetic, enabling calibration of energy resolution using sources like ^{60}Co. However, if the

emitting nucleus is in motion, Doppler broadening occurs. This effect arises when the excited nucleus decays before coming to rest, causing an angular-dependent energy spread of ~1% in the detected gamma rays [24].

Doppler broadening impacts both energy and angular resolution in Compton camera systems. The magnitude of the broadening depends on the recoil direction relative to the detector, and geometrical misalignments can amplify resolution loss. Accurate modeling of this anisotropic broadening is critical, as discussed further in Section 6.3.1.

2.2 SOLID GAMMA-RAY DETECTORS

Solid gamma-ray detectors can be classified into two main types: semiconductors and scintillators. Due to their higher density compared to gas-based systems (such as ionization chambers), these detectors are more effective at capturing gamma rays that might otherwise pass through with minimal interaction. Scintillators, being denser and available in larger sizes, generally offer higher detection efficiencies. On the other hand, semiconductors have significantly lower ionization energies, leading to the production of more charge carriers per ionizing event, resulting in superior energy resolution. The CC systems investigated incorporate both solid detector types. The relevant mechanisms of action of each detector type are described in this section.

2.2.1 Scintillation Detectors

Scintillators are materials that emit light immediately upon exposure to ionising radiation. This occurs when the ionising photons transfer their kinetic energy to the scintillator material through mechanisms such as photoelectric absorption, Compton scattering, and pair production, leading to electron excitation and ionisation. The de-excitation of these electrons results in the emission of light. The intensity of the emitted light is proportional to the energy of the incident radiation and can be detected by a photodetector, as seen in the instrumentation process depicted in Fig. 2.2.1.

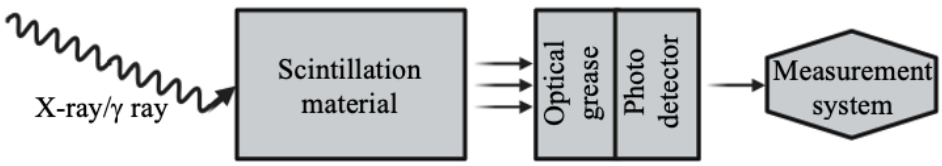

Figure 2.2.1: A schematic showing a typical instrumentation setup associated with the scintillation process.

Scintillators can be categorised into two broad types: organic and inorganic [24]. Organic scintillators are commonly used for detecting fast neutrons and beta particles, while inorganic

scintillators are typically employed for gamma-ray detection. The structure of a scintillating detector is made up of two parts: (1) the scintillation material, and (2) a photodetector to create electrical signals from the ultraviolet (UV) or visible-light photons emitted by the scintillating detector. Photodetectors relevant to this study are discussed in more detail in Section 2.3.

The potential of a material to be used as a scintillator is dependent on the excited state lifetime, luminosity, and the emission maxima [37]. Scintillation efficiency (η_{scint}) is characterised by the relationship between conversion (β), luminescence (S), and transfer (Q) in Eq. 2.2.1. The parameter $2 \leqslant \beta \leqslant 3$ holds true for most scintillation materials [38].

$$\eta_{scint} = \beta SQ \tag{2.2.1}$$

Given the relevance to this study, the following discussion will concentrate on inorganic scintillators and their scintillation mechanisms. The materials of interest are $LaBr_3$:Ce, SrI_2:Eu, and Cs_2LiYCl_6:Ce. These scintillators have high light output, fast decay times, and good energy resolution, making them ideal for use in CCs.

2.2.1.1 *Inorganic Scintillators*

The mechanism of scintillation in the crystal is dependent on the structure of the crystal lattice itself and whether the crystal is pure or activated. In a pure crystal lattice, electrons are restricted to specific energy bands, characterised by the conduction band and the valence band. The valence band contains electrons that are bound to the crystal lattice, while the electrons in the conduction band have enough energy to move freely through the lattice structure. The region between the valence and conduction bands is the energy band gap, and it represents the region with no available energy states for electrons.

The complex process of scintillation can be simplified into three consecutive stages: absorption, migration, and emission. Figure 2.2.2 shows the effect of an incoming high energy particle across the three stages until the emission of a photon. As ionising photons pass through the scintillation material crystal lattice, they transfer kinetic energy to electrons along their path via photoelectric absorption, Compton scattering, and pair production. The kinetic energy is absorbed in the first stage, forming excitons whose momentum determines whether they are trapped or free to migrate, creating electron-hole pairs. In the second stage, migration occurs, whereby the energy transfer can excite electrons across the valence band. When electrons recombine with holes in the valence band, scintillation photons are emitted by the material. The efficiency of this luminescence process is given by S in Eq. 2.2.1. However, this process is inefficient because the absorption and emission spectra of pure crystals often overlap, known as non-radiative recombination, causing the emitted photons to be reabsorbed. Consequently, few photons are emitted per decay, and those that are released frequently have too high an energy to be effectively detected. The remaining electron-hole pairs recombine in the emission stage, and the intrinsic efficiency is quantified here by Q.

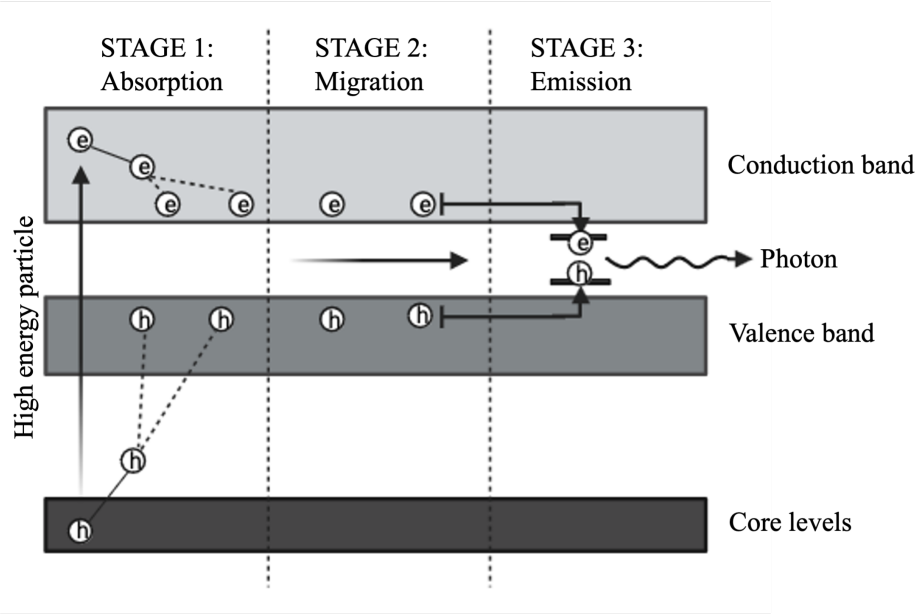

Figure 2.2.2: A schematic of the various stages involved in a doped scintillator, where the labels e and h are electrons and holes respectively.

To enhance the likelihood that scintillation photons with suitable energies are emitted, small amounts of impurities, known as activators, are typically introduced into inorganic scintillators (e.g. ^{nat}Eu in SrI_2:Eu). These activators create specific energy states within the crystal's band gap, known as luminescent centres. Unlike the pure crystal structure, the presence of activators introduces unique, more closely spaced energy regions within the previously inaccessible band gap. Electrons in the conduction band can now thermalise through these various energy states created by the activators until they reach a configuration that allows a transition to the ground state. Upon de-excitation to the ground state, there is a high probability of photon emission. Additionally, the energy sites created by activators increase the wavelength of the emitted photons, ensuring that their energy remains within the band gap. This results in lower energy photon emissions and prevents re-absorption, improving the overall performance of the material as a scintillator. Overall, the introduction of these luminescent centres helps in the efficient conversion of absorbed ionising radiation into visible light, which can then be detected by photodetectors. The overall conversion efficiency of a scintillation material is defined by the number of photons generated per unit energy ($N_{e/h}$) of the incoming particle:

$$N_{e/h} = \frac{E_{inc}}{\beta E_g} SQ \tag{2.2.2}$$

Where the multiplication stage electron-hole pairs are represented by $N_{e/h}$, S is the efficiency as described above by which an energy carrier excites, and Q is the quantum efficiency.

2.2.2 Semiconductor Detectors

Semiconductor detectors are materials that generate an electrical signal when exposed to ionising radiation. This process occurs when photons transfer their energy to the material via interactions such as photoelectric absorption, Compton scattering, and pair production, resulting in the excitation and ionisation of electrons within the material lattice. The movement of these charge carriers (electrons and holes) creates an electric current that is proportional to the energy of the incident radiation. This electrical signal can be measured and analysed to determine the properties of the radiation [24].

On an atomic level, semiconductor detectors have a lattice crystal structure consisting of a periodic array of atoms, resulting in the formation of band gaps of permitted energy states for electrons. The magnitude of this band gap characterises a material into an insulator, semiconductor, or a conductor. As illustrated in Fig. 2.2.3, a conducting material has no band gap and charge flows freely between the valence and conduction band, whereas the band gap of an insulator is too large to overcome. A semiconductor is an interesting case because charge can flow under certain circumstances. When an electron transitions from the valence band to the conduction band, it leaves behind a vacancy. This vacancy, known as a hole, has a positive charge relative to the remaining electrons because of the decreased screening of the protons in the crystal lattice. Holes act as positively charged carriers within the semiconductor. Under the influence of an applied electric field, these charge carriers will drift to opposite sides of the semiconductor.

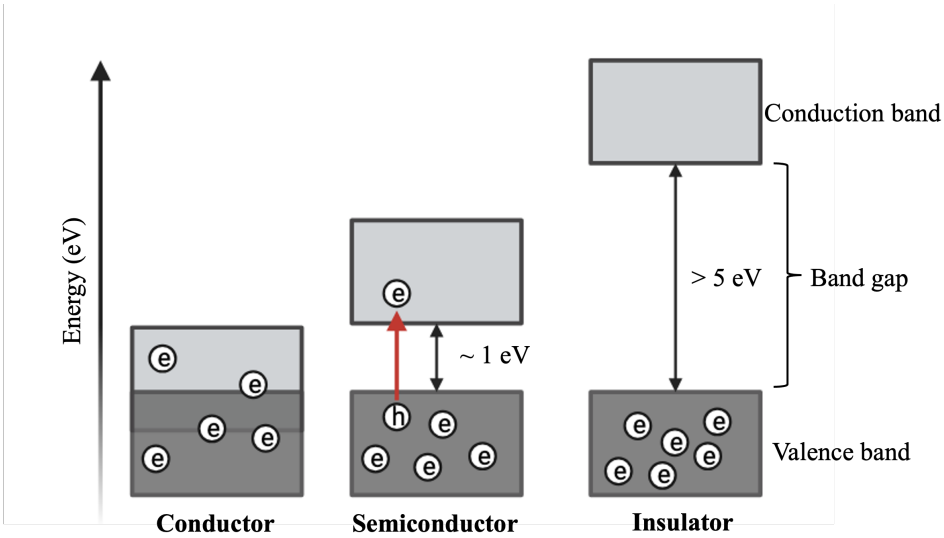

Figure 2.2.3: A schematic representing the role of a band gap in determining a material type, where the labels e and h are electrons and holes respectively.

Semiconductor detectors rely on adding impurities known as dopants to enhance their detection capability, not unlike the activators discussed in Section 2.2.1.1. If a semiconductor detector has no impurities, it is known as intrinsic and the number of holes in the detector valence band should equal the number of electrons in the conduction band. Doping in semiconductor detectors involves the intentional introduction of impurities into the semiconductor material to modify its electrical properties, creating extrinsic semiconductors. Common

dopants include elements from group III (e.g., boron) or group V (e.g., phosphorus) of the periodic table. Doping with group III elements creates p-type semiconductors, while group V elements create n-type semiconductors. The primary purpose of doping is to increase the number of free charge carriers (electrons or holes), which improves the conductivity of the semiconductor and enhances the efficiency of charge collection. When a semiconductor is doped, the added impurities introduce additional energy levels within the band gap. These new levels facilitate the excitation of electrons in the conduction band or the creation of holes in the valence band, thus enhancing the material's sensitivity to ionising radiation.

CZT, discussed further in Section 3.1, is the semiconductor material used in this study. CZT is a wide band gap semiconductor alloy capable of functioning as an x-ray and gamma-ray detector at room temperature due to its sufficiently large band gap. It offers an energy resolution of ~ 1% at 511.0 keV, making it advantageous for high-resolution gamma spectroscopy without requiring the cryogenic cooling necessary for other semiconductor detectors, such as hyper-pure germanium (HPGe). While manufacturers do not disclose the exact composition of their CZT crystals, the crystals used in this work comprised roughly 48% cadmium, 2% zinc, and 50% tellurium. It is created by merging p-type and n-type semiconductors in thermal equilibrium to form a p-n junction, introducing more charge carriers. Under these circumstances, the difference in carrier concentrations leads to the mass diffusion of free charge carriers across the junction. This diffusion results in recombination, leaving only static charges within the crystalline lattice. These static charges establish an internal electric field that stops further migration of charges. The region where this occurs is known as the depletion region. A schematic illustrating this process is provided in Fig. 2.2.4.

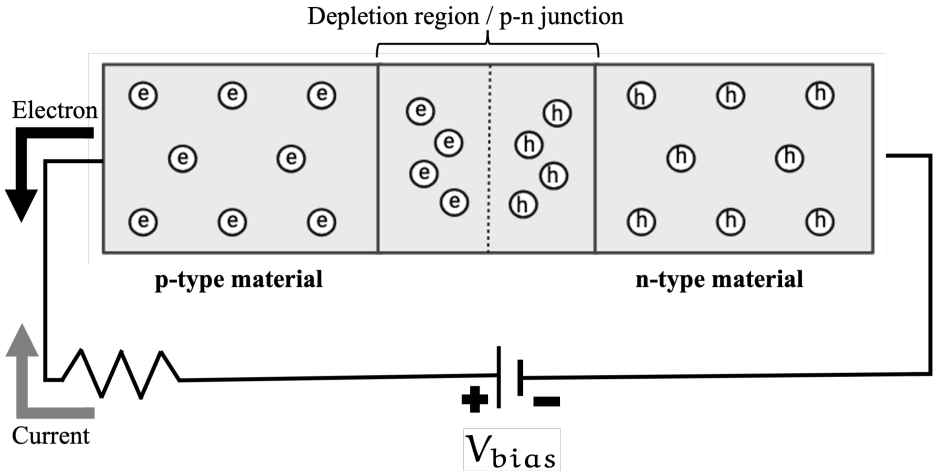

Figure 2.2.4: An illustration of the principle working of a semiconductor p-n junction.

When a potential difference is applied, the bias voltage (V_{bias}) increases the internal field (V_{int}) and, consequently, the width of (W) of the depletion region, given by:

$$W = \sqrt{\frac{2\epsilon(V_{int} - V_{bias})}{q}[\frac{1}{N_a} + \frac{1}{N_d}]} \sim \sqrt{\frac{2\epsilon V}{qN}} \tag{2.2.3}$$

Where ϵ is the dielectric constant, the charge of an atom is given by q, N is the concentration of the dopant in the region with the least doping, and N_a and N_d are acceptor (p-side) and donor (n-side) concentrations respectively. Electrons generated in the depletion region are driven by the electric field, resulting in a current. The field's bias is selected to optimise carrier mobility saturation without reaching levels that would cause breakdown or runaway currents. The movement and collection of these charges by the electric field form the fundamental principle of signal generation. When radiation is fully absorbed by the semiconductor, the quantity of liberated charge carriers is directly proportional to the energy of the incident radiation.

2.3 SIGNAL COLLECTION

To use scintillation detectors, the photons generated through the scintillation process need to be converted into an electrical signal. The most established way to do this is by using a PMT, a device that has existed since the 1940s [39]. PMTs are still widely used in present-day experiments, such as in this work; however, alternate signal collection methods exist. The rapid advancements in solid-state physics have spurred significant innovations in photon detection technologies, including the development of semiconductor-based alternatives to PMTs. Among the most successful of these is the silicon photomultiplier (SiPM), first introduced in the late 20^{th} century [40, 41].

2.3.1 Photomultiplier Tubes

A PMT is a sophisticated vacuum tube that converts scintillation light into a highly sensitive electronic signal, as shown in Fig. 2.3.1. When photons from the scintillator reach the photocathode, they release electrons via the photoelectric effect. These primary electrons are accelerated towards a series of dynodes, where each dynode impact releases multiple secondary electrons, amplifying the signal. This process continues through the dynode chain, providing a gain of up to 10^5 to 10^8 electrons per initial photoelectron, depending on the applied voltage and number of dynode stages [24, 42]. Finally, the amplified electron cloud reaches the anode, where it's transmitted as a measurable pulse to the analysis circuitry.

The time spread of the electron transit, or the single photoelectron transit time spread (SPT), is determined by several factors: the time taken by electrons to travel from the photocathode to the first dynode, transit between dynodes, and the path to the anode. The initial photoelectron velocity and focusing geometry of the photocathode significantly impact this spread, and it can be minimised by adjusting voltages between the photocathode and first dynode [43]. However, increasing the gain excessively can lead to space charge effects near the last dynodes or at the anode, introducing non-linearity in the PMT response, which reduces energy resolution [42].

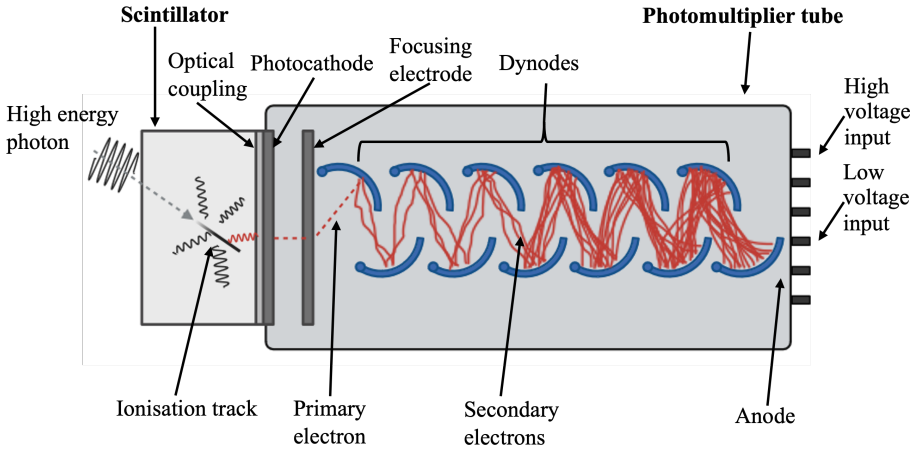

Figure 2.3.1: An illustration of a scintillation crystal optically coupled to a PMT, including a schematic of the detector's operational principle. Reflective material coats the scintillator's outer surfaces to reduce scintillation light loss. Inside the vacuum tube, the photocathode and anode, along with additional electrodes, capture and amplify the light signal. The dynode chain is powered by a voltage divider circuit, ensuring efficient signal processing.

Common materials used for the photocathode, such as Na_2KSb or K_2CsSb, have low work functions, optimising electron emission efficiency. Dynodes are typically coated with secondary emissive materials such as Cs_3Sb or magnesium oxide to enhance secondary electron yield. For improved light capture, the PMT is coupled to the scintillator with silicone-based optical grease, and a reflective coating around the scintillator maximises photon capture by redirecting light toward the PMT. Additionally, optical coupling materials are applied to match the refractive indices of the scintillator and PMT, minimising reflection losses, while magnetic shielding prevents external interference that could alter electron trajectories within the PMT [43]. In this work, an eight-stage Hamamatsu R2083 PMT was used for signal amplification. The photocathode of the PMT was made from a semi-transparent ∅46 mm bialkali metal material. In this work, the detector energy response was taken from the anode, after the last dynode. This signal has optimal energy resolution but poorer timing resolution after undergoing the full signal amplification. For the best time output, the fast timing signal was extracted at the first dynode, compromising on energy resolution. These two signals are explained in more detail in Section 3.2.

2.3.2 Silicon Photomultipliers

SiPMs are highly sensitive semiconductor devices composed of an array of microcells, typically ranging from 100 to 1000 per mm², each functioning as a Single Photon Avalanche Diode (SPAD) [44]. These microcells work in parallel to detect low-intensity light levels, particularly in photon-counting applications. The SPAD within each microcell is based on a silicon p-n junction. When a photon penetrates the silicon, it can be absorbed, transferring its energy to an electron. This causes the electron to jump from the valence band to the conduction band, generating an electron-hole pair. By applying a reverse bias across the p-n junction, the electron-hole pairs are accelerated—electrons toward the cathode and holes toward the anode.

If the reverse bias exceeds a threshold known as the breakdown voltage (around 24 V for the SiPMs used in this work CapeScint Website [45]), the charge carriers gain sufficient kinetic energy to cause impact ionisation, resulting in a cascade of secondary charge pairs. This process is known as an avalanche breakdown [46].

SiPMs typically operate at an overvoltage, which is a voltage higher than the breakdown voltage, usually around 10–25% above the threshold, to ensure efficient photon detection. The exact recommended overvoltage varies with specific products. To prevent uncontrolled avalanches and stabilise the operation, a quenching resistor is integrated in series with each SPAD, limiting the current and quickly restoring the bias voltage once the avalanche has subsided [46]. This self-quenching mechanism allows the diode to rapidly reset and be ready for the detection of subsequent photons.

Two critical performance metrics for SiPMs are photon-detection efficiency (PDE) and noise characteristics. PDE refers to the ratio of detected photons to incident photons, and is highly dependent on the wavelength of the incoming light [47]. For this reason, careful consideration must be given to pairing SiPMs with scintillators that emit light within the optimal spectral range of the SiPM [48]. Noise, primarily manifesting as dark counts, represents the occurrence of false signals in the absence of light. These events are caused by thermally generated charge carriers initiating an avalanche within the device. Since dark count rates (DCR) are temperature-dependent, the SiPM's performance is closely tied to environmental conditions, with higher temperatures leading to increased noise. Both PDE and noise also scale with the applied overvoltage; higher overvoltages enhance PDE but simultaneously increase the dark current, necessitating a careful balance to optimise performance.

2.4 PRINCIPLES OF COMPTON SCATTERING AND IMAGING

A CC relies on the principles of Compton scattering (see Section 2.1.1.2) to determine the direction of incoming gamma rays. It typically consists of two detection layers: a scatter layer and an absorber layer. Gamma rays ideally undergo a single Compton scatter in the scatter layer, where the recoil electron energy is measured (E_1), and the scattered photon is then absorbed in the absorber layer, where its energy is recorded (E_2). The gamma-ray initial energy E_0 is given by:

$$E_0 = E_1 + E_2$$

The scattering angle can be calculated using the Compton equation:

$$\theta_1 = \cos^{-1}[1 + m_e c^2 (\frac{1}{E_0} - \frac{1}{E_0 - E_1})] \tag{2.4.1}$$

Eq. 2.4.1 is a rearranged version of the Compton scattering equation, described in Eq. 2.1.2.

The source of the gamma rays is located on the surface of a cone, known as the Compton cone, with an opening angle of $2\theta_1$. The axis of this cone is defined by the interaction points in the scatter and absorber layers, and its vertex is at the Compton scattering interaction point. Each validated event pair provides a Compton cone, as is represented by Fig. 2.4.1 where a gamma-ray source is seen to emit a gamma ray which scatters in the scatterer module and is fully absorbed in the absorber, and whose position is reconstructed by the angle θ_1 into the surface of a Compton cone. The intersection of multiple cones can pinpoint the gamma-ray source. The kinematics of a CC can be validated by plotting the energy-energy matrix across the scatterer and absorber modules, as seen in Fig. 2.4.2 [49]. The diagonal line in the scatterer-absorber energy-energy matrix represents the events where the sum of the energies deposited in the scatterer (E_1) and absorber (E_2) equals the total energy of the incident gamma-ray photon. The Compton-scattered coincidence events across the CC are surrounded by the white rectangle.

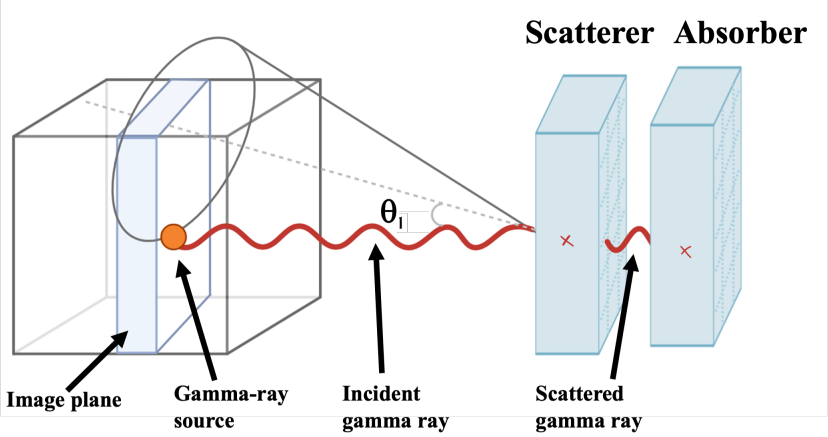

Figure 2.4.1: An illustrative representation of the principal mechanism for a two-stage CC. The Compton scattering angle defines the cone's opening angle. The axis of the cone is formed by the line connecting the two interaction points in the detectors, with the apex located at the interaction point in the scatterer detector. The convergence of multiple such cones reveals the source position.

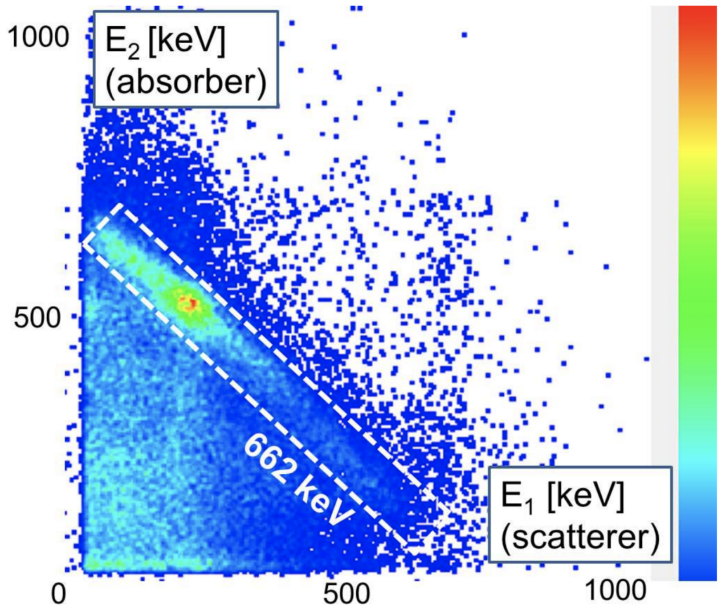

Figure 2.4.2: An example event map from a prototype Compton camera is shown, comparing the energy deposits in the scatterer (E1) and the absorber (E2). The region enclosed by a dashed line of white rectangles corresponds to events involving 662 keV gamma rays. Taken from [49].

2.4.1 Performance Characterisation

The performance metrics of a CC, such as efficiency, angular resolution, and image resolution, are essential for evaluating its effectiveness. This section details the efficiency parameters used in this work and their impact on performance.

2.4.1.1 Compton Camera Efficiency

Several interdependent factors influence the performance of a CC, with efficiency serving as a key figure of merit. CC efficiency is defined as the ratio of the number of successfully reconstructed (imageable) Compton events to the total number of emitted gamma rays. This metric captures the overall capability of a given design to convert available photon interactions into usable image data.

The source-to-detector distance significantly affects this efficiency due to geometric attenuation and increased probability of gamma rays scattering outside the FOV. To mitigate this, the FOV of the scatter detector—which corresponds to the solid angle subtended by the source-should be maximised. This is typically achieved by enlarging the surface area of the scatter layer to intercept a greater fraction of the incident gamma flux.

Efficiency also depends on the interaction probability within the scatter layer, governed by the material's density, atomic composition, and thickness. Materials with higher Compton scattering cross-sections and optimised geometries increase the likelihood of primary photon interaction. However, these interactions must not result in photon absorption; instead, the

scattered photon should exit the scatter layer without being attenuated, which is influenced by both the photon energy and the self-absorption properties of the material.

Similarly, the absorber layer must be designed to maximise the solid angle coverage relative to the scatter layer, typically by reducing their separation and expanding the absorber surface area. The probability that a scattered photon undergoes photoelectric absorption in the absorber increases with both material Z and detector thickness.

By encapsulating the entire interaction chain from gamma emission through to successful imageable events, CC efficiency serves as a comprehensive and quantifiable performance metric. It enables objective comparison across different camera configurations and material choices. A value approaching 1 would imply that nearly all emitted gamma rays result in usable Compton events, signifying an ideal system. While such performance is practically unachievable, improvements in efficiency directly correlate with higher imaging sensitivity and reduced acquisition times, which are critical for clinical and research applications.

2.4.1.2 Image Resolution

Image resolution refers to the ability to distinguish between closely spaced gamma-ray sources or features within the field of view (FOV). Good image resolution in a CC is crucial because it directly impacts the camera's ability to accurately locate and characterise gamma-ray sources. The resolution determines the sharpness and clarity of the images produced, affecting both the spatial accuracy and the practical applications of the camera in its ability to accurately pinpoint the location of gamma-ray sources. A small resolution value reduces the likelihood of ambiguity in identifying the source of gamma rays, which is important when dealing with complex environments where multiple sources or background radiation might be present. With optimal resolution, the images generated by the CC require less post-processing and can be analysed more quickly and accurately. This efficiency is especially important in real-time applications, such as monitoring radioactive sources or guiding radiation therapy.

The image resolution of a CC is critically influenced by the image reconstruction technique employed. The techniques employed are described in more detail in Section 5.2.7. The quality of image reconstruction depends on several factors, including the algorithms used to process the raw data and the methods for correcting distortions and artefacts.

For instance, techniques such as FBP and maximum likelihood expectation maximisation (MLEM) offer different advantages and limitations. FBP is known for its simplicity and computational efficiency, but may suffer from noise amplification and resolution degradation, particularly in the presence of high noise levels [50]. In contrast, MLEM, an iterative method, often provides improved resolution by refining the image through multiple iterations, although it can be computationally intensive and sensitive to initial guesses and noise. Additionally, advanced methods such as iterative reconstruction algorithms that incorporate Bayesian approaches or spatial constraints can further enhance resolution by incorporating prior knowledge and mitigating noise effects. These techniques can significantly improve the ability to resolve fine details and enhance image clarity. Overall, the choice of reconstruction

technique directly impacts the achieved image resolution, with iterative methods generally offering superior resolution capabilities at the cost of increased computational requirements. The performance of these techniques in achieving high-resolution images is essential for accurate source localisation and detailed gamma-ray imaging in CC systems.

The image resolution in this work was calculated from the full width at half maximum (FWHM) of the Gaussian fit to the 1D projection of each Cartesian dimension (x,y,z), taken from the 2D or 3D image matrices, discussed in more detail in Section 5.2.7. Two different methods of image reconstruction were investigated, and their parameters were optimised. Optimisation aimed to enhance the source position while maintaining the balance between clear image edges and adequate denoising. The method that produced the best quality image resolution was then selected for the main analysis. Smaller values of FWHM are indicative of better image resolution.

2.4.1.3 Angular Resolution

The angular resolution of the system is often evaluated using the angular resolution measurement (ARM). This measure accounts for the uncertainties related to gamma-ray interaction positions and energy deposition, and is not influenced by the performance of the reconstruction algorithm, but is rather a function of energy and position resolution as well as Doppler broadening [51, 52]. The ARM is the angular distance between the known source position and the nearest reconstructed Compton cone, i.e. it is a measure of the width of the Compton cone, as illustrated in Fig. 2.4.3(a), and calculated using the following formulae:

$$\theta_{geo} = \cos^{-1}\left[\frac{(r_S - r_0)\cdot(r_A - r_S)}{|r_S - r_0||r_A - r_S|}\right] \tag{2.4.2}$$

where r_A and r_S are the magnitudes of the (x,y,z) position vectors for the scattering position in the absorber and scatterer respectively, and r_0 is the known source position in (x,y,z). Figure 2.4.3(a) shows a schematic of the ARM distribution, which is calculated as the difference between Eq. 2.4.1 and 2.4.2, measured in units of degrees.

The ability of the CC to resolve adjacent point sources is then calculated as the FWHM of the Gaussian fit to the ARM distribution, as seen in Fig. 2.4.3(b), where it can be represented with respect to the FOV of the detector by taking into account the distance between the gamma-ray source origin and the scatterer component of the CC using the following equation:

$$\theta = \tan^{-1}\left[\frac{\frac{1}{2}\text{FWHM}_{\text{ARM}}}{\text{distance to detector}}\right] \tag{2.4.3}$$

where the $\text{ARM}_{\text{FOV}} = 2\theta$, calculated using Eq. 2.4.3. A smaller ARM value is desired as it indicates a better ability to distinguish between image sources.

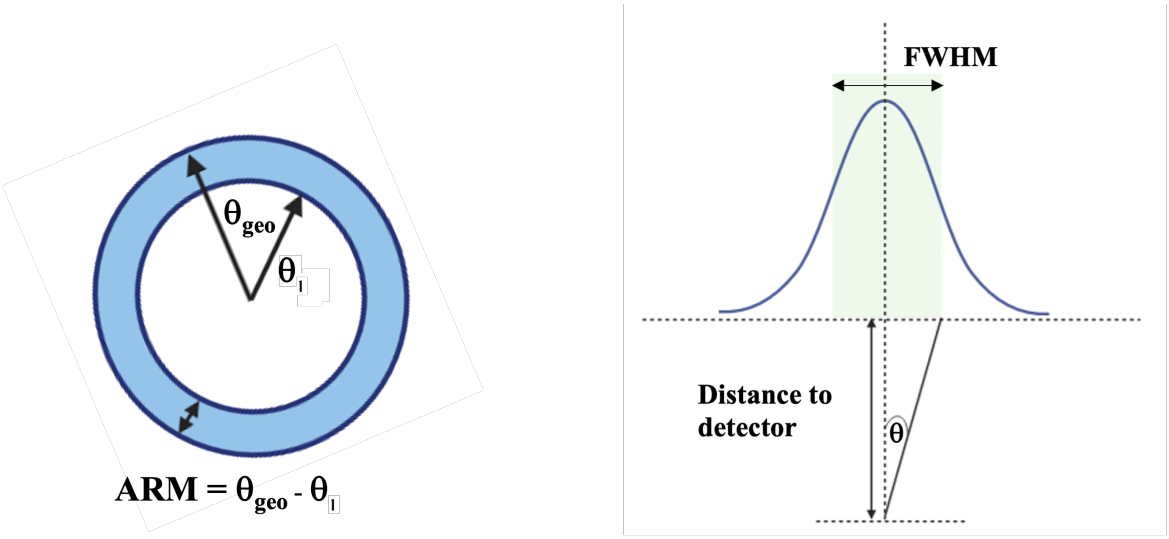

Figure 2.4.3: Illustrative representations of the angular resolution measurement: (a) a 2D slice of a CC cone, where the angular resolution is the difference between the known geometrical source angle (θ_{geo}) and the nearest reconstructed Compton cone (θ_1), and (b) shows the ability of the CC to resolve adjacent point sources, calculated as the FWHM of the Gaussian fit to the ARM distribution. The angle θ between the gamma-ray source origin and the scatterer component of the CC accounts for the FOV of the camera.

2.4.2 Compton Line Filtering

The Compton line filtering (CLF) technique is used in CCs to enhance the signal-to-noise ratio by discriminating against non-Compton events that can degrade image quality [53]. The justification for using the CLF technique lies in its ability to improve image quality by reducing the impact of events that do not contribute useful information to the imaging process. In a CC, gamma rays interact with the detector in ways that include not only Compton scattering but also photoelectric absorption, pair production, and various types of noise such as detector electronics noise and background radiation.

Without filtering, these non-Compton events could be incorrectly interpreted as valid scattering events, leading to erroneous positioning of gamma-ray sources and overall poor image quality. By applying CLF, only those events that satisfy the Compton scattering kinematics are selected, which reduces the likelihood of including non-physical events in the image reconstruction. This selective approach is crucial for applications such as performed in this study, where high-resolution and accurate imaging are essential.

For each detected event, the measured energies and scattering angle are compared against the angle measured using Eq. 2.4.1. To apply CLF for each gamma ray, it is evaluated whether the measured E_1 for a specific θ_1 lies within a predefined range around the theoretical value. The CLF can thus be expressed mathematically as:

$$E_1 <= CLF^{+*}E_0\frac{\alpha(1-\cos\theta_1)}{1+\alpha(1-\cos\theta_1)} \tag{2.4.4}$$

$$E_1 >= CLF^{-*}E_0 \frac{\alpha(1-\cos\theta_1)}{1+\alpha(1-\cos\theta_1)} \tag{2.4.5}$$

where $\alpha = E_0/m_e c^2$ and CLF^+ and CLF^- are the acceptable percentage of the upper and lower limits above or below the the theoretical value of E_1. Figure 2.4.4 shows an E_1 vs θ_1 plot taken from Draeger et al. [53] for measurements with a ^{60}Co source. Fig. 2.4.4(a) shows the unfiltered data, where the regions of high intensity correspond to the 1.33 MeV, 1.17 MeV, 661.7 keV and 511.0 keV gamma rays originating from ^{60}Co, ^{22}Na, and ^{137}Cs sources used in the measurements. The Compton lines from the 511.0 and the 661.7 keV gamma rays were visible across all θ_1, whereas the higher energy ^{60}Co gamma lines are obscured at higher θ_1 angles by background not correlated to Compton events. To demonstrate the effect of the distance of closest approach (not used or discussed in this work) and the CLF methods, Fig. 2.4.4(b) shows the measured three point source data after filtering is applied, where the high intensity Compton scatter events are clearly seen and were used for image reconstruction [53].

Energy windowing can be applied prior to CLF, the method of which is described in Section 5.2.6. In Compton scattering, θ_1 is the angle at which a gamma-ray photon is deflected after colliding with an electron. This angle can theoretically range from 0° (where the photon continues in its original direction) to 180° (where the photon is scattered directly backward). These angles correspond to physically possible interactions, and the CC events that obey this relationship are retained for further processing.

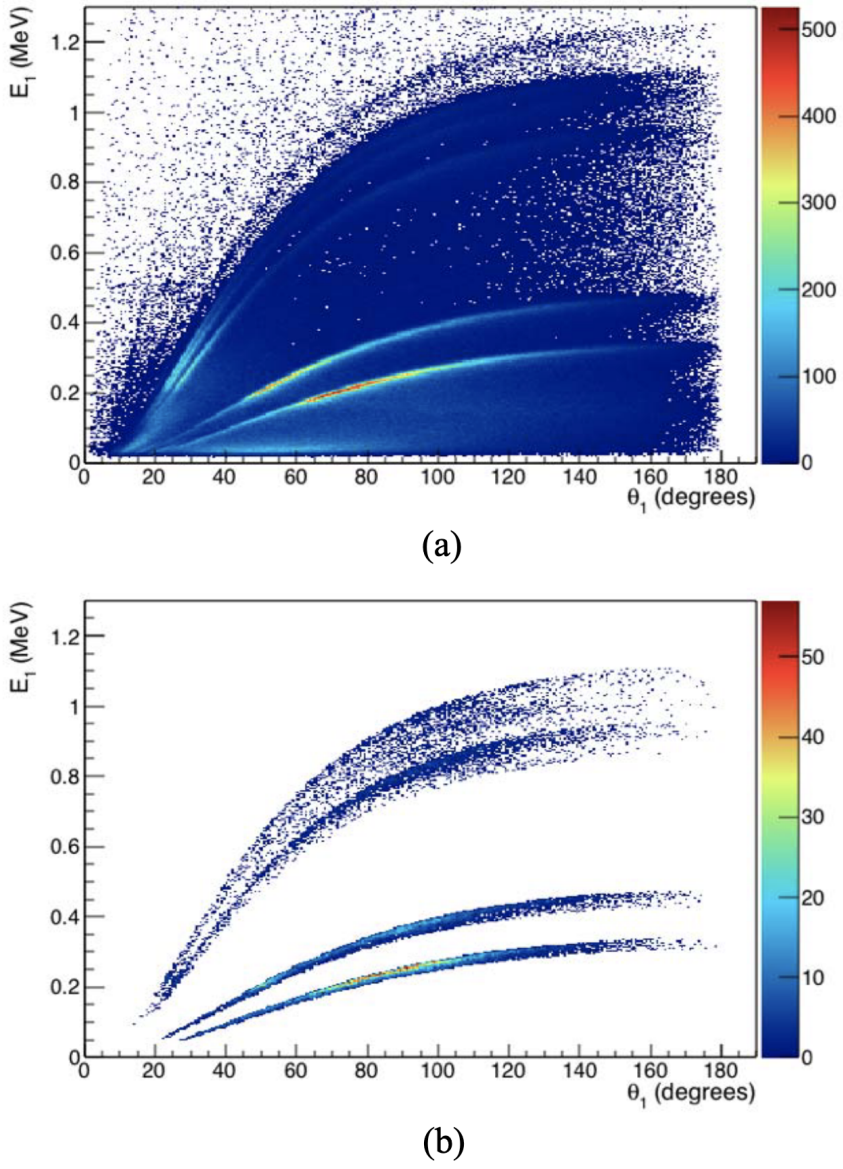

Figure 2.4.4: Measured E_1 values versus calculated θ_1 for (a) unfiltered three point source data and (b) distance of closest approach + CLF data. The CLF lines from the 1.33, 1.17 MeV, 661.7 and 511.0 keV gamma rays originating from ^{60}Co, ^{22}Na, and ^{137}Cs sources are visible in the data. Taken from [53].

3 INSTRUMENTATION AND METHODOLOGY OF CC1 DETECTORS

The first CC investigated in this thesis, referred to as CC1, features a hybrid design, combining a commercial CZT Polaris-J detector as the scatterer and a 2″ × 2″ $LaBr_3$:Ce detector as the absorber. This chapter delves into the detector geometries, signal processing methodologies, and experimental measurements undertaken to characterise the CC layers. Hybrid CC systems such as CC1 are becoming increasingly prominent due to their ability to leverage the advantages of different detector types, providing a balance between energy resolution, timing, and detector efficiency. The CZT Polaris-J detector, with its superior energy resolution and high stopping power, excels as a scatterer, while the $LaBr_3$:Ce detector was chosen for its excellent timing resolution and high light output, making it an ideal absorber for gamma-ray detection.

The combination of these detectors, along with advanced high-speed digital readout electronics, represents a significant step forward in developing a clinically viable two-stage Compton imaging system. This hybrid approach aims to optimise several critical factors necessary for medical imaging applications, including double scatter efficiency, energy and position resolution, and the ability to operate under high event count rates (up to several MHz), which are encountered in clinical PT treatments [54].

The performance of the CC1 system was evaluated using various radioactive sources and a 66.67 MeV proton beam provided by the separated sector cyclotron at iThemba LABS in Cape Town, South Africa. This chapter discusses the experimental data collection and signal processing techniques used to analyse the system's performance. The results from these tests are presented and discussed in Chapter 6.3 with particular emphasis on the CC timing requirements. Monte Carlo (MC) simulations of CC1 were performed, described in Chapter 5, and the results are presented in Chapter 6.3 with particular focus drawn to CC efficiency, ARM, and the reconstructed image resolution of the CC1.

As this work aims to develop a detector system for use in a clinical setting, understanding the interplay between the Polaris-J and $LaBr_3$:Ce detectors was vital. The Polaris detector CZT crystals have high density, making it an ideal material to be used as the CC1 scatterer. The aim was to use the strengths of the $LaBr_3$:Ce detector to offset some of the limitations of the Polaris detector: while the Polaris detector is known to have high position sensitivity (<2 mm) and excellent energy resolution (<0.8% FWHM at 661.7 keV), the timing resolution is mediocre (~ 100 ns) and the maximum dynamic energy range is limited to 3.0 MeV, restricting its ability to handle high-count rates such as those encountered during a PT irradiation of a patient [55, 56].

3.0.1 Design

The Polaris CZT semiconductor detector was combined with the 2″ × 2″ $LaBr_3$:Ce scintillation detector, creating a hybrid CC with the goal of producing high-quality gamma-ray images. The $LaBr_3$:Ce detectors, manufactured by Saint-Gobain Crystals, have outstanding timing resolution (<350 ps), great energy resolution (<2.5% at 1332.5 keV), and a higher maximum dynamic energy range (>2.0 MeV) [57].

The geometry of the CC is pictured in Fig. 3.0.1

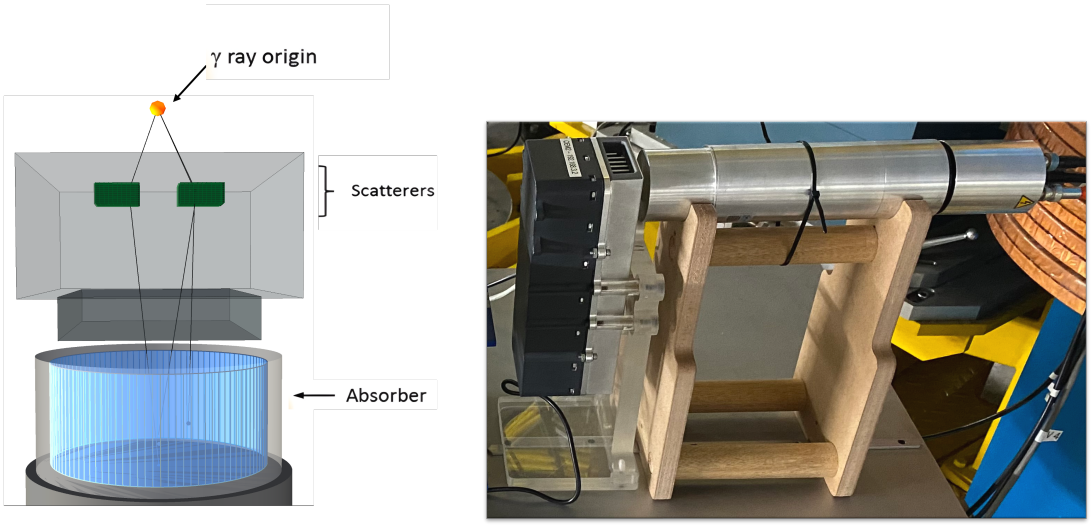

Figure 3.0.1: The CC geometry, seen in an illustration on the left and a photograph of the scatterer detector situated in front of the absorber detector, both mounted to their stands to achieve the optimum height.

3.1 POLARIS-J DETECTOR

The Polaris-J detector, manufactured by H3D Inc. (Ann Arbor, MI, USA), forms part of the UCT POLARIS system of detectors owned by the University of Cape Town Department of Physics, and commissioned for research in PG imaging by Dr. Steve Peterson. At the time of the proposal of this work, there were two Polaris detectors available for research; however, one of the detectors suffered an irreparable electronics failure soon afterward, making it unusable for this work.

The Polaris detector, referred to as "Polaris" hereafter, is a self-contained semiconductor detector (this detector type is described in Section 2.2.2 in more detail) module such that the processing electronics are integrated into the detector housing. It is designed for low-energy gamma-ray imaging (<2.0 MeV) [58]. The detector is capable of hosting a 2 × 2 array of four CZT crystals, separated by a gap of 2 mm. A photograph of the detector with the front cover removed is seen in Fig. 3.1.1(a) where the CZT crystals are clearly labelled. It can be seen that the Polaris detector used in this work housed two crystals in the uppermost quadrants, used

as the scatterer detector in CC1, with no crystals in the lower quadrants. The crystals have dimensions (x,y,z) of $(20 \times 20 \times 10)$ mm^3, and are situated on top of the pixelated anode array (11×11) in the x and y directions such that the pixel size is 1.8 mm, with a planar cathode [22].

To remain consistent with the literature, in this work the detector housing that contains the electronics and the crystals is termed the "module" or "Polaris" detector, and "crystal" will refer to individual CZT crystals within the Polaris detector.

Figure 3.1.1(b) shows the Polaris detector module front and side view, where the positioning of the detector crystals within the housing is marked by the 2×2 quadrant on the front face of the detector to guide the user. The detector is a compact, portable device, with the detector housing measuring $(165 \times 60 \times 212)$ mm in (x,y,z) that operates at room temperature. It has four external ports, namely the 12 V input power supply, the USB port for data storage, the Ethernet port for use in data streaming and sending external commands to the detector, and the coaxial input port for synchronisation with other detectors through a synchronisation-timing module (STM) pulse. For a more comprehensive explanation and characterisation of the CZT detector modules and the Polaris-J CC, please refer to [22]. For information regarding the readout electronics, see [59].

Figure 3.1.1: The Polaris CZT detector module: (a) a photograph of the Polaris module with the cover removed and the two CZT crystals labelled, and (b) the front (left) and side-view (right) photographs of the Polaris CZT detector module with the external ports labelled.

The modules can be operated in sub-pixel mode, which uses electronic processing to pinpoint the interaction site within an individual pixel, enhancing pixel resolution from 11 to 0.23 mm at a photon energy of 661.7 keV [55]. However, this increased resolution tripled the analysis time per event, reducing the overall data acquisition rate and increasing detector dead time effects [56, 60]. The timing resolution in non-sub-pixel mode was given as <100 ns by the manufacturer. A detailed investigation into the processing electronics was performed by [61].

3.1.1 Timing

The Polaris detector was designed for Compton imaging, featuring the ability to connect Polaris modules to one another via the coaxial cable. This allows for coincidence measurements

between the detector stages, achieved by means of an onboard STM pulse that was sent from the main module to successive modules via the coaxial port in 2 s intervals to align clock times and, therefore, events. The STM pulse is seen photographed in Fig. 3.1.2. This provides functionality whereby gamma rays can be measured within each detector stage independently (single-stage mode) or across multiple modules (multi-stage mode) in coincidence. Any events that meet the user-defined coincidence multiplicity (i.e. the number of detector modules that must detect an event) within a 1.5 µs window are recorded. If a trigger does not meet the coincidence requirement within this window, all detectors reset in about 10 µs. The readout time once a valid multiplicity has been detected was ~ 100 µs. It should be noted that the STM cannot distinguish between single and multiple scatter events within a detector, and these events must be filtered offline for further analysis.

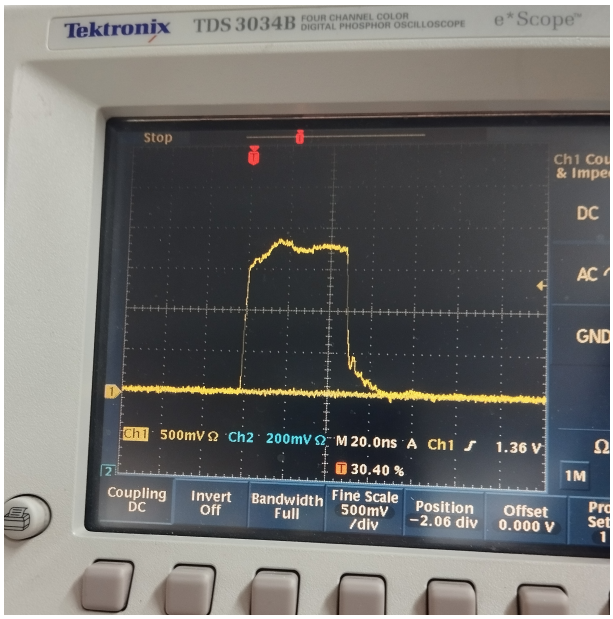

Figure 3.1.2: A photograph of the square-wave STM pulse sent in 2 s intervals from the Polaris detector and received on the oscilloscope. The x-axis time scale is 20 ns/division and the y-axis amplitude scale is 500 mV/division.

In previous studies, dead time behaviour studies were performed by Hyslop et al. using a short-lived ^{68}Ga source with an initial activity of 4.72 ± 0.24 MBq [55]. The source was attached to the tip of a hypodermic needle and positioned centrally between two Polaris detectors arranged in a face-to-face configuration, creating a FOV with dimensions of $(62 \times 42 \times 20)$ mm^3. The initial tracer activity was chosen to heavily dead time limit the module performances, determined through trial-and-error. Observations were conducted over five half-lives, allowing the activity to decay until the detectors responded linearly to the decreasing activity (down to 160 kBq). To ensure accurate centring within the FOV, a vernier caliper was used to position the source equidistantly from the edges of both modules, and event rates were monitored to keep them approximately equal. The positions of the source and modules remained fixed throughout the experiment. These measurements were conducted using the same Polaris detector as used in this work. The second Polaris detector suffered an irreparable electronics failure in the first year of this study. For these reasons, the dead time behaviour of Hyslop et al. is quoted [55].

The results of the study revealed primarily non-paralysable dead time, with a fitted parameter of 24.177(96) µs. Paralysable dead time effects were not seen during this study. Further, a coincidence window of 10 µs was chosen to process the raw, unfiltered data. This window was chosen to encompass buffering effects of the detector electronics, ensuring that no true coincidences are missed in post-processing. The prompt coincidence rate peaked at ~ 7 kHz at 3.5 MBq, while the random coincidence rate reached a maximum of 6.5 kHz. The true coincidence rate achieved a peak of 600 Hz at a source activity between 0.8 and 1.5 MBq, corresponding to a raw measured singles rate of 15 to 20 kHz in the detectors.

3.1.2 Data Collection and Output

The Polaris detector data acquisition system (DAQ) generated data in a proprietary binary format, which could be outputted in two ways: either streamed through the Ethernet port using the TCP protocol or saved directly onto the detector module's USB storage. Although H3D Inc. provided software to convert the binary data into a text file for processing, all conversions in this thesis were performed using a custom Python script. The detector was controlled via an Ethernet connection, where a TCP connection was established to send commands such as start, stop, and reset. The control and monitoring of the modules were managed through a custom Python GUI, developed by Haijian Chen from the University of Maryland, Baltimore. The final output was a human-readable text file containing a list of all triggered signals, where the structure is shown in Table 3.1.1. For this work, all interaction counts were filtered to be 1, such that only single scatter events in the detector crystals were considered.

#	Datum	Description
1	**Interaction Count**	Number of interactions within the module detected in a 10 ns window after the initial signal trigger. For a single scatter signal, this value is "1", etc.
2	**Module ID**	Specifies the module where the signal was captured. In this work, the signal was recorded in module 1.
3	**Deposited energy**	The energy deposited in the crystal, measured in keV.
4	**X-coordinate**	The x-coordinate of the interaction in the module's coordinate system, measured in millimetres.
5	**Y-coordinate**	The y-coordinate of the interaction in the module's coordinate system, measured in millimetres.
6	**Z-coordinate**	The z-coordinate of the interaction in the module's coordinate system, measured in millimetres.
7	**Timestamp**	The time of the signal detection in units of tens of nanoseconds.

Table 3.1.1: Table detailing the structure of data information from the Polaris detector module. The table summarises the details of a single scatter event, with each row corresponding to a specific data point recorded during the event.

A critical aspect of this work was the time synchronisation process between the CC detectors. This involved the Polaris DAQ connected to a channel in the Pixie-16 module via a coaxial cable, and sent to the Pixie-16 DAQ (described in Section 3.2.3.1) such that it was time-stamped. The Polaris DAQ periodically transmitted the STM pulse every 2 s, accompanied by a timestamp and an ID number, which were inserted into the data streams. H3D

manufactured their detectors to have the STM pulse for the situation whereby multiple Polaris detectors are used simultaneously. Here, a main module is designated, and the pulses are used to adjust the event times in the additional modules to align with the main module to ensure temporal synchronicity. In this work, the sync pulses were used to adjust the event times, as detailed in Section 3.3.7 to align timestamps across detector DAQs, ensuring that the final event file contained all detected events in the correct temporal order.

3.1.3 Operating Procedure

The operation of the Polaris detector during a typical experiment was carried out as follows:

1. The detector was connected to a laptop via Ethernet cables through a network switch and to the Pixie-16 module (see Section 3.2.3.1 for a more detailed description of the Pixie-16 module) channel 15 via coaxial cables.

2. Upon powering up, the detector initiated an internal boot sequence.

3. The Python script was run from the laptop terminal, establishing a TCP connection via a Python-based graphical user interface (GUI). The GUI provided real-time monitoring of the detectors, reporting on event rates, internal temperature, humidity, and other relevant information.

4. The "connect camera" button was executed from the GUI, initiating the detector to begin sending STM pulses to the Pixie-16 module. At this stage, the module monitors the environment without saving any data or STM pulses as output.

5. Once the detectors were set to record, data was streamed through the TCP connection to the laboratory computer in a list-mode binary format, which was then saved onto the computer's storage for post-experiment analysis.

6. Data processing commenced by reading the binary data from all modules, combining the data into a single array, and transforming the coordinates from the module's coordinate system to a predefined laboratory coordinate system, known as the isocentric coordinate system. This transformation was achieved by converting the positions into a 3D vector format, determining the matrix that represented the translation and rotation required for the transformation, and applying the inverse of this matrix to each position vector. The processed array was then written to a text file in a human-readable format. Although it is recognised that a binary format would have been more efficient for storage, it was deemed unnecessary for the purposes of this work, as the file sizes obtained during the experiment rarely exceeded a gigabyte of data.

3.2 2" × 2" $LaBr_3$:Ce DETECTOR

In CC development, achieving high-efficiency gamma-ray detection with excellent energy and timing resolution is crucial for accurate tracking of events across detector geometries. Historically, there were challenges in achieving both full energy peak events and excellent timing resolution because scintillator detectors typically had poor energy resolution. However, the introduction of $LaBr_3$:Ce detectors revolutionised this field by providing both excellent timing resolution and good energy resolution, along with easy maintenance. These detectors are notable for their high light output of $\sim 61 \times 10^3$ photons/MeV, substantially higher than that of NaI scintillators (38×10^3 photons/MeV) [62, 63]. This is advantageous for energy resolution, as it improves the signal-to-noise ratio and provides better statistical data. $LaBr_3$:Ce is an inorganic crystal (described in Section 2.2.1.1) with a hexagonal UCl3-type structure and a P63/m space group [64]. Due to its high density, $LaBr_3$ offers a 43% efficiency increase at 1.3 MeV compared to NaI detectors, with a significant improvement in energy resolution from 5.4% for NaI to 2.1% for $LaBr_3$ [65]. Beyond these advantages, the scintillation decay time is extremely short, meaning that the timing resolution is primarily constrained by the propagation speed of the scintillation photons [65]. For these detectors, the single-channel coincidence timing resolution is ~ 350 ps, enabling the measurement of half-lives as short as a few tens of picoseconds, depending on the experimental setup.

The Cerium (Ce^{3+}) dopant acts to enhance luminescence in the blue/UV part of the electromagnetic spectrum, with a peak emission wavelength (λ_{max}) of 380 nm [65]. The shape of the crystal is designed to optimise the solid angle, improving light collection and timing resolution. $LaBr_3$:Ce detectors come in various sizes, commonly ranging from 1" × 1" to 3.5" × 8". Selecting the optimal crystal size involves balancing intrinsic time resolution and detector efficiency. As the crystal size increases, intrinsic time resolution tends to decrease, while detector efficiency increases.

The two 2" × 2" $LaBr_3$:Ce detectors used in this study were manufactured by Saint-Gobain and each coupled to Hamamatsu R2083 PMTs and removable voltage dividers (AS2612), as seen in Fig. 3.2.1. A high voltage (HV) of -1200 V was applied to the PMT base of the $LaBr_3$:Ce detector, creating a potential difference across the cathode and anode [66]. The low voltage (LV) power supply was biased through a model 572a ORTEC pre-amplifier. These detectors, forming part of a larger array of eight detectors, were commissioned for gamma spectroscopy fast-timing measurements at iThemba LABS in Cape Town by a group led by Dr. Pete Jones [57].

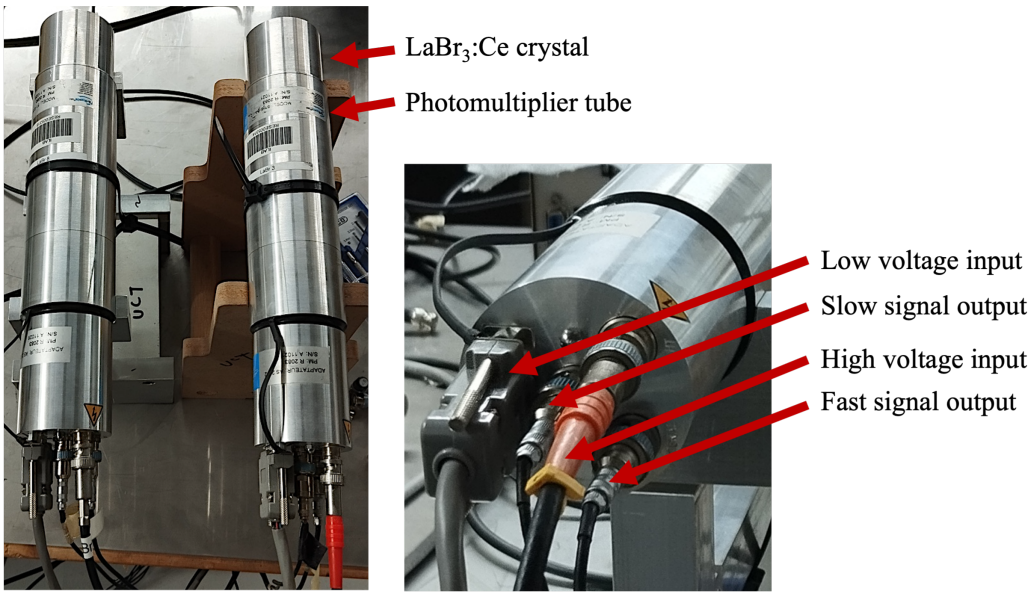

Figure 3.2.1: Labelled photographs of the detector coupled to the PMT (left), and the external ports where the PMT was biased and the signals were read out (right).

3.2.1 Energy and Timing Signals

The voltage divider provides two output signals, as seen in Fig. 3.2.2, are:

1. the slow signal, read out at the anode, after the eighth dynode of the PMT, and used to measure energy resolution, and
2. the fast signal with a negative amplitude as read out from the first dynode of the PMT.

The slow signals were shaped after amplification by the eight dynodes of the detector PMT, resulting in an overall better energy resolution and positive amplitude but compromising on the timing of the signal, with a typical decay constant (τ) of 30 µs. The negative amplitude fast signal has a much faster decay of $\tau \sim 10$ ns, seen in Fig. 3.2.2 in how quickly the signal rises or decays from its peak to the baseline. The rise time of the signal is the time between 10 % and 90 % of the signal amplitude. It was for this reason that the fast signal was best suited to timing measurements, whereas the slow signal was used for energy. The energy spectrum shown in Fig. 3.2.3 shows the emission spectrum from a ^{22}Na source, where the slow signal was seen to have a better energy resolution of 4.99(3) % than the fast signal with energy resolution of 6.77(3) % at 511.0 keV.

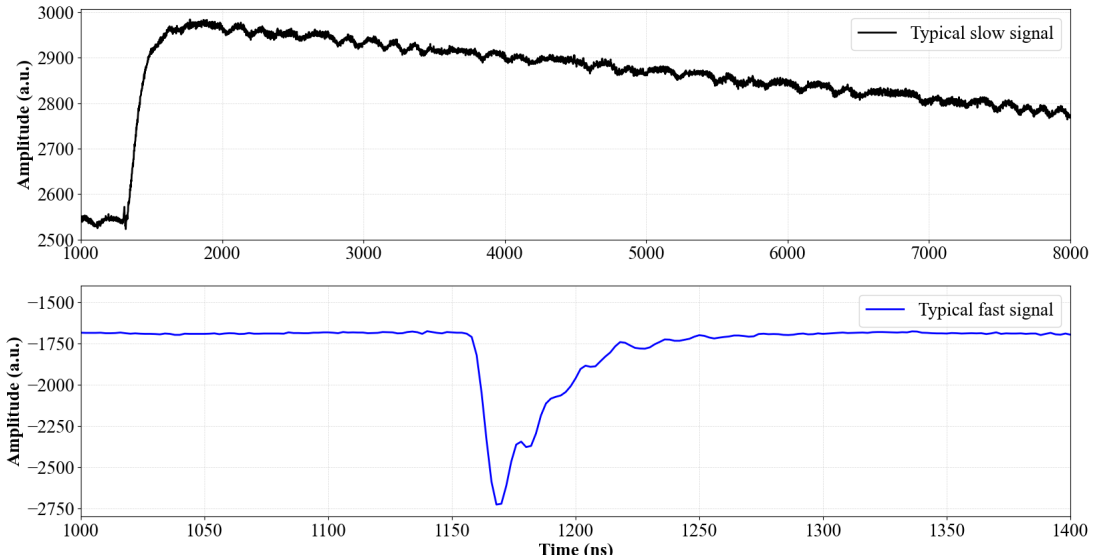

Figure 3.2.2: An example of signal traces, as read out by the $LaBr_3$:Ce detector, for slow (top) and fast (bottom) signals.

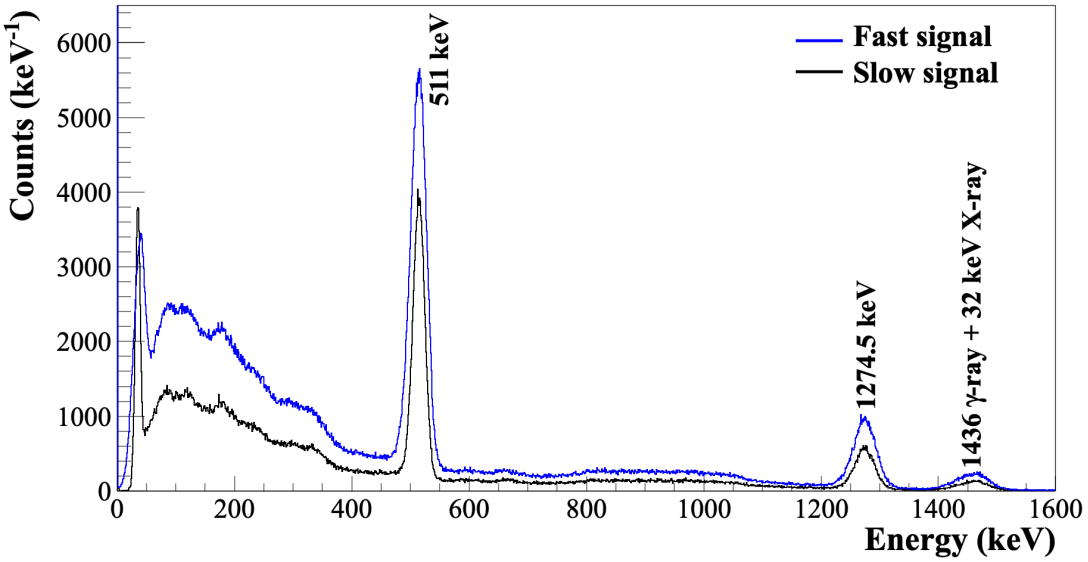

Figure 3.2.3: A plot of energy spectra from the fast (blue) and slow (black) $LaBr_3$:Ce detector signals. A ^{22}Na source was used for measurements and the gamma emission peaks have been labelled. The sum peak contribution at ~ 1460.0 keV was attributed to the ^{138}Ba contribution, a daughter isotope of ^{138}La [67].

3.2.2 Intrinsic Internal Radioactivity

$LaBr_3$:Ce detectors have a relatively high intrinsic background radiation, up to two orders of magnitude greater than that of NaI(Tl) detectors, which restricts its use in experiments with low counting rates [68]. The internal radiation within $LaBr_3$:Ce crystals arises from two primary sources: the naturally occurring radioisotope ^{138}La and the impurity ^{227}Ac. These isotopes can reduce the detection sensitivity for gamma rays with energies up to ~ 2.5 MeV. Understanding the self-activity of these isotopes was crucial for designing accurate experiments.

Natural radioactivity of ^{138}La: ^{138}La is the only naturally occurring radioactive isotope of lanthanum, with an abundance of 0.09% and a long half-life of 1.02×10^{11} years. From Fig. 3.2.4, it can be seen that ^{138}La decays through two main processes, contaminating the energy spectrum below 1.5 MeV [67]. The dominant process, EC, causes ^{138}La to decay to ^{138}Ba, emitting the characteristic 1435.8 keV gamma ray and the X-rays of barium ranging from 31.0–38.0 keV. This background peak is labelled in Fig. 3.2.3 and can obscure photopeaks of interest in the region. In the second process, ~ 34.4% of ^{138}La undergoes beta decay, resulting in a maximum beta energy of 263.0 keV, and adding to the overall β-continuum of the region. This is labelled in Fig. 3.2.6 where the peak is seen to have high intensity.

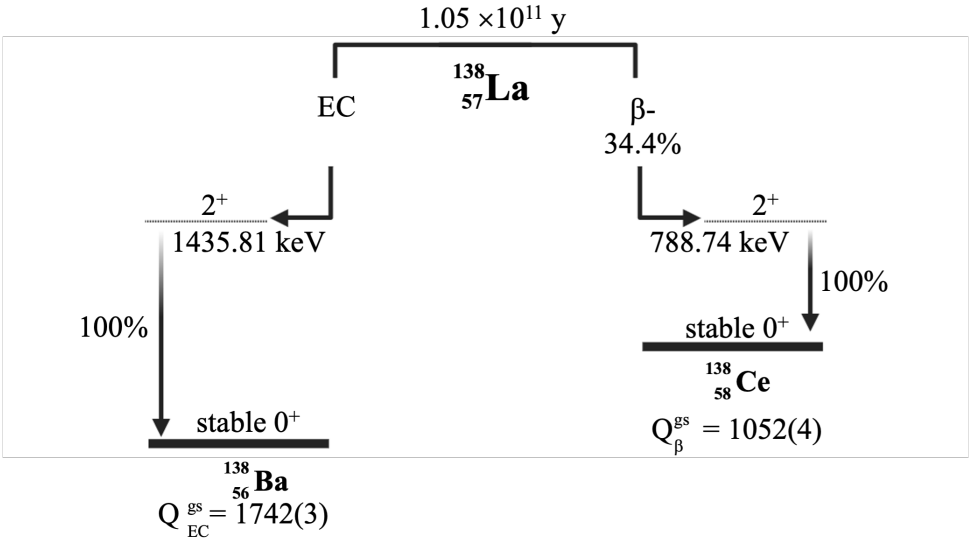

Figure 3.2.4: The decay level scheme of ^{138}La. Data was obtained from [69].

Contamination by ^{227}Ac: Due to its chemical similarity to lanthanum, the LaBr$_3$:Ce detector crystal can contain ^{227}Ac crystals as a contaminant. This isotope has a half-life of 21.77 years, and its decay chain contributes to background in the measured detector spectrum via several alpha and beta emitters, as seen in Fig. 3.2.5. The decay of ^{227}Ac, its daughter and granddaughter nuclei result in a higher energy background due to alpha particle emissions and contributes to a beta continuum up to ~ 1400.0 keV from the beta decays of ^{211}Pb and ^{207}Tl [24, 67], labelled in Fig. 3.2.6.

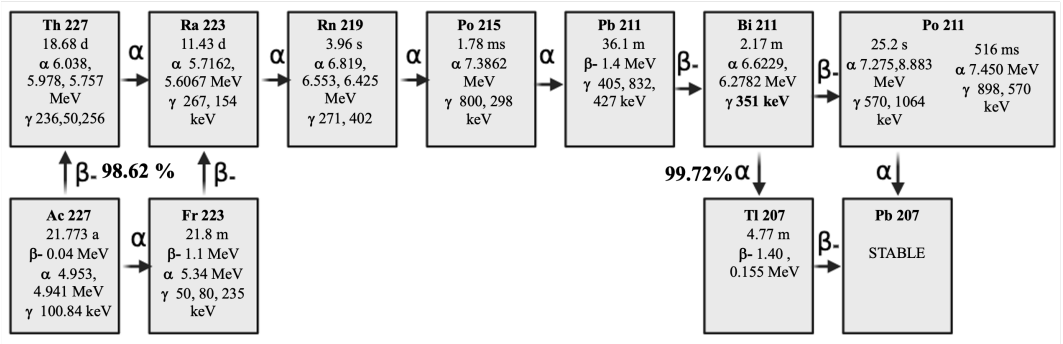

Figure 3.2.5: The actinide decay chain where the data, obtained from [69], is half life, energy of high intensity alpha and gamma rays, and the nuclide beta minus decay end-point.

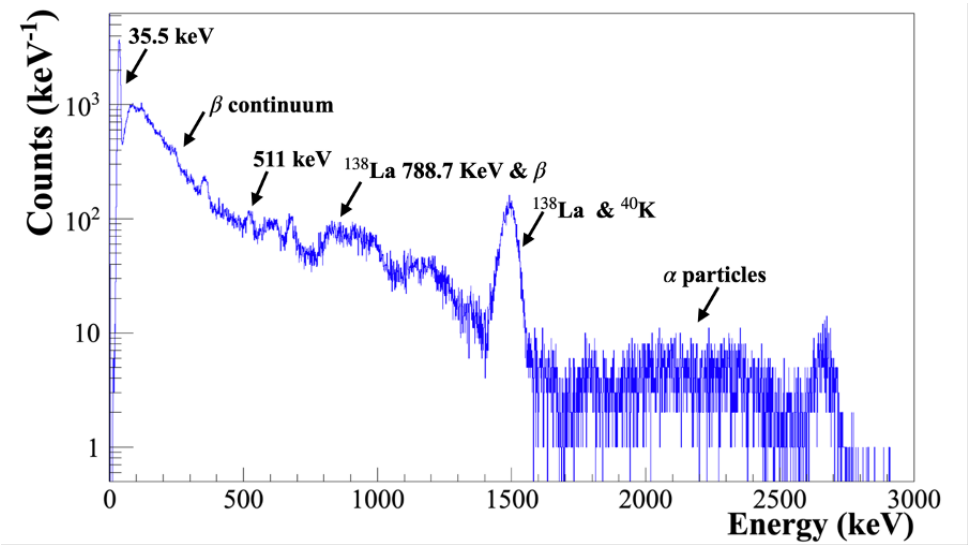

Figure 3.2.6: Background spectrum of the 2"x2" $LaBr_3$:Ce detector obtained from a 10-minute measurement. The labelled peaks arise due to the intrinsic internal radioactivity of the detector due to the material make-up of the detector.

3.2.3 Signal Processing and Data Acquisition

$LaBr_3$:Ce detectors are often used with conventional analogue acquisition systems, but this work employs them alongside high-speed digital readout electronics. Digital pulse processing (DPP) modules offer on-board processing capabilities, including pulse pileup detection, energy filtering, timestamp recording, coincidence triggering, and pulse shape analysis. The emission of scintillation light from excited states in a crystal directly influences the timing resolution, and the short decay time of $LaBr_3$:Ce detectors ensures they are not significantly affected by dead time, even at high count rates.

3.2.3.1 Pixie-16 500 MHz Data Acquisition System

In the past decade, advancements in hardware have enabled fast sampling rates of 500 MHz and above, with bit depths typically 14-bits or greater. Fast-timing scintillation detectors, such as $LaBr_3$:Ce, produce small amplitude fast signals, usually in the tens of millivolts over a range of 20.0–40.0 ns. To handle this digitised data, a powerful digital signal processing unit, typically operating at clock frequencies exceeding 100 MHz, is necessary. This setup must support parallel pipelining of data and possess sufficient processing capacity to extract spectroscopic information, such as energy signals. Additionally, it must provide a precise timing reference with a granularity significantly finer than the sampling frequency. This can be achieved through methods such as constant-fraction discriminator (CFD) (see Section 3.2.3.2) or leading-edge discrimination, where the sampling rate greatly surpasses the detector's time resolution.

The XIA Pixie-16 module is a 16-channel all digital signal processing unit, which accepts the input signals from the detector PMT. The data acquisition of each of the 16-channels were independently gated by the channel gate inputs (0-15) [70]. Data movement within

the hardware starts at the analogue front end, where incoming signals undergo analogue signal conditioning before digitisation. Analogue-to-digital converters (ADCs) then digitise these signals and the digitised data was sent to a signal processing field programmable gate array (FPGA), which performed real-time analysis. The FPGA calculates the signal's energy, arrival time, and charge-to-digital converter (QDC) sums, which form the header of the record. Additionally, the FPGA can store a copy of the incoming data stream, referred to as the trace. The combination of the header information and the trace constitutes a complete record. Each channel was self-triggered, with data being independently read out per channel. Refer to Section 3.2.3.6 for a more detailed description on the list mode data readout.

The module continuously samples signals from the detectors and uses several digital filters to extract timing and energy information from the detector pulses. Three primary filters were utilised: a digital CFD, a fast trapezoidal filter, and a slow trapezoidal filter. A detailed description of the filters used in this work follows:

3.2.3.2 Constant Fraction Discrimination

The CFD filter was used to accurately determine the time of arrival of individual pulses. This was a critical piece of information, as it enabled the precise measurement of the time difference between the delayed and non-delayed sums, providing the zero-crossing point (ZCP). Figure 3.2.7 shows how the CFD filter operates. The initial waveform (solid blue line) represents the attenuated version of the original signal, while the delayed and inverted waveform (dotted blue line) is shifted to coincide with the CFD peak. The zero-crossing point (ZCP) is marked by the intersection of the attenuated and delayed signals, providing a consistent trigger point for time-of-arrival determination, independent of the pulse amplitude. This method enhances timing precision by aligning the crossing point (black dot) with the signal peak, resulting in improved timing accuracy across variable pulse amplitudes [71].

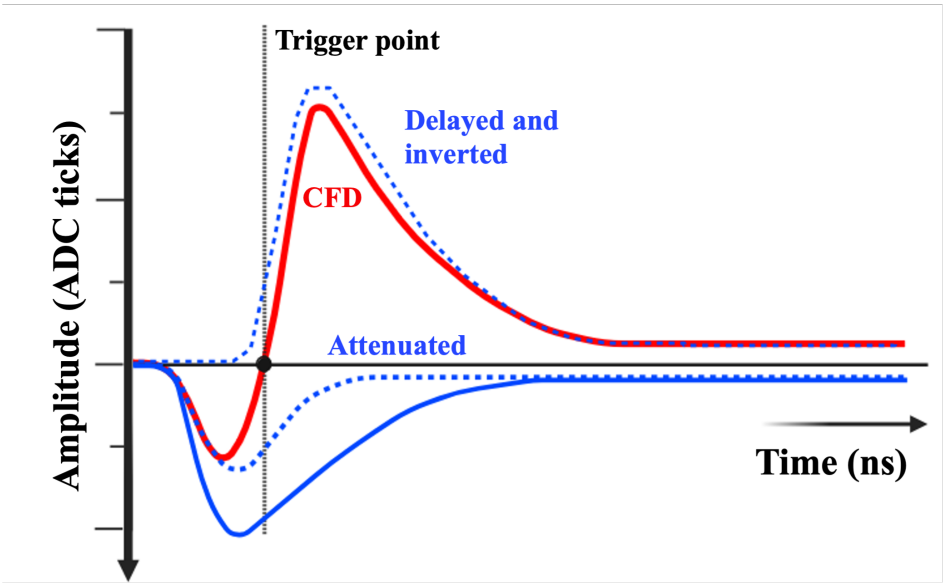

Figure 3.2.7: The digital constant fraction discriminator technique.

To improve the quality of the timing signal in fast-timing measurements, variations in the amplitude and rise time of the incoming logic signal must be minimised. These variations, which cause the output pulse to shift in time relative to the input pulse, are known as time "walk", and severely degrades the timing signal. Another factor that negatively impacts the timing signal quality is jitter. This arises from noise and statistical fluctuations in the detector signal. Achieving a signal that accurately corresponds to the event time is challenging. A critical development in this area is creating a trigger that activates at the optimal fraction of the input height, regardless of the signal's amplitude. The CFD effectively performs this function, ensuring precise and reliable timing.

The 500 MHz modules have unique characteristics compared to the 100 and 250 MHz modules due to their parameter adjustment capabilities. In the 500 MHz modules, the ADC data is reduced by a factor of 5 when entering the FPGA, effectively achieving a processing rate of 100 MHz, or every 10 ns. Within the 10 ns window, the FPGA captures five 2 ns ADC samples and determines the CFD trigger point by summing and calculating differences between delayed and non-delayed samples to find the zero crossing/trigger point. However, the FPGA in the 500 MHz modules lacks the resources to build sums for all five ADC samples in parallel with variable delays. Consequently, the CFD algorithm for these modules uses a set of fixed CFD parameters, where $w = 1$, $B = 5$, $D = 5$ and $L = 1$, determined to be the best parameters for $LaBr_3$:Ce detectors. The CFD algorithm is as follows:

$$CFD(k) = w \cdot \left(\sum_{i=k}^{k+L} a(i) - \sum_{i=k-B}^{k-B+L} a(i) \right) - \left(\sum_{i=k-D}^{k-B+L} a(i) - \sum_{i=k-D-B}^{k-D} a(i) \right) \tag{3.2.1}$$

where the ADC trace data is given by $a(i)$, the index is k, and w, B, D and L are CFD parameters.

The CFD time provided by the 500 MHz modules consists of two components: a shift within the five ADC samples and a fractional time between two ADC samples where the CFD zero-crossing occurs. The shift within these five ADC samples is represented by a 3-bit CFD trigger source represented by $[2:0]$. This fractional time is calculated by:

$$CFD_{frac} = \frac{CFD_i}{CFD_i + CFD_f} \tag{3.2.2}$$

where CFD_i and CFD_f are the absolute values of the CFD filter before and after the ZCP respectively. Making the assumption that the CFD filter has a linear trend between these values, the ZCP can be calculated:

$$t_{ZCP} = \left(\frac{CFD_{frac}}{8192} + 1\right) \times 2 \text{ ns} \tag{3.2.3}$$

3.2.3.3 *Trapezoidal Filter*

The fast trapezoidal filter was used to generate the trigger signal that initiates the DAQ process. This filter is designed to detect the leading edge of the pulse and output a signal with a fast rise time, allowing for the rapid collection of data. The slow trapezoidal filter, on the other hand, was used to measure the height of the pulse. Overall, the combination of these filters with the CFD filter enables the Pixie-16 DAQ module to provide accurate and high-speed measurements of radiation signals, making it a critical component [72].

The trapezoidal shaping algorithm used in signal processing is an approximation of the output waveform obtained from a resistor-capacitor (RC-CR) circuit driven by an idealised delta function (delta wave). In practical radiation detectors, when a radiation signal is detected, the output signal typically resembles a pulse with a fast rise and a slow exponential decay, similar to the response of an RC circuit to a delta function input. The trapezoidal shaping algorithm is designed to approximate this behaviour by shaping the detected signal.

The fast trapezoidal filter:

$$F_n = \sum_{i=n-f_r}^{n} a(i) - \sum_{i=n-2f_r-f_f}^{n-f_r-f_f} a(i) \tag{3.2.4}$$

where f_r denotes the risetime of the trapezoid and f_f indicates the flattop duration of the trapezoid. A trigger is generated when the output of this trapezoidal filter exceeds a user-defined threshold.

The slow trapezoidal filter:

$$E_n = p1 \sum_{i=n-e_r}^{n} a(i) + \sum_{i=n-e_r-e_f}^{n-e_r-e_f} a(i) + p0 \sum_{i=n-2e_r-e_f}^{n-e_r-e_f} a(i) - (p0e_r + e_f + p1e_r)b \tag{3.2.5}$$

$$p0 = \frac{e^{-e_r/\tau}}{e^{-e_r/\tau-1}} \tag{3.2.6}$$

$$p1 = -\frac{1}{e^{-e_r/\tau-1}} \tag{3.2.7}$$

where e_r and e_f are the trapezoidal filter set risetime and flattop, respectively, and measured in ADC ticks. These variables are discussed in more detail relevant to this study in Section 3.2.3.4. The variable τ is the decay constant of the tail, assuming exponential decay, and b is the signal baseline value measured as the average ADC ticks in the absence of detector pulses.

In conclusion, the accurate CFD time value is obtained by merging the integer timestamp with the fractional time derived from ADC samples surrounding the ZCP. This technique guarantees precise time measurements within the 100 MHz sampling rate limitations of the ADC in the Pixie-16 module.

3.2.3.4 Digital Data Acquisition System

For this study, data collection was conducted using the multi-instance data acquisition system (MIDAS) software, which formed part of the digital data acquisition system (DDAS), and was installed on a Linux PC [73]. This software facilitated access to all data readouts from the hardware electronics via the PCI. The DDAS software allows user control over optimisation parameters used in the moving-window deconvolution (MWD) used to shape the digitised data. Figure 3.2.8 shows a photograph of the graphical user interface where the parameters were set in the software. The relevant parameters to this study are detailed below:

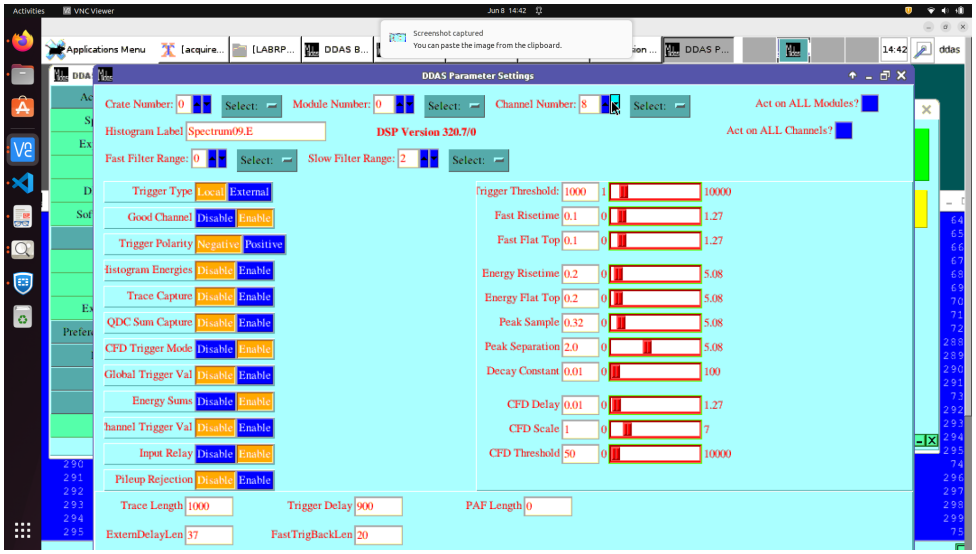

Figure 3.2.8: A screenshot of the PC window hosting the DDAS, interfaced through the MIDAS GUI and showing the parameters that can be set by the user for each channel. The parameters on the right-hand side (and before the CFD parameters) are measured in microseconds, for which the granularity was controlled using the fast and slow filter ranges.

- **Trigger threshold** The trigger threshold sets the minimum amplitude level a signal must reach to be considered a valid trigger. The waveforms were continuously captured. When a fast signal from the detector exceeds this threshold, a timestamp was recorded for that trigger, alerting the DAQ to store the waveform information. Setting an appropriate trigger threshold was critical to avoid recording noise or irrelevant low-amplitude signals, thereby reducing the data size and improving the overall signal-to-noise ratio. If the threshold was not set outside the noise, the MWD mistakenly amplified the noise. The top plot of Fig. 3.2.2 shows a fast signal. The threshold gated on the amplitude of this pulse.

- **Fast filter parameters:** Overall, the fast filter was controlled by the fast risetime and flat top parameters individually and was used to detect the arrival time of gamma rays with great precision. The fast risetime parameter forms part of the fast trapezoidal shaping described in Eq. 3.2.4, represented by f_r. It was used to determine how quickly the pulse leading edge of the incoming signal should be sampled and digitised. A shorter risetime allows for capturing the early portion of the pulse with higher time resolution. This was particularly important for signals with fast risetimes, such as the scintillation detectors in

this study. By accurately capturing the fast rise, the system can provide precise timing information about the signal.

The risetime can be affected by the type of particle causing the signal. For example, alpha particles being heavier and more massive tend to create denser ionisation tracks in the detector material, leading to faster signal risetimes. In contrast, beta particles and gamma rays, being lighter and less massive, produce more extended and less dense ionisation tracks, resulting in slower signal risetimes. Ballistic deficit, a phenomenon observed particularly in semiconductor detectors, also affects the risetime. It refers to the time delay introduced in the signal due to the finite velocity at which charge carriers (electrons and holes) drift within the detector material. When a particle deposits energy in the detector, charge carriers are created and must drift to the detector electrodes to produce a measurable electrical signal. This drifting process takes time and introduces a delay in the signal's risetime.

The fast flat top parameter controls form part of the fast shaping described in Eq. 3.2.4, represented by f_f. This parameter controls the duration over which the signal was digitised after the fast risetime window. It defines the time interval during which the signal amplitude was expected to remain relatively constant. For the fast signal, there was not enough time for the flat top to be truly flat. As such, it can be considered as a fall time. This parameter was essential for signals that exhibit a plateau-like behaviour. By capturing the flat top, the system obtains accurate information about the signal's energy deposition or amplitude. A fast detector will have a faster risetime. LaBr$_3$:Ce fast signal is ~ 400 ps, whereas a germanium detector is in the order of ~ 200 ns. For the slower risetime, a longer energy flat top value was required to give the integration sufficient time to obtain a good energy resolution out of the trapezoid.

- **Slow filter parameters:** The slow filter was used for the measurement of energy with good energy resolution and was controlled through the risetime, flat top and peak sample parameters. Figure 3.2.9 depicts the trapezoidal fitting.

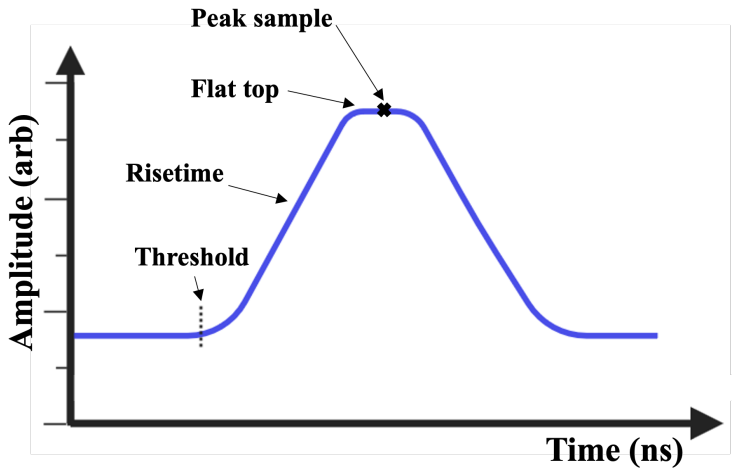

Figure 3.2.9: An illustration of the energy shaping trapezoid, labelled with the shaping parameters.

The risetime parameter, described in Eq. 3.2.4 and represented by e_r, refers to the duration it takes for the pulse to rise from the baseline at a time determined by the trigger threshold. It is a measure of how fast the detector's output signal increases when an

signal is triggered. A shorter risetime typically indicates a faster response of the detector to incoming pulses. The energy risetime is an important factor for systems that require accurate timing information and have high count rates.

The energy flat top parameter represents the duration for which the pulse remains at its maximum amplitude. It is the time interval between the leading edge and the trailing edge of the pulse when the signal remains constant at its peak value. A longer flat top indicates that the pulse retains its amplitude for a more extended period, providing better energy resolution and reducing pulse pile-up effects in high count rate situations.

Peak sample refers to the sample after trigger of the ADC sample that corresponds to the peak amplitude of the pulse, seen as the region between the dotted lines of Fig. 3.2.9. The peak sample is used to determine the pulse height (energy) of the detected radiation signal. Accurate peak sample determination is crucial for obtaining precise energy measurements and improving the system's energy resolution. The peak sample should be in range of risetime + 0.2×(flat top) to risetime + 0.8×(flat top). If the peak sample is varied within this range and the flat top is indeed flat, then any peak should not move channels. The peak sample should be preferred to be towards of the end of the flat top as this provides a better integration range, but this depends on the shape of the input signal.

- **Peak Separation:** Peak separation is the minimum time interval required between two consecutive pulses for them to be resolved as separate signals. It is an essential parameter for pulse processing in systems with a high event rate. The peak separation time should be optimised to avoid pile-up effects, where two or more pulses overlap, leading to inaccurate energy measurements. A suitable peak separation value allows the system to handle a higher count rate without losing resolution.

- **Decay Constant:** The decay constant is associated with the shaping time of the pulse processing electronics. It determines the time it takes for the pulse to decay from its peak value back to the baseline. It resembles an exponential decay (as seen in Fig. 3.2.13).

3.2.3.5 QDC Integration

Eight QDC sums, seen in Fig. 3.2.10, for which the user may set a different length to individual sums, are calculated in the FPGA of a Pixie-16 module for each channel. If enabled by the user in the DDAS software (see Section 3.2.3.4), these sums can be included in the list mode output data. The process begins at a waveform point specified by the trace delay, occurring just before the trigger point, which is determined by either the CFD trigger or the channel fast trigger, depending on the CFD trigger mode's status. The eight QDC sums are computed sequentially without overlap and are completed when all intervals have been processed.

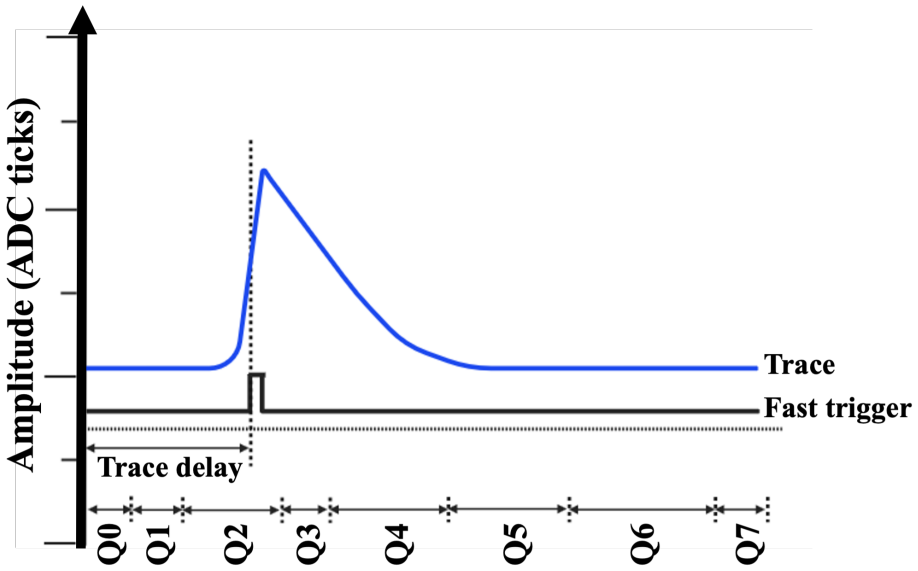

Figure 3.2.10: The eight QDC sums (labelled Q1-8) of a triggered signal.

3.2.3.6 List-Mode Data Structure

Recording measurements using list-mode enables free-running data collection, capturing energies, timestamps, pulse shape analysis values, and waveforms. The list-mode data output buffer was organised into three main sections: the buffer header, data headers for each signal, and channel headers accompanied by possible waveform data for each active channel, as illustrated in Fig. 3.2.11.

Buffer header: It was composed of six 32-bit words and includes information on the number of words in the buffer, module number, run type, and start time of the run.

Signal header: Each signal header was composed of three 32-bit words and contains data on the hit pattern (indicating which channels were read out), and the arrival time of each signal. Signals were recorded sequentially based on their detected arrival times.

Channel header: Each channel header includes nine 32-bit words and contains details on the number of 32-bit words for that channel, fast trigger time, energy, and pulse shape analysis values. This information was followed by any waveform data recorded for that channel, where each 32-bit word consists of two 16-bit trace data samples.

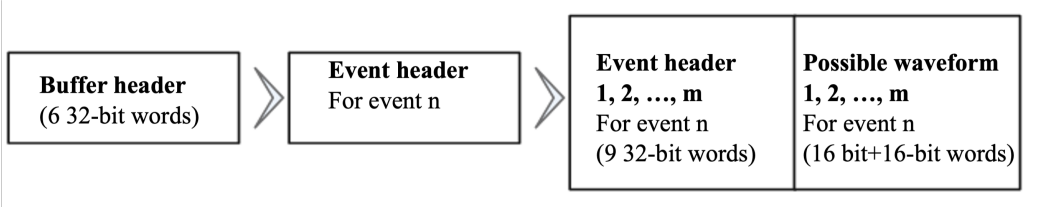

Figure 3.2.11: A diagram representing how the list mode data was recorded for signal n, where signal n provides data to m channels.

3.2.3.7 Data Sorting

The list mode data output was sorted using a C++ code adapted from the base code written by Dr. Pete Jones to suit the requirements of this study. The code was designed to process and sort list mode binary data measured by the Pixie-16 DAQ and generate ROOT files for subsequent analysis (for information on the ROOT software, see the website: ROOT v6.32 [74]). The code was adapted for handling data from two detectors and operates with a user-defined 7 ns time window to sort signals based on their timestamps and then calibrate energy readings. The code increments through the number of files associated with the run number of interest. The extraction of timestamp, ADC data, and channel identity from the binary data involves parsing specific bits of the 64-bit data words read from the list mode binary file. Each signal data word was read from the buffer header and was processed to extract these components. The data structure is explained in Section 3.2.3.6.

The data variable, which holds the second 32-bit part of the 64-bit data word, was examined to determine the type and content of the data. The channel identity of the Pixie-16 module was extracted from the data variable by masking and shifting bits: `ident = (data & 0x0fff0000) » 16`. This operation masks the lower 16 bits and then shifts the remaining bits to the right by 16 positions, yielding the identifier value which indicates the channel or type of data. The ADC data was obtained by masking the lower 16 bits of the data variable. This isolates the ADC data value from the rest of the bits. The timestamp was composed of two 32-bit parts: the bottom part of the timestamp (TSbot) and data. The TSbot value was directly read from the buffer, and data was used to complete the timestamp. The purpose of this was to reduce the handling of large amounts of data unnecessarily, as the first part of the timestamp remained largely unchanged during a run. The timestamp was then reconstructed by combining these two parts.

For the readout of the fast timing channels, timing information was extracted through a combination of FPGA processing and CFD techniques (described in Section 3.2.3.2). The FPGA parses the ADC data to obtain the timing components necessary for accurate signal reconstruction. Specifically, the "tock" value, derived from bits 13–15 of the ADC data, provides coarse timing information within a 2 ns sampling window. The "tick" value, obtained from the lower 13 bits, represents the fine time difference between consecutive 2 ns samples. This tick value was then converted into a precise time measurement in nanoseconds using a scaling factor of 16384 for the 500 MHz module. The calculated time was adjusted by combining it with the previously recorded timestamp and stored in a vector if it meets certain criteria (the ZCP location cannot have created an invalid trigger). This process ensures that the timing information was accurately recorded and can be used for detailed analysis, taking advantage of the high sampling rate of the module to achieve precise timing resolution.

The slow channel readout focused on obtaining good energy resolution from the ADC energy. A predetermined polynomial calibration was applied (see Section 3.3.3 to the ADC value). The sorting of the raw data results in a ROOT file containing fast and slow channel time, and calibrated slow channel energy information for each detector of interest. The fast and slow times were both saved in the output file for the analysis performed in Section 3.3.6.

The ROOT file also contains time and energy information from the square-wave STM pulse sent from the Polaris detector in 2 s intervals, as described in Section 3.1. In the case of the proton beam experiment that was performed, the file also contains the time information of the beam-bunched cyclotron radio-frequency signal, for which more information can be found in Section 3.4.

3.2.4 Operating Procedure

The two detectors used in this work were powered by a HV and LV power supply, and the signals generated by the PMT's cathode (slow) and first dynode (fast) were read out. These signals were then digitised at 500 MHz by the 16-channel Pixie-16 all digital signal processing unit. The readout was performed from detector PMT via RG58 coaxial cables (low loss and good shielding characteristics) with BNC-to-SMB connections to a 14-bit, 500 MHz Pixie-16 digital data acquisition module, ensuring minimal to no dead-time [70]. This module continuously samples signals from the detectors and uses several digital filters to extract timing and energy information from the detector pulses. The module was placed in a crate which allows for power, computer control from the back-plane (e.g. compact PCI, peripheral component interconnect (PCI), etc.), data readout and (dependent on the back-plane) clock distribution. The system was read out by a PC over a single PCI bridge (PXI-8360). The data acquisition of each of the 16-channels were independently gated by the channel gate inputs (0–15), with data being independently read out per channel. A simplified flow diagram of this process is illustrated in Fig. 3.2.12. The HV value was set to -1200 V for the source measurements described in Section 3.3, and -1050 V for the beam-time measurements described in Section 3.4. Refer to Section 3.2.3.6 for a more detailed description in the list mode data readout.

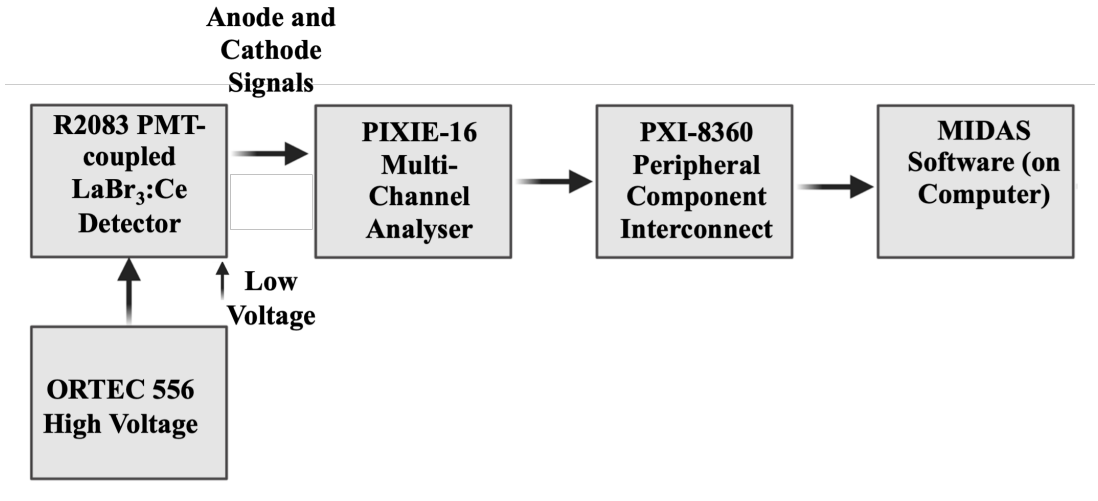

Figure 3.2.12: A diagram of the operation of the 2″ × 2″ LaBr$_3$:Ce detector. All electronics were housed in a crate and NIM bin.

All 16 channels (both the fast and slow signals) were terminated with 50 Ω to prevent internal reflections in the cable that degrade the quality of the measured signal. Photographs of the Tektronix TDS 3034B digital oscilloscope in Fig. 3.2.13(b) show the improvement in

the signal quality after the termination has been added, such that the signal demonstrates the expected exponential decay without the additional structures seen in 3.2.13(a) originating from internal reflections in the cable (likely due to termination on only one end of the cable).

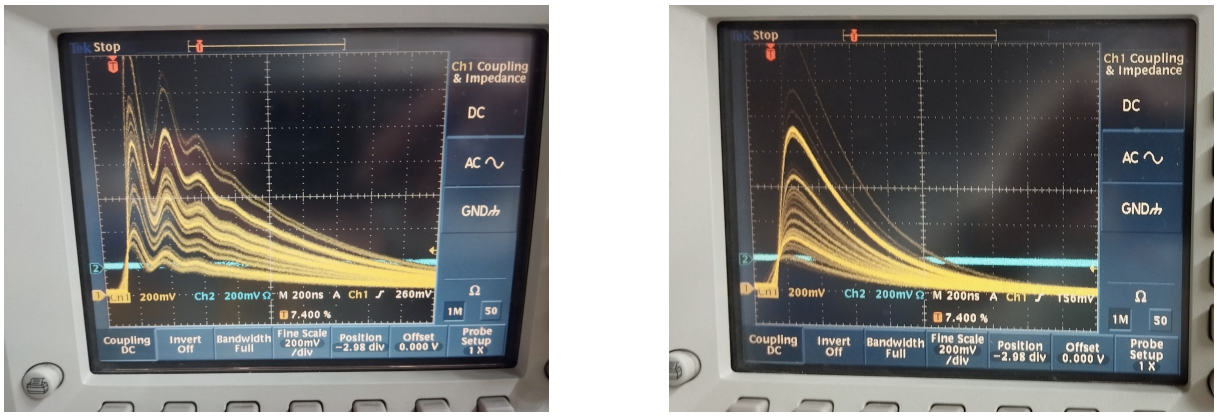

(a) (b)

Figure 3.2.13: Photographs taken of the digital oscilloscope: (a) the unterminated signal, and (b) the 50 Ω terminated signal. The x-axis time scale is 100 ns/division and the y-axis amplitude scale is 200 mV/division in both photographs.

The DDAS software parameters (see Section 3.2.3.4) used in the data acquisition were optimised twice. The first iteration of the optimisation was implemented for the beam measurements described in Section 3.4. The parameters were then further improved upon in an attempt to achieve an ~ 3% energy resolution at 661.7 keV. The parameters used are discussed in detail in Section 3.3.2.

3.3 SOURCE CHARACTERISATION OF CC1 DETECTORS

A series of measurements with radioactive sources were conducted to assess the detector system and determine its suitability for imaging PGs emitted during PT. All measurements were performed at iThemba LABS in Cape Town, South Africa, and using the resources provided by the laboratory, except for the Polaris detector and a number of low-activity gamma-ray sources that are the property of the Department of Physics at the University of Cape Town, South Africa.

The peak fitting software used to obtain the centroid bin and sigma values for use in the energy resolution and calibration calculations, as well as the peak area values used in the efficiency calculations was Radware (refer to the website for comprehensive information on this interactive gamma spectroscopy tool: Radware [75]). The nonlinear fitting of one peak (nf) function was chosen to fit each peak in the spectra of interest, as it allows the user to adjust several key parameters to optimise the fit. The `nf -1` function typically models gamma-ray peaks using a Gaussian function or a Gaussian-Lorentzian hybrid, which represents the response of the detector. The Gaussian component models the statistical fluctuations in the detector response, and the Lorentzian component (if used) can account for natural broadening effects in nuclear transitions. The user has control over the initial guesses for the parameters,

as well as constraints set, e.g., fixing the width or centroid to known values). The user can also choose the fitting function (Gaussian, Gaussian-Lorentzian hybrid, etc.). For each peak, the constant or linear background under the peak was subtracted to isolate the peak's area accurately. An example of the peak and background fit is graphically shown on a spectrum, as seen in Fig. 3.3.1, where the residual is the undulating line.

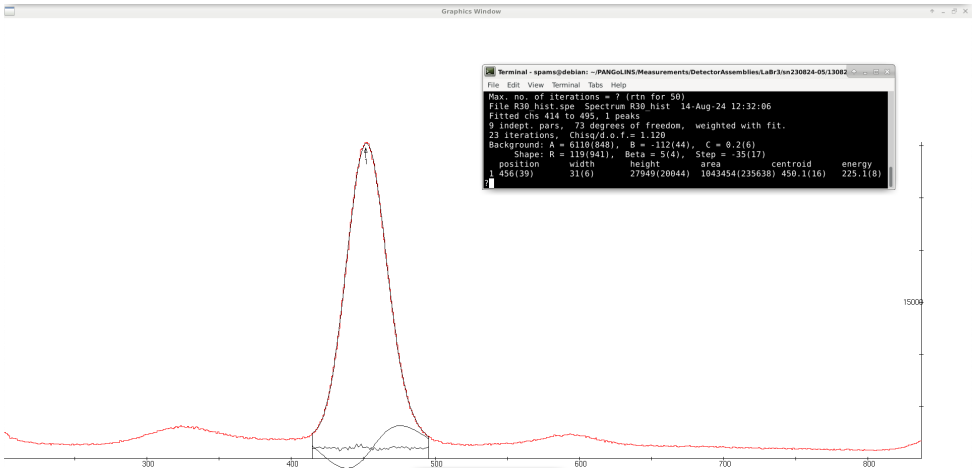

Figure 3.3.1: An example of a Gaussian peak fit performed using the Radware software gf3 option and the non-linear peak fitting function. The three black line fits to the spectrum (red) are the Gaussian fit, the background estimation (curve under the peak), and the residual.

3.3.1 Decay Constant

The decay constant of the $LaBr_3$:Ce detector needed to be characterised for input into the DDAS software. A longer decay constant can reduce noise but may sacrifice energy resolution, while a shorter decay constant can improve energy resolution but may increase noise. Setting the incorrect decay constant will distort the shape of the trapezoidal function.

In excess of 10000 signal traces of 8000 ns length were stored for the slow and the fast signal. These traces exhibit an exponential decay characterised by the function $\sim e^{-t/\tau}$, where τ represents the decay constant, the physics of which is explained in Section 2.1.2. By fitting an exponential function to each trace, the τ value can be determined.

The fitting procedure is illustrated in Fig. 3.3.2 for the slow signal, and Fig. 3.3.3 for the fast signal. The process began with the recording of the signal trace from the detector, as shown in Fig. 3.3.2(a) and Fig. 3.3.3(a). Next, in Fig. 3.3.2(b) and Fig. 3.3.3(b), a constant function was fitted to the base of the trace to determine the constant offset, which was then subtracted from the original trace. The resulting trace, shown in Fig. 3.3.2(c) and 3.3.3(c), was then fitted with the exponential decay function to extract the amplitude (A) and the decay constant (τ).

This fitting process was applied to each of the 10000 recorded traces, resulting in a corresponding set of τ values. These τ values were then binned into intervals of 2 ns, producing the distribution shown in Fig. 3.3.4(a) for the slow signal and (b) for the fast signal. The most frequently occurring τ value for the slow signal (τ_s) was identified from this distribution, pro-

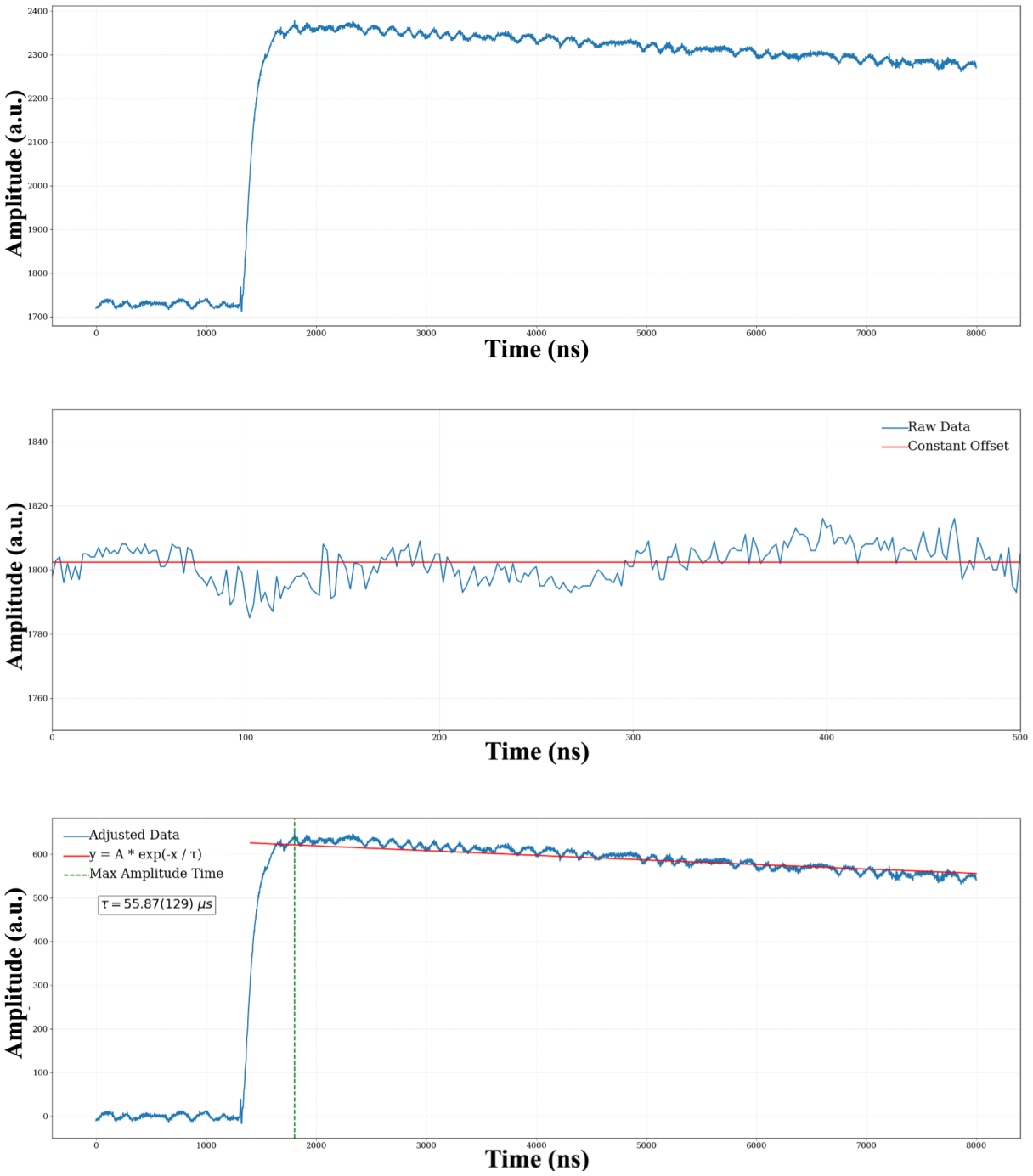

Figure 3.3.2: The fitting procedure used to determine the decay constant τ for the $2'' \times 2''$ $LaBr_3$:Ce slow signal involves several key steps: (a) a typical slow signal trace is displayed, (b) a constant function was fitted to the data to establish the value of the constant offset, and (c) the trace was adjusted by subtracting the constant offset, and an exponential fit was applied to the corrected trace to extract the decay constant τ.

viding the optimal τ setting for achieving the best energy resolution. This value of τ_s was determined to be 49.25(308) µs for the slow signal and 22.50(14) ns for the fast signal. These measurements were performed using a ^{137}Cs source.

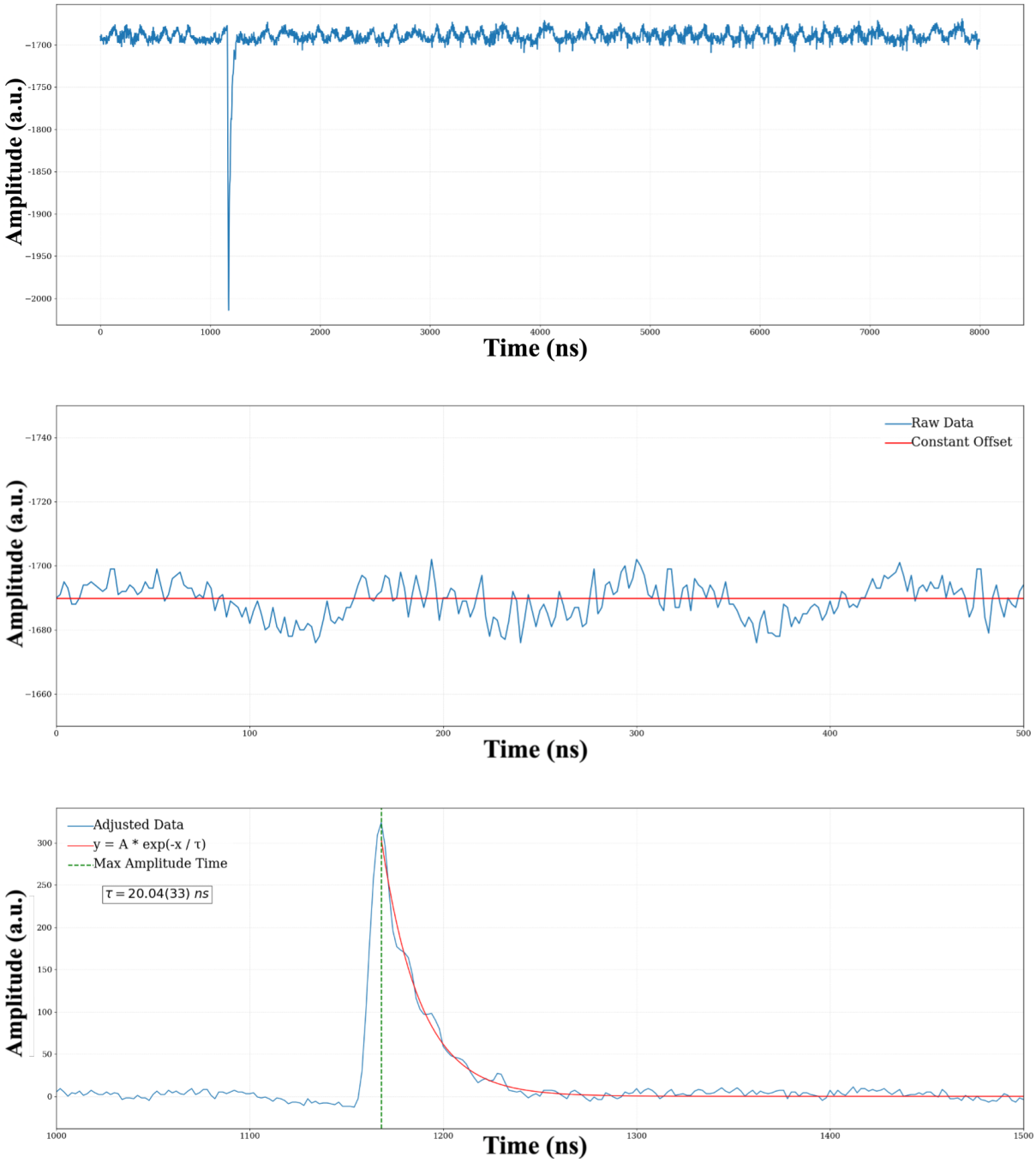

Figure 3.3.3: The fitting procedure used to determine the decay constant τ for the $2'' \times 2''$ $LaBr_3$:Ce fast signal involves several key steps: (a) a typical fast signal trace is displayed, (b) a constant function was fitted to the data to establish the value of the constant offset, and (c) the trace was adjusted by subtracting the constant offset, and an exponential fit was applied to the corrected trace to extract the decay constant τ. This last step was performed after inverting the signal to have a positive amplitude for more convenient fitting and because the DDAS software does not prescribe signal polarity.

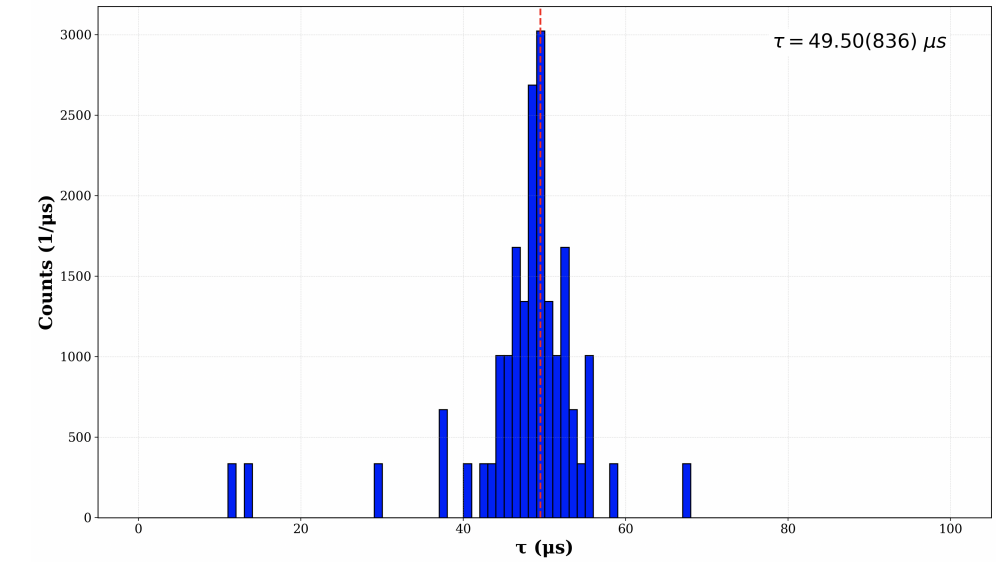

(a)

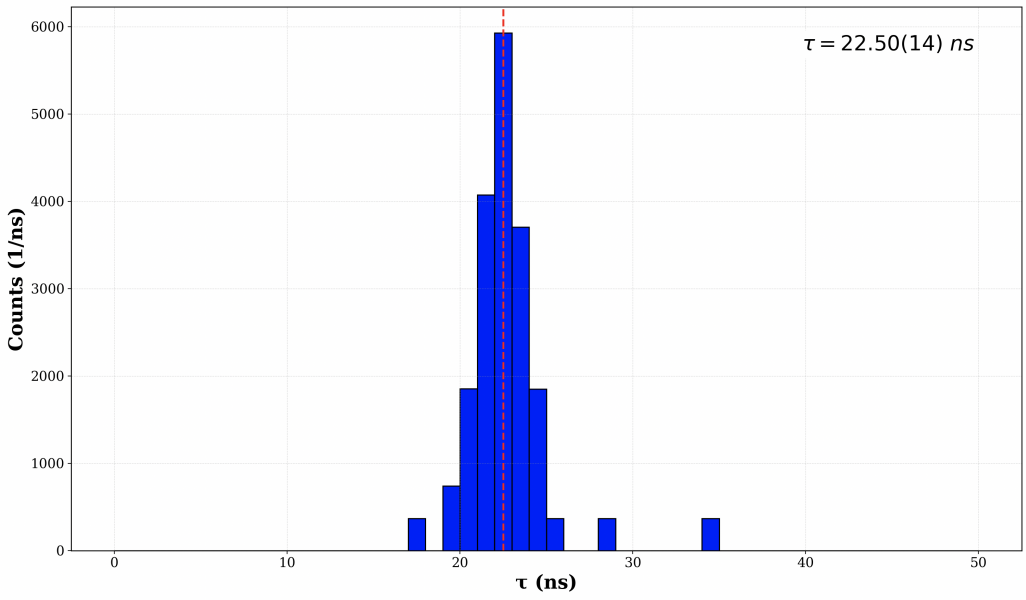

(b)

Figure 3.3.4: The decay constant τ for: (a) the slow signal, for which the most frequent value was measured to be 49.5(836) μs, for which the energy resolution was at a desired minimum, and (b) the fast signal, for which the most frequent value was measured to be 22.5(14) ns.

3.3.2 Energy Resolution

In gamma-ray spectroscopy, energy resolution is a critical factor in distinguishing closely spaced energy peaks and obtaining high-quality spectra. The energy resolution of a detector is dependent on the material of the detector as well as the energy of the incident photon. It is expressed as the FWHM of the photopeak, normalised to the calibrated centroid energy (C_0), as shown in the following equation:

$$\Delta E/E = \frac{FWHM}{C_0} \tag{3.3.1}$$

The superior energy resolution of $LaBr_3$:Ce scintillator detectors can be largely attributed to their high light yield, ranging between 47000 and 63000 photons/MeV [76]. This high light output contributes to better energy resolution by increasing the number of detected photons, which reduces statistical fluctuations in the detected signal.

The energy resolution ($\Delta E/E$) of a PMT-coupled scintillator system can be expressed as a combination of several factors:

$$\Delta E/E = \sqrt{\sigma_{intr}^2 + \sigma_{tran}^2 + \sigma_{st}^2} \tag{3.3.2}$$

- The intrinsic resolution (σ_{intr}) reflects inhomogeneities in the scintillator crystal itself, such as variations in the crystal lattice that affect light production and collection [77].
- The transfer resolution (σ_{tran}) relates to the optical coupling between the scintillator and the PMT. This includes factors such as the quantum efficiency of the photocathode, the transmission of light through the coupling medium (self-absorption, opaqueness, etc.), and the optical alignment of the system.
- The statistical resolution (σ_{st}) is influenced by the number of photoelectrons produced at the photocathode and their collection efficiency at the first dynode of the PMT [78]. The statistical uncertainty follows a Poisson distribution, leading to the well-known relationship between energy resolution and incident photon energy:

  $$\Delta E/E \propto \frac{1}{\sqrt{E}}$$

  As the energy of the incident gamma ray increases, the number of detected photons also increases, reducing the relative statistical fluctuation and improving the energy resolution. However, this improvement diminishes with increasing energy, as the number of photoelectrons saturates due to detector limitations, optical losses, and noise. Plotting the detector energy resolution versus $1/\sqrt{E}$ should yield a linear relationship [79].

To better understand the contributions to energy resolution, it is important to consider that $LaBr_3$:Ce detectors, while highly efficient, also experience effects from electronic noise

and environmental factors. For instance, mechanical vibrations and electronic noise from the signal processing electronics can introduce additional broadening of the photopeak, affecting the overall energy resolution.

A ^{137}Cs source was used to measure the energy resolution of $LaBr_3$:Ce detectors at the 661.7 keV photopeak. Both the fast and slow signals from the $LaBr_3$:Ce detector underwent the trapezoidal filtering described in Section 3.2.3.3, where the parameters were controlled in the DDAS software. Figures 3.3.5(a) and 3.3.5(b) show the energy resolution of the 661.7 keV photopeak as a function of trapezoidal rise time and flat top for the fast and slow detector signals, respectively, measured in units of µs. It was seen that a minimal resolution of 4.233(77)% was produced by setting the rise time to 0.12 µs and flat top to 0.14 µs for the fast signal, and 4.073(85)% by setting the rise time to 0.3 µs and flat top to 1.3 µs for the slow signal.

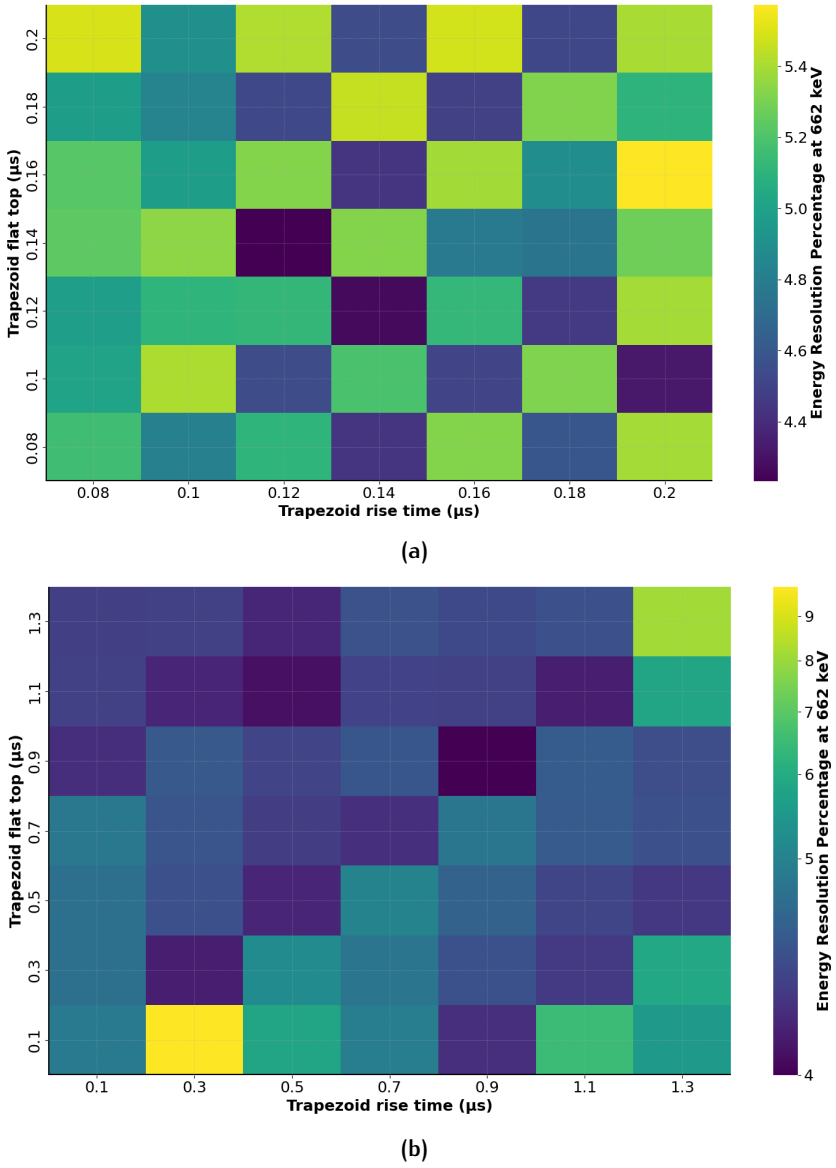

Figure 3.3.5: Matrices showing the effect of varying the DDAS parameter settings for energy filter rise time and flat top on energy resolution for the 2″ × 2″ $LaBr_3$:Ce detector: (a) the fast signal, and (b) the slow signal.

The optimised trapezoidal fitting parameters were applied, and a 10-minute measurement was performed using a combination of ^{152}Eu,^{137}Cs and ^{60}Co sources positioned 10 mm

away from the centre of the detector face. The energy resolution for each of the following photopeaks in the spectra was measured, where the first 11 peaks originate from the ^{152}Eu source, the 661.7 keV peak from the ^{137}Cs, and the final two from the spectrum of ^{60}Co: 41.1, 121.8, 244.7, 344.3, 411.12, 443.98, 778.9, 867.4, 964.1, 1099.0, 1408.0, 661.7, 1173.2, and 1332.5 keV. Figure 3.3.6(a) shows the approximately linear relationship between energy resolution and $1/\sqrt{E}$ for Polaris, where the equation of the fit was R(E) = $\frac{169.03(736)}{\sqrt{E}} - 1.52(42)$ for the $LaBr_3$:Ce detector. The quality of the fit was measured as the chi-squared per degrees of freedom and the fit was poor in the very low energy region (<150.0 keV), which was not of significance. Note that the detector crystals are non-linear at low energies, which might affect the energy resolution if estimated after the calibration. Figure 3.3.6(b) shows the linear relationship between energy resolution and $1/\sqrt{E}$, where the relationship between the two parameters was characterised by R(E) = $\frac{25.94(122)}{\sqrt{E}} - 0.16(5)$. The energy resolution of the Polaris detector was excellent, with a resolution of 1.38(25)% at 661.7 keV. There was no energy resolution optimisation technique onboard the Polaris DAQ. The spectra of both CC1 detectors are plotted on the same axes in Fig. 3.3.7, where the energy resolution performance difference between the two detectors is seen clearly at 511.0 keV. The ~ 1460.0 keV peak observed in the gamma spectrum background originates from the natural radioactive decay of ^{40}K, a naturally occurring isotope of potassium. This peak is not observed in the energy response of the Polaris detector as the detector has a smaller geometry, and the size of the detector affects the efficiency according to the Bethe-Bloch formula seen in Eq. 2.1.6. The user-defined functions described in Section 3.2.3.1 were fine-tuned to maximise energy resolution, with the typical values presented in Table 3.3.1.

Parameter	Slow signal (μs)	Fast signal (μs)
Fast risetime	0.1	0.02
Fast flat top	0.1	0.01
Energy risetime	0.9	0.14
Energy flat top	0.9	0.12
Peak sample	1.36	0.2
Peak separation	2	0.1
Decay constant	55.87	0.02
CFD delay	0.01	0.01

Table 3.3.1: The parameters adjusted for the 2" × 2" $LaBr_3$:Ce detector, chosen to achieve the best energy resolution.

The manufacturer specifies an energy resolution of 2.1% at 1332.5 keV for 2″ × 2″ $LaBr_3$:Ce detectors, while the optimised resolution achieved in this work was 3.24(19)% at the same energy [79]. The experimental results suggest that external factors, such as noise and imperfect calibration, may degrade the performance. The noise could be induced by a number of factors such as cable impedance, length, power supply, etc. A guaranteed source of background originated from a switched-mode uninterrupted power supply (UPS) module, operating at ~ 200 kHz and situated quite near to the experiment area. This frequency was seen as a constant background on the oscilloscope with continuous 20 ns bunches and 6 mV amplitude. Additionally, variations in light collection efficiency and coupling between the scintillator and PMT can account for the discrepancies in energy resolution.

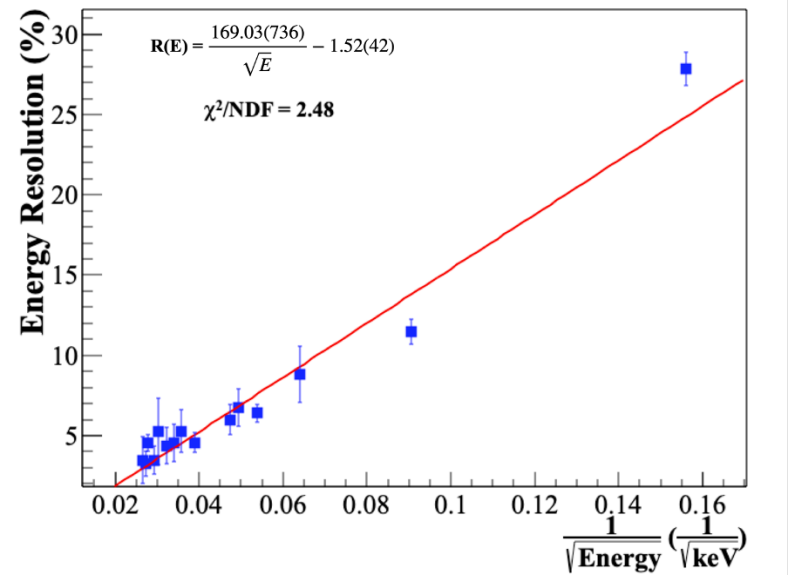

(a)

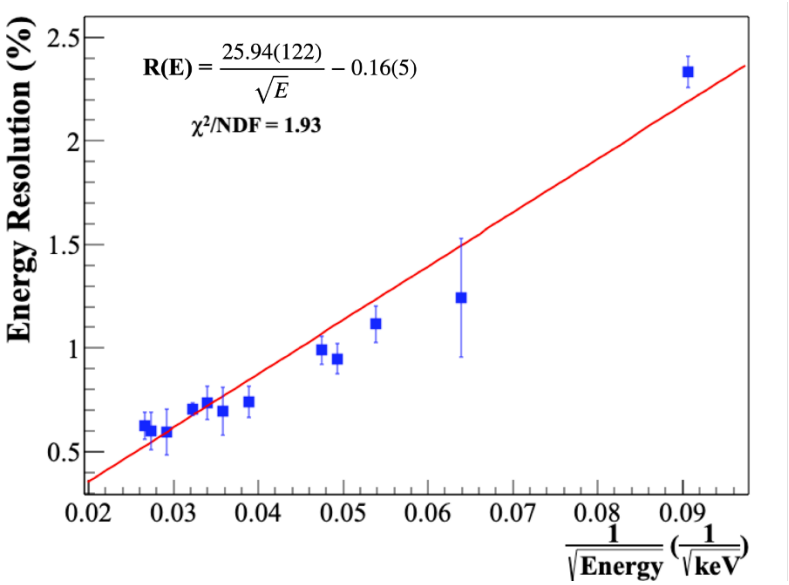

(b)

Figure 3.3.6: Energy resolution curves obtained using ^{152}Eu,^{137}Cs and ^{60}Co sources placed 10 mm from the detector face for the: (a) the 2"x2" $LaBr_3$:Ce detector, and (b) the Polaris detector. The fit used for each detector is labelled on the plot.

3.3.3 Energy Calibration

Energy calibration was carried out for the slow signal of the $LaBr_3$:Ce detector. The Polaris detector does not require the user to manually calibrate it, but rather undergoes re-calibration by the manufacturer every two years. This calibration process involved using radioactive sources with well-known gamma-ray emission energies, and matching the resulting energy photopeaks to specific channels in the spectrum. The well-defined gamma and x-ray peaks in the energy spectrum of ^{152}Eu were employed to calibrate the energy spectrum: 41.1, 121.8, 244.7, 295.9, 344.3, 411.12, 443.98, 778.9, 867.4, 964.1, 1099.0, 1408.0 keV, ensuring the accuracy of the detector across a broad energy range. This is particularly important in CC applications, where accurate energy measurements are critical for reconstructing gamma-ray interactions,

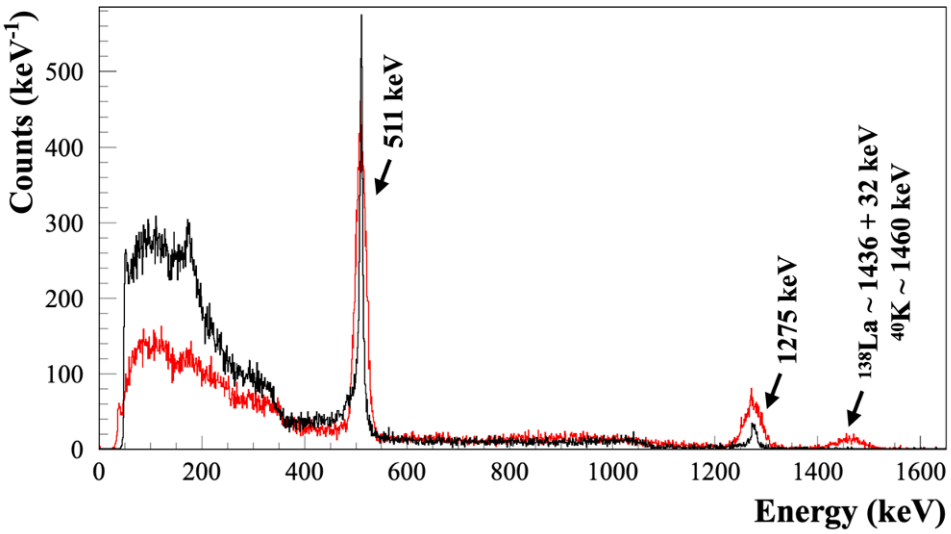

Figure 3.3.7: The labelled gamma-ray energy spectrum for a ^{22}Na source for the Polaris (black) detector and $LaBr_3$:Ce (red) detector plotted on the same axes.

aiding in determining the detector's ability to distinguish between close-lying energy peaks. The peaks were fitted after background subtraction (see Section 6.3.1) and using the Radware software gf3 option.

To obtain the calibrated energy spectrum, the goodness of fit for each detector was measured by fitting first, second, and third order polynomials to a plot of the channel number versus known peak energy. The residual energy was calculated as the difference between the known peak energy and the calculated energy from the obtained polynomial fit parameters. The uncertainty in the residual energy calculation was calculated to account for the uncertainties involved in both the measured channel centroids and the polynomial fit as follows:

The residual for each point was calculated as:

$$\text{Residual}_i = E_{\text{known},i} - E_{\text{fit},i} \tag{3.3.3}$$

where $E_{\text{known},i}$ is the known energy value, and $E_{\text{fit},i}$ is the energy value obtained from the fit for the i-th channel.

The uncertainty on the fitted energy value $E_{\text{fit},i}$ can be propagated from the uncertainties in the channel centroid and the uncertainties in the polynomial coefficients. For a polynomial fit of the form:

$$E_{\text{fit}}(x) = a_0 + a_1 x + a_2 x^2 + \cdots + a_n x^n$$

the uncertainty in $E_{\text{fit}}(x)$ due to the fit can be calculated using the covariance matrix $\text{Cov}(\mathbf{a})$, where $\mathbf{a} = [a_0, a_1, \ldots, a_n]$. The variance in the fitted energy $\sigma^2_{E_{\text{fit},i}}$ is:

$$\sigma^2_{E_{\text{fit},i}} = \sum_{j,k=0}^{n} \frac{\partial E_{\text{fit}}(x_i)}{\partial a_j} \frac{\partial E_{\text{fit}}(x_i)}{\partial a_k} \text{Cov}(a_j, a_k)$$

Since $E_{fit}(x)$ is a polynomial:

$$\sigma^2_{E_{fit,i}} = \sum_{j,k=0}^{n} x_i^{j+k} \mathrm{Cov}(a_j, a_k)$$

The total uncertainty on the residual $\sigma_{\mathrm{Residual}_i}$ is given by combining the uncertainties from the centroid position and the fit:

$$\sigma_{\mathrm{Residual}_i} = \sqrt{\sigma^2_{E_{known,i}} + \sigma^2_{E_{fit,i}}}$$

Since the known energy values E_{known} have negligible uncertainty, this simplifies to:

$$\sigma_{\mathrm{Residual}_i} \sim \sigma_{E_{fit,i}}$$

If the channel centroid x_i has an associated uncertainty σ_{x_i}, the uncertainty in the fitted energy due to the centroid uncertainty needs to be included:

$$\sigma_{E_{centroid,i}} = \sqrt{\left(\frac{\partial E_{fit}(x_i)}{\partial x_i}\sigma_{x_i}\right)^2 + \sigma^2_{E_{fit,i}}}$$

This gives the final uncertainty on the residual:

$$\sigma_{\mathrm{Residual}_i} = \sqrt{\sigma^2_{E_{fit,i}} + \left(\frac{\partial E_{fit}(x_i)}{\partial x_i}\sigma_{x_i}\right)^2} \tag{3.3.4}$$

Figure 3.3.8 shows the obtained residual energy values and uncertainties for a first, second and third order polynomial plotted for each energy value in the spectrum of ^{152}Eu. A grey shaded region between -1.0 and 1.0 keV has been added to the plot to guide the eye toward lower and higher obtained residual values. The median residual energies and their associated uncertainties are included in a box underneath the figure. The second order polynomial fit was determined to be the most suitable calibration, as it demonstrates the highest agreement with the known energy values. This was the calibration used in Fig. 3.3.9. The polynomial fit was applied to the channel values, and the resulting energy value was then smoothed by adding a random noise value. This noise was generated by extracting random values from a Gaussian distribution, where the standard deviation was determined based on the scaling factor between the uncalibrated channel values and the known energy values for the photopeaks. This approach ensured that the energy values reflected both the calibration process and inherent uncertainties, thereby providing a more accurate representation of the detected energy.

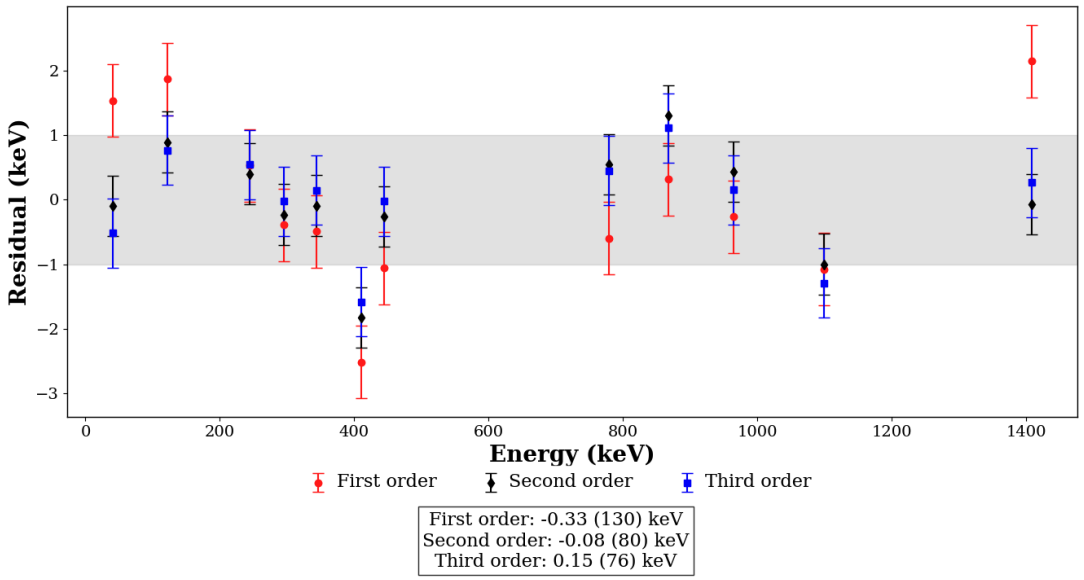

Figure 3.3.8: The obtained residual energy values and uncertainties for a first, second and third order polynomial fit to the channel versus energy values is plotted for each energy value in the spectrum of ^{152}Eu. The median values of each fit and their associated uncertainties are included in the box underneath the legend. The second order polynomial fit was determined to be the most suitable calibration.

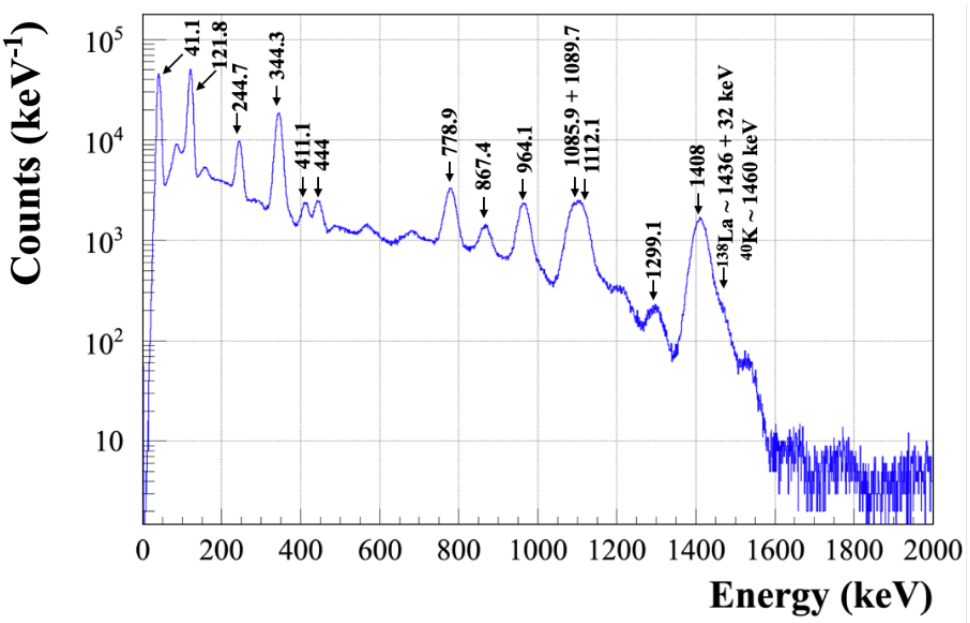

Figure 3.3.9: The calibrated and labelled energy spectrum of the 2″ × 2″ $LaBr_3$:Ce detector, measured with a ^{152}Eu source. The labels encompass gamma and x-ray peaks, as well as the dominant background ^{138}La contribution originating from the detector internal radioactivity.

3.3.4 Efficiency

When detecting uncharged radiation, such as gamma rays, it is commonly observed that the efficiency of a detector is significantly less than 100%. This is primarily because uncharged radiation has a much lower interaction probability compared to charged particles such as alpha and beta particles, which interact through the long-range Coulomb force [24]. The absence of this force in uncharged radiation results in a lower likelihood of interaction within

the detector. The full-energy peak efficiency percentage (FEPE) can be calculated from gamma-ray spectroscopy measurements using the following equation [24]:

$$\epsilon_{FEP}(E_\gamma)(\%) = \frac{N_p}{A_c \times t \times I_\gamma(E_\gamma)} \times 100 \tag{3.3.5}$$

where E_γ is the energy of the emitted gamma ray, N_p represents the total number of counts in the photopeak corresponding to the energy E_γ, A_c is the current activity of the radioactive source, t is the measurement duration, and $I_\gamma(E_\gamma)$ denotes the gamma ray intensity per decay at energy E_γ, for which the value was obtained from the NUDAT database [69].

The uncertainty in FEPE is calculated by propagating the uncertainties associated with each variable in the equation. The uncertainty in the total counts N_p is obtained from the Radware effit, assumed to follow Poisson statistics, where the uncertainty is given by the square root of N_p. The uncertainty in source activity A_c is determined from the calibration certificate of the source (taken in this work to be 10% for all sources), while the uncertainty in the gamma-ray intensity $I_\gamma(E_\gamma)$ is obtained from the NUDAT database [69]. These uncertainties are combined using standard uncertainty propagation methods to estimate the overall uncertainty in the FEPE.

The FEPE was calculated for both of the CC1 detectors. Since the FEPE relies on knowing the current activity of the measurement source with a reasonable degree of certainty (typically 10%), a sanity-check was performed between an iThemba LABS (Cape Town) owned ^{152}Eu 119.56 kBq source and an assortment of UCT-owned (^{22}Na,^{137}Cs,^{60}Co, ^{57}Co and ^{54}Mn) sources placed 30 mm from the 2″ × 2″ $LaBr_3$:Ce detector face. The sources were set in plastic containers, and the point source was assumed to be located at the geometric centre of each container. The energy spectra for which the peak areas were obtained for these measurements are seen in Figs. 3.3.9 and 3.3.10, however, background subtraction was first performed using background spectra obtained for the same measurement duration (see Section 6.3.1). The FEPE vs energy spectrum of the $LaBr_3$:Ce detector for this comparison is shown in Fig. 3.3.11 where good agreement was seen between measurements with the two different sources, where the combined data was fitted with a logarithmic-polynomial function ($\ln(\epsilon(E)) = a_0 + a_1\ln(E) + a_2(\ln(E))^2 + a_3(\ln(E))^3$). The activities of the sources used can be found in Table 3.3.2

Source	Manufactured date (dd/mm/yyyy)	Manufactured activity (kBq)	Current activity (kBq)
^{57}Co	01/10/2020	37(4)	1.18(12)
^{22}Na	01/10/2020	37(4)	13.80(138)
^{137}Cs	01/10/2020	37(4)	33.97(340)
^{54}Mn	01/10/2020	37(4)	1.83(18)
^{60}Co	01/10/2020	37(4)	22.74(227)
^{152}Eu	06/01/2004	343.6(364)	119.56(1196)

Table 3.3.2: Table detailing the sources used in the detector efficiency measurements and their activities.

The FEPE was calculated at four different source-to-detector distances for the Polaris and $LaBr_3$:Ce detectors, seen in Fig. 3.3.12(a) for the 2"x2" $LaBr_3$:Ce detector, which was fitted by the logarithmic-polynomial function $\ln(\epsilon(E)) = a_0 + a_1\ln(E) + a_2(\ln(E))^2 + a_3(\ln(E))^3$) and

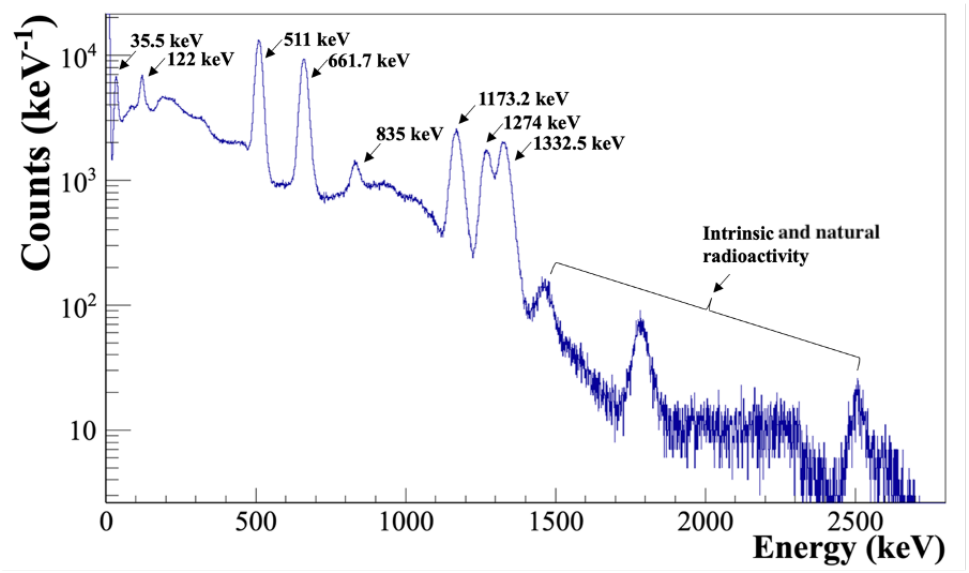

Figure 3.3.10: The 2″ × 2″ $LaBr_3$:Ce detector measured gamma-ray energy spectrum of ^{22}Na, ^{137}Cs, ^{60}Co, ^{57}Co and ^{54}Mn sources placed 30 mm from the detector face.

Fig. 3.3.12(b) for the Polaris detector, best fitted with the same function with an additional term ($\ln(\epsilon(E)) = a_0 + a_1\ln(E) + a_2(\ln(E))^2 + a_3(\ln(E))^3 + a_4(\ln(E))^4$). The $LaBr_3$:Ce detector efficiency was in agreement with the work published by Msebi et al. [57].

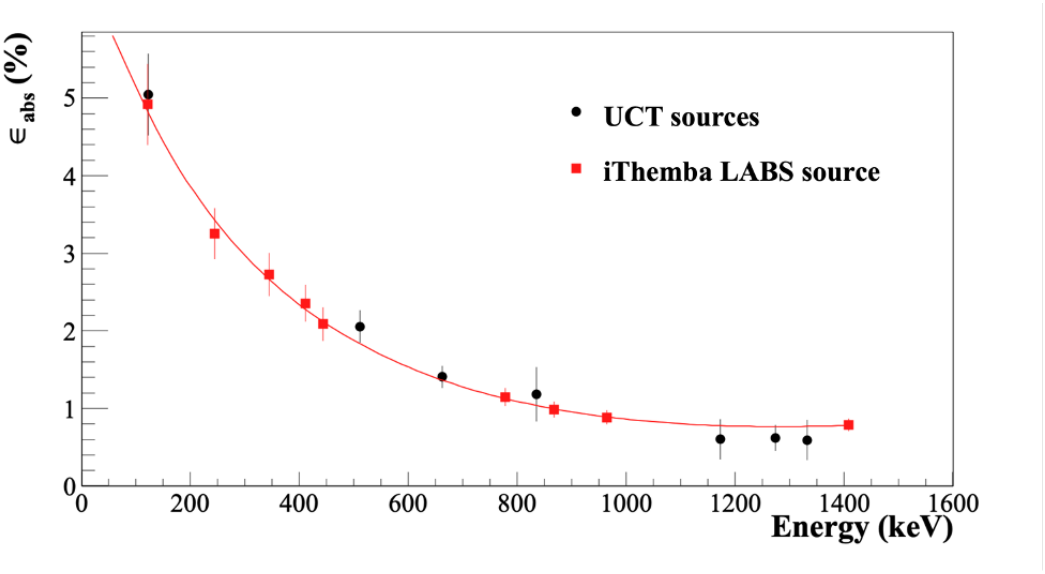

Figure 3.3.11: The FEPE vs energy plot demonstrating a good agreement between the 2″ × 2″ $LaBr_3$:Ce detector measured full-energy peak efficiencies at 30 mm source-to-detector distance for UCT sources (^{22}Na,^{137}Cs,^{60}Co, ^{57}Co and ^{54}Mn) and iThemba LABS ^{152}Eu source.

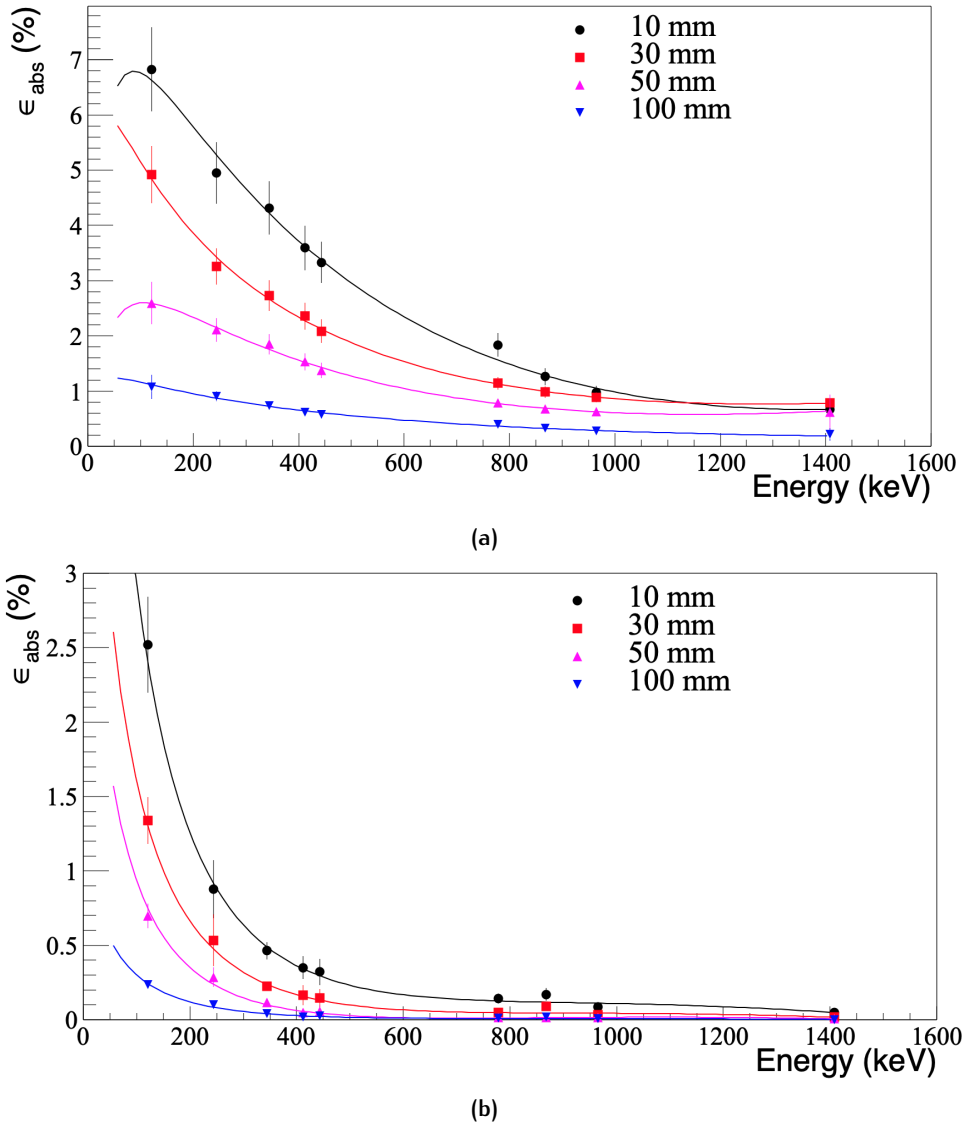

Figure 3.3.12: The FEPE measured using a ^{152}Eu source placed at four different distances from each detector: (a) 2″ × 2″ $LaBr_3$:Ce detector (fit equation: $\ln(\epsilon(E)) = a_0 + a_1\ln(E) + a_2(\ln(E))^2 + a_3(\ln(E))^3$), and (b) the Polaris detector (fit equation: $\ln(\epsilon(E)) = a_0 + a_1\ln(E) + a_2(\ln(E))^2 + a_3(\ln(E))^3 + a_4(\ln(E))^4$).

3.3.5 Timing Resolution

The timing resolution of the Polaris detector is discussed in Section 3.1. As only one Polaris detector was available for measurements at the time of this study, coincidence timing measurements could not be performed to ascertain the resolution in more detail.

The timing resolution of the $LaBr_3$:Ce detector fast signal was investigated by using two 2″ × 2″ $LaBr_3$:Ce detectors in a face-to-face coincidence measurement configuration, as seen in Fig. 3.3.13.

The time difference between energy-gated coincident events between each detector within the timing window specified in Section 3.2.3.7 was calculated using data obtained from a 30-minute measurement with a ^{60}Co source placed 10 mm away from each detector face. The data within this time window were considered to be one event, although they do not occur

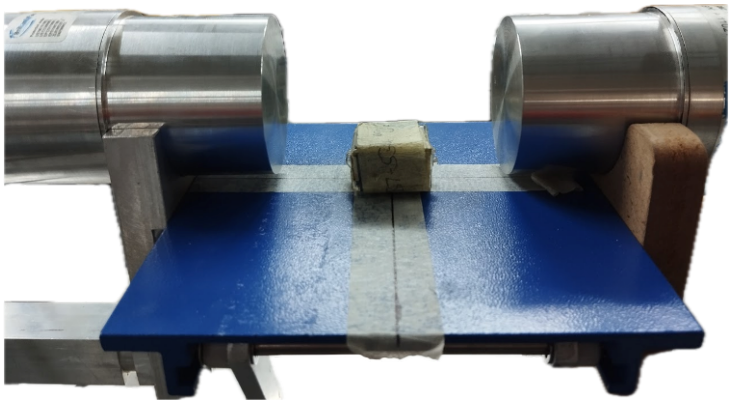

Figure 3.3.13: A side-view photograph of the geometrical configuration of the coincidence timing resolution measurement performed. Two 2″ × 2″ $LaBr_3$:Ce detectors were placed face-to-face, with each detector face situated 10 mm from a ^{60}Co source.

simultaneously in reality; the gamma-gamma coincidence of the ^{60}Co decay, in particular the prompt 1173.2 and 1332.5 keV cascade, was used because the decay of 0.9 ps between the energy states of the isotope is less than the time resolution of our detector and can therefore be considered effectively coincident. A time resolution with FWHM 218.08(11) ps was measured for the detector, obtained from the Gaussian fit to the time difference spectrum seen in Fig. 3.3.14(a).

The energy-energy matrices are plotted in Fig. 3.3.14(b) where the top figure shows the result of a background gate taken from outside the fitted Gaussian peak (from Fig. 3.3.14(a)) and was used to isolate random coincidences or background events. In this matrix, self-coincidence was observed, meaning some events were detected in the same energy channels or detectors. This indicates that these events were not true coincidences (from ^{60}Co decay) but rather background radiation or random noise. These background coincidences could originate from environmental radiation or detector noise, which does not follow the expected energy relationships of true nuclear transitions.

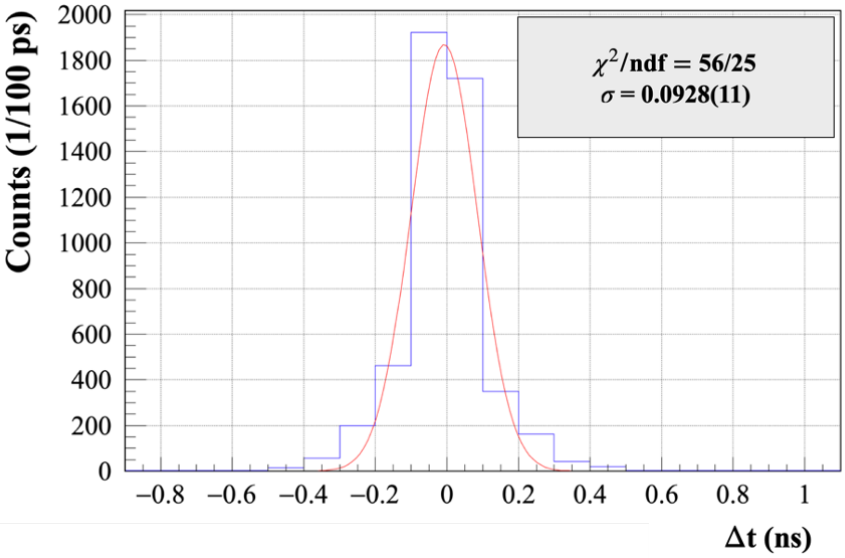

(a)

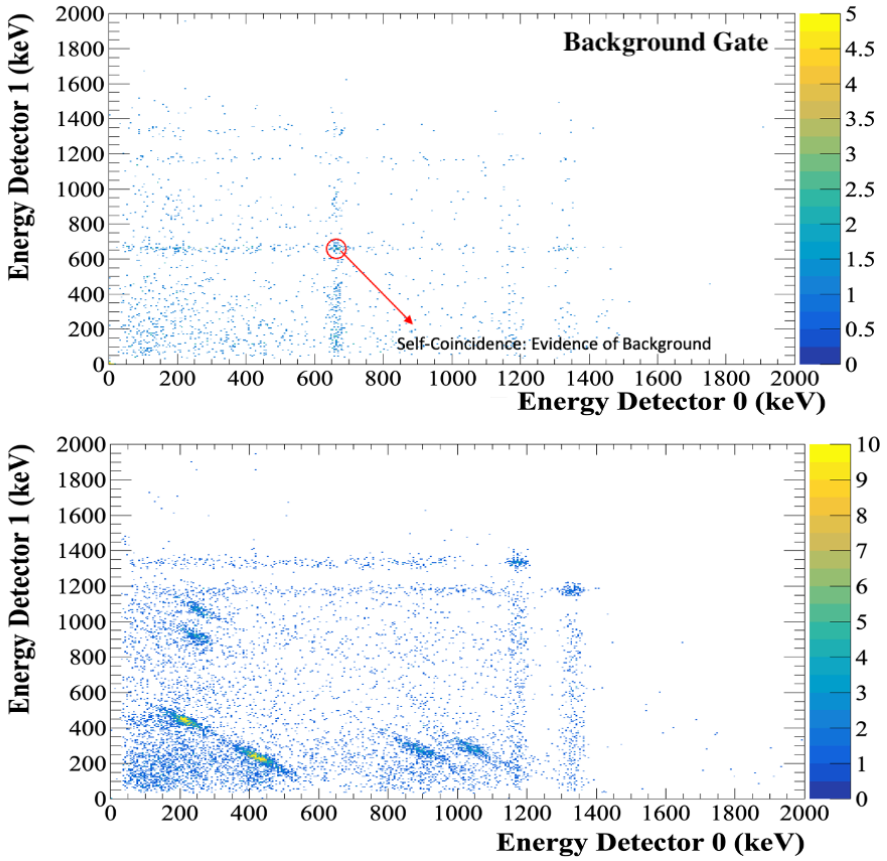

(b)

Figure 3.3.14: The time difference between coincident events measured using a ^{60}Co source: (a) the Gaussian-fitted time difference distribution (Δt) between the two 2″ × 2″ $LaBr_3$:Ce detectors measured in nanoseconds, and (b) the top matrix shows the detector energy-energy matrix when a background gate to the time difference distribution was applied, and the bottom plot shows the energy-energy matrix obtained by gating on the Gaussian-fitted peak region.

3.3.6 Time-Walk Correction

Time-walk refers to the variation in the delay of the discriminator caused by the input signal's amplitude, which can degrade the time resolution in fast-timing setups. Correcting for this phenomenon is important in CC experiments, where accurate timing measurements are crucial. Despite the use of the CFD to mitigate time-walk, residual effects can still be present, seen in the non-linear time-energy dependence in both source and beam data in the top energy-time matrices of Figs. 3.3.16 and 3.3.18. Here, the time offset measured in nanoseconds on the x-axis is the time difference between the slow and fast signal times for the same event.

Correcting for time-walk is essential to achieve optimal time resolution. Time-walk arises from the inherent non-linearity of the discriminator's response to varying signal amplitudes, introduced in this work due to the CFD trigger behaving as a leading-edge discriminator for small signal amplitudes. This effect causes two signals generated simultaneously but with different amplitudes to cross the discrimination threshold at different times. Due to time-walk, a low-energy PG appears to arrive later than a high-energy PG, even though this does not physically occur.

Methods to mitigate the time-walk were investigated, but it was found that the problem came down to the set of fixed (suboptimal) CFD algorithm parameters, as discussed in Section 3.2.3.2, which were implemented by the manufacturer due to the FPGA in the 500 MHz module lacking the resources to build sums for all five ADC samples in parallel with variable delays. These parameters cannot be changed by the user. The optimisation of the parameters was investigated by Lee et al., where different CFD delay and scale values were suggested to improve the time resolution of the CFD [80]. Improvements such as this could not be made to the hard-coded parameters and, as such, the work that follows uses the values set by the manufacturer. Time-walk can result in degradation of time resolution if not corrected.

Various methods exist for time-walk correction, including higher PMT operation voltage adjustments and mathematical corrections based on empirical data. For scintillator detectors, ignoring time-walk can adversely affect time resolution. Therefore, precise correction techniques are necessary. The method described here takes in the output data generated by the sorting code detailed in Section 3.2.3.7 and

To model the energy-time dependency, the time projection of 50.0 keV energy slices of the energy-time matrix were extracted, and the distribution was fitted with a Gaussian curve. The centroid time for the extracted energy slice was determined from the Gaussian fit, where the uncertainty was represented by the sigma value. The resulting centroid energy-time matrix was plotted to model the behaviour of the detector and best fitted with the sum of four exponential functions, as seen in Fig. 3.3.15. As a result, the corrected time-walk adjusted the bend shape in the data seen in the 2D energy time matrix in Fig. 3.3.16. This correction is seen in Fig. 3.3.17 in the time distribution of the x-projection of Fig. 3.3.16, where the top shows the uncorrected walk and the bottom plot shows the Gaussian-fitted time spectrum with 8.272(1) ns resolution between the fast and slow detector channels.

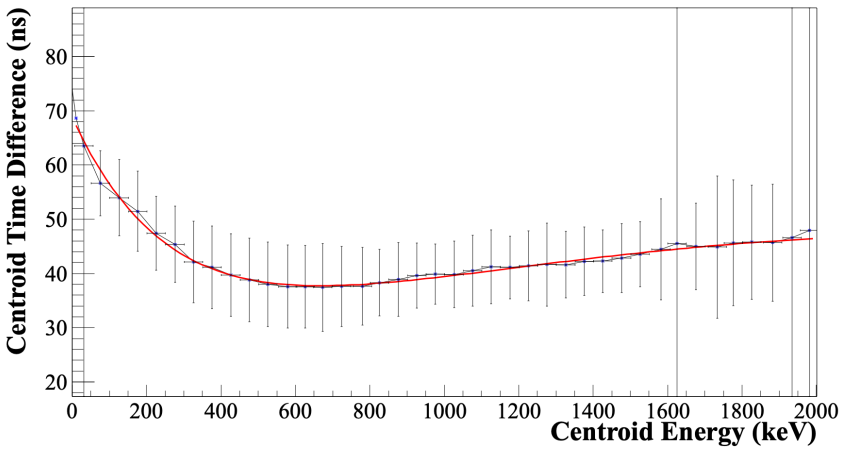

Figure 3.3.15: The average arrival time of events as a function of the energy, along with the fit function (represented by the red solid line) used to model the energy-time relationship to correct for the walk.

This correction was simpler in application for the source measurement as only one structure was seen in the data, however, the high count rate introduced more detector effects to the in-beam data, as seen in Fig. 3.3.18 where a time delay clearly distinguishes the CFD triggered energy region on the left from the lower energy leading edge discrimination on the right. Furthermore, the time-walk correction was not able to fully correct for the energy region below 200.0 keV for the in-beam data, seen in the matrix as the tail in the low energy. The poorer time resolution between the slow and fast signals in this region was negligible to this study as the PG emission lines of interest emerging from the water target, and labelled in Fig. 6.3.2, do not fall in this low-energy region and, as such, do not form part of the energy-filtered data used in the CC reconstruction.

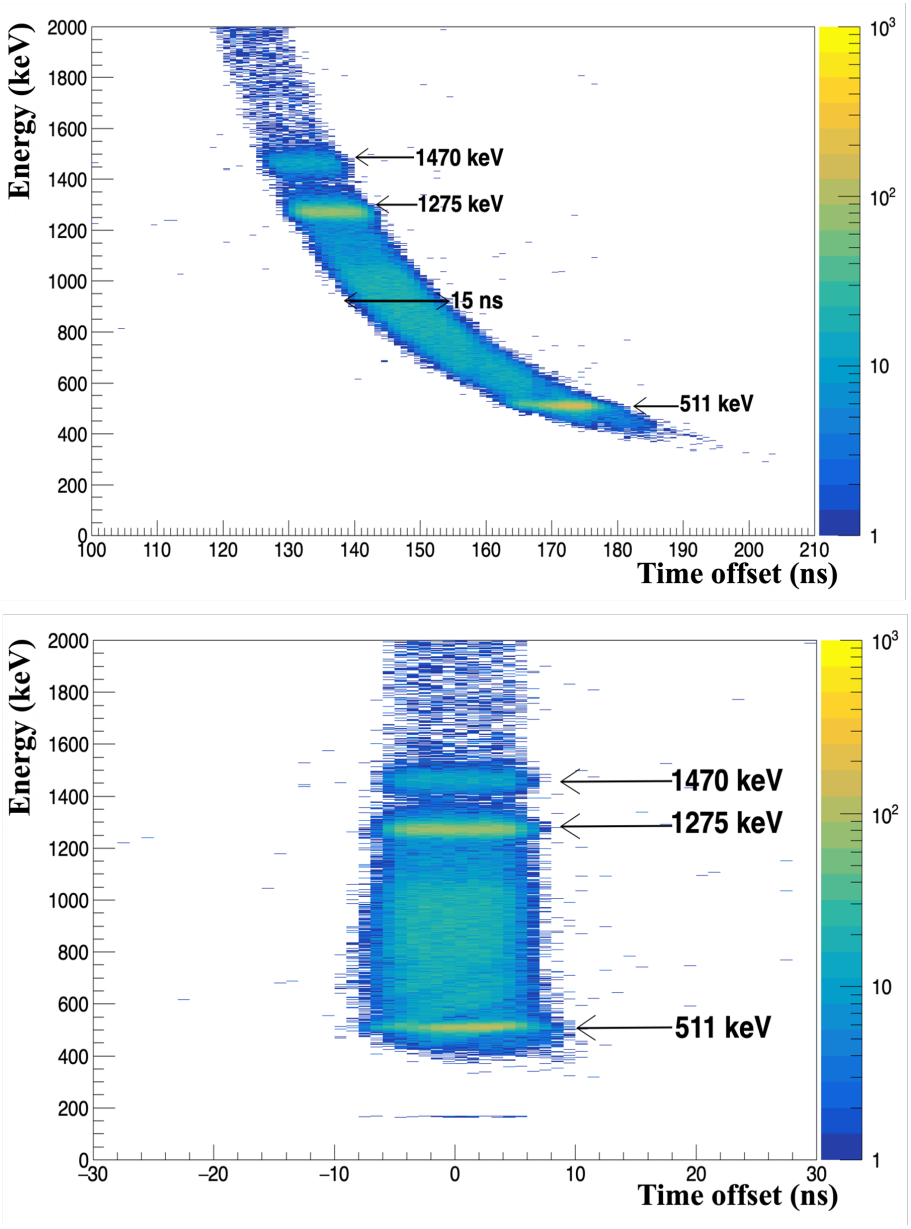

Figure 3.3.16: The time-walk present in ^{22}Na source data. The 2D energy-time matrices with the PG emission lines labelled. The time-walk is clearly visible in the top matrix before the correction is applied, and eliminated in the bottom after correction.

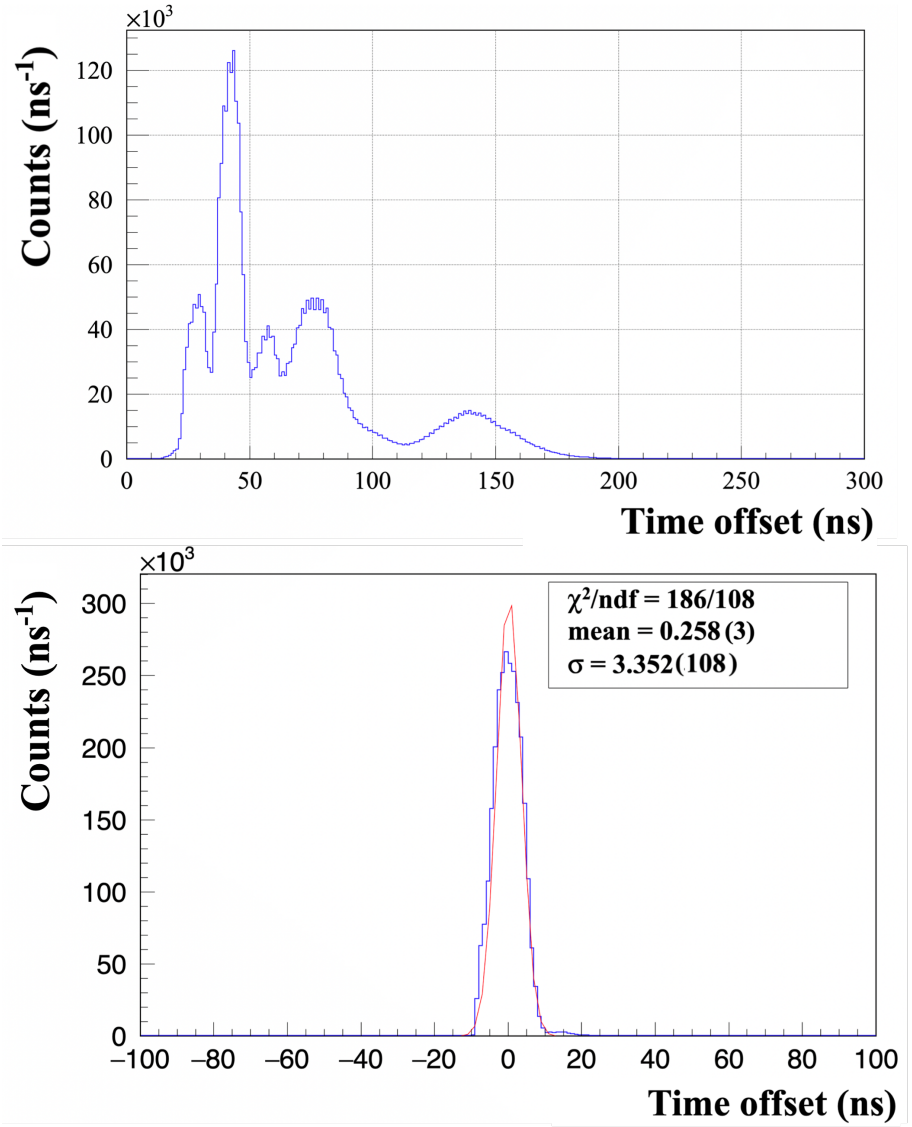

Figure 3.3.17: The time-walk present in ^{22}Na source data. The 1D time offset matrix corresponding to the x-projection of the 2D energy-time matrices, where the top shows the uncorrected walk and the bottom plot shows the Gaussian-fitted time spectrum with 7.87(1) ns FWHM time resolution between the fast and slow detector channels.

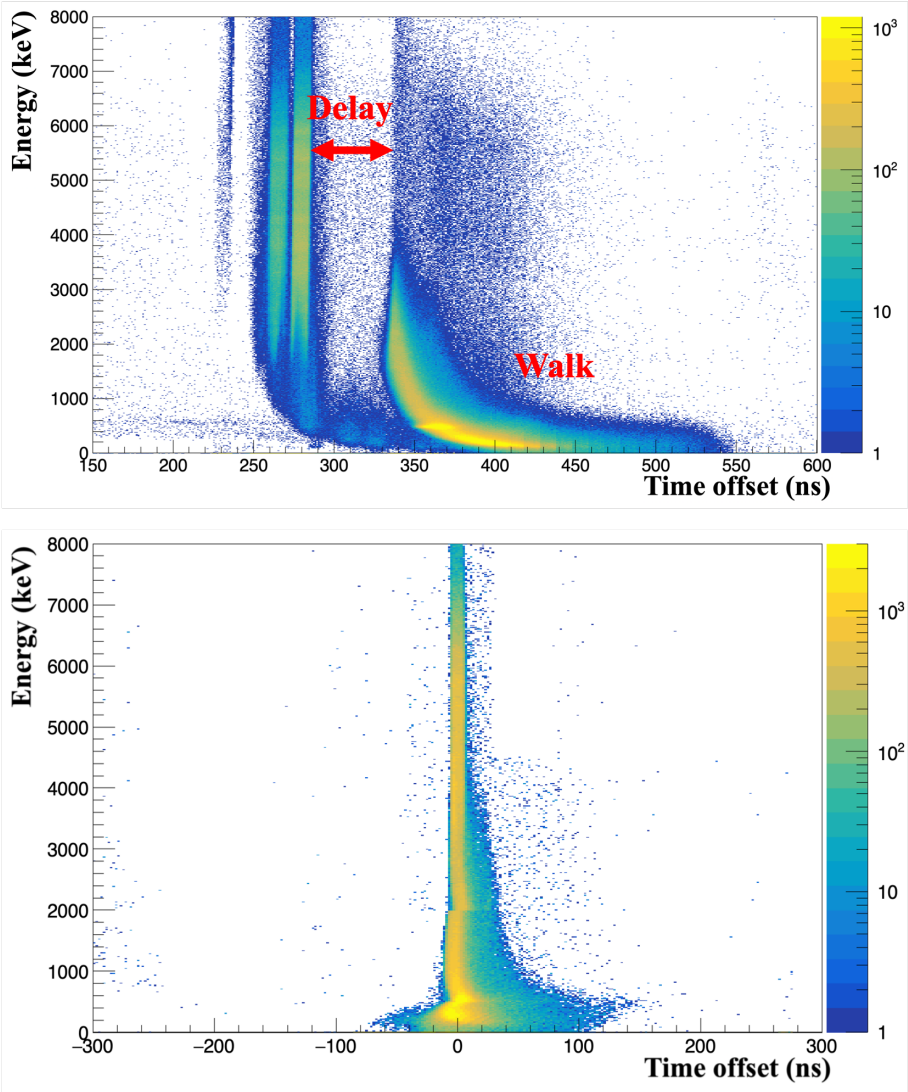

Figure 3.3.18: The 2D energy-time matrices for the 66.67 MeV proton beam data, where a time delay adds a structure to the spectrum in the region of ~ 290.0–330.0 ns in the top matrix before walk correction. The bottom matrix shows the result after time-walk was corrected for.

3.3.7 STM Time Synchronisation of Detector DAQs

The synchronisation method offered flexibility and modularity, allowing for a simple way to communicate events across the two different DAQs. However, it also imposed a limitation on the timing resolution of events across the two systems, which was restricted by the precision of the sync pulses' transmission and recording. If the sync pulses' timing was accurate only to microseconds due to Polaris, then the event timing window had to be of the same order, potentially introducing significant noise into the coincidence files. This issue was encountered during the work, as the Polaris was not originally designed for high-resolution coincidence counting.

Data collection for each detector was carried out as described in Sections 3.2.4 and 3.1.3. When taking measurements with the two detectors in a CC configuration, the $LaBr_3$:Ce detector was set to begin data collection before the Polaris detector. Once the $LaBr_3$:Ce detector was active, the Polaris "connect camera" function was enabled, allowing the Polaris DAQ to send STM pulses to channel 15 of the $LaBr_3$:Ce DAQ.

The Polaris detector's Python GUI allows for the specification of a fixed run time, after which data collection ceases, and no further STM pulses were sent. Due to this setup, the outputted $LaBr_3$:Ce data contained more STM pulses than the Polaris data, corresponding to events recorded before the Polaris detector began collecting data. To address this, all $LaBr_3$:Ce events that occurred before the first "valid" STM pulse in time were removed. The remaining events in the $LaBr_3$:Ce data were then synchronised, with the first valid STM pulse marking the start of the synchronised dataset. Finally, the duration of the remaining $LaBr_3$:Ce events was checked to ensure that it matched the expected run time.

The process of aligning timestamps between the Polaris and $LaBr_3$:Ce detectors was essential for synchronising data and ensuring accurate event correlation. Initially, data from the Polaris detector were read and filtered to isolate single scatter events and STM pulses, producing filtered Polaris data. Simultaneously, data from the $LaBr_3$:Ce detector were read and validated to ensure the integrity of the measurements, resulting in validated $LaBr_3$:Ce data.

Next, coordinate transformations were applied to the Polaris data based on pre-defined transformation matrices specific to each experimental run. These transformations were crucial in aligning the spatial data collected from the Polaris detector to the same coordinate system used by the $LaBr_3$:Ce detector. Following the transformations, sync pulses were extracted from the Polaris data, and their corresponding timestamps were validated. The first valid sync pulse was identified, and all subsequent sync pulses were used to correct the timing of the $LaBr_3$:Ce data.

Once both sets of sync pulses were correctly identified and validated, a time synchronisation process was employed to align the $LaBr_3$:Ce and Polaris data based on these STM pulses. This synchronisation ensured that events detected by both systems could be accurately correlated in time. Finally, the synchronised data from both detectors were merged and sorted, producing a unified dataset that reflected the combined detector event information, where the

scatterer and absorber modules were each assigned their own ID, allowing for precise analysis and interpretation.

3.4 ITHEMBA LABS 66.67 MEV PROTON BEAM MEASUREMENTS

One day of beam time was allocated to this study, during which an experiment was conducted at iThemba LABS in Cape Town, South Africa, to evaluate the potential of CC1 for detecting PGs emitted during PT. The experimental configuration is shown in Fig. 3.4.1. A monoenergetic proton beam with an energy of 66.67 MeV and 1 in 5 pulse selections of 300 ns bunches was directed at a water target ($64 \times 64 \times 162$) mm^3 encased in high-density polyethylene (HDPE) and positioned isocentric with respect to the beam exit and detectors. Water in a HDPE holder was considered in this study as a tissue-equivalent material, as generally used in nuclear medicine experiments, having discrete γ emission peaks from the excited nuclei of ^{12}C, ^{16}O and ^{14}N, the most abundant elements in human tissue. The initial beam energy was chosen such that the beam would fully stop within the target geometry, information which was obtained with simulation by scoring the incident proton energy as a function of beam penetration depth, where the range of 66.67 MeV in water is approximately 4 cm (see Fig 3.4.2). The continuously slowing down approximation (CSDA) range is obtained when one simply integrates the inverse stopping power of the particle energy to obtain the average range (r_{CSDA}) as seen in Eq 3.4.1.

$$r_{CSDA} = \int_0^{E_{inc}} \frac{1}{\rho} \frac{1}{S(E)} dE \tag{3.4.1}$$

Where $S(E)$ is the stopping power of the particle in that material, and E_{inc} is the energy of the incident particle. This is an oversimplified view that is based on no other physics being taken into consideration.

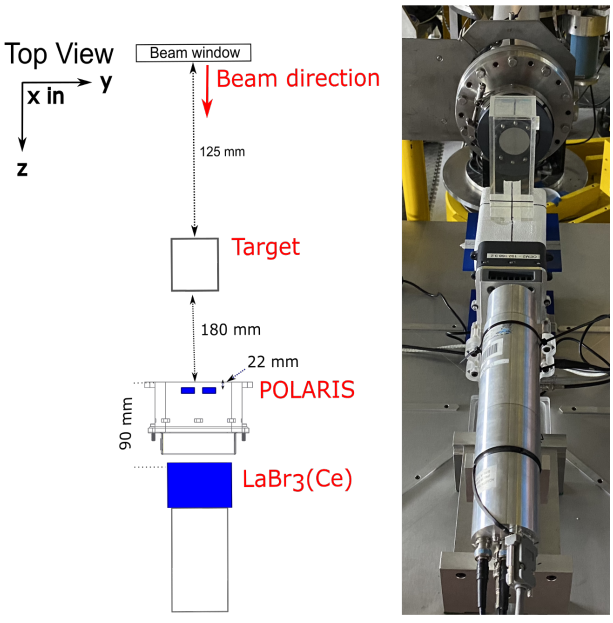

Figure 3.4.1: Left: Picture of the experiment setup, Right: Schematic of the experiment setup with geometrical distances.

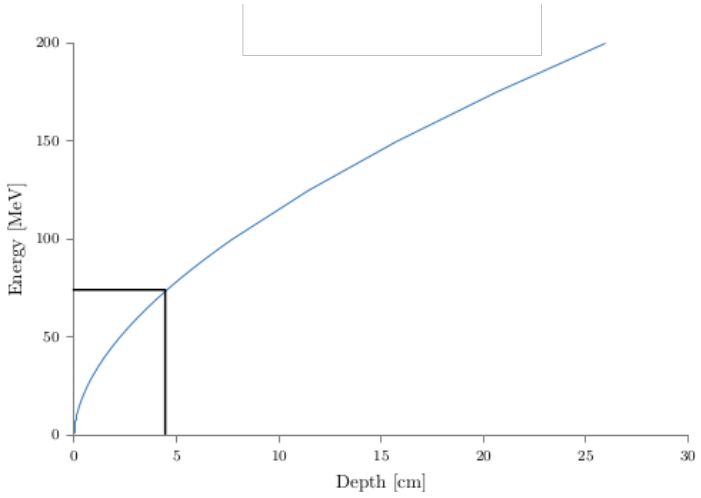

Figure 3.4.2: A plot showing proton range in water as a function of energy measured in MeV, as computed in the CSDA. The 66.67 MeV proton beam stops at ~ 4 cm.

The $LaBr_3$:Ce detector was operated at a HV of -1050 V, supplied by an ISEG unit and coupled to the R2083 PMT, for which the output signals from the PMT anode (slow) and first dynode (fast) were transmitted to the 16-channel digital signal processor Pixie-16 500 MHz module, as described in Section 3.2, and the data was read out via the DDAS software. The Polaris detector data was read out by the regular process described in Section 3.1.3. Measurements were taken for a duration of 20-minutes, during which the POLARIS DAQ was configured to send the TSM pulse to channel 15 of the XIA Pixie-16 module every 2 seconds.

3.4.1 Cyclotron Radio-Frequency Guided Background Subtraction

One drawback of the $LaBr_3$:Ce detector is the background introduced as a result of the internal radioactivity of the detector crystals. This radioactivity is seen in the large peak at 1436 keV and the continuum of β and γ attenuation pictured in Fig. 3.2.6 and discussed in more detail in Section 3.2.2. This could limit the PG detection in the low energy region between 1.0 -2.0 MeV if the statistics are very low. This $LaBr_3$:Ce internal radioactivity introduces a source of background to the measured spectra of the experiments.

To mitigate this issue, the time difference between the detected events and the radio-frequency (RF) signal from the cyclotron was measured. Since the proton beam was not continuous but delivered in bunches with a specific time structure, this approach was effective. For the experiment, the beam was structured into 300 ns bunches with a 1 in 5 pulse selection, ensuring a well-defined time structure, as seen in the banded regions of Fig. 3.4.3(a). The additional artefacts preceding the beam bunch are themselves repeating in nature and originate from the structure of the bunched beam, suggesting an additional current was present and was omitted from the analysis.

Utilising the cyclotron RF signal, background reduction was achieved through a time-of-flight (TOF) approach. This method leveraged the time difference between the arrival of particles at the detector and the RF signal of the proton beam to distinguish signal from back-

ground events. Specifically, PGs emitted almost simultaneously with the proton interaction at the target were detected in-sync with the periodicity of the beam structure. In contrast, background events either originated from beam line components and were synchronised with the primary protons, or were uncorrelated with the beam structure, such as those from $LaBr_3$:Ce internal radioactivity, or had a different emission time-scale, such as delayed gammas and secondary neutrons.

By defining a 2 ns time window centred around the bunch band, synchronised events were identified, while a shifted time window captured out-of-sync events. Subtracting the out-of-sync events from the in-sync events allowed the isolation of the PG energy spectrum, effectively suppressing background noise, particularly that caused by the detector's internal radioactivity. The in-sync, out-of-sync and the difference between the two spectra, resulting in the PG spectrum, is seen in Fig. 3.4.3(b).

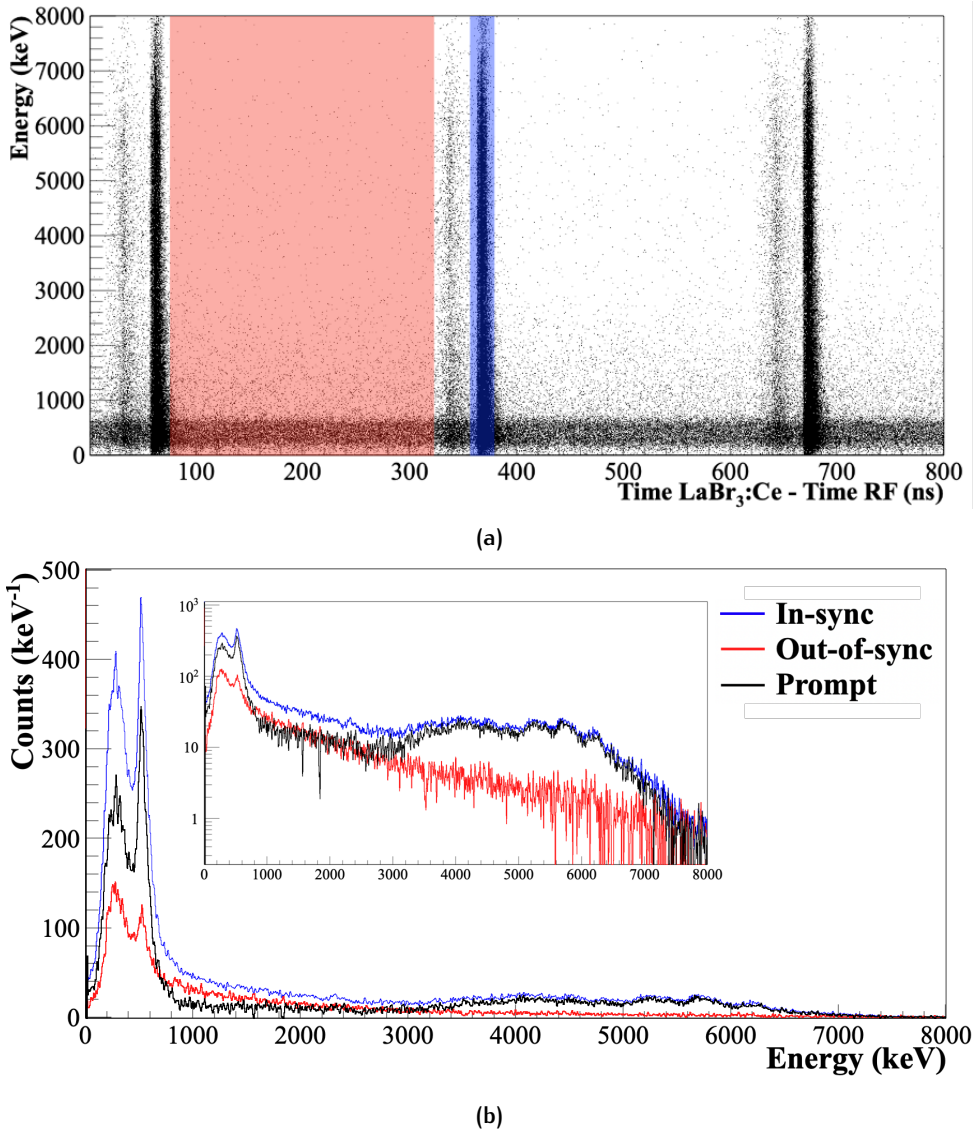

Figure 3.4.3: The cyclotron radio-frequency proton beam was bunched with a 1 in 5 pulse selection and 300 ns between bunches, seen in: (a) the time-energy matrix, where the time is the difference between a detected event and the radio-frequency time. The bands of higher density correspond to regions in time when the proton beam was in-sync (example region is shaded blue) with the detector, and the out-of-sync regions fall between the 300 ns bands (example region is shaded red), and (b) the energy spectrum showing the number of PG events after cyclotron radio-frequency guided background subtraction, obtained by subtracting the out-of-sync spectrum from the in-sync to obtain the PG events energy spectrum. The inlay plot shows the log of the y-axis, highlighting the behaviour of the spectra in the high energy region.

4 INSTRUMENTATION AND METHODOLOGY OF CC2 AND CC3 DETECTORS

The second CC investigated in this thesis, referred to as CC2, featured a novel design that incorporated the MacroPixel LB-14x25c-SiPM-T scintillation detector assemblies (DAs) in 4×2 arrays as the scatterer and absorber layers. These assemblies were pre-coupled high-performance SiPM readout electronics by the manufacturer, providing significant advantages in low-voltage operation and modularity. The third CC investigated in this thesis, referred to as CC3, incorporated the DAs in 6×1 array as the scatterer module with the $2'' \times 2''$ $LaBr_3$:Ce detector detailed in Chapter 3 as the absorber layer. These assemblies were pre-coupled high-performance SiPM readout electronics by the manufacturer, providing significant advantages in low-voltage operation and modularity.

This chapter delves into the design, operation, and characterisation of these DAs, focusing on their application in CC systems. The MacroPixel DAs, specifically $LaBr_3$:Ce and SrI_2:Eu crystals, were thoroughly evaluated for their energy resolution, efficiency, and suitability for Compton imaging. A detailed analysis of the detector geometries and the advanced signal processing methodologies used to assess their performance is included, along with the experimental setup and the DAQs employed to measure and analyse detector performance. The characterisation of gamma-ray sources used for calibration is also discussed. Through these evaluations, the chapter aims to highlight the potential of these DA modules in advanced gamma-ray detection systems.

Due to project constraints, only one DA electronics housing was constructed for experimental measurements, as detailed in Section 4.3.1. The CC performance of CC2 and CC3, which involve up to eight DA modules, were primarily explored through simulation, as outlined in Chapter 5. These simulations were essential for understanding the feasibility of the proposed designs until additional instrumentation becomes available.

As this work seeks to advance CC technology, understanding the interplay between the MacroPixel DAs was crucial. The high-performance SiPM readout electronics in these detectors offer the potential for enhanced modularity and low-voltage operation, promising significant improvements in energy resolution and timing capability compared to traditional detector systems. This chapter thus provides an in-depth examination of how these innovations contribute to the development of effective CC systems for gamma-ray detection.

4.1 DETECTOR ASSEMBLIES

The MacroPixel DAs are pre-assembled, cuboid scintillator-SiPM detectors manufactured by CapeScint [81]. These assemblies use a SensL (now Onsemi) MicroC60035 SiPM, a (6 × 6) mm^2 photodetector with 22292 microcells at a 35 µm pitch and a breakdown voltage of 24.7 V. The high-performance scintillation crystal, measuring (14 × 14 × 25.4) mm^3, was coupled to the SiPM array and equipped with a serial bus T-sensor, as shown in Fig. 4.1.1. The entire unit was housed in a hermetically sealed aluminium enclosure with 0.5 mm thick walls. The detector crystals studied were $LaBr_3$:Ce and SrI_2:Eu, each with identical geometry, differing only in the scintillation crystal material within the DA geometry. The use of SiPM readout electronics for these scintillation detectors offered a modular design that operated at a lower voltage than traditional PMTs, with the potential for position sensitivity in the 2 × 2 SiPM array configuration.

The system was designed to investigate the feasibility of these detectors in a CC system by measuring the performance of these detectors in terms of Compton efficiency, angular, and image resolution. Before CC investigation could take place, the characterisation of these newly acquired detectors was performed by measuring the detector energy resolution response and efficiency with different gamma-ray sources and at different geometries.

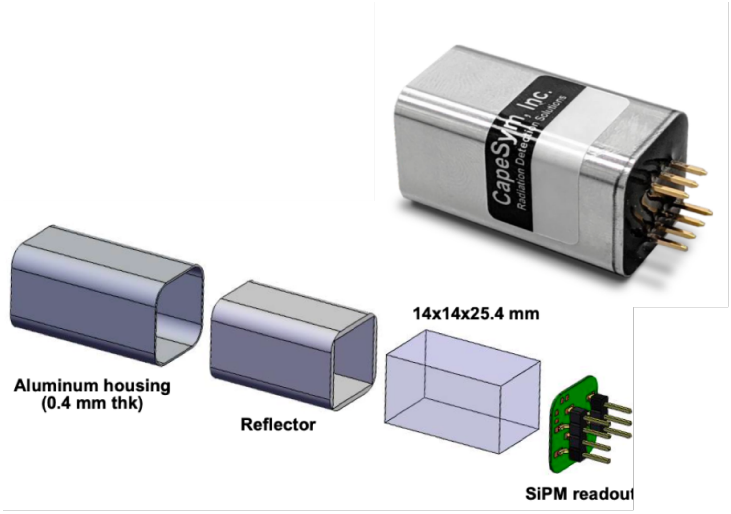

Figure 4.1.1: The DA in a photograph and a schematic where the labelled components that make up the detector are visualised.

4.1.1 $LaBr_3$:Ce

The manufacturer indicated an energy resolution of 3% at 661.7 keV. The greatest performance difference between the cuboid (14 × 14 × 25.4) mm^3 performance when compared to the 2″ × 2″ detector was seen in the presence of the background intrinsic radioactivity. This is emphasised in Fig. 4.1.2 where the background was measured for 10-minutes for each detector in the same laboratory environment. The DA crystal dimensions were too small to stop the characteristic

1435.8 keV gamma ray from the ^{138}La decay to ^{138}Ba. The photon emission wavelength of $LaBr_3$:Ce is in the range from 320.0–440.0 nm [64].

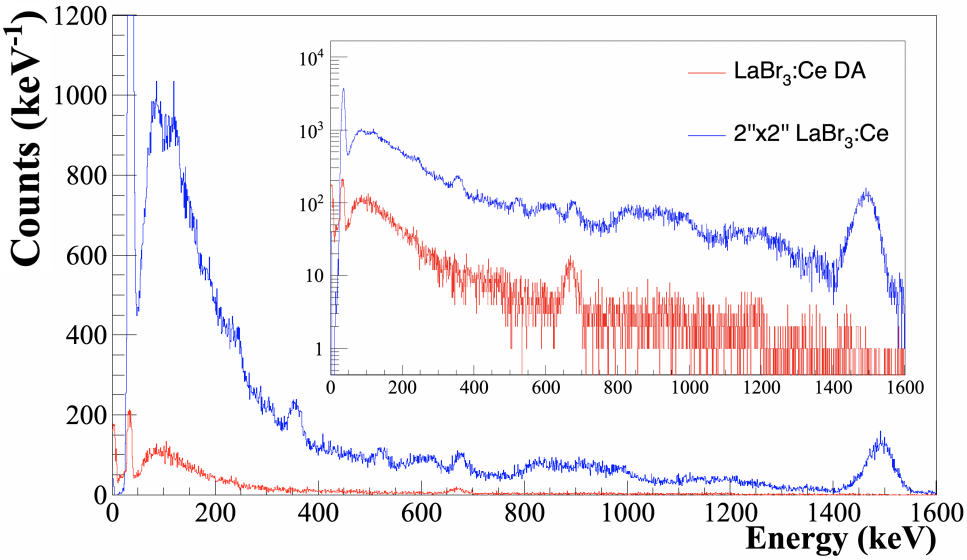

Figure 4.1.2: The internal radioactivity measured for a duration of 10-minute for both the 2″ × 2″ and SiPM-coupled $LaBr_3$:Ce detectors. It can be seen that there was a reduced contribution for the DA, particularly in the higher energy region.

4.1.2 SrI_2:Eu

Strontium iodide was first recognised as a scintillating material by Hofstadter in 1968 [82]. In recent years, there has been renewed interest in SrI_2 due to its exceptionally high light output (~ 100000 photons/MeV) and its impressive energy resolution of ~ 3% at 661.7 keV. A key advantage of SrI_2:Eu over other high-resolution scintillators, such as $LaCl_3$:Ce, $LaBr_3$:Ce, Lu_2SiO_5:Ce, and LuI_3:Ce, is the absence of naturally occurring long-lived radioactive isotopes (such as the ^{138}La in lanthanum, and the ^{176}Lu in lutetium). This makes SrI_2:Eu an attractive option for various applications, such as for use in a CC.

The orthorhombic crystal structure, belonging to the Pbca space group, consists of 24 atoms per unit cell. This includes eight equivalent Sr atoms and two distinct sets of eight iodine atoms. Due to the nearly identical ionic radii of Sr^{2+} (r = 0.12434 nm) and Eu^{2+} (r = 0.11696 nm in mono-clinic and r = 0.11107 nm in rhombic positions), the Eu^{2+} ion readily replaces the isovalent Sr^{2+} ion in the crystal lattice [83, 84, 85].

Research by Cherepy et al. demonstrated that SrI_2:Eu crystals with high Eu concentrations can achieve or surpass the performance of $LaBr_3$:Ce in terms of both light yield and proportionality [86]. Despite recent active research into the scintillation properties of these crystals, their spectroscopic behaviour and the mechanisms of scintillation, along with the energy transfer processes, remain poorly understood. This gap in knowledge is primarily due to limited studies in the vacuum UV region across a broad range of temperatures and energies. Furthermore, the band gap of these crystals has not been accurately determined, partly due to their highly hygroscopic nature, which complicates even basic investigations. The emission

spectrum of the crystal features a narrow peak (0.1 eV) centered at 433 nm, whereas the excitation spectrum displays a broad range from 275.0–440.0 nm [87]. The overlap between the excitation and emission spectra can result in self-absorption of the emitted photons.

Figure 4.1.3 shows the internal radioactivity of the SrI_2:Eu DA. The contributions to the background were identified to primarily originate from the ^{222}Rn decay chain, and not the detector crystal itself. The Sr_2:Eu detector demonstrated a very low (negligible) background contribution.

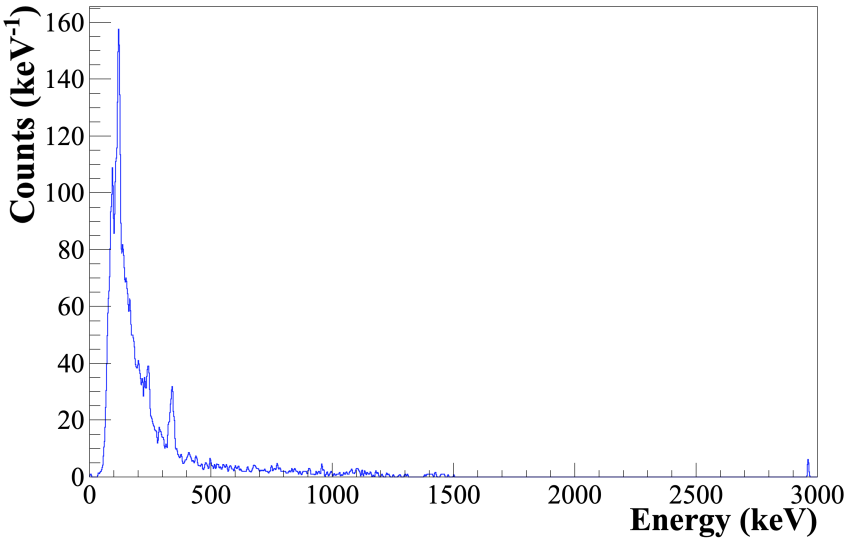

Figure 4.1.3: The background spectrum of the Sr_2:Eu DA, measured for 10 minutes. The peaks at 295.0 and 352.0 keV are attributed to well-known gamma lines from ^{214}Pb, part of the ^{222}Rn decay chain, a naturally occurring source of background.

4.2 SIGNAL COLLECTION AND DATA ACQUISITION

The XIA Pixie-16 500 MHz DAQ was used to shape, digitise and process the signals from the DAs. Each channel independently handles digitisation, triggering, and real-time processing using FPGAs to calculate energy, timing, and charge values (refer to Section 3.2.3.1 for full details). This system operates with fast-timing scintillators, ensuring precise energy and timing measurements by employing digital filters such as CFD and trapezoidal filters. The list mode data collection procedure is described in Section 3.2.11.

4.3 SOURCE CHARACTERISATION OF DETECTORS

In the characterisation of gamma-ray detectors such as $LaBr_3$:Ce, and SrI_2:Eu, the use of various radioactive sources such as ^{152}Eu, ^{60}Co, ^{22}Na, and ^{137}Cs plays a critical role in determining both energy resolution and absolute efficiency. These sources emit gamma rays at

well-defined energies, which allows for the precise calibration of the detectors across different energy ranges.

4.3.1 Instrumentation of the Detector Assemblies

Before investigating the performance of the DA, proper biasing of the detectors was essential. The manufacturer's guide, based on Onsemi's J-Series SiPM datasheet, outlined four biasing configurations, each addressing the handling of standard and fast signal outputs [81]. While all configurations supported standard output, only two were recommended for fast signal use. In this study, the standard signal output was employed for all measurements, but the chosen bias configuration preserved flexibility for future fast signal work. The selected setup used positive polarity for both the standard and fast signals with a positive bias voltage, seen in Fig. 4.3.1. A 10 nF, 50 V low equivalent series resistance ceramic decoupling capacitor was initially included but later removed due to signal reflections that degraded quality. The final configuration is shown in Fig. 4.3.2 (right), where the detector was centrally housed within a Hammond 1590 series aluminium enclosure, securing the biasing and signal electronics. On the left side of Fig. 4.3.2 a photograph shows the detector crystal extending from the electronics box.

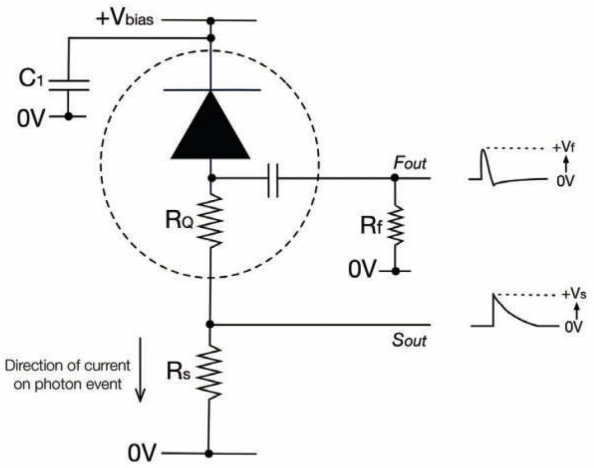

Figure 4.3.1: A diagram of the chosen signal and bias configuration for all DAs. Where the abbreviations used are as follows: V_{bias}: Bias voltage applied to the SiPM, S_{out}: standard output signal, F_{out}: fast output signal, R_s: load resistor for the standard output, R_f: load resistor for the fast output, V_s: standard output voltage, V_f: fast output voltage, R_Q: quench resistor (internal to the SiPM), C_1: decoupling capacitor [81].

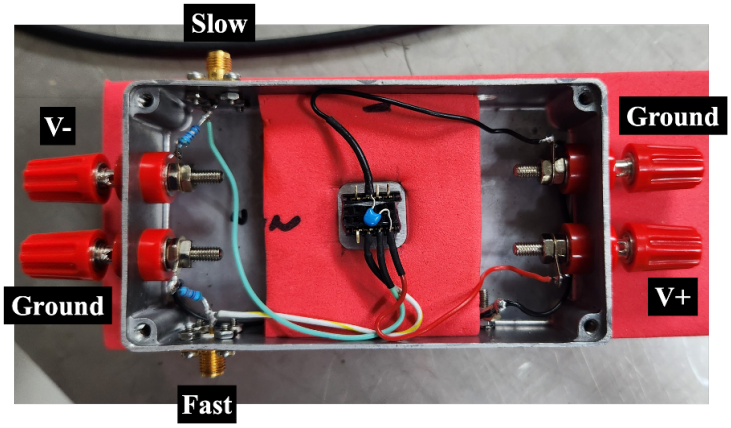

(a)

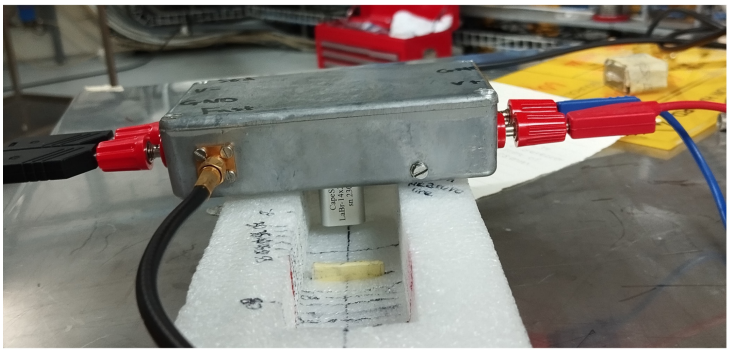

(b)

Figure 4.3.2: The DA seen in photographs as: (a) the custom in-house built housing and biasing for the SiPM-coupled detector with labelled output ports and biasing, shown with the cover removed. The voltage was connected using banana clips and the signal read-out through SMA connectors, (b) a side view to demonstrate how the DA crystal was situated outside the electronics box.

4.3.1.1 Bias Voltage of the SiPM

The investigation into varying bias voltages of SiPMs aimed to understand how changes in overvoltage impacted key performance parameters, including channel gain and energy resolution, and to identify the optimal bias voltage for the detectors. The manufacturer specified the breakdown voltage at 24.7 V and a maximum operating voltage of 30.7 V [81]. By incrementally adjusting the operating voltage, the corresponding effects on the SiPM's gain and PDE were examined. These adjustments ultimately shaped the signal output and influenced the detector's ability to resolve distinct energy levels. The LV power supply, provided by a QL564TP bench top module, supplied power via banana clips, with the detectors drawing a current between 1.0–2.0 mA.

The relationship between SiPM overvoltage and the detector's channel response stems from the combined effects of gain and PDE. Overvoltage, defined as the difference between the applied operating voltage and the SiPM's breakdown voltage, directly impacts both. As overvoltage increases, so does the SiPM's gain, which scales linearly with the applied overvoltage [47]. Gain refers to the multiplication of charge carriers within the SiPM after photon detection, meaning higher overvoltage generates more charge carriers per photon, boosting the resulting signal.

PDE, which represents the likelihood of a photon triggering a detectable signal, also rises with overvoltage but at a slower, non-linear rate. Initially, PDE increases linearly a few volts above the breakdown voltage, but eventually reaches a plateau, meaning additional overvoltage yields minimal improvement in photon detection.

The peak position in the detector's spectrum (the channel number corresponding to a gamma-ray peak) was influenced by both the number of detected photons and the SiPM gain. Since the number of detected photons is PDE, and gain increases linearly with over-voltage, their combined effect results in a parabolic relationship between the peak position and overvoltage. This parabolic trend arises because while the gain rises steadily, the increase in detected photons is more modest, leading to a quadratic scaling of the peak position as overvoltage continues to rise, as illustrated in Fig. 4.3.3(a). Thus, the peak position shifts to higher channel numbers as overvoltage is increased, following this parabolic trend.

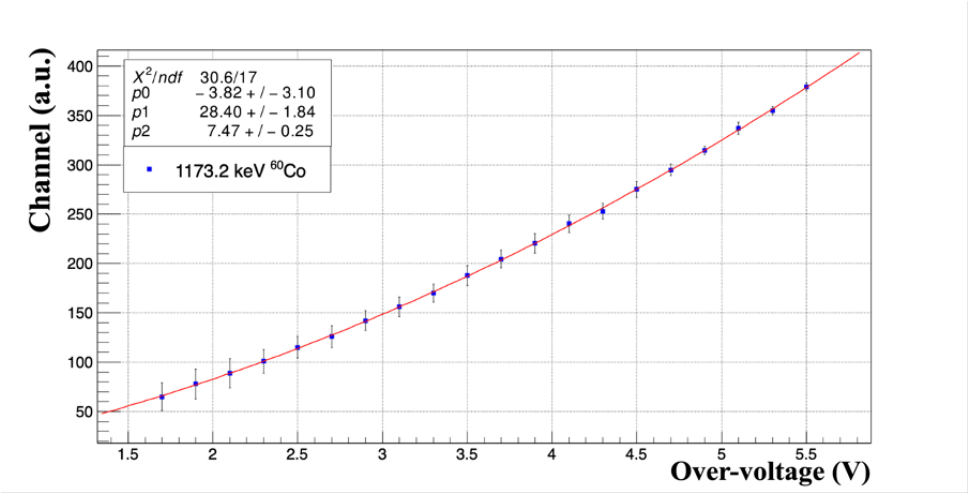

(a)

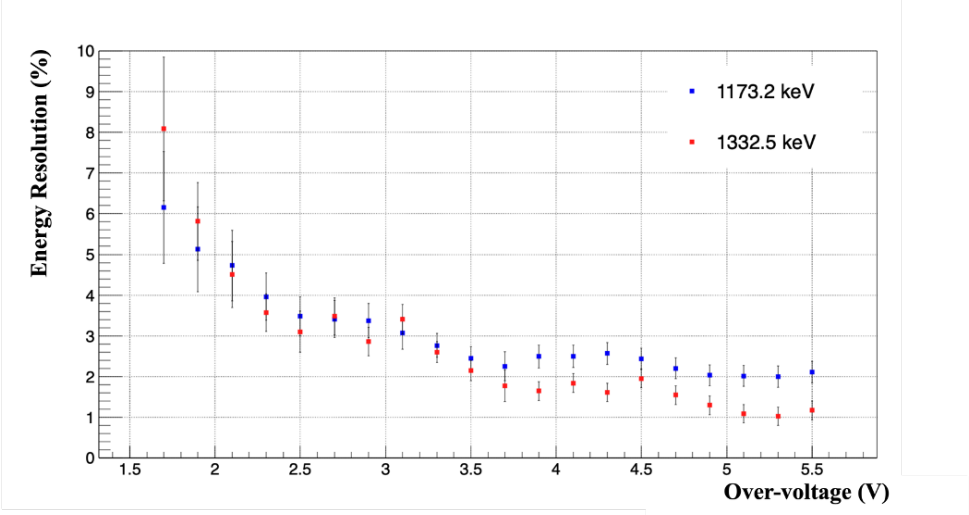

(b)

Figure 4.3.3: The SiPM over-voltage behaviour, measured by the $LaBr_3$:Ce DA for a ^{60}Co source, seen in the relationship between: (a) the SiPM over-voltage and channel number as measured at the 1173.2 keV peak, and (b) the SiPM over-voltage and energy resolution for the 1173.2 and 1332.5 keV peaks.

As PDE increases, more photoelectrons contribute to the signal, reducing statistical fluctuations in the number of detected photons. This decrease in statistical noise, driven by Poisson statistics, leads to improved energy resolution. However, once PDE saturates at higher overvoltage values, further increases in overvoltage have diminishing returns on energy resolution. Figure 4.3.3(b) illustrates this trend by showing the energy resolution improvement as overvoltage increases, observed in the two prominent ^{60}Co gamma peaks.

This enhanced energy resolution is seen in measurements conducted with the SrI_2:Eu and $LaBr_3$:Ce detectors and a ^{137}Cs source in Figs. 4.3.4(a) and (b) respectively. The plots show that a bias of 30 V (5.3 V overvoltage) yields higher gain across the detector channels, leading to significantly better energy resolution. Based on these results, an operating voltage of 30 V was selected for this study, as it optimises energy resolution without pushing into regions of diminishing returns.

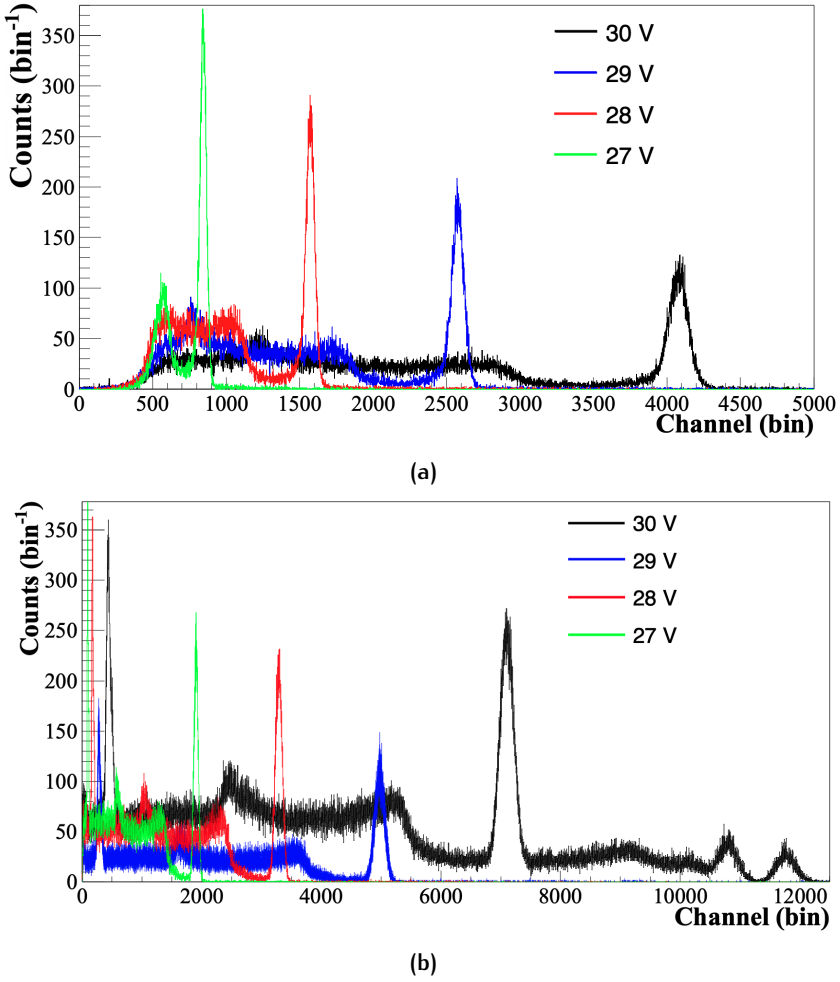

Figure 4.3.4: The uncalibrated gamma-ray energy spectrum measured for different SiPM bias voltages by: (a) the SrI_2:Eu detector with a ^{137}Cs source, and (b) the $LaBr_3$:Ce detector with ^{137}Cs and ^{60}Co sources.

Beyond 5 V of overvoltage, as shown in Fig. 4.3.3(b), the energy resolution improvements level off, with further increases providing no significant benefit. Moreover, raising the voltage beyond 30 V could introduce unwanted effects such as an elevated DCR, caused by higher gain. At greater overvoltages, the SiPM becomes more sensitive to thermal fluctuations and

background radiation, which can lead to false signals. According to the manufacturer, the DCR was ~ 150 kHz/mm² at an overvoltage of 6 V [81].

4.3.2 Detector Signal Shaping

To accurately characterise each detector, the pulse shaping settings were investigated using the ORTEC 572 amplifier. This amplifier enhances and shapes signals, making them suitable for further analysis. The key parameters of the amplifier that were adjusted included gain control, pole-zero (PZ) adjustment, and shaping time.

The Palmtop MCA was employed for this part of the study, interfacing with both the amplifier and the detector through BNC cables. The Palmtop MCA, a compact device for acquiring, analysing, and displaying energy spectra, was used to read out the shaped signal. It digitised the shaped signal, binned it into energy channels, and constructed a spectrum, allowing for detailed analysis of gamma ray energy distribution.

The process began by routing the standard DA signal to the amplifier's input. Subsequently, the amplifier's output was connected to the Palmtop MCA for signal analysis. A critical adjustment was minimising the PZ such that it was carefully tuned to match the decay time constant of the detector signal, crucial for avoiding baseline shifts or undershoots, especially at high count rates.

Each detector was carefully characterised by varying the shaping times and gain settings to achieve the best possible energy resolution and spectrum peak shape. This iterative process ensured that an optimal energy response was measured from each detector. Figure 4.3.5 provides a visual representation of the apparatus and measurement setup used during these adjustments, illustrating the configuration and work flow employed to refine the detector performance. Correct PZ correction stabilised the baseline and improved energy resolution.

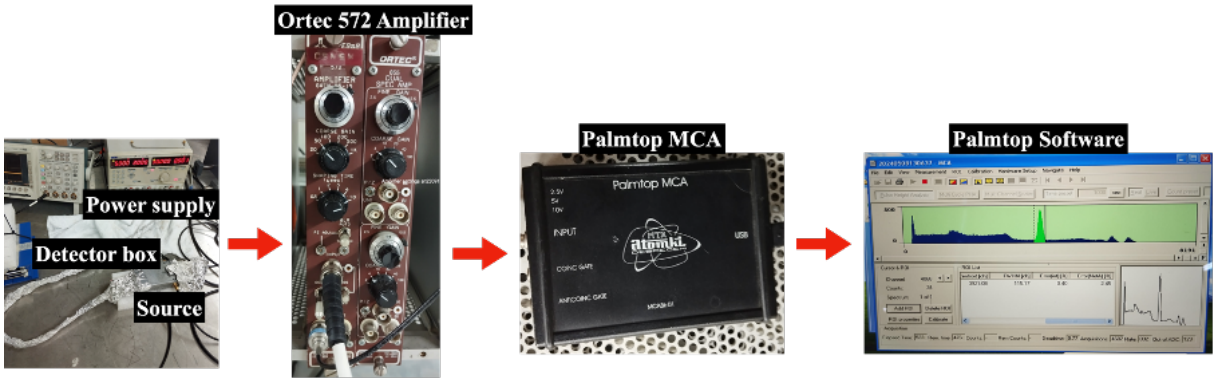

Figure 4.3.5: A labelled visualisation of the measurement process. The signal from the DA was shaped by the amplifier, after which the unipolar response was measured by the Palmtop MCA.

Gain control was adjusted to ensure the input signal was appropriately amplified for the MCA, optimising it for analysis. The shaping time was varied among the available settings (0.5, 1, 2, 3, 6, or 10 µs). Shorter shaping times provide faster signals but can increase noise, while longer shaping times improve energy resolution by filtering out noise, albeit at the

expense of a slower response. The shaping time was adjusted to strike a balance between optimal energy resolution and spectrum peak shape. For improved signal quality, as illustrated in Fig. 3.2.13 for the 2″ × 2″ $LaBr_3$:Ce detectors, a 50 Ω impedance was added using jumpers to enhance signal shape and energy resolution. Measurements were performed for both the $LaBr_3$:Ce and SrI_2:Eu DA. The manufacturer quoted energy resolution values for these detectors were stated to be 3% at 661.7 keV. Fig. 4.3.6 shows the energy spectrum of the $LaBr_3$:Ce DA, measured at the optimal shaping time of 1 μs and 30 V operating voltage, for which the energy resolution was 3.12% at 661.7 keV.

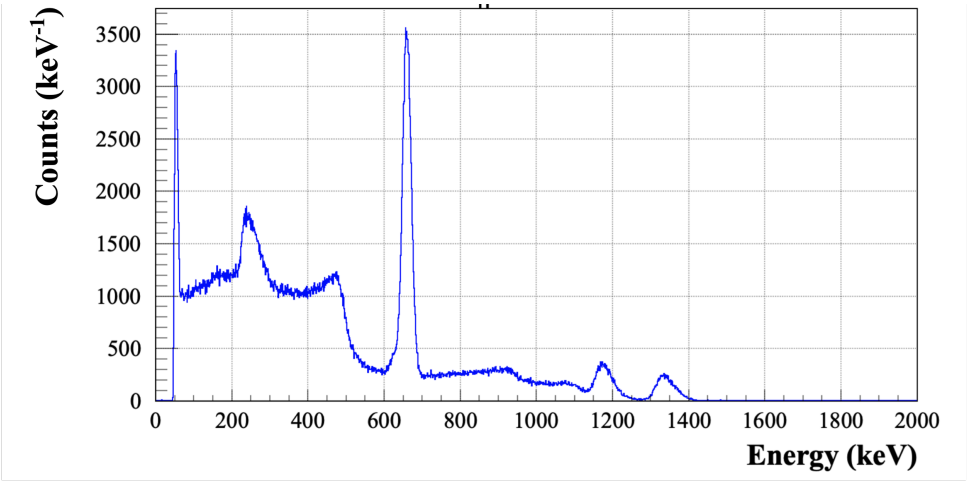

Figure 4.3.6: The energy spectrum of the $LaBr_3$:Ce DA, measured at the optimal shaping time of 1 μs, a gain of 10 and 30 V operating voltage, for which the energy resolution was 3.12 % at 661.7 keV. The measurement was performed for 10-minute using both ^{137}Cs and ^{60}Co sources.

The SrI_2:Ce DA required a much longer shaping time of 10 μs, which was chosen as shorter shaping times resulted in a prominent tailing effect in the photopeaks. The energy spectrum response for the 10 μs shaping is seen in Fig. 4.3.7(a) to be 3.41% at 661.7 keV, and the signal energy resolution response improvement with longer applied shaping times is seen in Fig. 4.3.7(b). The work of [88] investigated the effect of shaping time on a 1″ × 1″ SrI_2:Ce crystal coupled to a PMT, where it was also found that 10 μs provided the best energy resolution.

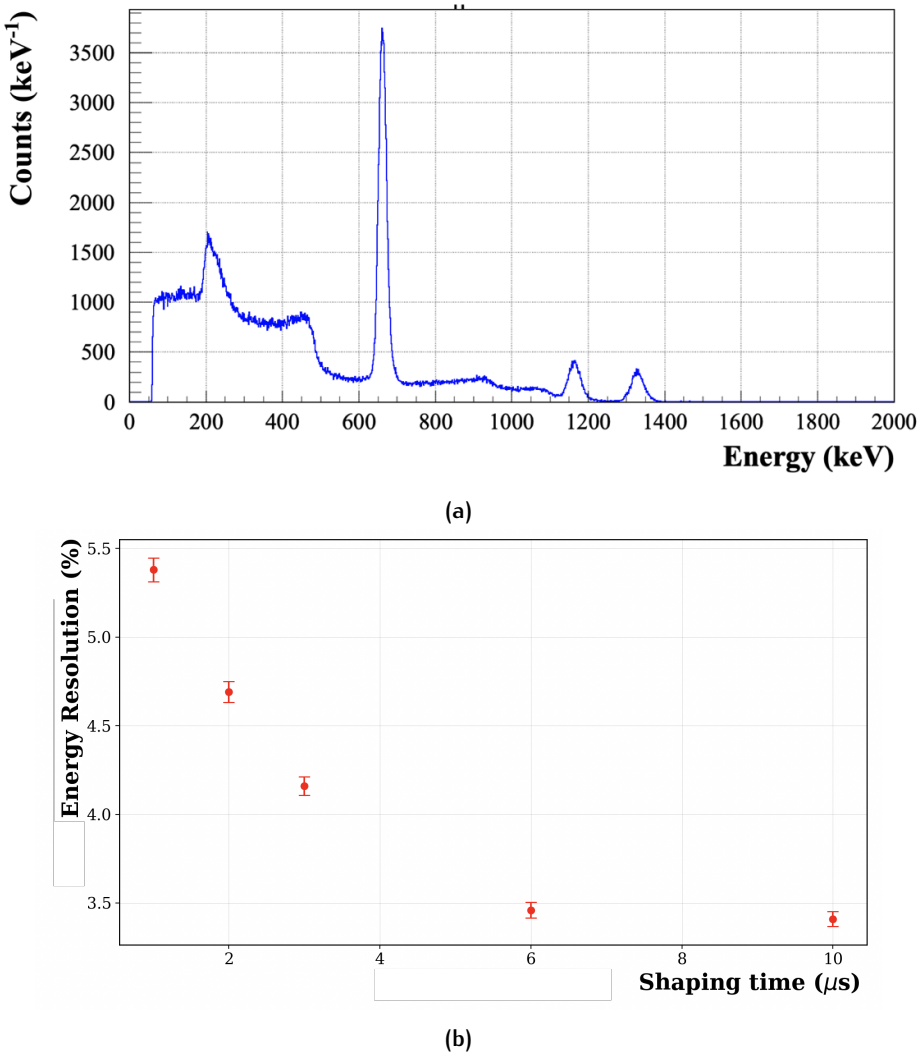

Figure 4.3.7: The SrI_2:Eu DA detector: (a) the gamma-ray energy spectrum measured at the optimal shaping time of 10 µs, a gain of 37.5 and 30 V operating voltage, for which the energy resolution was 3.41 % at 661.7 keV, where the measurement was performed for a 10-minute period using both ^{137}Cs and ^{60}Co sources, and (b) the relationship between signal shaping time and energy resolution response at 661.7 keV of the detector, which was seen to improve with longer signal shaping times.

4.3.3 Decay Constant

The decay constants of the DAs were characterised to be input to the DDAS software to ensure optimal energy resolution performance. A longer decay constant helps reduce noise but may compromise energy resolution, whereas a shorter decay constant enhances energy resolution but can increase noise. An incorrect decay constant setting can distort the shape of the trapezoidal function.

To characterise the decay constant, over 10000 signal traces, each 8000 ns in length, were collected for both the slow and fast signals. These traces exhibit an exponential decay described by the function $\sim e^{-t/\tau}$, where τ represents the decay constant (for more details, see Section 2.1.2). By fitting an exponential function to each trace, the value of τ was determined.

The fitting procedure is illustrated in Figs. 4.3.8 and 4.3.9 for the standard signals of the $LaBr_3$:Ce and SrI_2:Eu DAs. The process begins with the recording of the signal trace from the detector, as shown in Figs. 4.3.8(a) and 4.3.9(a). The longer shaping time of the SrI_2:Eu detector is observed in the fall time of the detector when compared to the very quick drop-off of the $LaBr_3$:Ce DA signal. Next, in Figs. 4.3.8(b) and 4.3.9(b), a constant function was fitted to the base of each trace to determine the constant offset, which was then subtracted from the original trace. The resulting trace, shown in Figs. 4.3.8(c) and 4.3.9(c), was then fitted with the exponential decay function (described in more detail in Section 2.1.2) to extract the amplitude and the decay constant (τ).

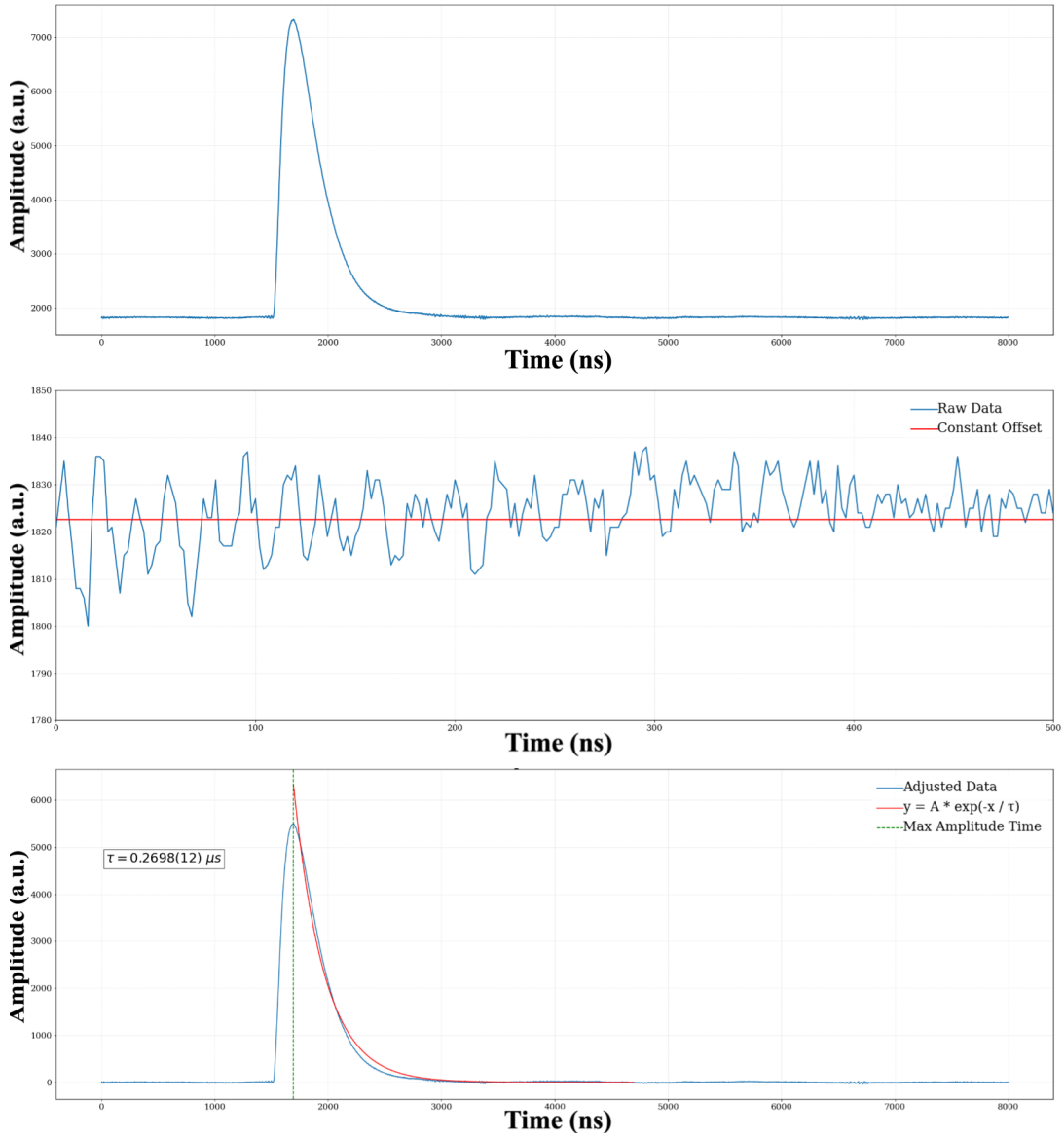

Figure 4.3.8: The fitting procedure used to determine the decay constant τ for the $LaBr_3$:Ce DA standard signal involves several key steps: (a) a typical slow signal trace is displayed, (b) a constant function was fitted to the data to establish the value of the constant offset, and (c) the trace was adjusted by subtracting the constant offset, and an exponential fit was applied to the corrected trace to extract the decay constant τ.

This fitting process was applied to each of the 10000 recorded traces, resulting in a corresponding set of τ values. Figure 4.3.10 shows the τ values for the $LaBr_3$:Ce DA, for which the most frequently occurring value was identified from this distribution to be 266.50(37) ns. The

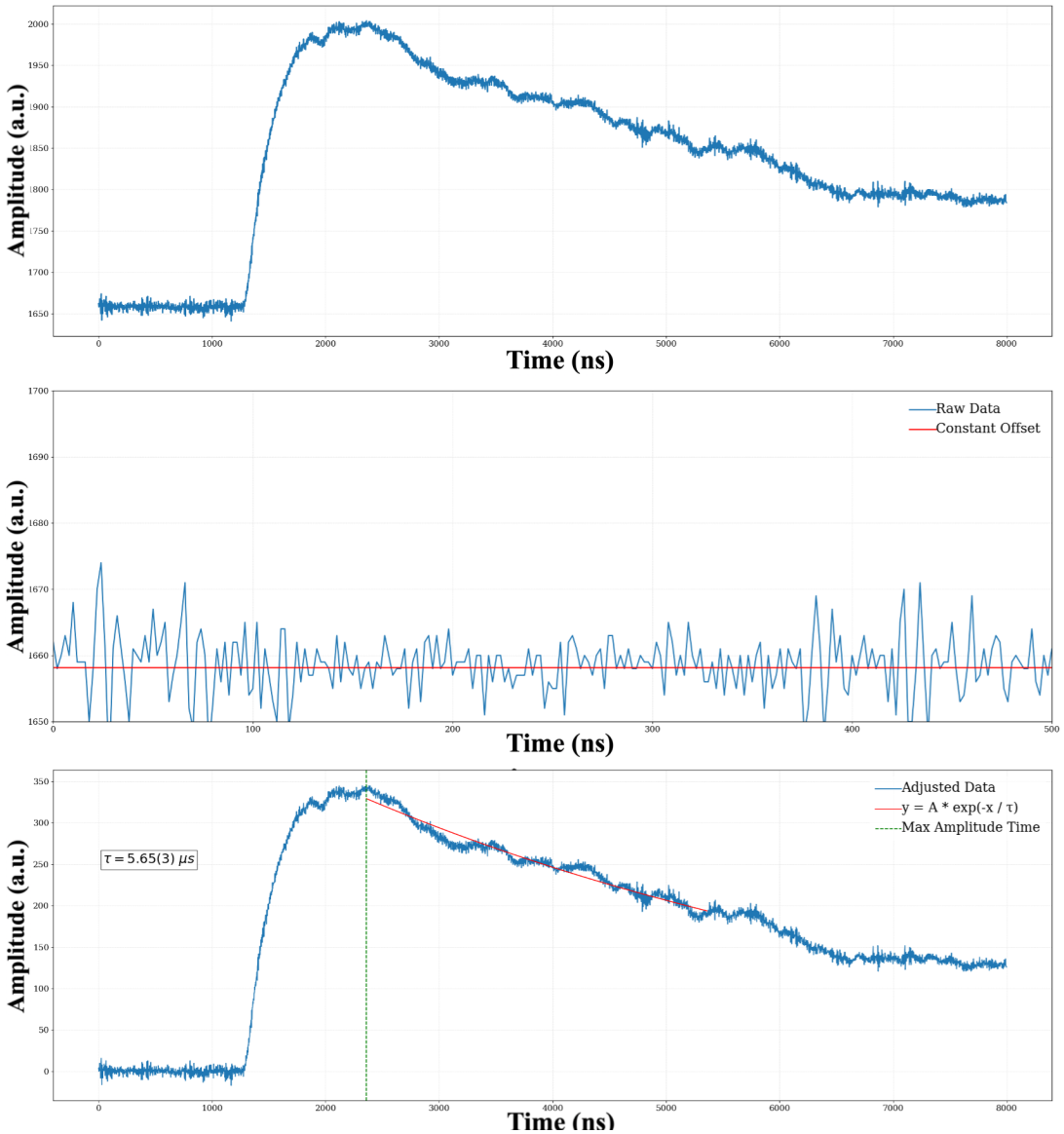

Figure 4.3.9: The fitting procedure used to determine the decay constant τ for the SrI_2:Eu DA standard signal involves several key steps: (a) a typical slow signal trace is displayed, (b) a constant function was fitted to the data to establish the value of the constant offset, and (c) the trace was adjusted by subtracting the constant offset, and an exponential fit was applied to the corrected trace to extract the decay constant τ.

τ value for the SrI_2:Eu detector was calculated to be 6.50(138) μs. These measurements were performed using a ^{137}Cs source.

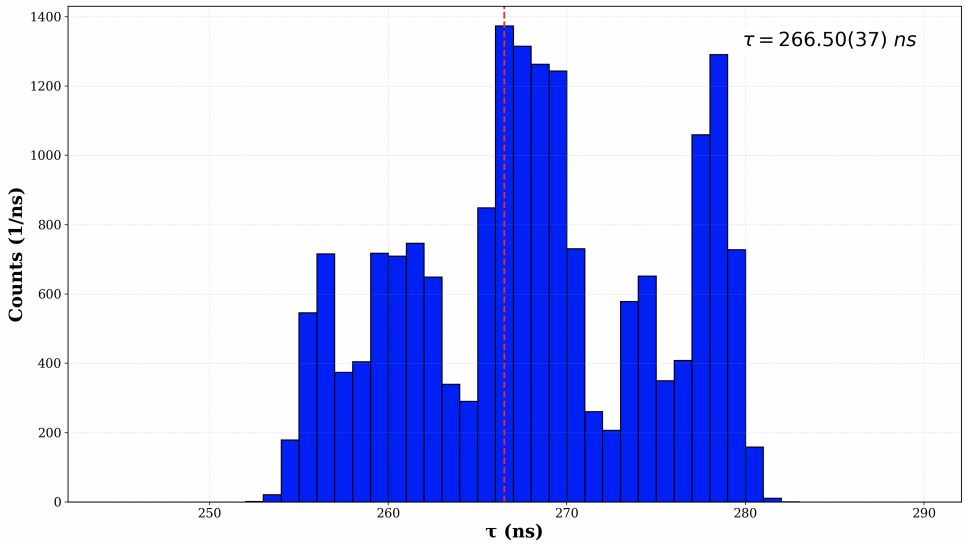

(a)

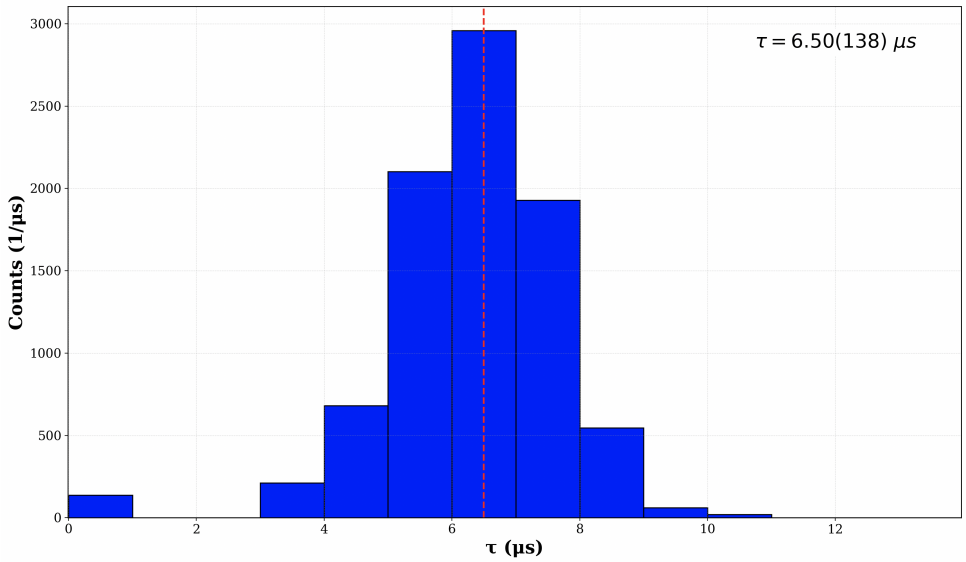

(b)

Figure 4.3.10: The decay constant τ for: (a) the $LaBr_3$:Ce DA signal, for in excess of 10000 traces. The most frequent value was measured to be 266.50(37) ns, for which the energy resolution was at a desired minimum, and (b) the SrI_2:Eu DA signal for in excess of 10000 traces. The most frequent value was measured to be 6.50(138) μs.

4.3.4 Energy Resolution

Energy resolution (ΔE/E) of a SiPM-coupled scintillator system can be expressed as a combination of several factors [89, 90]:

$$\Delta E/E = \sqrt{\sigma_{intr}^2 + \sigma_{dark}^2 + \sigma_{st}^2} \tag{4.3.1}$$

The intrinsic resolution (σ_{intr}) includes the inherent resolution of the scintillator material and the probability of light transmission from the scintillator to the light-collecting device. The enhanced energy resolution from the larger array of SiPMs can be attributed to the improve-

ment in σ_{intr}, resulting from the increased probability of light transmission. The statistical contribution is inversely related to the number of photoelectrons, while the dark current contribution (σ_{dark}) increases as the gain rises. Adjusting the SiPM over-voltage influences both σ_{stat} and σ_{dark}, but in opposite ways. In this case, the improvement in energy resolution at higher bias voltages is due to the reduction in σ_{stat} outweighing the increase in σ_{dark}.

Further optimisation of the DDAS shaping parameters involved determining which flat top and rise time parameters were most suitable to the shaping. Measurements with the ORTEC preamplifier and Palmtop MCA, as well as the signal trace capturing and τ calculations, showed that the shaping time requirements of the two detector crystals would differ considerably. The energy resolution measurements were performed using the same methodology detailed in Section 3.3.2.

A ^{137}Cs source was used to measure the energy resolution of the detectors at the 661.7 keV photopeak in the detectors. The $LaBr_3$:Ce detection was measured at various energy flat top and rise time parameters (detailed in Section 3.2.3.3), controlled in the DDAS software. Figures 4.3.11(a) and 4.3.11(b) show the energy resolution of the 661.7 keV photopeak as a function of trapezoidal and triangular shaping, respectively, measured in units of µs. The triangular shaping was the shaping of the signal with the energy flat top set to zero. The peak sample region from which the signal was at a maximum was therefore equal to the trapezoidal rise time. In terms of signal shape, triangular shaping may be preferred over trapezoidal shaping when a simpler, faster response is needed. Triangular shaping produces a peak that rises linearly to a maximum and then falls linearly, creating a sharp and well-defined pulse. This shape was beneficial for reducing pulse pile-up and ensuring that successive signals do not overlap in time-sensitive applications. Due to the nature of the signal decay constant, trapezoidal shaping was investigated. It was seen that a minimal resolution of 3.47(23)% was produced in the trapezoidal shaping by setting the rise time to 0.06 µs and flat top to 0.5 µs, while a slightly lower energy resolution of 3.41(20)% was measured by setting the rise time to 1 µs and flat top to 0 µs (omits the flat top) for the $LaBr_3$:Ce DA.

The triangular shaping was seen not to distort the energy spectrum, as seen in Fig. 4.3.13 for the SrI_2:Eu detector, where a 10-minute measurement was performed using ^{137}Cs and ^{60}Co sources. Figure 4.3.13(a) shows that a rise time of 17.92 µs and flat top of 0 µs produced the optimal energy resolution of 3.82(18)% at 661.7 keV, the gamma-ray energy spectrum of which is shown in Fig. 4.3.13(b). The typical DDAS parameter values for the $LaBr_3$:Ce DA, discussed in Section 3.2.3.1, are presented in Table 4.3.1.

Parameter	Slow signal (µs)
Fast risetime	0.1
Fast flat top	0.1
Energy risetime	1
Energy flat top	0
Peak sample	1
Peak separation	1
Decay constant	12
CFD delay	0.01

Table 4.3.1: The parameters adjusted for the LaBr−3:Ce DA, chosen to achieve the best energy resolution.

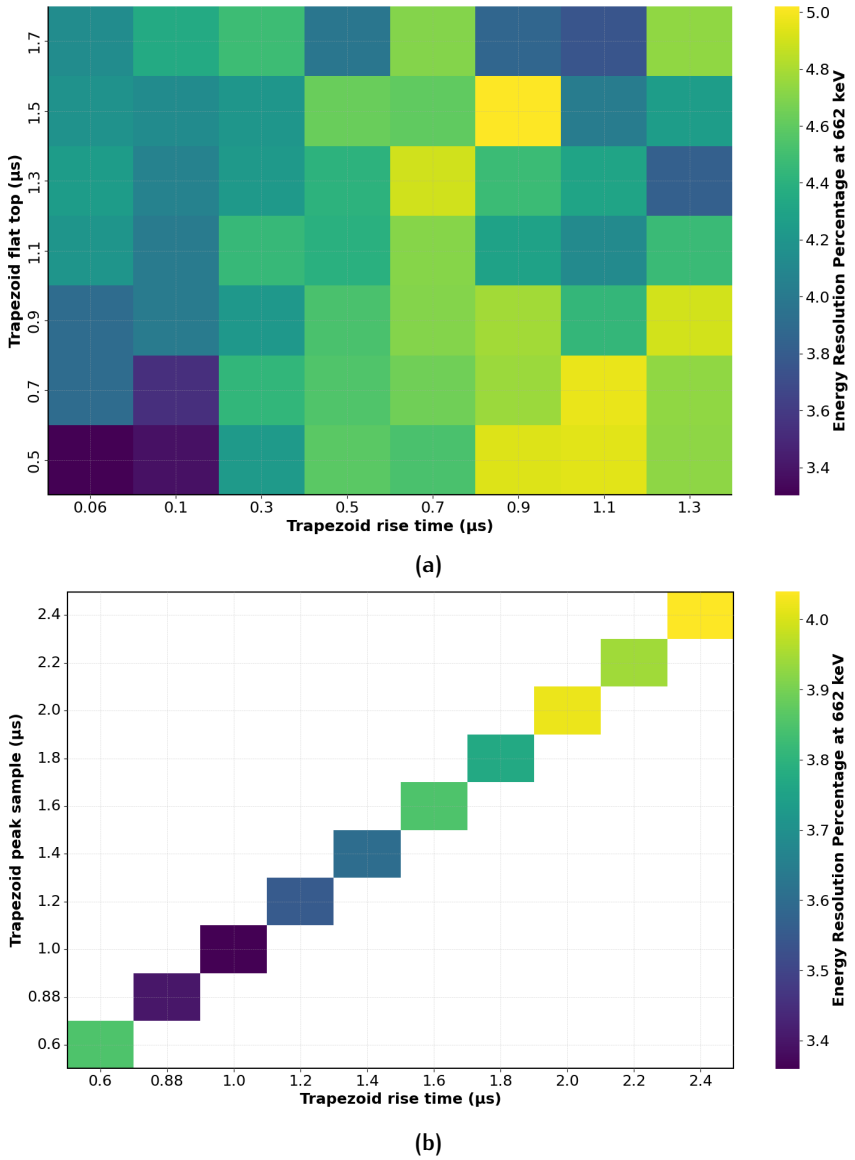

Figure 4.3.11: Matrices showing the effect of varying the DDAS parameter settings on energy resolution for the $LaBr_3$:Ce DA: (a) the trapezoidal shaping varying of the energy filter rise time and flat top values, and (b) the triangular shaping (trapezoidal flat top = 0) of the rise time and the peak sample value.

Investigation into the optimisation of the DDAS energy shaping parameters for the SrI_2:Eu detectors favoured the triangular shaping technique, as trapezoidal shaping of this detector signal was tricky as the signal began to produce tailing in the photopeaks. The typical values for the SrI_2:Eu DA user-defined functions, as described in Section 3.2.3.1, are presented in Table 4.3.2.

A 10-minute measurement was conducted with optimised triangular fitting parameters, using a combination of ^{152}Eu, ^{137}Cs, and ^{60}Co sources placed 10 mm from the centre of the detector face. Energy resolution was determined for the photopeaks in the spectrum, with the first 11 peaks originating from ^{152}Eu, the 661.7 keV peak from ^{137}Cs, and the final two peaks from ^{60}Co. The measured photopeak energies were 41.1, 121.8, 244.7, 344.3, 411.12, 443.98, 778.9, 867.4, 964.1, 1099.0, 1408.0, 661.7, 1173.2, and 1332.5 keV.

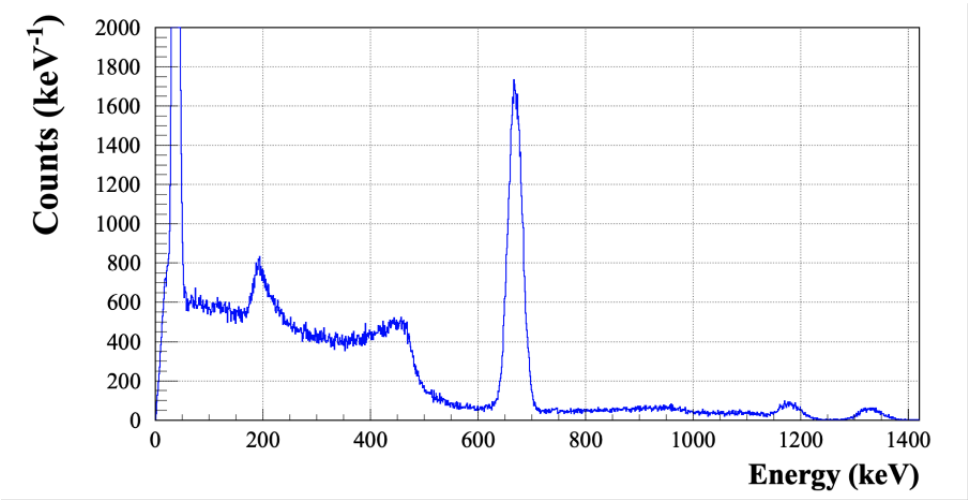

Figure 4.3.12: Energy spectrum of the $LaBr_3$:Ce DA response using triangular signal shaping (rise time of 0.06 µs and flat top of 0.5 µs), showing an energy resolution of 3.41% at 661.7 keV. The measurement was conducted over a 10-minute duration using ^{137}Cs and ^{60}Co sources.

Parameter	Slow signal (µs)
Fast risetime	0.1
Fast flat top	0.1
Energy risetime	17.92
Energy flat top	0
Peak sample	17.92
Peak separation	4
Decay constant	6.5
CFD delay	0.01

Table 4.3.2: The parameters adjusted for the SrI_2:Eu DA, chosen to achieve the best energy resolution.

Figure 4.3.14(a) illustrates the approximately linear relationship between energy resolution and $1/\sqrt{E}$, where the fit equation for the Sr_2:Eu DA was given by $R(E) = \frac{84.25(1263)}{\sqrt{E}} + 0.13(41)$. Similarly, Figure 4.3.14(b) presents the linear relationship for the $LaBr_3$:Ce DA, characterised by the equation $R(E) = \frac{59.41(1291)}{\sqrt{E}} + 1.31(46)$. The constant term represents the constant dark current or noise in the system.

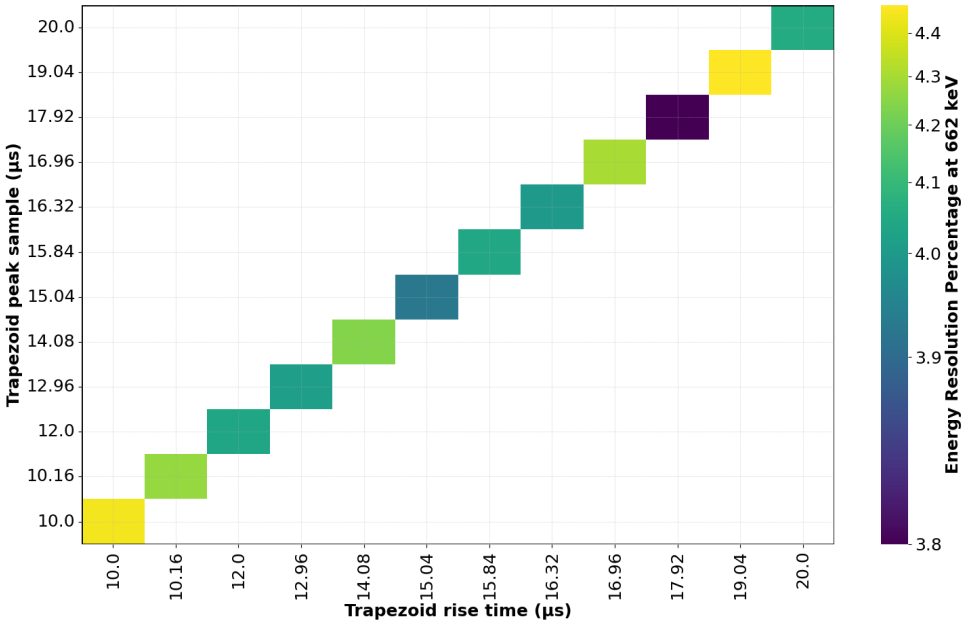

(a)

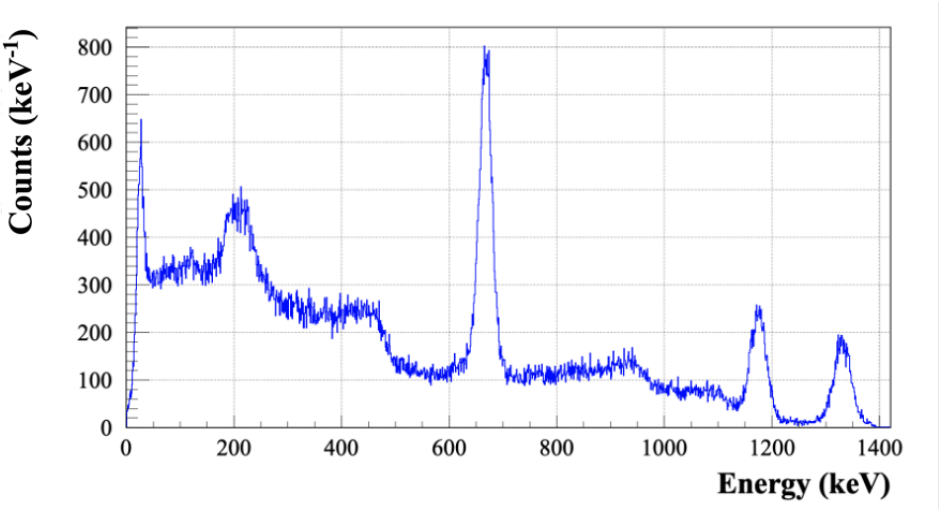

(b)

Figure 4.3.13: Triangular shaping of the Sr_2:Eu DA signal: (a) the energy resolution matrix obtained by varying of the rise time and the peak sample values (trapezoidal flat top = 0), and (b) the energy spectrum of the SrI_2:Eu DA response using triangular signal shaping (rise time of 17.92 µs and flat top of 0µs), showing an energy resolution of 3.82% at 661.7 keV. The measurement was conducted over a 10-minute duration using ^{137}Cs and ^{60}Co sources.

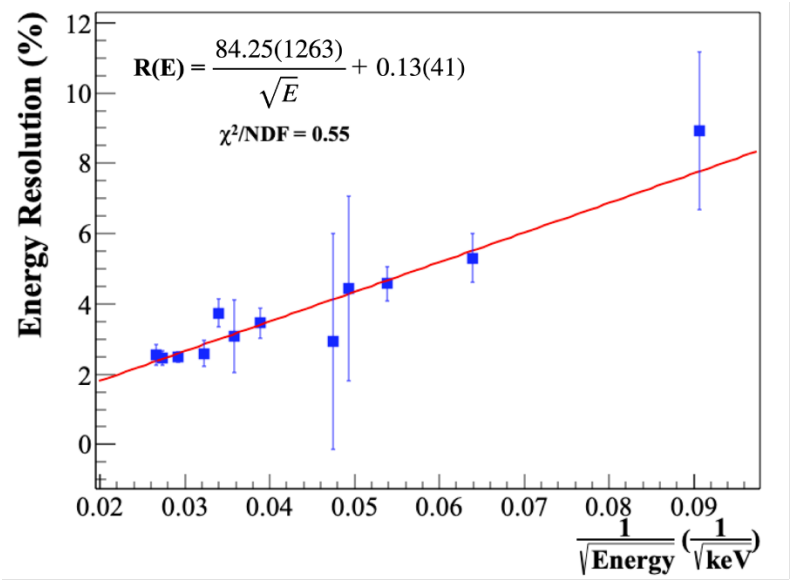

(a)

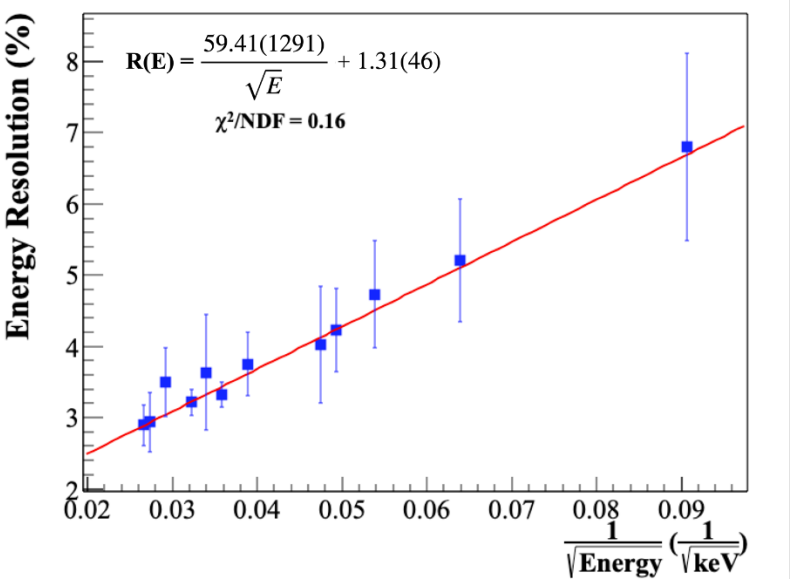

(b)

Figure 4.3.14: Energy resolution curves obtained using ^{152}Eu, ^{137}Cs and ^{60}Co sources placed 10 mm from the detector face for: (a) the SrI_2:Eu, and (b) the $LaBr_3$:Ce DAs. The fit used for each detector is labelled on the plot.

4.3.5 Energy Calibration

The energy calibration for both the $LaBr_3$:Ce DA and SrI_2:Eu DA detectors were performed using radioactive sources with well-known gamma-ray emission energies. This process involved aligning the energy photopeaks from these sources with specific channels in the spectrum. To ensure accuracy across a wide energy range, the well-defined gamma and x-ray peaks of ^{152}Eu were utilised: 41.1, 121.8, 244.7, 295.9, 344.3, 411.12, 443.98, 778.9, 867.4, 964.1, 1099.0, 1408.0 keV. Accurate energy calibration is critical for CC applications, as it enhances the detector's ability to precisely reconstruct gamma-ray interactions. After background subtraction (see Section 6.3.1), the peaks were fitted using Radware effit.

Figures 4.3.15 and 4.3.16 show the energy calibration residuals for each order of polynomial fit to the detector channel-energy data, plotted for each of the known peak energy values used in the spectrum of ^{152}Eu for the $LaBr_3$:Ce and SrI_2:Eu detectors, respectively. The median residual energies and their associated uncertainties are included in a box underneath each of the Figs 4.3.15 and 4.3.16. A grey shaded region between -1.0 and 1.0 keV has been added to the plot to guide the eye toward lower and higher obtained residual values. Both detector responses favour a third-order polynomial fit to convert channel values into energy values, as this approach minimises residuals. This nonlinearity arises because the incident gamma-ray energy is not always deposited entirely in a single interaction [24]. Instead, the energy can be shared among multiple secondary electrons due to single or multiple Compton scattering events, followed by photoelectric absorption. Additionally, when photoelectric absorption occurs, the remaining excited atom can release its energy through various processes, such as emitting Auger electrons, which further contribute to the observed variability in the energy spectra. These combined effects lead to deviations from a perfectly linear response. This is not unusual, as scintillators can exhibit non-linear responses, especially at higher gamma-ray energies. The conversion of gamma-ray energy to light output is not perfectly linear in scintillators such as $LaBr_3$:Ce and SrI_2:Eu [24]. As energy increases, this non-linearity becomes more pronounced, requiring higher-order calibration functions, such as a third-order polynomial, to accurately map energy to channel values [57].

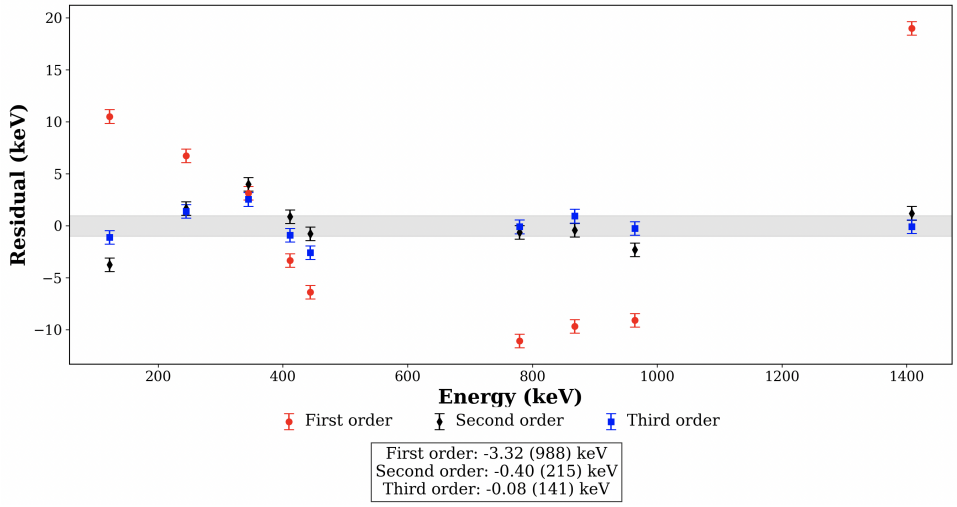

Figure 4.3.15: The energy calibration residuals and associated errors for each order of polynomial fit to the detector channel-energy data are shown, plotted for each of the known peak energy values used in the spectrum of ^{152}Eu for the $LaBr_3$:Ce DA. A grey shaded region between -1.0 and 1.0 keV has been added to the plot to guide the eye toward lower and higher obtained residual values.

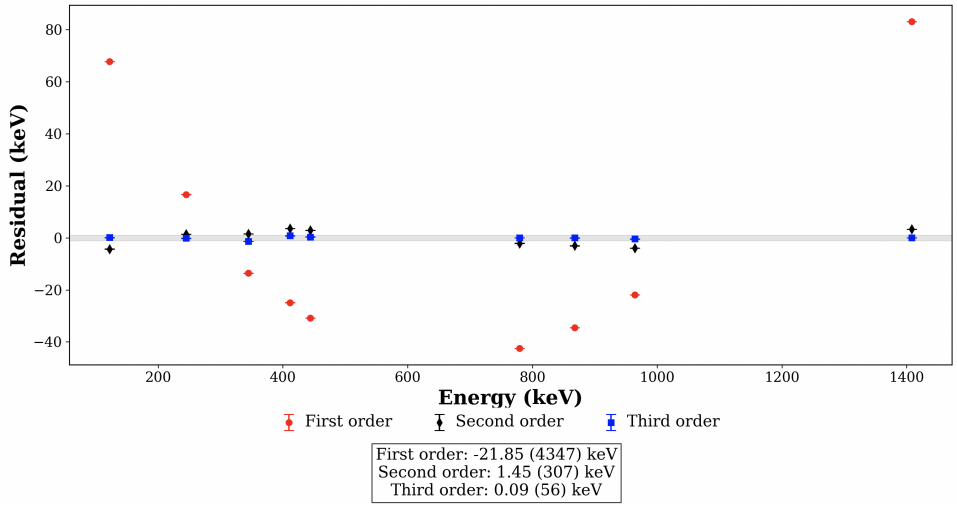

Figure 4.3.16: The energy calibration residuals and associated errors for each order of polynomial fit to the detector channel-energy data are shown, plotted for each of the known peak energy values used in the spectrum of ^{152}Eu for the SrI_2:Eu DA. A grey shaded region between -1.0 and 1.0 keV has been added to the plot to guide the eye toward lower and higher obtained residual values.

4.3.6 Measurements at Detector Side and Face

The orientation and geometry of a detector can significantly influence the gamma spectroscopy measurements, particularly in the Compton region. The DA dimensions ($14\times 14 \times 25.4$ mm^3) mean it has a larger depth along the 25.4 mm axis compared to the 14 mm axes. When measuring gamma rays from the face (14×14 mm^2) versus the side (14×25.4 mm^2), the effective volume of scintillating material that the gamma rays interact with changes. For side measurements, gamma rays interact over a shorter depth, which might limit the number of interactions and thus affect the Compton scattering results. For face measurements, the longer

depth allows for more interactions, potentially capturing a wider range of scattered gamma rays.

Further concerns regarding detector measurements with the source incident on the side of the detector versus the detector face (see Fig. 4.3.17 include the light collection due to variations in the light path and potential light losses affecting the SiPM performance, and thus the energy resolution. Measurements were performed with ^{137}Cs and ^{60}Co sources placed at 30.5, 60.5, and 90.5 mm from the detector face for 10-minute intervals. Of particular interest was whether the Compton backscatter and edge peaks would appear reduced or distorted when comparing the geometries, as well as the efficiency and energy resolution performance comparison of the photopeaks.

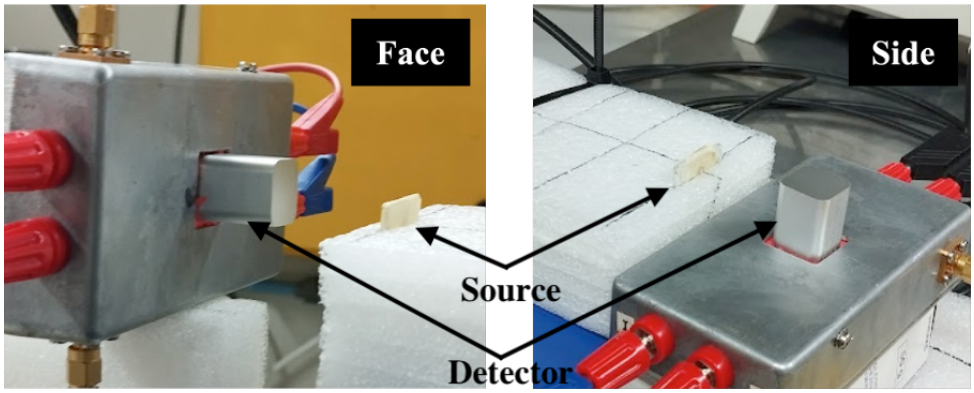

Figure 4.3.17: A photograph demonstrating the difference between a detector measurement with the source incident on the detector face (left), or with the source incident on the detector side (right).

The energy resolution of the 661.7 keV peak in the uncalibrated spectrum of ^{137}Cs in Fig. 4.3.18(a) was measured to be 3.07(61)% for the side positioning and 3.04(67)% for the face positioning, indicating that the energy resolution was unaffected by the geometrical change in the measurements. Further, the Compton distribution shows the equivalent response for each geometry. The most notable difference observed in Figs. 4.3.18(a) and 4.3.18(b) is the reduction in statistics between the two geometries. The source-to-side geometrical configuration contains just 66% of the statistics of the source-to-face configuration, which was attributed to the difference in depth of the detector.

The FEPE was measured for both the face and side configurations of the $LaBr_3$:Ce DA at 30.5, 60.5 and 90.5 mm source-to-detector distances for the 1173.2 and 1332.5 keV photopeaks in the decay of ^{60}Co. The FEPE is plotted for the face (■) and side (•) measurements for each energy, seen in Fig. 4.3.19. It was observed that the FEPE was ~ 0.1% higher for the side-to-source than the face-to-source configuration. This was attributed to the greater surface area of the side (14×25.4) mm^2 versus the face (14×14) mm^2 of the detector, increasing the probability of interactions in the crystal.

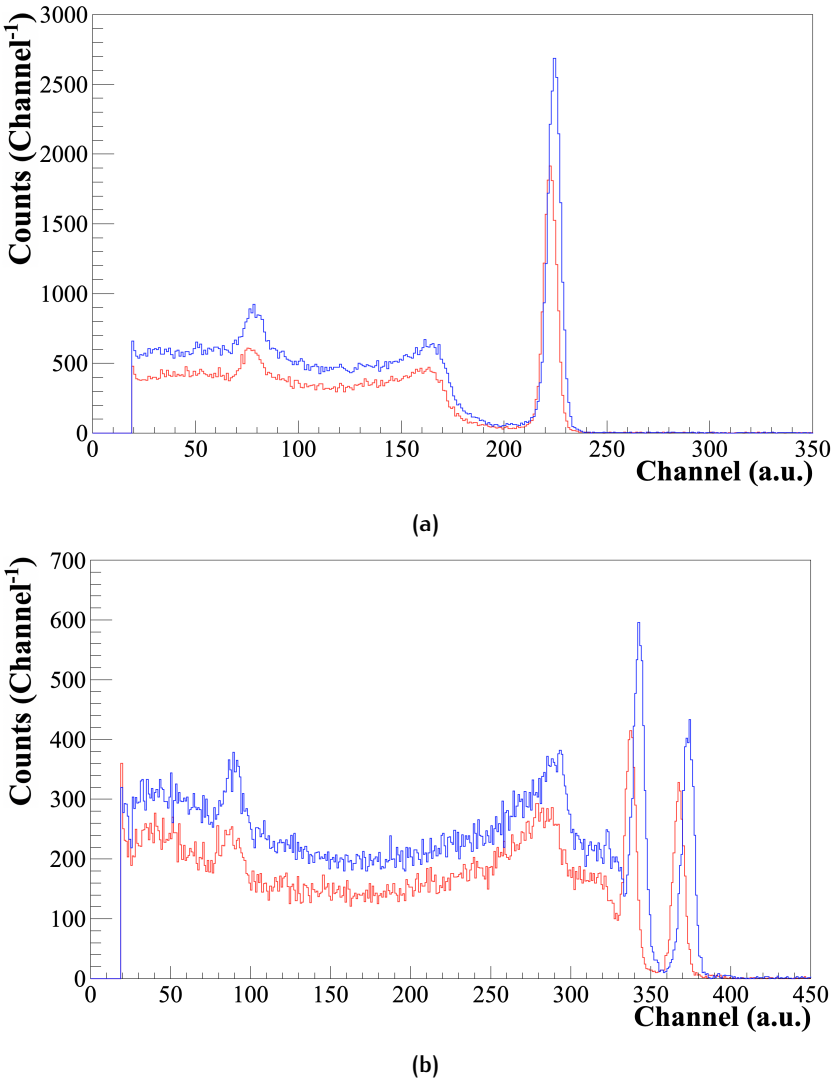

Figure 4.3.18: A comparison of the uncalibrated $LaBr_3$:Ce DA energy response when the source was positioned 30.5 mm from the face (blue) or the side (red) of the detector: (a) for a ^{137}Cs source, and (b) for a ^{60}Co source for 10-minute durations each.

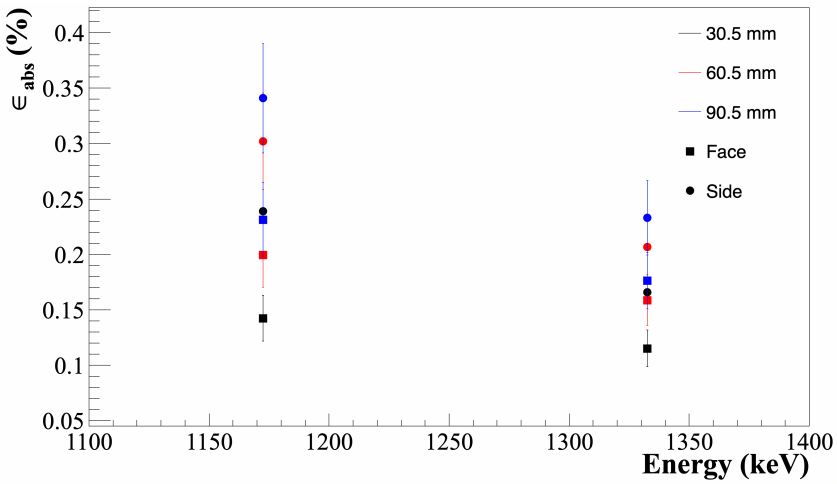

Figure 4.3.19: A comparison of the $LaBr_3$:Ce DA FEPE response when the source was positioned 30.5 (black), 60.5 (red) and 90.5 (blue) mm away from the face (■) or side (●) of the detector.

4.3.7 Efficiency

The efficiency measurements for the SiPM-coupled detectors were performed in the same manner as those of the CC1 detectors discussed in Section 3.3.4. Radware was used to obtain the number of counts under each photopeak and subtract the background for the spectrum of a ^{152}Eu source. The decay of ^{152}Eu emits multiple gamma-ray energies in the range of 121.8–1408.0 keV, making it particularly valuable for FEPE measurements and calibration. Its complex decay scheme provides numerous peaks across this wide energy spectrum, which was ideal for constructing an efficiency curve that accurately represents the detector's response to various gamma-ray energies, thereby ensuring precise quantification of the detected signals.

The gamma energy spectrum of the SrI_2:Eu DA with the source positioned 10 mm from the detector face exhibited reduced energy resolution due to pulse pile-up effects. This was seen in the gamma energy spectrum of the detector at various source-to-detector distances in Fig. 4.3.20 where the spectrum for the 10 mm distance (black line) suffers degradation in energy resolution compared to the sources placed further away from the detector. Pulse pile-up occurs when two or more gamma-ray events happen in rapid succession, causing their signals to overlap before the system can fully process the first event. In this case, the proximity of the source to the detector likely increased the event rate, leading to a higher probability of signals overlapping. When signals overlap, the DAQ system struggles to distinguish individual pulses, resulting in distorted pulse shapes. This distortion can affect the accurate measurement of the energy deposited by each event, as the system integrates the combined signals instead of treating them separately. Consequently, this degradation of pulse clarity reduces the overall energy resolution of the detector. Instead of sharp, well-defined photopeaks, the spectrum becomes broadened, leading to less precise identification of gamma-ray energies. For this reason, the 10 mm distance was not included in the FEPE calculations for the SrI_2:Eu DA.

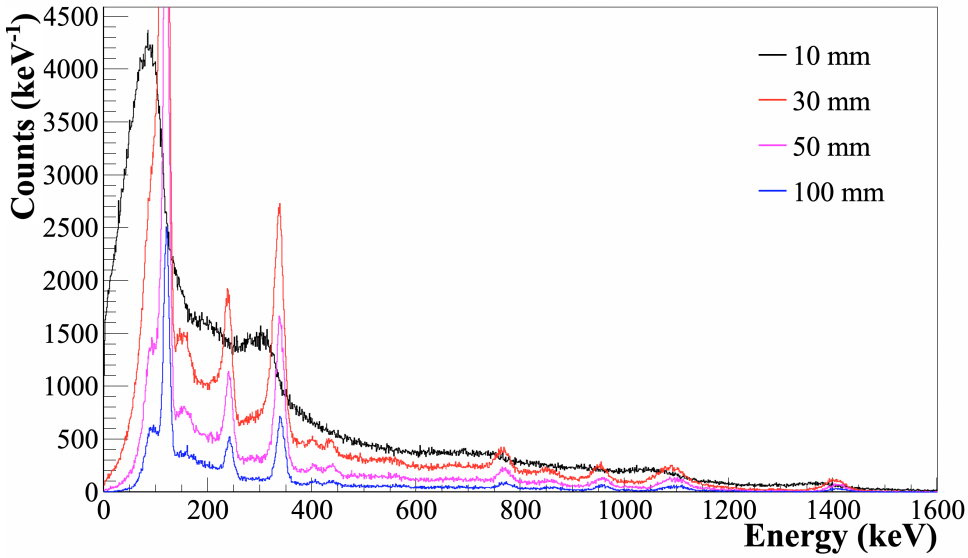

Figure 4.3.20: The SrI_2:Eu detector energy spectrum measured with a ^{152}Eu source placed at various source-to-detector distances. At near distances, the detector suffers from pulse pile-up effects, decreasing the energy resolution considerably.

The FEPE was calculated at different source-to-detector distances for the DAs, seen in Fig. 4.3.21(a) for the SrI_2:Eu DA and Fig. 4.3.21(b) $LaBr_3$:Ce DA, and were each fitted with the logarithmic-polynomial function $\ln(\epsilon(E)) = a_0 + a_1\ln(E) + a_2(\ln(E))^2 + a_3(\ln(E))^3$).

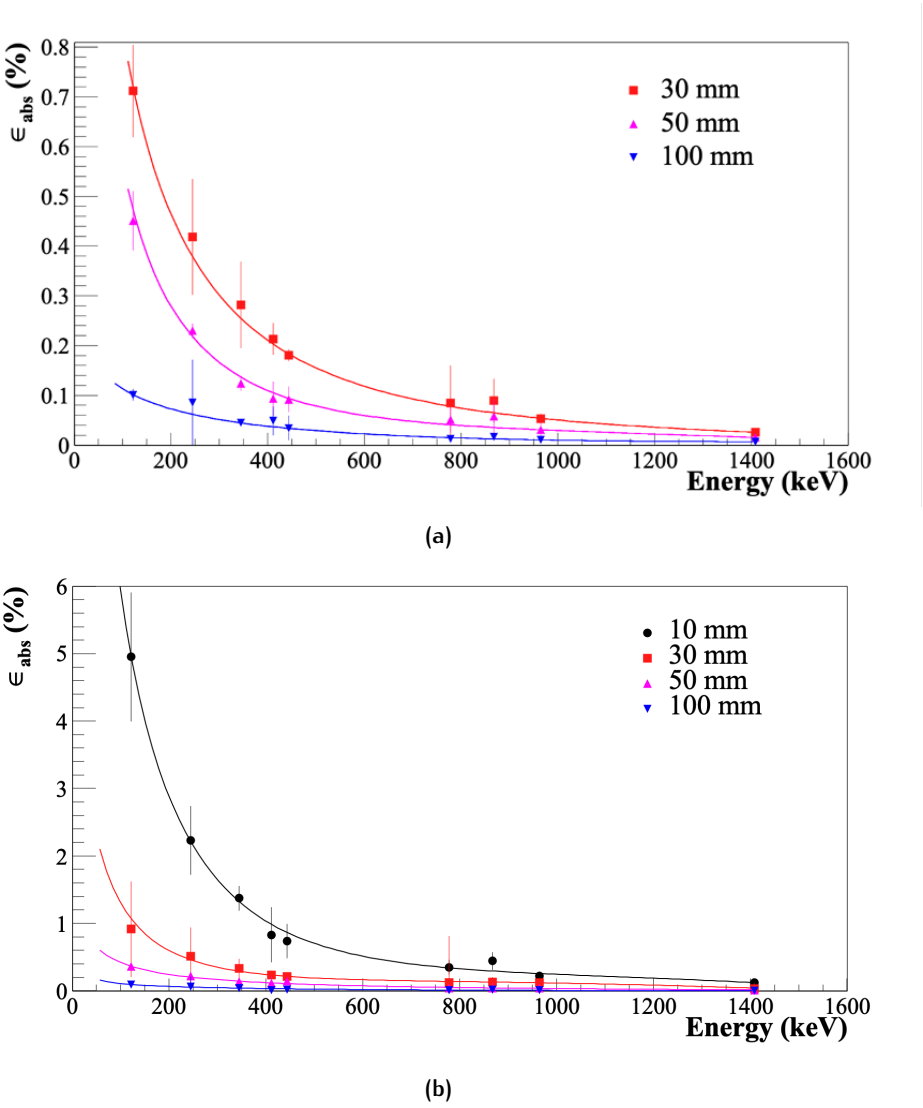

Figure 4.3.21: The FEPE, fitted with the logarithmic polynomial function $\ln(\epsilon(E)) = a_0 + a_1\ln(E) + a_2(\ln(E))^2 + a_3(\ln(E))^3$), and measured using a ^{152}Eu source placed at four different distances from each detector: (a) the SrI_2:Eu DA, and (b) the $LaBr_3$:Ce DA.

4.4 OVERVIEW OF DAS FOR USE IN CC DESIGNS

In early 2024, SiPM-coupled DAs were purchased and characterised to explore their application within a CC system. The detector materials under investigation included $LaBr_3$:Ce and SrI_2:Eu crystals, each paired with SiPM readouts. These DA systems were tested for their energy resolution and efficiency, crucial metrics for evaluating their potential in CC applications. Notably, the $LaBr_3$:Ce and SrI_2:Eu crystals demonstrated excellent energy resolution when trapezoidal shaping was applied to the signal using the XIA Pixie-16 DAQ system. Specifically, a minimum energy resolution of 3.47(23)% was achieved by setting the rise time to 0.06

µs and the flat top to 0.5 µs. A slightly better energy resolution of 3.41(20)% was observed, with a risetime of 1 µs and a flat top of 0 µs. These parameters were optimised to enhance signal processing for high-precision gamma spectroscopy.

The DA modules were compared against a 2″ × 2″ $LaBr_3$:Ce detector in terms of FEPE, as shown in Fig. 3.3.12 and Fig. 4.3.21. Across a range of energies and distances, $LaBr_3$:Ce consistently exhibited superior performance in FEPE, making it the preferred detector material in most scenarios. This was particularly evident at lower energies and shorter source-detector distances, where high PDE is critical for imaging systems such as CCs. The SrI_2:Eu and Polaris CZT detectors, while still viable, generally demonstrated lower efficiency compared to $LaBr_3$:Ce, indicating that $LaBr_3$:Ce is better suited for applications demanding high sensitivity, especially at low energies.

4.4.1 CC Design Configurations

A further two CC configurations were proposed and investigated through simulation to assess the effectiveness of the DA modules in a CC setup. These designs focused on various scatterer-absorber geometries aimed at optimising the ARM, efficiency, and reconstructed image quality. The design and geometries investigated for each CC are shown in Fig. 4.4.1, where CC2 and CC3 are the relevant designs for this discussion and CC1 was discussed in Section 3.0.1. Images of the CCs are seen as taken from the simulation, along with the scatterer and absorber detectors that make up each design.

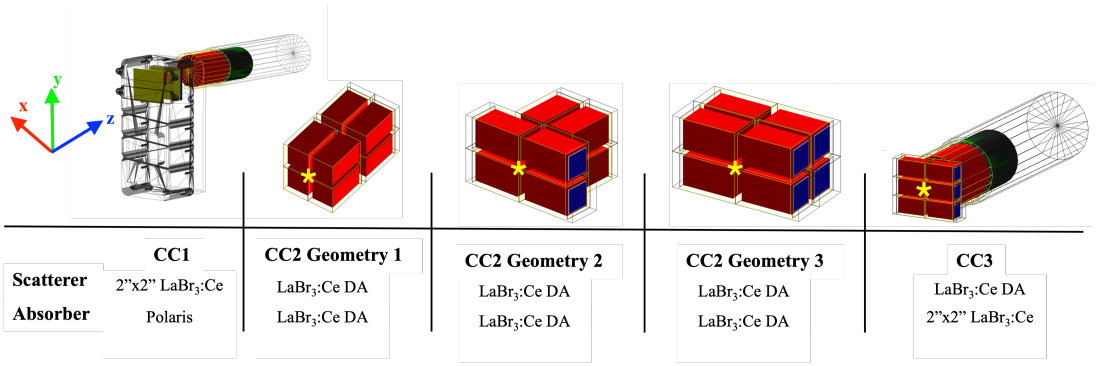

Figure 4.4.1: A schematic of all CCs simulated and the detectors that make up their scatterer and absorber modules (not to scale). The yellow star shape is a demonstrative representation of the gamma-ray source position relative to the scatterer module for each CC design. The source was moved in the x-z plane.

CC2 utilised 4 × 2 array of MacroPixel LB-14x25c-SiPM-T DA modules as scatterers and absorber layers each, while CC3 featured a 6 × 1 array of DA modules as scatterers, with a single 2″ × 2″ $LaBr_3$:Ce detector from Saint-Gobain as the absorber. Details on these configurations can be found in Section 5.2.2, which provides insight into their geometry, energy deposition, and expected performance in simulation.

Due to the project timeline, only one DA electronics housing (see Fig. 4.3.2) was constructed for initial measurements. The proposed CC configurations require up to eight DAs

to be biased and read out simultaneously, a requirement that currently exceeds available instrumentation. As a result, the designs were primarily explored through simulation until further hardware becomes accessible. These simulations, detailed in Chapter 5, provide key performance insights such as ARM distribution, FEPE, and image reconstruction capabilities.

5 MONTE CARLO SIMULATION

This chapter describes the MC simulation techniques used in this work, specifically utilising TOPAS MC to model the three CC designs, focusing on how different detector configurations impact imaging performance. Key aspects of the simulation include the construction of realistic materials and geometries, the selection of appropriate physics models, and the implementation of custom scoring techniques. The methodologies for incorporating detector resolution effects and image reconstruction algorithms, such as FBP with Wiener filtering and Octane EM, are explored to enhance the fidelity of reconstructed images. This chapter covers the detailed setup and execution of simulations, optimisation of reconstruction techniques, and analysis of simulation performance.

5.1 TOPAS MC

MC methods are powerful tools for obtaining numerical solutions to problems involving stochastic processes. These methods rely on probability distributions to model the behaviour of complex systems, with (pseudo) random numbers used to sample these distributions and determine quantities of interest. MC simulations are crucial for modelling the interaction of radiation with matter. While the physics governing radiation interactions is well understood, developing an analytical solution to describe particle transport in a medium remains impractical [91]. This is where MC methods excel, offering superior accuracy over analytical approaches, especially in contexts such as radiotherapy CC event tracking.

A bench-marked MC system can play a vital role in evaluating the feasibility of experiments, allowing researchers to compare simulated scenarios with experimental data. Additionally, MC simulations enable the exploration of scenarios that may be challenging or impossible to recreate in a physical experiment. This capability is particularly important in radiation therapy, where ethical considerations prevent using patients as experimental subjects and experimental beam-time is not always available.

In this study, the TOPAS MC (TOol for PArticle Simulation) (v3.9) tool kit was selected due to its reputation as a leading software for particle therapy simulations [1, 92]. Released in 2012, TOPAS enhances the Geant4 MC tool kit by providing a user-friendly interface that simplifies parameter management [93, 94]. TOPAS is capable of accurately simulating the passage of ionising radiation through intricate geometries, including patient CT scans, detectors, and medical instruments. It allows users to activate physical models that describe various par-

ticle interactions with matter, and it supports the simulation of different particles and physics processes.

The TOPAS MC software is structured into four main components, namely: Geometry, Particle Source, Scoring, and Physics. The geometry aims to best reproduce an experimental set-up. These parameters come together to form the heart of the simulation. Once the experimental geometry has been constructed, the scoring quantity is chosen and physics lists set, the simulation starts. Particles are tracked until they reach E = 0 eV. The particle trajectory is the sum of the particle steps determined by interactions or geometric boundaries. The simulation environment used in this study was designed to replicate that of the experiment. For a more general description of the TOPAS capabilities, refer to the website: TOPAS MC [1, 92].

5.2 TOPAS SIMULATIONS

To investigate the feasibility of various detector performances as CC imaging devices, TOPAS MC was used to simulate three different CCs. The combination of detectors used for each CC was chosen carefully to maximise on the strengths of each detector as either a scatterer or an absorber component. Having a reliable model of the experiment and detector geometries is critical for simulated investigation into the system. It is important to mention that this study does not account for correlated and non-correlated noise sources such as DCR, cross-talk, and after-pulsing in the SiPM components of the DAs. The simulation readout for the DAs was within the detector crystal and not the electrical signals of the SiPMs. Further, the simulation does not incorporate the intrinsic internal radioactivity of the SrI_2:Eu and $LaBr_3$:Ce detectors. Rather, the background was subtracted from the experiment before comparison with simulation. Future enhancements to the simulation framework will address these aspects.

The first CC design investigated, CC1, was detailed in Section 3.0.1. The motivation for this hybrid CC was to balance the strengths of different detector types in an effort to offset their respective limitations. The CZT detector serves as the scatterer, owing to its superior energy resolution and high stopping power, as discussed in Section 3.1, while the $LaBr_3$:Ce detector acts as the absorber placed directly behind it, selected for its rapid timing and high light output, as detailed in Section 3.2. This research investigates the integration of these detectors with high-speed digital readout electronics and assesses their potential application in a clinical setting.

5.2.1 Materials

To construct a material in TOPAS MC, the baseline requirements include specifying the material's chemical composition, density, and fractions of its constituent elements. Additionally, users can define various optical properties, such as refractive index, absorption length, reflectivity, and scintillation yield, which are essential for simulating how light propagates, reflects,

and is absorbed within the material. By setting these properties, TOPAS MC enables the creation of realistic models that account for the complex optical behaviour of materials used in radiation detection and imaging systems. Table 5.2.1 comprises all materials used to construct the various detectors in the simulation. The composition percentages, density, and properties columns refer to how the material was created in the simulation. The material information was acquired from the various specification sheets from the detector manufacturers, as well as correspondence with the companies themselves where necessary. The materials are referred to by the material name or chemical formula interchangeably in the sections to follow.

Material Name	**Chemical Formula**	**Composition (%)**	**Density (g/cm^3)**	**Properties**
Lanthanum Bromide	$LaBr_3$	La:36.69, Br:63.31	5.07	-
Cerium-doped Lanthanum Bromide	$LaBr_3$:Ce (5%)	$LaBr_3$:95, Ce:5	5.20	Scintillation Yield: 63000 photons/MeV
Aluminium	Al	Al:100	2.70	Reflectivity: 0.90
Aluminium (6061)	Composite	Al:97.2, Cr:0.2, Cu:0.3, Fe:0.3, Mg:1, Mn:0.1, Si:0.6, Ti:0.1, Zn:0.2	2.70	-
PTFE (Teflon)	$(C_2F_4)_n$	C:24.02, F:75.98	2.20	Reflectivity: 0.95 (various energies), Dielectric material
Plexiglass (PMMA)	$(C_5H_8O_2)_n$	C:62.06, H:8.13, O:29.81	1.19	Reflectivity: 0.90; Absorption Length: 1.0 m (600 nm) (various energies)
SiPM (SensL J-Series) [81]	Si	Si:100	2.33	PDE: ~ 40 (at 400 nm)
Borosilicate Glass	Composite	B:4.01, O:53.96, Na:2.82, Al:1.16, Si:37.72, K: 0.33	2.23	Reflectivity: 1.49
Optical Grease	$(C_2H_6OSi)_n$	Si: 10, O:10, C:20, H:60	0.97	Refractive Index: 1.4; Absorption Length: 10 cm (various energies)

Continued on next page

Material Name	Chemical Formula	Composition (%)	Density (g/cm^3)	Properties
Bialkali Material	Composite	Sb:33.33, Rb:33.33, Cs:33.33	3	Reflectivity: $1(10^{-6})$ (at various energies)
Strontium Iodide	SrI_2	Sr:33, I:67	4.20	-
Europium-doped Strontium Iodide	SrI_2:Eu (5%)	SrI_2:95, Eu:5	4.20	Scintillation Yield: 80000 photons/MeV
Ceramic	Al_2O_3	Al:47.07, O:52.93	3.97	-
Copper	Cu	Cu: 100	8.94	-
CZT	$Cd_{14}ZnTe_{13}$	Cd:48, Zn:2, Te:50	5.78	-
Epoxy Resin 1	C_4H_8O	C:68.42, H:10.53, O:21.05	1.16	-
Epoxy Resin 2	$C_8H_{14}O_2$	C:45, H:10, O:45	1.10	-
Epoxy Resin 3	CH_4N	C:40, H:13, N:47	1.16	-
Epoxy Resin	Composite	Epoxy Resin 1: 56, Epoxy Resin 2: 24, Epoxy Resin 3: 20	1.19	-
Silicon Dioxide	SiO_2	Si:33.33, O:66.67	1.19	-
Tetrabromophenol	$C_{11}H_6Br_4O_4$	C:46.15, H:15.38, Br:30.77, O:7.69	2.12	-
FR4	Composite	Epoxy Resin:38, SiO_2:55, Tetrabromophenol:7	1.8	-
Nylon (610)	$C_6H_{16}N_2$	C:55.88, H:8.82,N:35.30	1.14	-
Nylon FR4 Mix	Composite	Nylon:50, FR4:50	3	-
Nylon (12)	$C_{12}H_{21}NO$	C:54.50, H:33.30, N:10.60, O:1.60	1.01	-
Magnesium Oxide	MgO	Mg:60.30, O:39.70	3.58	Dielectric material
Mu-metal	Composite	Ni:77, Fe:16, Cu:5, Cr:2	8.7	-

Table 5.2.1: Summary of material compositions and properties used in the simulation.

5.2.2 Geometry of the Compton Camera Designs

The specific geometries and their materials were defined to match each manufacturer specification. Simulating the materials situated behind the detector crystal was crucial for accurately modelling the performance of a CC system. Gamma rays interacting with materials behind the crystal can scatter back into the detector, altering the signal. Including these materials in the simulation ensures that backscattered photons were accounted for, leading to more accurate energy spectra and ARM. Energy can be absorbed or attenuated by the materials behind the detector, affecting the overall energy resolution and detection efficiency. Simulating these materials allows for a better understanding of how energy losses occur and how they influence the detector's response.

The $2'' \times 2''$ $LaBr_3$:Ce cylindrical detector (Table 5.2.2) was constructed with an outer casing of aluminium, which houses a magnesium oxide (MgO) reflector surrounding the $LaBr_3$:Ce crystal. The detector dimensions was 50.8 mm in diameter, with a height matching the crystal length. Behind the crystal was the PMT, enclosed in an aluminium casing, optically coupled by layers of optical grease, a bialkali metal cathode, mu-metal shielding, and borosilicate glass. These layers were included in the simulation to account for backscatter effects and energy losses that occur as gamma rays interact with materials behind the detector. The Polaris CZT detector (Table 5.2.3) features a cuboid geometry, encapsulated by a plastic cover made from PA12 material, with an internal aluminium electronics box. The CZT crystals were housed within a protective structure, which includes nylon and copper plates for shielding and structural integrity. These geometrical details were essential to model accurately, as the housing materials may affect the scattering of gamma rays and impact the detector's energy response.

In the CC1 setup, the Polaris detector was used as the scatterer and the single $2'' \times 2''$ $LaBr_3$:Ce detector as the absorber. The $LaBr_3$:Ce detector was oriented to maximise gamma-ray interactions and detector efficiency by placing the detector crystal isocentric with CZT crystal, along the z-axis. The isometric view of the simulated CC design is seen in Fig. 5.2.1. Both the CZT and $LaBr_3$:Ce crystals are coloured as red within each geometry. The PMT was enveloped by the mu-metal shield and is not seen in Fig. 5.2.1.

For the MacroPixel DAs, both $LaBr_3$:Ce and SrI_2:Eu crystals were contained within aluminium casings (Table 5.2.4). These detectors have a cuboid geometry, with the scintillating crystal encased in a Teflon reflector. The SiPM pixels were mounted behind the crystal, and a PMMA board provides structural support. These assemblies were compact compared to the cylindrical $LaBr_3$:Ce detector. For the CC2 design, a different scatterer-absorber design was explored using the DAs. In this setup, the design employed four DA modules as scatterers and another four as absorbers. The optimal geometric arrangement of the DAs in the different CC layers was investigated, allowing for comprehensive analysis of the scatterer-absorber interactions. The $LaBr_3$:Ce DAs were used for both scatterer and absorber modules for the reasons discussed in the validation of the simulation in Section 6.1. The three geometries investigated for CC2 are seen in Figs. 5.2.2, 5.2.3 and 5.2.4. The colours of the various parts that make up the detector geometry are listed in Table 5.2.4, where the scintillating crystals are always

Component	Parent	HL × R (mm^2)	Material	Colour
Casing	World	57.5 × 57.5	Aluminium	Grey
Reflector	Casing	56.5 × 56.5	MgO	Yellow
$LaBr_3$:Ce Crystal	Reflector	50.8 × 50.8	$LaBr_3$:Ce	Red
PMT Casing	World	87.75 × 62	Aluminium	Grey
Optical Grease	PMT Casing	1.0 × 52	Optical Grease	Green
Bialkali Cathode	PMT Casing	1.0 × 51	Bialkali Cathode	Blue
Shield	PMT Casing	52 × 52	Mu-Metal	Dark Green
PMT crystal	Shield	51 × 51	Borosilicate Glass	-

Table 5.2.2: Summary of materials and geometrical dimensions, as well as the colour assigned to the detector part in the visualisation, for the 2″ × 2″ cylindrical $LaBr_3$:Ce detector.

Component	Parent	HLX × HLY× HLZ (mm)	Material	Colour
Plastic Cover	World	85 × 106 × 60	PA12	Grey
Electronics Box	Plastic Cover	85 × 104 × 26	Aluminium (6061)	Grey
Nylon Plates	Plastic Cover	50 × 50 × 4	Nylon FR4 Mix	Yellow
Cu Plate	Plastic Cover	50 × 50 × 4	Copper	Blue
CZT Crystals	Plastic Cover	20 × 20 × 10	CZT	Red

Table 5.2.3: Summary of materials and geometrical dimensions, as well as the colour assigned to the detector part in the visualisation, for the cuboid Polaris detector.

seen as red. The assigned light perspective within the QT visualisation of the simulation is the reason for the variation in colour intensity across the figures.

Component	Parent	HLX × HLY × HLZ (mm^3)	Material	Colour
Casing	World	8.5 × 8.5 × 16	Aluminium	Grey
Reflector	Casing	8.1 × 8.1 × 13.48	Teflon	Yellow
Crystal	Reflector	7 × 7 × 12.7	$LaBr_3$:Ce or SrI_2:Eu	Red
SiPM pixels	Casing	3.88 × 3.88 × 0.32	Silicon	Blue
PMMA Board	Casing	7.95 × 7.95 × 0.16	PMMA	White

Table 5.2.4: Summary of materials and geometrical dimensions, as well as the colour assigned to the detector part in the visualisation, for the cuboid $LaBr_3$:Ce and SrI_2:Eu DAs.

The CC3 setup involved a more complex design where six DAs were used in a matrix as the scatterer module in combination with a single 2″ × 2″ $LaBr_3$:Ce detector as the absorber, seen in Fig. 5.2.5. The number of DA modules was chosen to maximise the scatterer surface area coverage. The combination of multiple scatterers and one absorber aimed to enhance detection capabilities and image reconstruction accuracy.

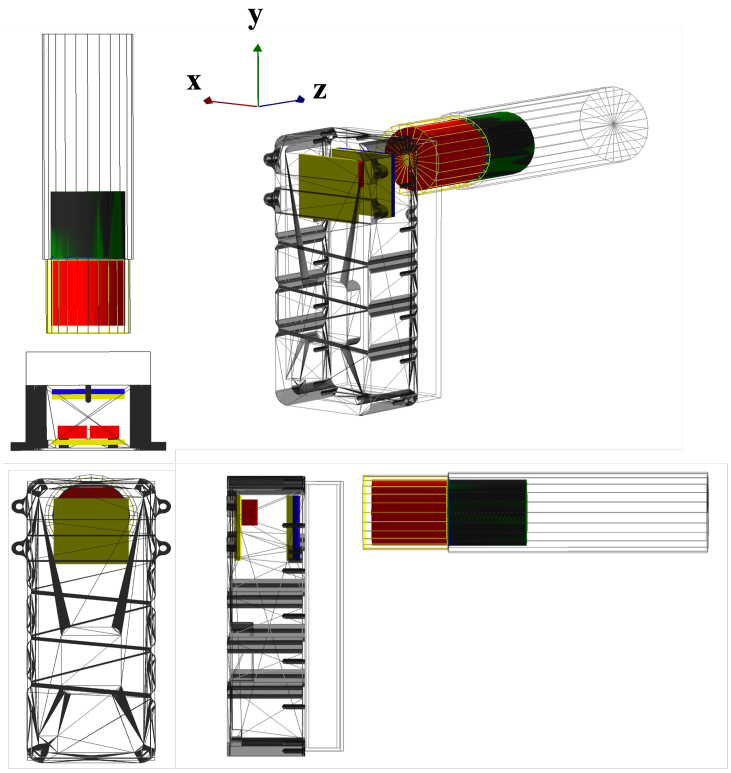

Figure 5.2.1: A schematic of the simulation geometry of CC1, shown as an orthographic perspective, which includes front, side, and top views to provide a comprehensive understanding of the spatial arrangement of components.

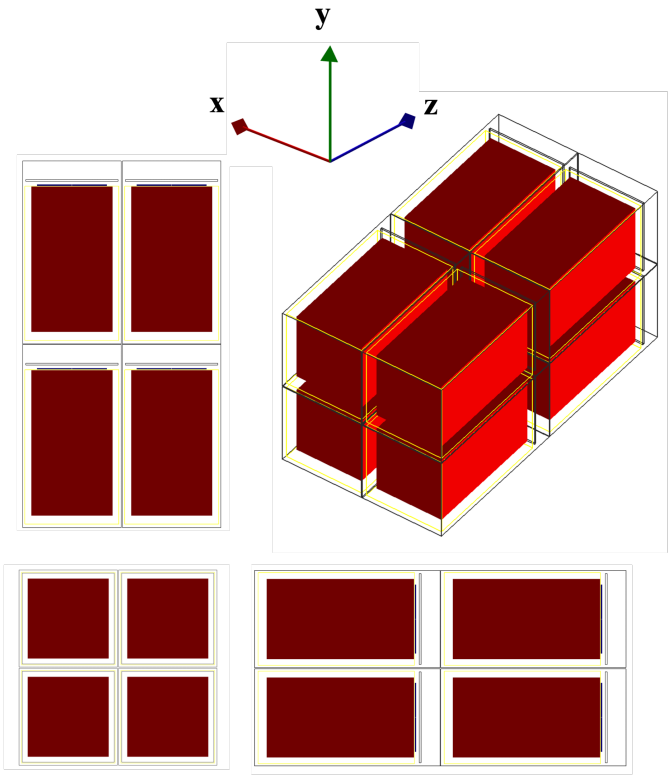

Figure 5.2.2: A schematic of the simulation geometry for the geometrical configuration 1 of CC2, shown as an orthographic perspective, which includes front, side, and top views to provide a comprehensive understanding of the spatial arrangement of components.

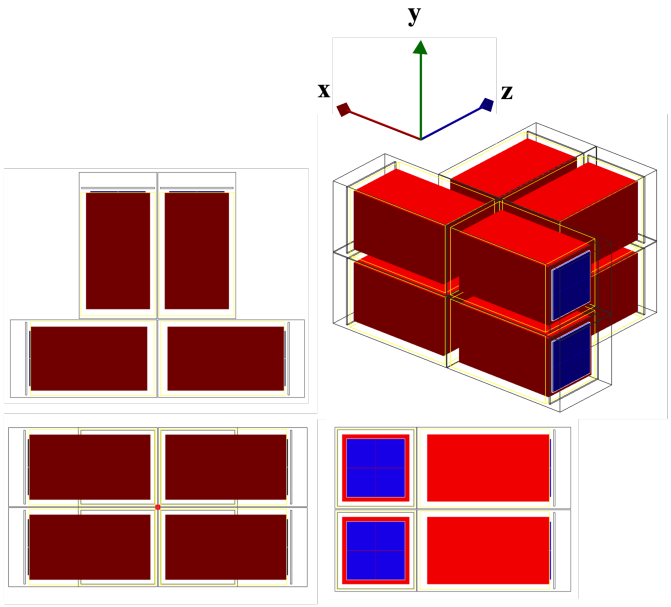

Figure 5.2.3: A schematic of the simulation geometry for the geometrical configuration 2 of CC2, shown as an orthographic perspective, which includes front, side, and top views to provide a comprehensive understanding of the spatial arrangement of components.

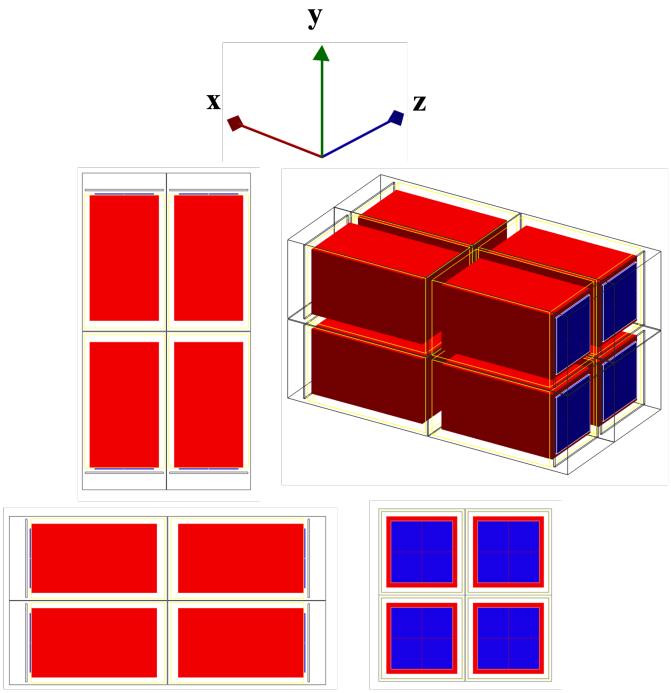

Figure 5.2.4: A schematic of the simulation geometry for the geometrical configuration 3 of CC2, shown as an orthographic perspective, which includes front, side, and top views to provide a comprehensive understanding of the spatial arrangement of components.

5.2.3 Physics

It is important for users to carefully construct and validate the physics list within TOPAS to ensure accurate results. In the simulation of a CC, the choice of physics models is critical to accurately capturing the interactions and transport of particles. The *G4RadioactiveDecay* model was employed to simulate the decay processes of unstable nuclei, a crucial aspect when deal-

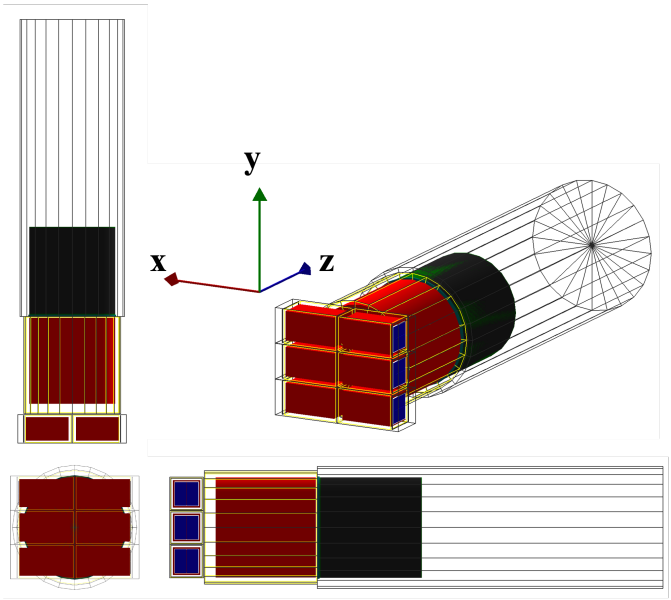

Figure 5.2.5: A schematic of the simulation geometry for CC_3, shown as an orthographic perspective, which includes front, side, and top views to provide a comprehensive understanding of the spatial arrangement of components.

ing with radioactive sources. This model incorporates the decay schemes, energy spectra, and angular distributions as provided by nuclear databases such as the Evaluated Nuclear Structure Data File database (ENSDF) [95]. The *G4Stopping* physics model was also incorporated as it was essential for accurately simulating the stopping power of ions in materials, ensuring that energy loss and range calculations for charged particles are precise. Equation 2.1.6 was among the key equations used for ionisation energy loss. This is particularly important in medical physics simulations, where understanding how particles slow down and deposit energy in tissue is vital [94]. Finally, the *G4EmStandardOption4* is a comprehensive electromagnetic model that includes detailed processes such as Compton scattering, photoelectric effect, and pair production, as described in Section 2.1.1.

TOPAS uses a step-by-step approach to transport particles. Each particle's trajectory is divided into small steps, and at each step, the relevant physics processes are invoked to determine how the particle interacts with the medium. For each possible interaction, the probability (cross-section) is calculated to decide whether an interaction occurs during the step. The outcomes (such as scattering angles, energy loss, or production of secondary particles) are then determined based on the specific physics model in use. If an interaction produces secondary particles (e.g., gamma rays, electrons, positrons), these particles are added to the simulation and transported in the same manner as the primary particles.

5.2.4 Scoring

TOPAS provides flexibility for users to extend its functionality by writing custom C++ scorer extensions, allowing for the collection of unique simulation data. In this work, a custom scorer was developed by tailoring the existing "MyNtupleScorer1" extension provided by

TOPAS. This custom scorer was specifically designed to meet the unique requirements of a CC simulation, where precise tracking of single-scatter events and their associated parameters is crucial for accurate data collection and subsequent image reconstruction.

The primary purpose of the extension was to capture detailed information about the energy deposition and scattering positions of gamma rays within the detector components. To achieve this, several modifications and additions were made to the original extension behaviour. The custom scorer was configured to record key variables such as the total energy deposited, smeared energy (accounting for detector resolution as described in Sections 3.3.2, and 4.3.4), particle identification (PID), event and track IDs, as well as the spatial coordinates of the scattering events. Additional columns were registered to store the process name responsible for the energy deposition and the volume names where interactions occurred.

These modifications were necessary to accurately characterise the interaction of gamma rays within different detector materials, such as $LaBr_3$:Ce, CZT, and SrI_2:Eu crystals. Each material's response was modelled by applying energy resolution functions specific to that material, which were embedded within the scorer (described in more detail in Section 5.2.5). The scorer also included logic to selectively store events based on the volume in which they occurred and the energy thresholds relevant to the CC's operational parameters.

In addition to the custom scorer, TOPAS includes built-in scorers such as the "OriginCount" scorer, which provides a general-purpose tool for tracking the emission of emitted particles from a source. The "OriginCount" was configured to capture the total number of gamma rays emitted by the radioactive source. It is important to note that the number of emitted gamma rays recorded by this scorer may differ from the number of histories generated by the simulation. The reason for this discrepancy lies in the fact that not all histories result in gamma ray emissions. Some histories may involve interactions where gamma rays are not produced, or they may involve particles that do not contribute to the gamma-ray count. The number of emitted particles was then used to compute the CC efficiency described in Section 6.2.1.

5.2.5 Detector Resolution Energy Smearing

Detector energy smearing in a simulation is a technique used to mimic the realistic response of a detector in a simulated environment. This process introduces random variations or "noise" into the simulated energy measurements to better replicate how a real detector would behave. Energy smearing accounts for the fact that real detectors have finite resolution and can produce measurements with some degree of uncertainty. Different detectors have specific intrinsic energy resolutions, which can vary with the type of detector, its material, and the energy of the detected photons. Smearing helps to incorporate these characteristics into simulations.

The simulated detector energy deposition values were smeared with the measured detector responses, described in Section 3.3.2. Specifically, for each deposited energy E_d, random

noise was introduced by sampling from a Gaussian distribution with mean E_d and a standard deviation determined by the experimental function:

$$FWHM(E_d) = 2.35 \cdot \sigma(E_d) = p_0 + \frac{p_1}{\sqrt{E_d}} \tag{5.2.1}$$

To replicate the detector's response more accurately, the smearing was implemented by first calculating the energy resolution at each deposited energy using the linear relationship between the variables:

$$E_{res} = \frac{p_1}{\sqrt{E_d}} + p_0 \tag{5.2.2}$$

where E_{res} is the relative energy resolution, and p_0 and p_1 represent energy-independent (baseline noise) and energy-dependent (statistical fluctuation) contributions, respectively. The standard deviation, σ, was then derived from this resolution by:

$$\sigma = \frac{E_{res} \times E_d}{2.35} \tag{5.2.3}$$

Finally, random noise was added by sampling from a Gaussian distribution centred at E_d with the calculated σ. The simulations do not incorporate the intrinsic radioactivity of the $LaBr_3$:Ce or SrI_2:Eu detectors. The energy deposition spectrum aligns with experimental data by factoring in the detector's intrinsic efficiency through the resolution smearing and simulating photon interactions within the material.

Further experiment detector effects were not implemented in simulation except for dead-time triggered event modeling of the Polaris detector. It was ensured that if the time elapsed between two energy depositions (above the threshold) in either of the two detector crystals did not exceed 15 µs, the event was not recorded in the simulation. This mimicked the processing time of the detector, which is a well-quantified value for the Polaris and was quantified by Maggi et al. [60], where the module's dead state was seen to vary in duration, ranging from 15.0–300.0 µs, depending on the characteristics of the recorded events. This period represents the time needed to process and read out the photon event and to reset the detector. After this interval, the module transitions back to its ready state. Therefore, 15 µs represents the minimum possible dead-time for the detector.

5.2.6 Post-Processing of Simulation Data

During this stage, the event IDs played a pivotal role in organising and analysing the data. The primary objective was to sort the data into meaningful CC events by applying specific gating criteria. Each simulated event was assigned a unique identifier, known as the event ID. This identifier was crucial for tracking the progression and interactions of particles within the simulation environment. When a primary particle was generated in the simulation, was

automatically assigned an event ID, which acts as a reference marker for all subsequent interactions and secondary particles produced within that event. This systematic assignment of IDs enables the precise tracking of particle histories, facilitating detailed analysis of the simulation results.

The custom scorer used in the simulation was tailored to record single-scatter events within the CC simulation. This scorer was designed to capture detailed information about each event, including energy deposits, interaction points, and the associated event ID. To accurately sort the data into CC events, several gating criteria were applied to filter and group the data based on their relevance to the imaging process. These gates were designed to isolate valid Compton scattering events from other types of interactions. The key gating criteria included:

- **Energy Windowing:** Events need to be selected based on their deposited energies to exclude those that could impair image quality. The total sum of the deposited energy across the scatterer and absorber modules must fall within the range $E_\gamma \pm 3\sigma_E$, where E_γ represents the incident gamma-ray energy, and σ_E is the energy's standard deviation. The standard deviation is determined based on the energy resolutions of the scatterer and absorber detectors obtained from experimental measurements (detailed in Sections 3.3.2 and 4.3.4).

  Forward-scattering events (FSE) occur when gamma rays first interact in the scatter layer, undergoing one or more Compton scatterings, and then the scattered photons interact in the absorber layer. Conversely, backward-scattering events (BSE) happen when gamma rays initially undergo Compton scattering in the absorber layer, with the scattered photons subsequently interacting in the scatter layer via the photoelectric effect. For optimal image reconstruction, BSE should be minimised or excluded, as they tend to degrade the image quality [96]. This can be achieved by applying an energy threshold to the deposited energy in the scatter detectors (for more detail, see Section 6.2.3). A benefit of applying energy windowing at this stage of the processing was the data reduction that it facilitated, allowing for only the relevant energies to be retained.

- **Sorting of CC events:** A gate was applied to check that the eventID of the interaction in the scatterer and absorber modules are equivalent, to ensure that they originate from the same incident gamma ray. The TrackIDs represent unique identifiers for each particle track within the simulation, while the ParentIDs link the interactions to their originating track, thus maintaining a coherent chain of events from the initial scattering to final absorption. A further sanity-check was then applied to ensure that the ParentID of the absorber was equivalent to the TrackID of the scatterer detector for FSE and vice versa for BSE. This step was crucial to confirm that the interactions recorded are correctly associated with their respective tracks and that the events are properly linked between the scatterer and absorber components of the CC. By verifying these IDs, it was ensured that the integrity and accuracy of event correlation, which was essential for reliable data analysis and image reconstruction.

  Subsequently, the sorting of the CC events was conducted as detailed in Section 2.4. For each event in the scatterer module that met the ID and energy gate criteria, it was

verified that the physics process was Compton scattering. A search was then carried out to identify subsequent interactions in the absorber module where the gamma ray was completely absorbed via the photoelectric effect. These FSEs were stored as Compton cones in a ROOT file, formatted as (E_1, x_1, y_1, z_1, E_2, x_2, y_2, z_2) for further analysis. BSEs were collected and stored similarly, though the physics processes were filtered to ensure that a Compton interaction in the absorber preceded a photoelectric absorption event in the scatterer temporally.

5.2.7 Image Reconstruction Algorithms

5.2.7.1 Filtered Back Projection with Wiener Filtering

This image reconstruction code was self-developed for the purposes of this CC investigation. The procedure focuses on reconstructing an image from CC data using the method of FBP, and subsequently refining the image resolution using Wiener filtering to generate 2D CC source images from double scatter Compton cones [97]. This algorithm can be applied to individual events, enabling real-time measurements. It offers improved image resolution compared to the simple back-projection method, though it encompasses a slightly increased computational expense, as was compared in the work of Xu et al. [98].

1. **Identification of Scatter Events:** Using either an experimental dataset or data obtained through simulations, the algorithm identifies the positions and angles of the double scatter events. The double-scatter events yield Compton cones, each defined by the geometry of the scatter points and their corresponding energies. The Compton cone was determined by the interaction points of Compton scattering and photoelectric effect, with its vertex at the Compton scattering interaction point. Each pair of validated events provides a Compton cone, which represents the locus of possible source positions.

2. **Compton Geometry:** Using the positions (x_1, y_1, z_1)and (x_2, y_2, z_2) and energies determined, the Compton scattering angle θ_c was calculated using the Compton Scattering Equation (see Section: 2.4).

3. **Radon Canonical Reconstruction:** The Radon conical method is an extension of the traditional Radon transform used for reconstructing images from projection data [99, 100]. The Radon transform was invented by the Austrian mathematician Johann Radon in 1917. Radon introduced this mathematical technique in his paper titled "On the determination of functions from their integrals along certain manifolds" [101]. This work laid the foundation for the mathematical framework behind tomography, which is now widely used in medical imaging techniques such as CT scans. Haefner et al. effectively connected 2D Compton 4π imaging to a 3D Radon transform, utilising a known solution [102].

   In the context of CCs, instead of integrating along straight lines (as in CT), integration is performed along the surfaces of cones due to the physics of Compton scattering. Each

scattering event defines a cone (through the scattering angle and interaction positions), and the image is reconstructed by superimposing these conical surfaces.

After filtering, the Radon canonical transformation method was applied to the data to generate an initial image. This process involves projecting the Compton cones onto an image plane.

The cone surface is defined by:

$$[n_x(x-x_1)+n_y(y-y_1)+n_z(z-z_1)]^2=(\cos\theta_c)^2[(x-x_1)^2+(y-y_1)^2+(z-z_1)^2] \tag{5.2.4}$$

where (x_1, y_1, z_1) is the vertex of the cone, θ_c is the cone's opening angle, and (n_x, n_y, n_z) is the unit vector along the cone's axis.

The intersection of the Compton cone with the image plane $z = z_0$ results in an ellipse. This is because the projection of a cone onto a perpendicular plane is an ellipse. The ellipse can be described by:

$$\frac{(x\cos\theta+y\sin\theta-t)^2}{a^2}+\frac{(x\sin\theta-y\cos\theta)^2}{b^2}=1 \tag{5.2.5}$$

where a and b are the semi-major and semi-minor axes of the ellipse, and θ is the projection angle.

In practice, the Radon transforms for discrete data can be approximated as:

$$P_i(\theta)=\sum_j f(i,j)w(i,j,\theta) \tag{5.2.6}$$

where $P_i(\theta)$ is the projection data for angle θ and $w(i,j,\theta)$ is the weight of a pixel (i,j) in the projection.

The code checks if the intersection point lies on the conical surface formed by the direction vector n and scattering angle θ_c. If so, this point contributes to the final image reconstruction.

4. **Image Formation:** The resulting image was stored in a 2D histogram (x-y), where each bin represents a pixel in the image plane. If the condition for lying on the cone was satisfied for a pixel, its corresponding bin was incremented.

5. **FBP with Wiener Filtering:** The initial image from the Radon transform was then processed using FBP. The FBP method reconstructs the image by back-projecting the filtered projections. The Wiener filter was applied to the projections to suppress noise and improve the reconstructed image quality by minimising the mean squared uncertainty between the filtered image and the original image.

   The Wiener filter function is given by:

$$H(u,v)=\frac{S(u,v)}{S(u,v)+N(u,v)} \tag{5.2.7}$$

where $H(u,v)$ is the Wiener filter function, $S(u,v)$ is the power spectrum of the signal, and $N(u,v)$ is the power spectrum of the noise.

The FBP reconstruction formula is:

$$f(x,y) = \int_0^{\pi} R(\theta,t) \cdot g(t,\theta)\, d\theta \tag{5.2.8}$$

where $R(\theta,t)$ is the projection data and $g(t,\theta)$ is the filter function applied to these projections.

The filter used is a non-local means denoising [103]. It is based on the principle that similar image patches should contribute similarly to the denoising process, regardless of their location in the image. The idea is that an image patch can be denoised by comparing it with similar patches from the entire image, rather than just its local neighbourhood. It removes noise while preserving edges by comparing each pixel to its neighbours.

For a given pixel (i,j) in the image, the denoised pixel value $\tilde{I}(i,j)$ is calculated as:

$$\tilde{I}(i,j) = \frac{\sum_{(k,l)\in \text{window}} w(i,j;k,l) \cdot I(k,l)}{\sum_{(k,l)\in \text{window}} w(i,j;k,l)} \tag{5.2.9}$$

where $w(i,j;k,l)$ is the weight for the patch centred at (k,l) and is calculated as:

$$w(i,j;k,l) = \exp\left(-\frac{\|I(i,j) - I(k,l)\|^2}{h^2}\right) \tag{5.2.10}$$

Here, $\|\cdot\|$ denotes the norm of the difference between patches, and h is the parameter controlling the strength of the filtering.

There was some user control at this stage of the filtering, where one has the ability to change various parameters with the aim of improving the resolution of the output image. For each pixel in the image, extract a local patch around it. The size of this patch was defined by the *templateWindowSize* $I(k,l)$) and the patch comparison compares the extracted patch with patches from the entire image within a *searchWindowSize* window. The comparison was performed based on a similarity measure, using the Euclidean distance between patches. A weighted average of similar patches was then computed, where the weights are determined by the similarity between patches; more similar patches are given higher weights. The weight of the current pixel was then updated with the weighted average computed from similar patches.

After filtering, the filtered data was used to generate the image. This enhances the quality of the reconstructed image, reducing noise and improving resolution.

5.2.7.2 Octane EM

This code, developed by Dennis Mackin of MD Anderson Cancer Centre, implements an imaging reconstruction algorithm known as Octane EM which utilises cones and spatial analysis to reconstruct images of the gamma-ray source through a CC geometry. Images of energy-window filtered gammas that double scattered in the CC were reconstructed using the Octane

EM algorithm. The Octane EM method was specifically developed for PG imaging applications, and the calculation steps followed by the image reconstruction are detailed as follows.

1. **Identification of Scatter Events and Cones** Using either an experimental dataset or data generated through simulations, the algorithm identifies the positions and angles of the double scatter events. The double-scatter events yield Compton cones, each defined by the geometry of the scatter points and their corresponding energies. The algorithm treats each event as a cone, which represents the possible locations of the gamma-ray source.

   Each double scatter event can be represented as a cone defined by the scatter points $\mathbf{S}_1$ and $\mathbf{S}_2$ and their corresponding energies. The cone equation in 3D space can be described as:

   $$\mathbf{C}(\mathbf{r}; \mathbf{S}_1, \mathbf{S}_2) = \mathbf{r}^T \mathbf{A} \mathbf{r} + 2\mathbf{b}^T \mathbf{r} + c = 0 \tag{5.2.11}$$

   where $\mathbf{r}$ is the position vector in the imaging space, $\mathbf{A}$ is the matrix representing the cone's curvature, $\mathbf{b}$ is the vector describing the conic's orientation, and c is a constant term.

2. **Distance of Closest Approach and Point of Closest Approach:** For each cone, the algorithm calculates the distance of closest approach (DCA) to a given point in space. This metric helps identify the proximity of the cone to potential source locations. Additionally, the algorithm calculates the point of closest approach (PCA) on the cone, which is the nearest point on the cone to the given point in space.

   For a point $\mathbf{P}$ in space, the DCA to the cone is given by the perpendicular distance from $\mathbf{P}$ to the cone:

   $$\mathrm{DCA}(\mathbf{P}; \mathbf{C}) = \frac{\|\mathbf{A}\mathbf{P} + \mathbf{b}\|}{\sqrt{\mathbf{A}^T \mathbf{A}}} \tag{5.2.12}$$

   The PCA $\mathbf{P}_{\mathrm{PCA}}$ on the cone can be found by solving:

   $$\mathbf{P}_{\mathrm{PCA}} = \arg\min_{\mathbf{r}} \|\mathbf{r} - \mathbf{P}\|^2 \text{ subject to } \mathbf{C}(\mathbf{r}; \mathbf{S}_1, \mathbf{S}_2) = 0 \tag{5.2.13}$$

   The DCA cut is a threshold value used to filter octants based on their proximity to the cones. Octants with a DCA below this threshold are considered more likely to contain the gamma-ray source. By adjusting the DCA cut, users control the balance between computational efficiency and image accuracy. A lower DCA cut means the algorithm is more inclusive, potentially capturing more detail, while a higher cut reduces the number of considered octants.

3. **Subdivision of Imaging Space into Octant Segments:** In a Cartesian coordinate system, the imaging space can be defined as a cuboid, which is then divided into a specified number of voxels. A voxel (short for "volume pixel") represents a small, discrete, three-dimensional element of the imaging space, analogous to a pixel in two-dimensional images. This cuboid imaging space is divided into smaller segments or "octants". The centre of each octant is calculated, and the DCA and PCA are evaluated for each octant

centre relative to the cones. This allows the algorithm to refine the search for the likely gamma-ray source location by focusing on octants where the DCA is minimal.

The imaging space is divided into voxels, each with centre coordinates $\mathbf{x}_{ijk}$:

$$\mathbf{x}_{ijk} = (x_i, y_j, z_k) \text{ where } x_i = i \cdot \Delta x,\ y_j = j \cdot \Delta y,\ z_k = k \cdot \Delta z \tag{5.2.14}$$

with i, j, and k ranging from 1 to N_x, N_y, and N_z respectively, and Δx, Δy, Δz being the voxel dimensions.

Each voxel is subdivided into smaller octants. The centre of each octant is recalculated, and the DCA and PCA are evaluated for each octant relative to the cones:

$$\text{DCA}_{\text{octant}} = \frac{\|\mathbf{A}_{\text{octant}}\mathbf{x}_{\text{octant}} + \mathbf{b}_{\text{octant}}\|}{\sqrt{\mathbf{A}_{\text{octant}}^{T}\mathbf{A}_{\text{octant}}}} \tag{5.2.15}$$

4. **Recursive Octant Refinement:** The algorithm recursively refines the octant segmentation, breaking down the imaging space into progressively smaller segments in a number of iterations defined by the user. For each segment, the DCA was recalculated. If a segment's DCA was below a specified threshold, the segment was further divided, and the process continues until the octants are small enough to yield precise localisation of the gamma-ray source.

   The algorithm refines octants recursively based on the DCA values:

   $$\text{If } \text{DCA}_{\text{octant}} < \text{threshold}, \text{ then divide octant and recompute DCA.} \tag{5.2.16}$$

   This process continues until the octants are small enough to provide accurate localisation. The number of octant iterations determines how many times the algorithm refines the octant segmentation. Adjusting the number of octant iterations allows users to control the trade-off between computational effort and image resolution. More iterations typically yield a higher-quality image but require more processing time.

5. **Density Estimation and Image Reconstruction:** Once the octants with the smallest DCA values are identified, the algorithm uses a density estimator to aggregate the likely origin points from all cones. The weighted contributions of these origin points form a density matrix, which represents the reconstructed image. This matrix was then visualised to produce the final image of the gamma-ray source. The initial binning of the histogram was important for the density estimation process. By varying the binning, users can adjust the trade-off between image detail and noise. Finer binning improves spatial resolution, but may require more sophisticated noise reduction techniques and higher computational time. The bin width was also an important parameter that was user-controlled and determines the size of each bin in the histogram, affecting the granularity of the density estimation. Adjusting bin width allows users to manage the resolution of the image and computational load. Smaller bin widths offer more detail but can increase processing time and noise, while larger bin widths simplify the image but may smooth out important features.

The density matrix $\rho(\mathbf{x})$ is computed as:

$$\rho(\mathbf{x}) = \sum_i w_i \cdot \text{Gaussian}(\mathbf{x} - \mathbf{x}_i; \sigma_i) \tag{5.2.17}$$

where w_i is the weight of the contribution from the i-th cone, $\mathbf{x}_i$ is the location of the contribution, and σ_i is the standard deviation of the Gaussian distribution.

6. **Image Reconstruction:** The final reconstructed image was visualised using the density matrix $\rho(\mathbf{x})$, representing the probability distribution of the gamma-ray source's location.

.

5.2.7.3 Optimisation of Filtered Back Projection with Wiener Filtering Reconstruction

The FBP Wiener filter required optimisation before it was evaluated for use as an image reconstruction technique in this work. The parameters described in Section 5.2.7.1 were varied for a set search window size of 21. This refers to the size of the window around the pixel being processed, where the algorithm searches for similar patches to compute the weighted average. A larger window allows the algorithm to find more similar patches, leading to better noise reduction, especially in areas with repetitive patterns. However, it also increases computational cost. A size of 21 was considered to be mid-range for 100 pixels.

In Wiener filtering, the threshold was applied to the power spectra ($S(u,v)$) of the signal and noise ($N(u,v)$) in the frequency domain of Eq. 5.2.7. The threshold controls the balance between preserving the signal and suppressing the noise by adjusting the ratio $\frac{S(u,v)}{S(u,v)+N(u,v)}$, resulting in a higher suppression of noise because the filter function ($H(u,v)$) approaches 1 in areas where the signal-to-noise ratio was high and approaches zero where the noise was dominant. This adjustment helps in minimising the mean squared uncertainty between the filtered image and the original image while effectively reducing noise.

The threshold value was incremented from 0 to 50, and the dataset obtained by simulating a ^{137}Cs source (0,0,10) mm from the face of CC1 was evaluated for each threshold setting, as seen in Fig. 5.2.6. Increasing the threshold value in Wiener filtering can improve the image quality up to a certain point by better balancing the trade-off between noise suppression and signal preservation. The effect of the noise suppression is clear when comparing Figs. 5.2.6(a), (b) and (c) for threshold values of 10, 20 and 30 respectively. The threshold value of 30 shows increased source localisation in comparison to the threshold of 10. However, it was observed that increasing the threshold beyond 40 began to degrade the image resolution, suppressing parts of the signal along with the noise, thereby entering a range of diminishing returns. This can lead to loss of important image details and reduce overall image quality. A threshold value of 30 was chosen as optimal.

The Wiener filter strength parameter, h, plays a crucial role in determining the balance between noise reduction and detail preservation, as it controls the aggressiveness of the noise suppression applied to the image. This parameter influences how the filter distinguishes

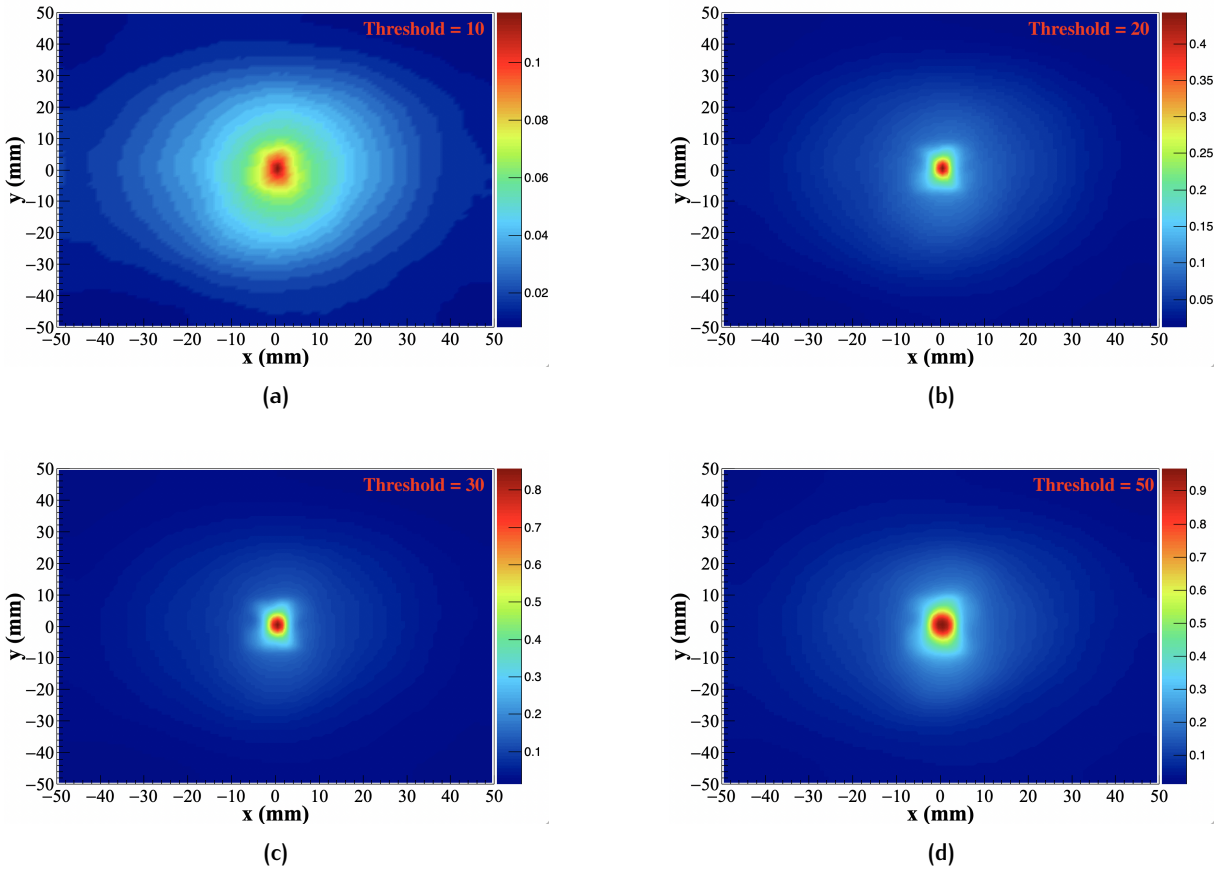

Figure 5.2.6: The 2D x-y image matrix of CC1 shown for different threshold settings in the Wiener filtering of the back-projection reconstruction. The reconstruction was performed on the Compton cone data to investigate the quality of the image resolution for threshold setting values of: (a) 10, (b) 20, (c) 30, and (d) 50.

between signal and noise components, as described by Eq. 5.2.10. The value of h must be chosen based on the noise level in the image. Higher noise levels necessitate larger h values for effective noise filtering, while lower noise levels benefit from smaller h values to preserve image details. The challenge lies in striking the right balance to achieve both optimal noise reduction and image clarity.

Figure 5.2.7 illustrates the impact of adjusting h across a range of scaling factors from 3 to 24. As seen in Fig. 5.2.7(a), an h value of 3 allowed residual noise artefacts from the FBP reconstruction, visible as the elliptical patterns originating from the Radon canonical transformation (Eq. 5.2.4). A moderate h value of 6, shown in Fig. 5.2.7(c), provided the best compromise, significantly reducing noise while maintaining clarity in the reconstructed image. However, further increasing h beyond 10, as seen in Fig. 5.2.7(d), resulted in excessive blurring, with the image losing fine details. Thus, $h = 6$ was selected as the optimal value for balancing noise reduction and preserving the structure of the source.

The third Wiener filter parameter optimised was the template window size; the region around each pixel used to compare its neighbourhood with other neighbourhoods in the search window. The similarity between patches, represented by the weights $w(i, j; k, l)$ as calculated by Equation 5.2.10, determines how much influence neighbouring pixels have on the denoising process. In this study, a search window size of 21 $\times$ 21 pixels was employed.

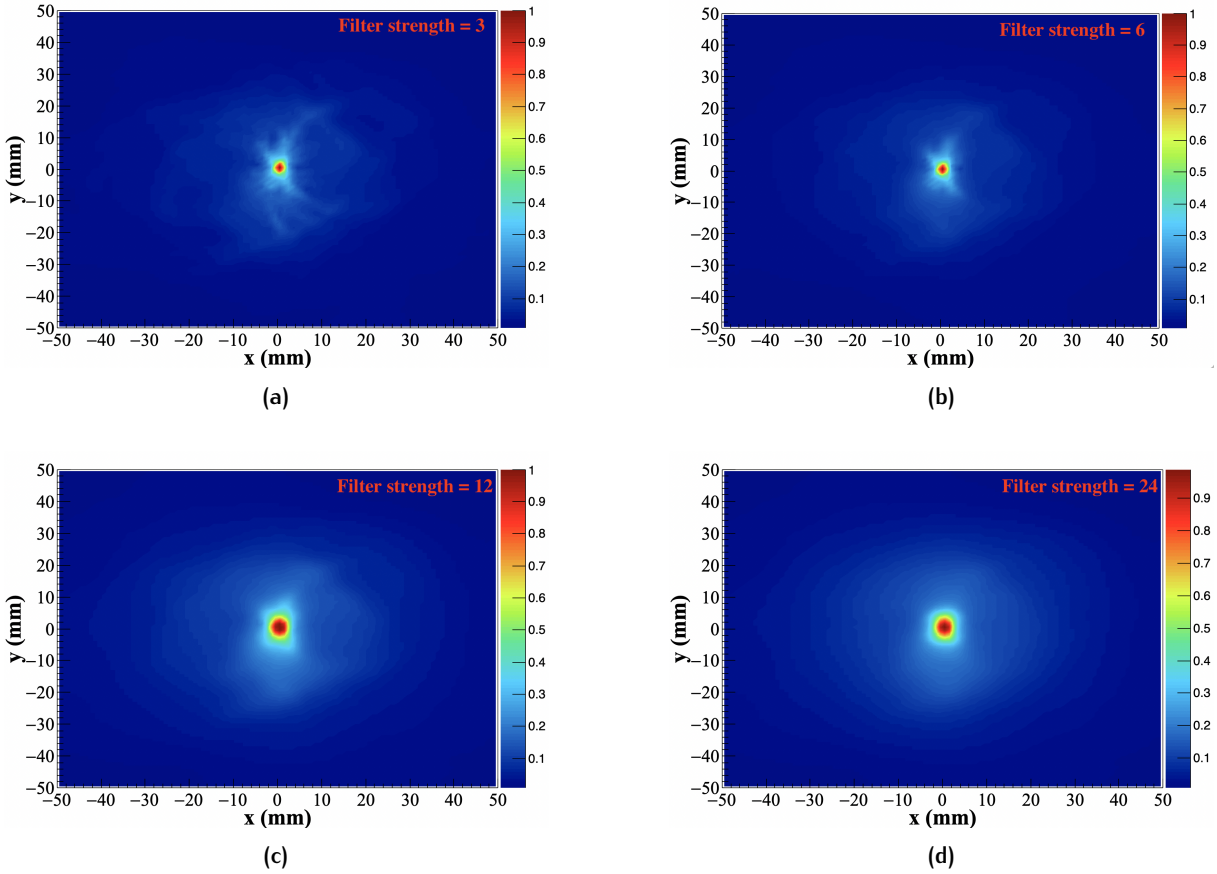

Figure 5.2.7: The 2D x-y image matrix of CC1 shown for different filter strength settings in the Wiener filtering of the back-projection reconstruction. The reconstruction was performed on the Compton cone data to investigate the quality of the image resolution for filter strength setting values of: (a) 3, (b) 6, (c) 12, and (c) 24.

As illustrated in Figure 5.2.8, increasing the template window size from 3 × 3 pixels to 10 × 10 pixels shows a notable trade-off between noise suppression and the preservation of fine details. A smaller patch, such as the 3 × 3 pixel window in Fig. 5.2.8(a), retains image sharpness but struggles with noise suppression, particularly in areas with lower signal-to-noise ratios at the periphery of the source. In contrast, a larger window, such as the 10 × 10 pixels in Fig. 5.2.8(d), reduces noise but introduces over-smoothing, as seen in the loss of finer details. The most balanced result was achieved with a 7 × 7 pixel window, as shown in Fig. 5.2.8(b) and (c), offering an optimal compromise between preserving critical image details and reducing noise. This informed the selection of a 7 × 7 pixel template window as the final setting. The optimised Wiener filter parameters for FBP are summarised in Table 5.2.5.

Noise Threshold (arb)	**Filter Strength (arb)**	**Template Window Size (x × y) (pixels)**
30	6	7 × 7

Table 5.2.5: The optimal Wiener Filter settings used in the FBP method for a search window size of 21 × 21 pixels.

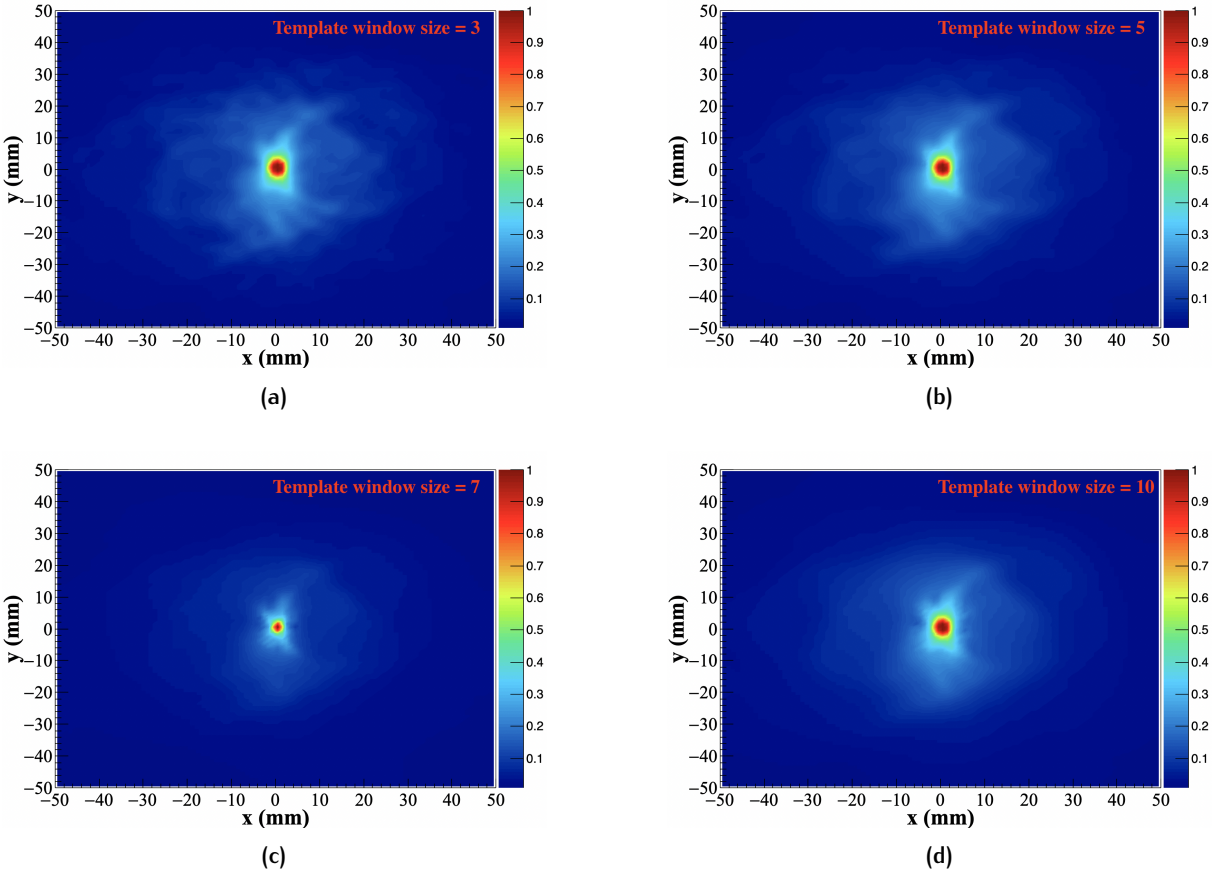

Figure 5.2.8: The 2D x-y image matrix of CC1 shown for different template window size settings in the Wiener filtering of the back-projection reconstruction. The reconstruction was performed on the Compton cone data to investigate the quality of the image resolution for template window sizes of: (a) 3×3, (b) 5×5, (c) 7×7, and (d) 10×10 pixels.

5.2.7.4 Optimisation of Octane EM Reconstruction

The number of iterations controls how many times the Octane EM algorithm refines the segmentation of the imaging space into smaller octants. With each iteration, the algorithm becomes more precise in localising the gamma-ray source, enhancing image accuracy. However, increasing the number of iterations also raises the computational load and processing time, making it less feasible for real-time applications.

As seen in Figure 5.2.9, the impact of running 10, 50, and 100 iterations on image reconstruction was evaluated. The results showed only subtle improvements in image quality beyond 50 iterations. When comparing the reconstructions from 50 and 100 iterations, both produced nearly identical results across different simulation environments. Given this minimal difference, it was determined that 50 iterations offered the optimal balance between image quality and computational efficiency, providing high-quality images while significantly reducing processing time compared to 100 iterations.

The most impactful optimisation in the Octane EM algorithm was the adjustment of the bin width in the histogram, a parameter that directly influences the granularity of the density estimation during image reconstruction. By fine-tuning the bin width, the algorithm can effectively balance image detail with smoothness. Smaller bin widths improve spatial

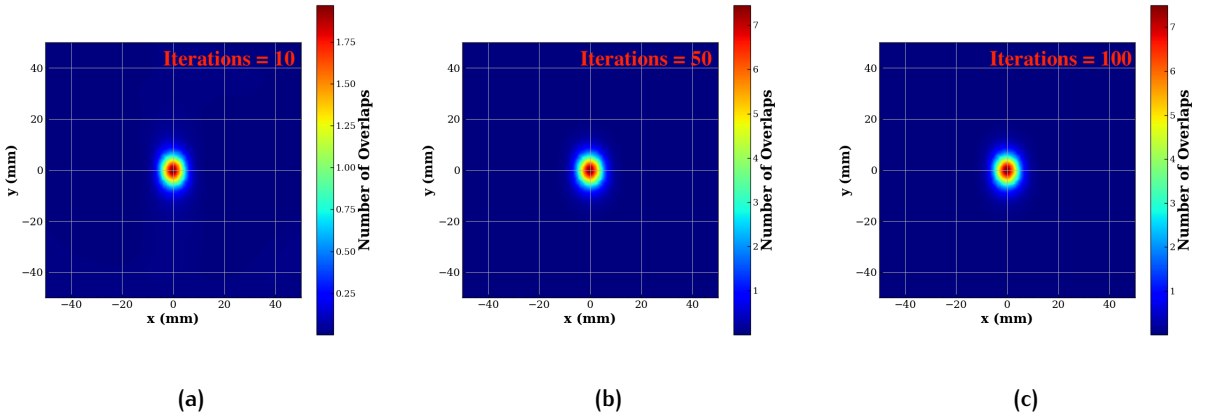

Figure 5.2.9: The 2D x-y image matrix of CC1 shown for a different number of iterations of the Octane EM reconstruction. The reconstruction was performed on the Compton cone data to investigate the quality of the image resolution for: (a) 10, (b) 50, and (c) 100 iterations.

resolution by capturing finer details of the gamma-ray source, as demonstrated in the x and y profiles in Fig. 5.2.10. In Fig. 5.2.10(a), a bin width of 5 mm produces a coarser image, whereas reducing the bin width to 2 mm in Fig. 5.2.10(b) significantly sharpens the source localisation but increasing the computational time. The reduction in bin width resulted in a notable improvement, with the FWHM decreasing by over two-thirds, leading to more precise reconstruction of the gamma-ray source.

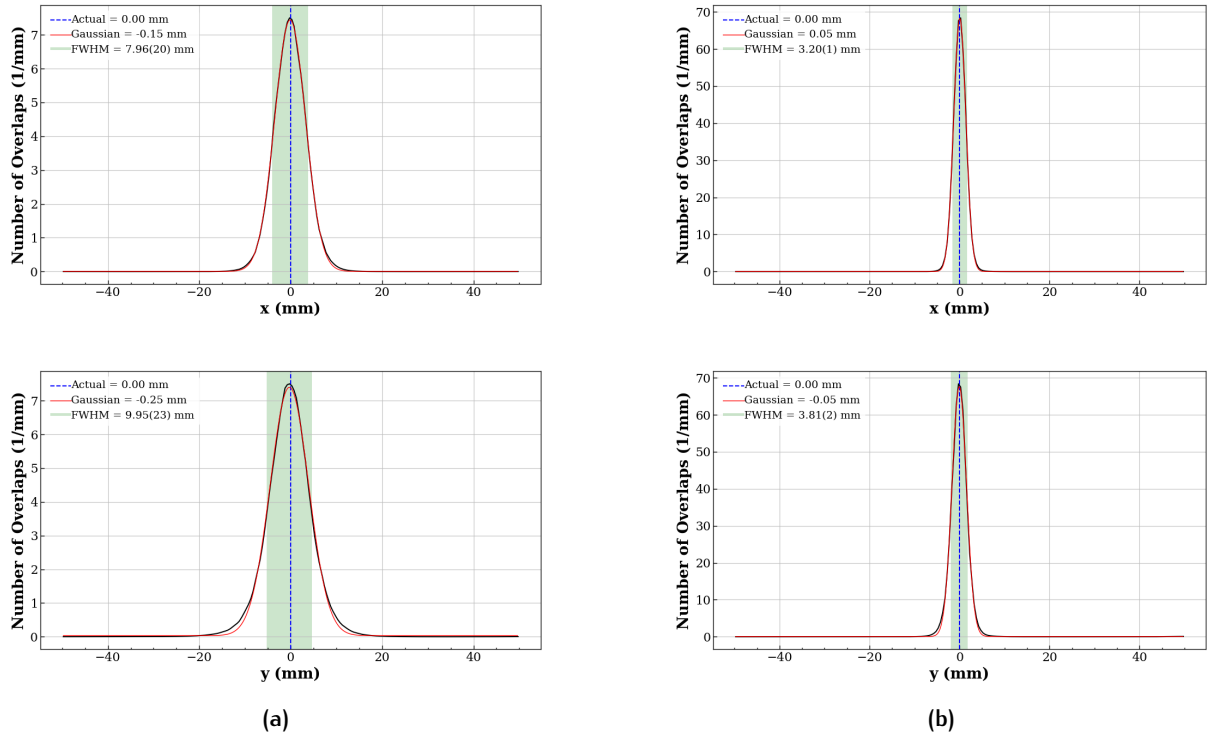

Figure 5.2.10: The x and y projections (sliced at the maximum y-z and x-z values respectively) of CC1 shown for different bin width in the Octane EM reconstruction. The reconstruction was run for 100 iterations. The reconstruction was performed on the Compton cone data to investigate the quality of the image resolution for: (a) 5 mm, and (b) 2 mm bin with values. The dotted blue line represents the actual source location. The distribution was fitted with a Gaussian function (red), and the FWHM of the Gaussian is shown in green and labelled with uncertainty.

5.2.7.5 *Comparison between Reconstruction Algorithms*

The advantages of a 3D FBP image reconstruction, especially when making use of the maximum intensity projections to extract dimensional profiles, are striking when compared with the 2D FBP method. This difference is illustrated in Fig. 5.2.11, where the x-y reconstructions of both algorithms are shown at the top, with their corresponding x profiles below. The 2D FBP, which incorporates Wiener filtering, reconstructs only the projections of Compton cones onto the x-y plane. While the Wiener filter effectively reduces noise and sharpens the image, the method was inherently limited to two dimensions, allowing for the extraction of profiles solely in the x and y directions. This restriction prevents the recovery or analysis of vertical (z-dimension) information, meaning 3D spatial distribution or depth localisation of sources remains out of reach.

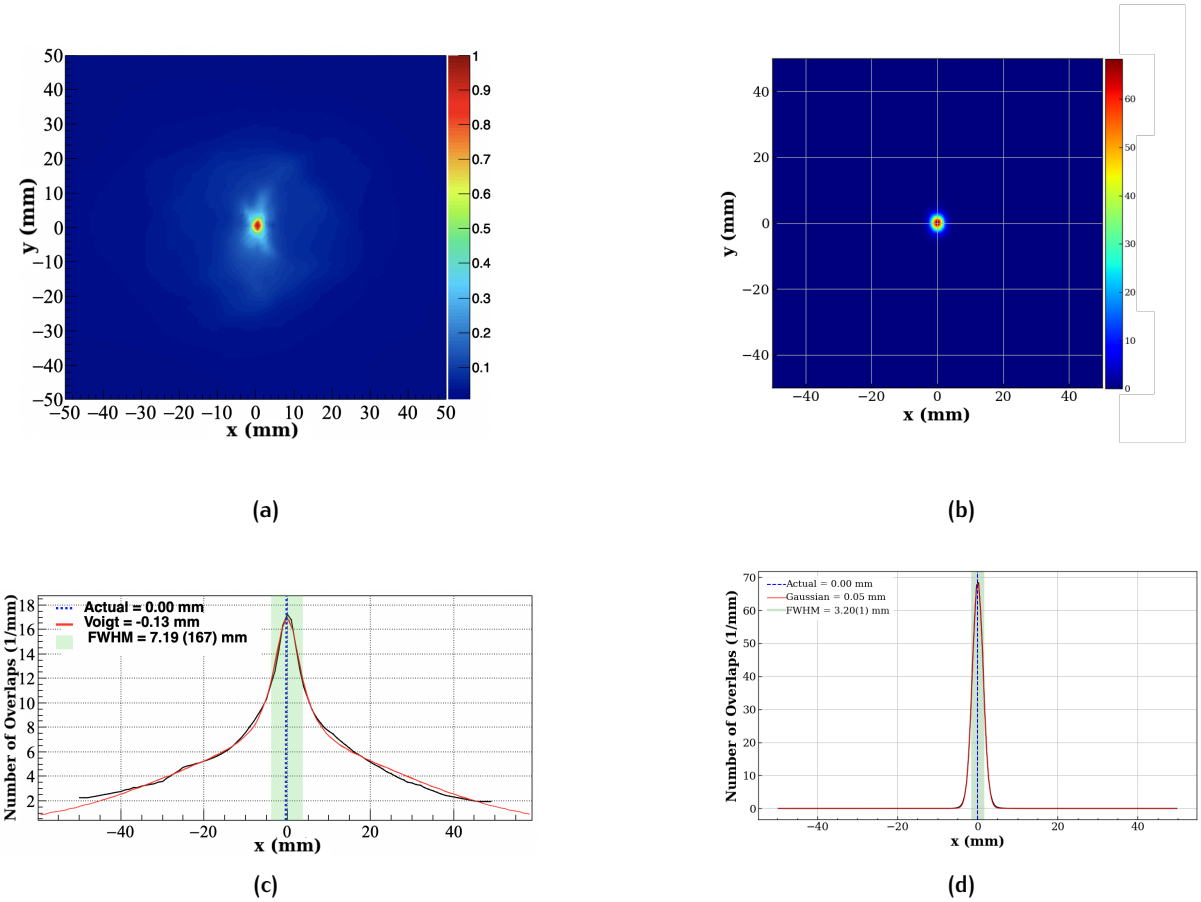

Figure 5.2.11: A comparison of the optimised results from two different image reconstruction algorithms: (a) the x-y source image matrix using the FBP Wiener filter method, (b) the x-y source image matrix using the Octane EM method, (c) the x-projection from the FBP Wiener filter method, and (d) the x-projection from the Octane EM method. The dotted blue line represents the actual source location. The distribution was fitted with a Gaussian function (red), and the FWHM of the Gaussian is shown in green and labelled with uncertainty.

The Octane EM algorithm, unlike traditional 2D methods, operates in a fully 3D space, allowing for the extraction of profiles along the x, y, and z axes. By employing cone analysis and recursive segmentation of the imaging volume, it significantly enhances spatial resolution across all three dimensions. This approach enables the identification of maximum intensity profiles, which results in more precise localisation of gamma-ray sources, particularly along

the depth (z-axis). As shown in Fig. 5.2.12(c), the reconstruction at maximum y-z intensities reveals the source position more accurately compared to images taken at arbitrary z distances for a source centred at (0,0,10) mm. When the maximum intensity was not used, the overall accuracy of the reconstruction was reduced. These images offer deeper insight into the effectiveness of 3D reconstruction and demonstrate the algorithm's ability to improve source localisation in a CC setup.

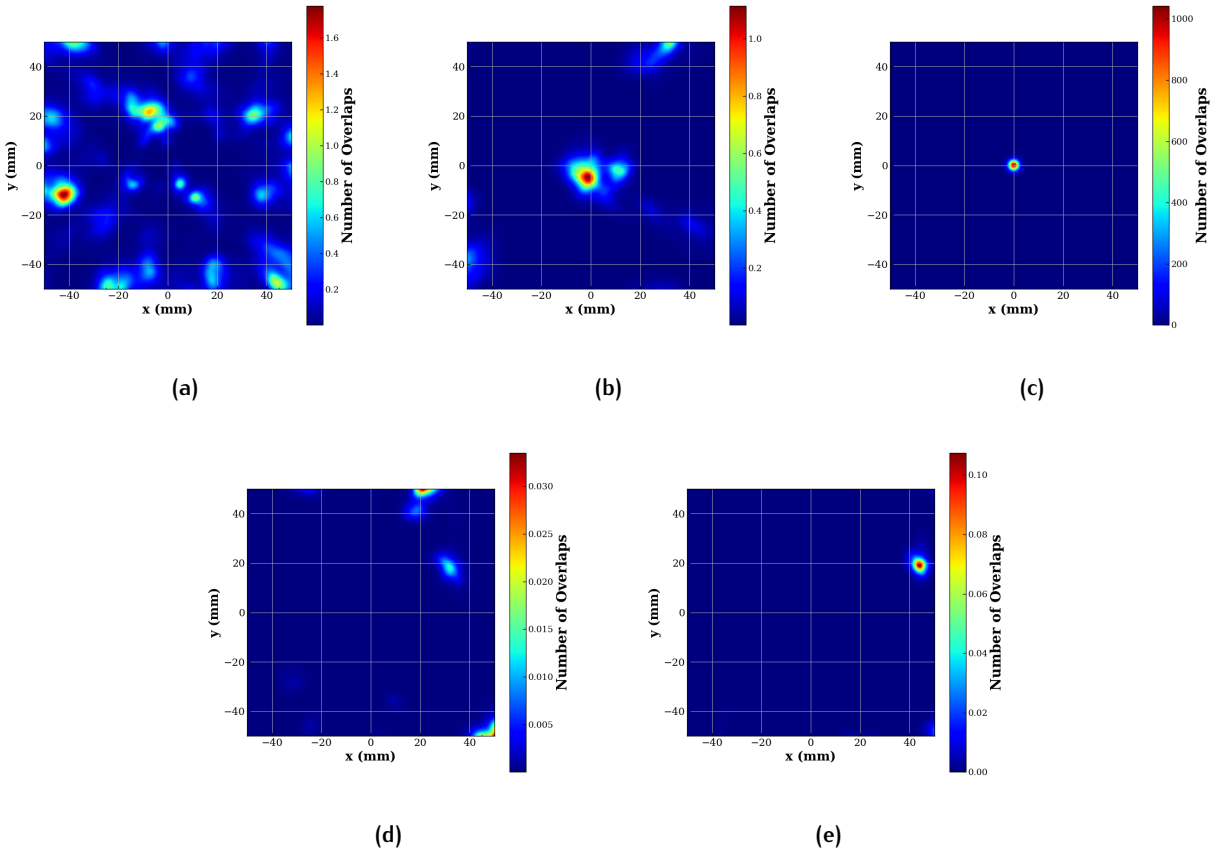

Figure 5.2.12: The x-y matrix of CC1 shown at different z slice values for the same Octane EM reconstruction. The reconstruction was run for 100 iterations and a bin width of 2 mm bins. The reconstruction was performed on the Compton cone data to investigate the quality of the image resolution for: (a) an arbitrary slice at z = 41.5 mm, (b) an arbitrary value of z = 20.7 mm, (c) a slice at maximum z intensity (z = -0.8 mm), (d) an arbitrary slice at z = -20.7 mm, (e) an arbitrary value of z = -41.5 mm.

The superiority of this 3D approach is evident in Fig. 5.2.11(b), where the Octane EM reconstruction is shown, compared to the 2D FBP reconstruction with Wiener filtering in Fig. 5.2.11(a). The 2D FBP results were fitted with a Voigt function (a Gaussian-Lorentzian hybrid) to account for tailing effects caused by compressing the z-dimension, which reduces the ability to distinguish sources. In this comparison, the FWHM of the 2D reconstruction measures 7.19(167) mm, whereas the 3D reconstruction achieves a far sharper 3.20(1) mm.

Therefore, the 3D algorithm not only offers a more comprehensive view of the gamma-ray source distribution but also provides greater insights into the interactions within the CC. The ability to extract profiles along all three dimensions significantly improves the accuracy of the reconstructed image, revealing details or artefacts that would otherwise go undetected in a 2D analysis. Additionally, the 3D approach is better suited for advanced studies, such as DOI analysis or handling more complex source geometries.

5.2.8 Simulations Performed

All simulations were run, and image reconstruction performed using the resources provided by the University of Cape Town Physics department's server. Access to this resource decreased the computational time required when compared to using PC, as simulations were able to be multithreaded over 50 cores. Further, the Octane EM code was also parallelised to run using the server's GPU over 50 cores. All simulations performed were run for $2(10^9)$ initial histories for each source. Each simulation took in excess of 26 hours to run, and the Octane EM image reconstruction averaged $\sim$ 11 hours for most simulations.

The choice of the number of initial histories to generate in the simulation was decided two-fold. The performance of a CC is best characterised when there exist at least 10000 Compton cones in the reconstruction, however, there exists a reasonable upper limit to the simulation run time and, a such, the resources required to compute the simulation. The number of Compton cones is dependent on a number of factors, including the detector geometry and material composition. It was decided that a reasonable normalisation would be to provide the same environment in to each CC investigated, such that each simulation was generated for the same number of histories, although this results in some CC configurations suffering orders of magnitude fewer statistics than their competitors for reasons mentioned, seen in Figs. 5.2.13(a) for CC1 and (b) for CC2 where each measurement involved a ^{137}Cs source placed (0,0,10) mm away from the detector scatterer. The efficiency is seen to fluctuate in Fig. 5.2.13(a), but with an overall increasing trend, however, the CC3 results in Fig. 5.2.13(b) show an overall decreasing trend as more run histories are accumulated. This decrease was less than a quarter of an order of magnitude when the number of events was increased by an order of magnitude. As such, it was not seen as a decreasing efficiency overall.

Table 5.2.6 details the simulations designed to be reasonable baseline comparisons between each CC configuration in terms of the performance metrics elaborated on in Section 2.4.1.

CC Configuration	**Source/s**	**Source to Scatterer Distance (x,y,z) (mm)**	**Scatterer to Absorber Distance (x,y,z) (mm)**
CC1, CC2 (all geometries), CC3	^{137}Cs	(0,0,10)	(0,0,0.1)
CC1, CC2 (all geometries), CC3	^{22}Na	(0,0,10)	(0,0,0.1)
CC1, CC2 (all geometries), CC3	^{137}Cs	(0,0,100)	(0,0,0.1)
CC1, CC2 (all geometries), CC3	^{137}Cs	(0,0,10)	(0,0,10)
CC1, CC2 (all geometries), CC3	^{137}Cs, ^{137}Cs	(-1,0,10), (1,0,10)	(0,0,0.1)
CC1, CC2 (all geometries), CC3	^{22}Na, ^{60}Co	(-4,0,10), (4,0,10)	(0,0,0.1)
CC2 (geometry 2 & 3), CC3	^{22}Na, ^{22}Na	(-16,0,10), (16,0,10)	(0,0,0.1)
CC1, CC2 (all geometries), CC3	^{22}Na, ^{22}Na	(-8,0,10), (8,0,10)	(0,0,0.1)
CC1	^{22}Na, ^{22}Na	(-11,0,10), (11,0,10)	(0,0,0.1)

Table 5.2.6: Table detailing the simulation sources and geometries investigated in the work, designed to be reasonable baseline comparisons between each CC configuration. Each simulation was run with 2×10^9 initial histories for each isotropic source present in the simulation.

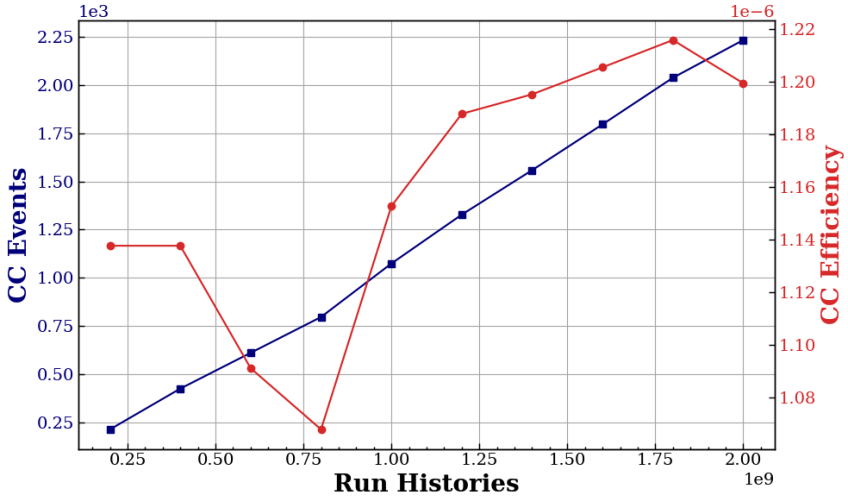

(a)

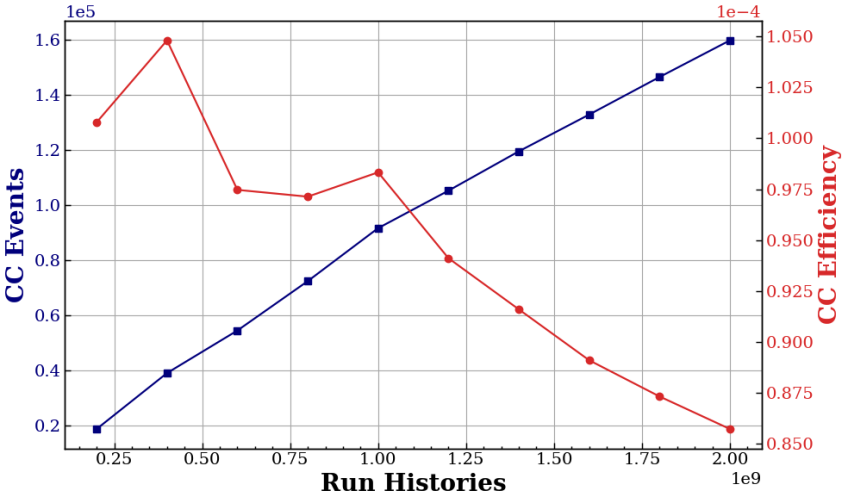

(b)

Figure 5.2.13: Plots showing how CC efficiency is influenced by the number of initial histories generated by the simulation for a ^{137}Cs source placed 10 mm away from: (a) CC1, and (b) CC3.

6 RESULTS AND DISCUSSION

This chapter concludes the investigation into the development and evaluation of three CC prototypes aimed at advancing gamma-ray detection technology for clinical applications. The first prototype, CC1, integrates a CZT Polaris-J detector as the scatterer with a $2'' \times 2''$ $LaBr_3$:Ce detector as the absorber, combining the high energy resolution and stopping power of CZT with the superior timing resolution of $LaBr_3$:Ce. This hybrid design was rigorously tested through a series of experiments involving gamma-ray sources and a 66.67 MeV proton beam, as well as MC simulations using TOPAS MC. These efforts provided valuable insights into the system's performance in terms of FEPE, timing accuracy, and image resolution.

The second and third prototypes, CC2 and CC3, explored novel detector configurations with MacroPixel LB-14x25c-SiPM-T scintillation DAs, focusing on their potential for enhanced modularity and low-voltage operation. The CC2 and CC3 designs were primarily assessed through validated simulations, with experimental validation of CC results pending additional instrumentation. This chapter summarises the key findings from both experimental and simulated results, highlighting the key achievements and limitations of each prototype, and offers recommendations for future research and development.

The investigated designs were (as seen in Fig. 4.4.1):

- **CC1:** A prototype with a scatterer made of CZT Polaris detector and an absorber of $2'' \times 2''$ $LaBr_3$:Ce crystal. Performance metrics were obtained from both simulations and experimental measurements conducted with source and beam-time data.

- **CC2:** A prototype with a featuring both the scatterer and absorber made from a 4×2 array of $LaBr_3$:Ce MacroPixel LB-14x25c-SiPM-T DAs. Results are based on simulation data.

- **CC3:** A prototype with a scatterer made of a 6×1 array of $LaBr_3$:Ce MacroPixel LB-14x25c-SiPM-T DAs and an absorber of $2'' \times 2''$ $LaBr_3$:Ce crystal. Results are based on simulation data.

The chapter encompasses various performance metrics, including timing accuracy, efficiency, ARM, and image resolution, with a focus on how well each prototype reconstructs the source position.

6.1 VALIDATION OF SIMULATION

Comprehensive TOPAS simulations of each detector, as discussed in Chapter 5, were conducted to verify the energy deposition and efficiency curve by comparing the simulated results with experimental data. The simulated geometry and corresponding materials that make up each detector were implemented in the simulation to reflect the specifications reported by the manufacturers.

Validating the FEPE and energy deposition is critical for accurate modelling of the CC systems. The FEPE ensures that the simulation correctly predicts the fraction of gamma rays that deposit their entire energy in the detector, a key parameter for both the sensitivity and the accuracy of the CC.

Additionally, validation of energy deposition ensures that the interaction physics modelled in the simulation accurately reflects real-world interactions, such as Compton scattering and photoelectric absorption. This was essential for reconstructing gamma-ray trajectories and determining the source of radiation with high spatial resolution. The validation process was fundamental for confirming the reliability of the simulation results and for optimising the detector's configuration for real-world applications.

The energy deposition of charged particles within each of the detectors was simulated for 2 $\times 10^9$ TOPAS histories and scored within the detector crystals. To reflect the physical detector resolution performance, energy smearing was applied in the simulation. Further, the threshold measurable energy of each detector was included in the simulation. The only detector for which dead-time effects were modelled was the Polaris detector, as significant timing delays were encountered in experiment. It was ensured that if the time elapsed between two energy depositions (above the threshold) in either of the two detector crystals <15.0 µs, the event was not recorded in the simulation [60]. This mimicked the processing time of the detector, which is a well-quantified value for the Polaris. However, it represents the minimum possible dead-time for the detector.

6.1.1 Physics

The validation of the simulation physics and each detector response energy smearing was evaluated by overlaying the simulated spectrum of each detector with the experimental measurement for a ^{152}Eu source placed 10 mm from the detector face, except for SrI_2:Eu, for which the measurements were performed at 30 mm due to the effect of high count rates on the crystal.

It was observed that the total counts in the simulated spectra were, on average, 20% lower than those in the experimental spectra, as quantified by the integrated area under the energy curves. This discrepancy, although somewhat unusual (since simulations often overestimate due to idealised conditions), may be attributed to several factors:

- **Unaccounted experimental effects**: Effects such as detector dead time, pile-up rejection algorithms, and intrinsic noise in the experimental electronics can artificially reduce recorded counts. These are not explicitly modeled in the simulations.
- **Source activity or geometry uncertainty**: While care was taken to replicate the experimental geometry, small deviations in the simulated source activity, emission isotropy, or collimation may contribute to reduced fluence at the detector face in simulation.
- **Simplified modelling of environmental scattering**: Experimental setups inherently include room-scattered photons and support structures that may contribute to additional low-energy counts, whereas these were omitted in the simulation geometry.

To facilitate direct comparison of spectral shape and validate the detector response functions, the simulated energy distributions in Figs. 6.1.1–6.1.4 were normalised by a factor of 5. This normalisation improves the visibility of signature peaks and allows a more reliable comparison of energy smearing and spectral structure.

Background subtraction was applied to the experimental spectra prior to comparison. The resulting overlays, such as that for the $2'' \times 2''$ $LaBr_3$:Ce detector in Fig. 6.1.1, demonstrate good agreement in both detector resolution and peak positions, confirming the accuracy of the implemented physics models and response functions within the TOPAS simulation toolkit.

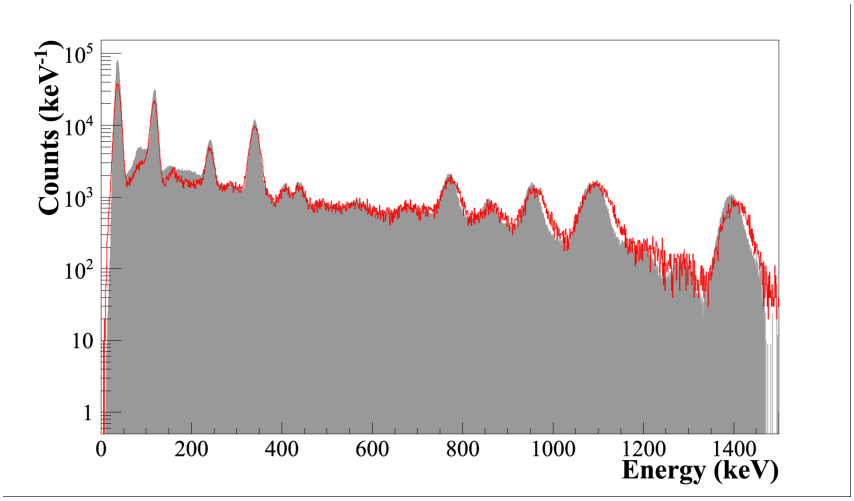

Figure 6.1.1: The energy spectra from a ^{152}Eu source showing the comparison between simulation (red) and background-subtracted experiment (grey) for the $2'' \times 2''$ $LaBr_3$:Ce detector. The statistics of the simulation have been increased by a factor of 5 for the purpose of visual comparison of the physics and energy smearing response.

Figure 6.1.2 shows the comparison for the Polaris detector. When comparing MC simulations to experimental measurements for CZT crystals, the discrepancy caused by charge build-up can lead to notable differences in results, particularly in terms of energy resolution. The experimental spectrum contains less structure for low intensity peaks such as the 367.79, 678.0 and 668.67 keV characteristic emissions that should appear in the spectrum for a detector of such high energy resolution. These low-intensity peaks are absorbed into a constant charge-trapping induced background continuum. In simulations, the charge collection process is idealised, and effects such as charge trapping, incomplete charge collection, and

excess charge build-up at the base of photopeaks are not naturally included unless explicitly modelled. Consequently, simulated photopeaks are generally narrower and have better resolution compared to experimental data [104, 105]. However, in experiment, the charge build-up broadens the photopeaks, which reduces the detector's ability to distinguish between closely spaced energy peaks. This discrepancy can result in overestimating the performance of the detector in simulations, as the experimental resolution was artificially degraded by the physical processes that TOPAS does not account for by default.

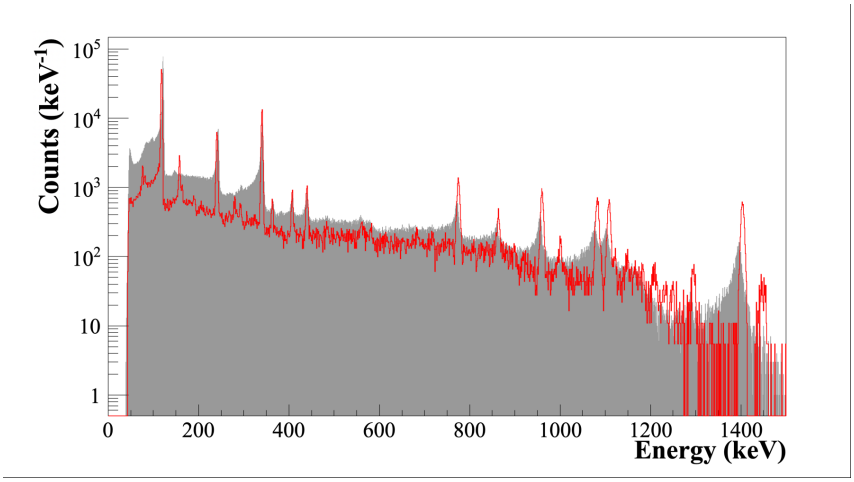

Figure 6.1.2: The energy spectra from a ^{152}Eu source showing the comparison between simulation (red) and background-subtracted experiment (grey) for the Polaris detector. The statistics of the simulation have been increased by a factor of 5 for the purpose of visual comparison of the physics and energy smearing response.

Recent advancements have addressed this issue by implementing DPP and improved electrode designs for CZT and other detector materials affected by the same effect. These approaches include correcting for charge trapping and drift effects by using algorithms that compensate for the incomplete charge collection. A recent study characterised the trapping effect as a function of interaction depth, revealing significant effects of intrinsic electron and hole trapping on the spectroscopic performance of segmented Germanium detectors and allowing for an improvement in the energy resolution [106]. For the purposes of this work, it was decided that correcting for the charge build-up in the experiment would be unnecessary as the timing of the Polaris detector posed a greater challenge.

Figures 6.1.3 and 6.1.4 show the simulated and experiment results of the $LaBr_3$:Ce and SrI_2:Eu DAs each. Overall, the agreement between simulation and experiment across the 0.0–1500.0 keV energy range was satisfactory, with the most notable discrepancies occurring in the 0.0–300.0 keV energy range for each detector. The $LaBr_3$:Ce DA shows greater agreement in the low energy, with any differences attributed to uncertainties in the detector energy smearing, as the fit displayed more deviation in the low energy region (see Section 4.3.4). The observed differences for the SrI_2:Eu detector, while not great, were attributed to a combination of the energy smearing response function and the loss of low-intensity peaks from pulse pile-up in the experiment.

Overall, the simulation was able to reproduce the physics seen in experiment, indicating that the material properties and geometries implemented in the simulated environment were in close agreement with the physical detectors.

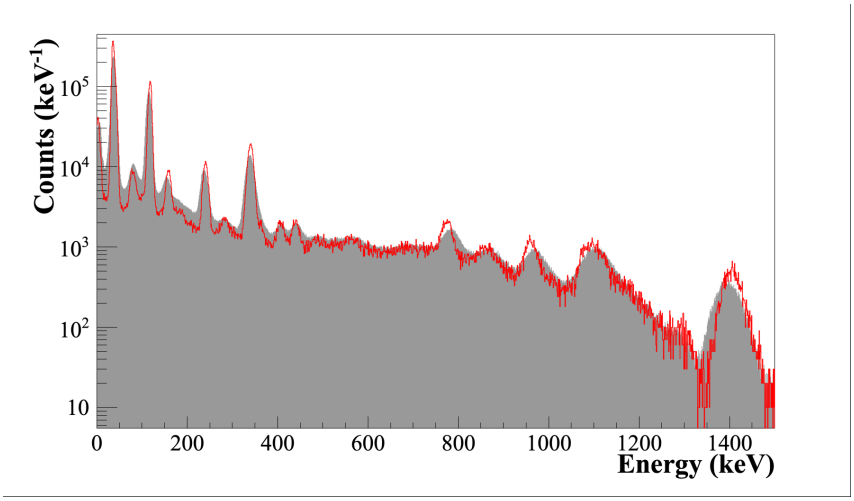

Figure 6.1.3: The energy spectra from a ^{152}Eu source showing the comparison between simulation (red) and background-subtracted experiment (grey) for the $LaBr_3$:Ce DA. The statistics of the simulation have been increased by a factor of 5 for the purpose of visual comparison of the physics and energy smearing response.

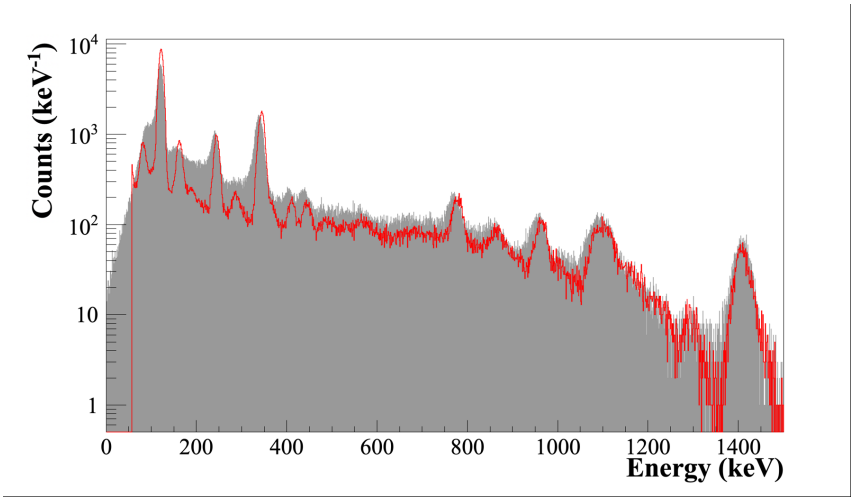

Figure 6.1.4: The energy spectra from a ^{152}Eu source showing the comparison between simulation (red) and background-subtracted experiment (grey) for the SrI_2:Eu DA. The sharp drop off in the simulated spectrum below 50 keV originates from setting the minimum detectable energy of the detector to 50 keV. The statistics of the simulation have been increased by a factor of 5 for the purpose of visual comparison of the physics and energy smearing response.

6.1.2 Detector Full-Energy Peak Efficiency

Further validation of the simulation was required to ensure that the detector efficiencies were in agreement between simulation and experiment. Experimental measurements were conducted at various source-to-detector distances using a ^{152}Eu source, detailed in Sections 3.3.4 and 4.3.7, due to the wide range of distinct gamma-ray emissions in its spectrum. Two such energies in the spectrum of ^{152}Eu decay were chosen to compare the FEPE of simulation and

experiment of each detector. The 344.28 and 964.08 keV gamma-ray peaks were chosen because they occur at lower and higher energies within the region of interest and due to their relatively higher intensity in the spectrum, guaranteeing accurate measurements across the different detector resolutions. The FEPE was calculated using the following equation:

$$\epsilon_{CC} = \frac{N_p}{N_{emitted}}$$

In experiment and simulation, N_p is a measure of the number of counts under the photopeak. The $N_{emitted}$ is calculated in experimental measures by multiplying the source activity by the live time and branching ratio of the gamma-ray peak of interest, described in Section 3.3.4. In simulation, it is the number of emitted gamma rays. Section 5.2.4 explains how the simulation calculates the quantity.

Validation of the simulation involves the simulated data reproducing the trend and values of the experimentally calculated FEPE data within some uncertainty. The sigma agreement between two independent, normally distributed quantities with uncorrelated uncertainties can be calculated using the following equation:

$$\sigma = \frac{|A - B|}{\sqrt{(\delta A)^2 + (\delta B^2)}} \tag{6.1.1}$$

for trivial $A \pm \delta A$ and $B \pm \delta B$, where the σ refers to the size of the uncertainty; or more specifically, it represents the 68% confidence interval in a normal distribution. For agreement values within 1σ, the difference between values is small compared to their uncertainties. This is typically considered excellent agreement because the likelihood of a true difference is very low. Agreement within 2σ means the difference is within a reasonable range of uncertainty, often considered good agreement but leaves a slightly higher chance (about 5%) that the difference could be significant. If the difference exceeds 2σ, the agreement becomes questionable. The FEPE values and uncertainties for each detector at gamma-ray energies of 344.38 and 964.08 keV are listed with agreement in Tables 6.1.1–6.1.4.

Referring to the 344.28 keV results, Table 6.1.1 shows the results of the $2'' \times 2''$ $LaBr_3$:Ce detector. The simulated and real detector responses for different source-to-detector distances were each within 2σ agreement of one another, with the most overlap seen at the 100 mm source-to-detector distance where simulation measured 0.737(74)% and experiment measured 0.627(7)%, compared to at 10 mm where simulation measured 4.32(48)% and experiment measured 3.89(10)%. Therefore, the FEPE of this detector showed satisfactory agreement between simulation and experiment, with the FEPE agreement between datasets were within 1σ at 964.08 keV. The improvement in FEPE agreement at higher energy is due to the energy smearing of the simulated detector energy response (Fig. 3.3.6), which demonstrated non-linearity in the low-energy region due to the intrinsic non-proportionality of light yield in the crystal.

Table 6.1.2 shows the comparison for the Polaris detector. Good agreement was shown within uncertainty, with the simulation showing the most deviation at 100 mm, where the

result was 0.042(5)%, nearly half the experiment value of 0.080(4)% and no agreement was present, with a σ value of nearly 6. The Polaris efficiency was well characterised overall, with an agreement of <1σ for both the 344.28 and 968.08 keV energy peaks. Interestingly, the charge build-up effects due to trapping within the detector in the experiment did not affect the FEPE comparison between simulation and experiment, as the effect causes tailing of the energy peak, such that the FWHM was unaffected.

Table 6.1.3 shows the detector response for the $LaBr_3$:Ce DA. The $LaBr_3$:Ce DA simulation showed good agreement, with σ values below 2 for all measurements, with most simulated responses falling within 1σ of the experiment value. The most disagreement between results for this detector FEPE was at 30 mm source-to-detector distance at 964.08 keV, where the simulation measured 0.123(31)% while the experiment measured 0.078(21)%. The low-energy response rendered simulated results consistently higher than the experiment.

The SrI_2:Eu detector FEPE comparison is shown in Table 6.1.4. The simulation and experiment show no agreement for the 344.28 keV peak until 100 mm source-to-detector distance. The simulated result at 30 mm was 0.045(6)%, while the experiment measured 0.060(34)%. FEPE measurements could not be shown at 10 mm due to pulse pile-up effects at near-source distances, discussed in Section 4.3.7, as the high rates flooded the detector and the peak was washed out, making Gaussian fitting of the peak not possible. The effect of this washout was shown in Fig. 4.3.20.

The SrI_2:Eu detector FEPE results at 964.08 keV showed better agreement with experiment than the 344.28 keV peak. The uncertainty in experimental measures was large due to the high Chi-squared value in peak-fitting for this detector, caused by the low statistics in the gamma-ray spectrum, rendering large statistical uncertainty in the Radware fitting tool. This problem could be overcome by a longer measurement time. For the purposes of this work, the simulation of the SrI_2 detector was decided to be non-physical for realistic investigation into CC behaviour due to the difficulty with the pulse pile-up effects in the low energy region. Work has been performed to simulate these detector effects; however, the TOPAS simulation has not been adapted for pulse shape analysis and investigations into correcting for this phenomenon would involve future work [107, 108].

Overall, it was seen that the FEPE decreased with the increasing gamma-ray energy for all detectors. The agreement between calculated and measured values was good for the 2″ × 2″ $LaBr_3$:Ce, Polaris and $LaBr_3$:Ce detectors. These three detectors were investigated further for their feasibility for use in two-layer CCs.

Distance (mm)	344.28 keV			968.08 keV		
	$\epsilon_{EXP,FEPE}$ (%)	$\epsilon_{SIMU,FEPE}$ (%)	Agreement (σ)	$\epsilon_{EXP,FEPE}$ (%)	$\epsilon_{SIMU,FEPE}$ (%)	Agreement (σ)
10.0	4.32(48)	3.89(10)	0.87	0.974(119)	0.849(51)	0.97
30.0	2.73(28)	2.25(20)	1.40	0.884(90)	0.789(49)	0.93
50.0	1.85(19)	1.48(20)	1.34	0.631(64)	0.541(72)	0.93
100.0	0.737(74)	0.627(7)	1.48	0.274(28)	0.282(36)	0.18

Table 6.1.1: Comparison of experimental and simulation results for the $2'' \times 2''$ $LaBr_3$:Ce detector absolute full-energy peak efficiencies and associated uncertainties for gamma-ray energies 344.28 keV and 968.08 keV at various source-to-detector distances.

Distance (mm)	344.28 keV			968.08 keV		
	$\epsilon_{EXP,FEPE}$ (%)	$\epsilon_{SIMU,FEPE}$ (%)	Agreement (σ)	$\epsilon_{EXP,FEPE}$ (%)	$\epsilon_{SIMU,FEPE}$ (%)	Agreement (σ)
10.0	0.463(57)	0.456(22)	0.12	0.087(22)	0.075(4)	0.54
30.0	0.227(26)	0.254(13)	0.93	0.034(9)	0.029(7)	0.44
50.0	0.115(13)	0.120(10)	0.31	0.015(4)	0.008(7)	0.87
100.0	0.042(5)	0.080(4)	5.94	0.006(3)	0.013(9)	0.74

Table 6.1.2: Comparison of experimental and simulation for the Polaris detector absolute full-energy peak efficiencies and associated uncertainties for gamma-ray energies 344.28 keV and 968.08 keV at various source-to-detector distances.

Distance (mm)	344.28 keV			968.08 keV		
	$\epsilon_{EXP,FEPE}$ (%)	$\epsilon_{SIMU,FEPE}$ (%)	Agreement (σ)	$\epsilon_{EXP,FEPE}$ (%)	$\epsilon_{SIMU,FEPE}$ (%)	Agreement (σ)
10.0	1.38(19)	1.50(10)	0.56	0.223(63)	0.196(13)	0.42
30.0	0.332(142)	0.449(90)	0.70	0.123(31)	0.078(21)	1.20
50.0	0.141(16)	0.204(53)	1.14	0.042(39)	0.039(12)	0.074
100.0	0.043(7)	0.044(9)	0.088	0.009(17)	0.009(10)	0

Table 6.1.3: Comparison of experimental and simulation for the $LaBr_3$:Ce DA absolute full-energy peak efficiencies and associated uncertainties for gamma-ray energies 344.28 keV and 968.08 keV at various source-to-detector distances.

Distance (mm)	344.28 keV			968.08 keV		
	$\epsilon_{EXP,FEPE}$ (%)	$\epsilon_{SIMU,FEPE}$ (%)	Agreement (σ)	$\epsilon_{EXP,FEPE}$ (%)	$\epsilon_{SIMU,FEPE}$ (%)	Agreement (σ)
30.0	0.282(87)	0.480(11)	2.26	0.053(10)	0.043(6)	0.86
50.0	0.124(15)	0.196(9)	4.12	0.031(15)	0.019(3)	0.79
100.0	0.045(6)	0.060(34)	0.43	0.011(3)	0.010(5)	0.17

Table 6.1.4: Comparison of experimental and simulation for the SrI_2:Eu DA absolute full-energy peak efficiencies and associated uncertainties for gamma-ray energies 344.28 keV and 968.08 keV at various source-to-detector distances.

6.2 COMPARISON OF THE SIMULATED PERFORMANCE OF THE COMPTON CAMERAS

The feasibility of using the CC designs investigated for use in a clinical setting, such as for range verification during charged particle therapy, was investigated by measuring the CC

response using various sources. The impact of varying the distance between the source and the CC on efficiency, ARM, and image resolution was also investigated. The three CC detector configurations that form the focus of this study are shown in Fig. 4.4.1. Images of the CCs are seen as taken from the QT simulation, along with the scatterer and absorber detectors that make up each CC design.

6.2.1 Compton Camera Efficiency

Several factors influence the efficiency of a CC design, where the CC efficiency is a measure of the number of imageable Compton cones divided by the number of emitted gamma rays. The distance between the gamma-ray source and the detector affects the efficiency, as increased distance leads to geometric attenuation and higher probabilities of scattering. The FOV of the scatter layer, which is the solid angle subtended by the source, should be maximised to enhance efficiency; this was achieved by enlarging the surface area of the scatter layer. The probability of Compton scattering occurring within the scatter layer also impacts efficiency and depends on the material properties (in particular, the density) and thickness of the detector. Additionally, the likelihood that a scattered photon will escape from the scatter layer without being absorbed is influenced by the photon energy and the material's self-absorption characteristics.

The CC efficiency was evaluated by placing the source at different distances to the CC scatterer face. For all simulations, the source was placed so that the x and y positions were isocentric with respect to the crystal so that the source was at the centre of the detector face for homogeneity in comparison between configurations. Table 6.2.1 shows the CC efficiency results for a ^{137}Cs source placed 10 mm and 100 mm away from the scatterer face for each CC design and geometry. CC3 exhibited the highest efficiency due to the greater material thickness of the absorber module, which effectively enhances photon capture and reduces losses due to scattering. High efficiency was measured at both distances for CC2 geometry 3, attributed to its larger scatterer surface area. The CC2 geometry 1 CC efficiency demonstrated lower performance than the other CC2 geometries due to the low scatterer surface area relative to the source position, decreasing the probability of a photon interacting with the detectors in a CC behaviour. The CC1 design exhibits the lowest efficiency overall, attributed to the geometry of the Polaris detector CZT crystals. The placement of the CZT crystals within the detector posed a design constraint that could not be overcome due to the nature of the detector electronics setup. Improved geometrical set-ups for the detector combination were explored, but this design was the optimal outcome. For the CC1 geometry, when the scatterer and absorber modules were at their nearest positioning, the face of the CZT detector crystals were situated 88 mm apart.

Table 6.2.2 presents the simulated CC efficiency as a function of the distance between the scatterer and absorber layers for distances of 0.1 mm and 10 mm. The data revealed that efficiency was significantly higher when the scatterer and absorber layers were closer together (0.1 mm) compared to when they were further apart (10 mm). It shows that increasing

CC Configuration	(0,0,10) (mm)	(0,0,100) (mm)
CC1	1.20×10^{-6}	3.13×10^{-8}
CC2 geometry 1	9.83×10^{-6}	4.36×10^{-7}
CC2 geometry 2	3.13×10^{-5}	9.45×10^{-7}
CC2 geometry 3	4.35×10^{-5}	1.31×10^{-6}
CC3	8.57×10^{-5}	2.49×10^{-6}

Table 6.2.1: Simulated CC efficiency as measured at source-to-scatterer distances of (0,0,10) mm and (0,0,100) mm for each CC detector and geometry investigated. As the distance between the source and detector increases, the efficiency declines roughly in proportion to the inverse of the distance squared. All simulations were performed with 2×10^9 initial histories.

the distance between these layers generally leads to a decrease in efficiency. At a shorter distance (0.1 mm), the efficiency was higher because the probability of a scattered photon being absorbed by the detector was increased, resulting in more detected events. This decrease in efficiency with increased distance (10 mm) was due to the higher likelihood of photons escaping without interaction, reducing the overall number of imageable Compton cones. CC3 consistently demonstrated the highest efficiency across both distances, indicating an effective design in capturing and processing scattered photons. In contrast, CC1 shows lower efficiency, highlighting its less optimal design for maximising photon capture in this setup. Geometries 2 and 3 of CC2 performed well for detectors of their size, with geometry 3 achieving notably high efficiency.

CC Configuration	(0,0,0.1) (mm)	(0,0,10) (mm)
CC1	1.20×10^{-6}	9.58×10^{-7}
CC2 geometry 1	9.83×10^{-6}	5.56×10^{-6}
CC2 geometry 2	3.13×10^{-5}	1.57×10^{-5}
CC2 geometry 3	4.35×10^{-5}	2.16×10^{-5}
CC3	8.57×10^{-5}	5.19×10^{-5}

Table 6.2.2: Simulated CC efficiency as measured for a ^{137}Cs source at scatterer-to-absorber distances of (0,0,0.1) mm and (0,0,10) mm for each CC detector and geometry investigated. All simulations were performed with 2×10^9 initial histories.

In Table 6.2.3, the efficiency of the CCs was compared for two different gamma-ray sources: ^{22}Na and ^{137}Cs, both measured at a source-to-scatterer distance of 10 mm. The ^{22}Na source emits gamma rays at two distinct energies: 511.0 keV and 1274.5 keV, while ^{137}Cs emits gamma rays at 661.7 keV. The differences in efficiency between these two sources arise from their distinct gamma-ray energies and interaction probabilities within the detector materials.

The efficiency for ^{22}Na was notably higher than that for ^{137}Cs across all detector configurations. This higher efficiency was attributed to the notably higher possible gamma rays per decay present in the^{22}Na isotope, which emits photons at 511.0 keV and 1274.5 keV. The 511.0 keV photons were also more likely to be fully absorbed within the detector due to their lower energy, leading to a higher likelihood of interaction. In contrast, the 661.7 keV photons from ^{137}Cs have a higher chance of escaping the detector or undergoing incomplete interactions, resulting in lower overall efficiency. The results show that CC3 and CC2 geometry 2 achieved the highest efficiency for both ^{22}Na and ^{137}Cs, further highlighting their effective design in cap-

turing and processing a broad range of gamma-ray energies. In contrast, CC1 demonstrates lower efficiency for both sources, reflecting the constraints of its design and material properties in managing different gamma-ray energies. This analysis underscores the importance of tailoring detector designs to the specific energy characteristics of the gamma-ray sources to optimise overall performance.

CC Configuration	^{137}Cs	^{22}Na
CC1	1.20×10^{-6}	4.72×10^{-6}
CC2 geometry 1	9.83×10^{-6}	2.80×10^{-5}
CC2 geometry 2	3.13×10^{-5}	1.07×10^{-4}
CC2 geometry 3	4.35×10^{-5}	1.53×10^{-4}
CC3	8.57×10^{-5}	3.04×10^{-4}

Table 6.2.3: Simulated CC efficiency measured at a source-to-scatterer distance of (0,0,10) mm for the sources ^{22}Na and ^{137}Cs for each CC detector and geometry investigated. All simulations were performed with 2×10^9 initial histories.

6.2.2 ARM

The key idea behind using ARM as a performance metric for CC comparison was to assess the camera's ability to precisely reconstruct the Compton scattering angle, θ_{CC}, which was critical for producing accurate images. The ARM is typically evaluated through metrics such as the FWHM of the ARM distribution, which quantifies the deviation between the reconstructed and true scattering angles. A CC with a smaller ARM value can more precisely identify the location of gamma-ray sources. This is especially important in applications such as medical imaging, astrophysics, and security, where accurate source identification is crucial. Figure 6.2.1 shows the comparison of CC1 and CC3 ARM for a ^{137}Cs source placed 10 mm from the scatterer faces, each. The geometry of the CCs was such that the scatterer and absorber modules were placed as near to one another as reasonably possible (0.1 mm).

For the CC1 geometry, when the scatterer and absorber modules were at their nearest positioning, the face of the CZT detector crystals were 88 mm apart due to the nature of the Polaris detector housing. The ARM measurements between CC1 and the results of CC2 and CC3 were therefore difficult to compare due to the increased distance that cannot be overcome due to the detector design. As the distance between the scatterer and absorber layers increases, the ARM generally improves. Larger distance between the two detectors allows for a more precise measurement of the geometric angle, reducing the uncertainty in the position of the interaction points. Consequently, the difference between the Compton scattering angle and the geometric angle becomes smaller, enhancing the ARM. Table 6.2.4 further demonstrates this phenomenon where the ARM is shown for each CC when the layers were very near and after the distance between layers was increased to (0,0,10) mm. It can be seen that for CC2 and CC3, increasing the distance between the layers, while seen in Table 6.2.2 to decrease the CC efficiency, improves the ARM of the CC. This trade off was further investigated in the image resolution in Section 5.2.7. Table 6.2.4 shows that the ARM of CC1 decreased when the scatterer-absorber layer distance was increased by 10 mm. This was because the

improvement introduced by increasing the layer distance may eventually reach a limit, as larger distances could introduce other uncertainties, such as detector alignment or position resolution uncertainties.

CC Configuration	**(0,0,0.1) (mm)**	**(0,0,10) (mm)**
CC1	1.87(4)	1.99(4)
CC2 geometry 1	1.85(3)	1.47(13)
CC2 geometry 2	2.37(4)	1.78(2)
CC2 geometry 3	2.25(4)	1.83(2)
CC3	3.30(9)	3.26(8)

Table 6.2.4: Simulated ARM distributions as measured at scatterer-to-absorber distances of (0,0,0.1) mm and (0,0,10) mm for each CC detector and geometry investigated.

The comparison of ARM between the results of CC2 and CC3 indicates that the CC2 geometry 1 design achieves the most narrow ARM, as seen in Fig. 6.2.2. While this design shows lower FEPE, its advantage lies in the thickness of the scatterer and absorber modules (25.4 mm). The increased thickness provides more material for gamma rays to interact with, particularly for the 661.7 keV gamma ray. The thicker design allows more energy to be deposited within the detector, enhancing its ability to accurately measure the energy and positions of interactions. As a result, the CC can more precisely reconstruct the source position by reducing uncertainties in the interaction positions and angles. Despite the reduced efficiency, the improved accuracy in source localisation makes this design better in terms of ARM.

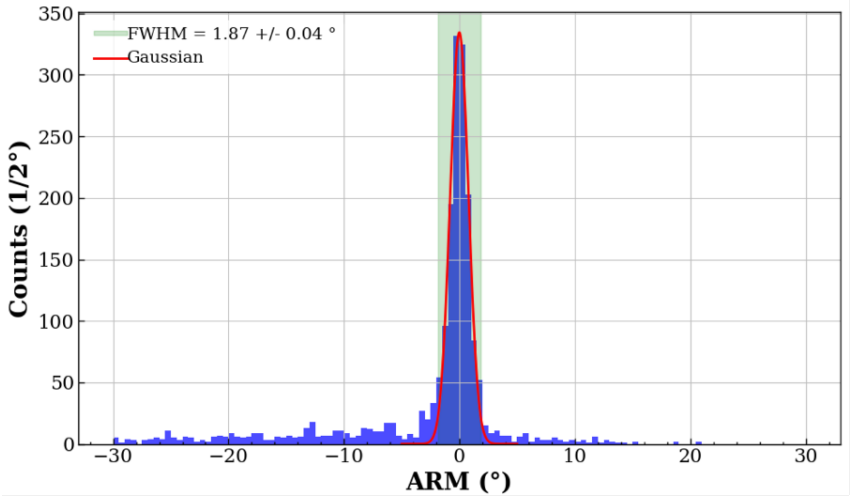

(a)

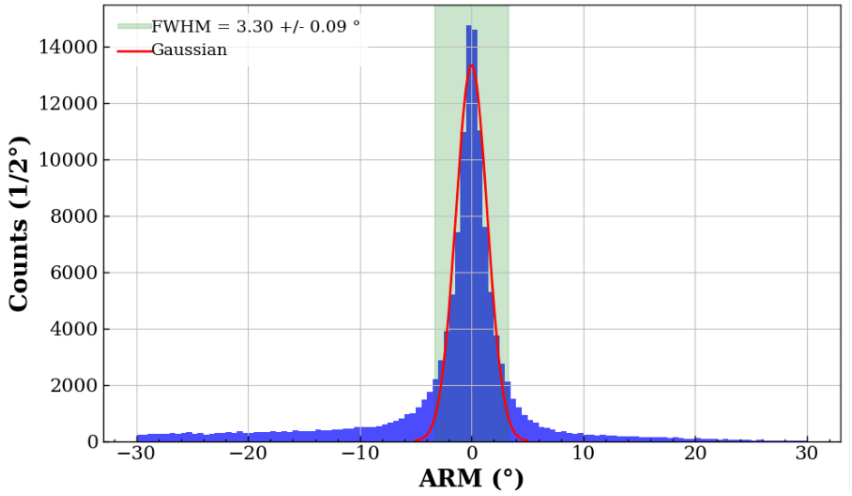

(b)

Figure 6.2.1: The ARM measurements simulated using a ^{137}Cs source placed 10 mm away from the centre of the detector face for each detector: (a) CC1, and (b) CC3. The measurements were taken with the scatterer and absorber modules placed as 0.1 mm away from one another.

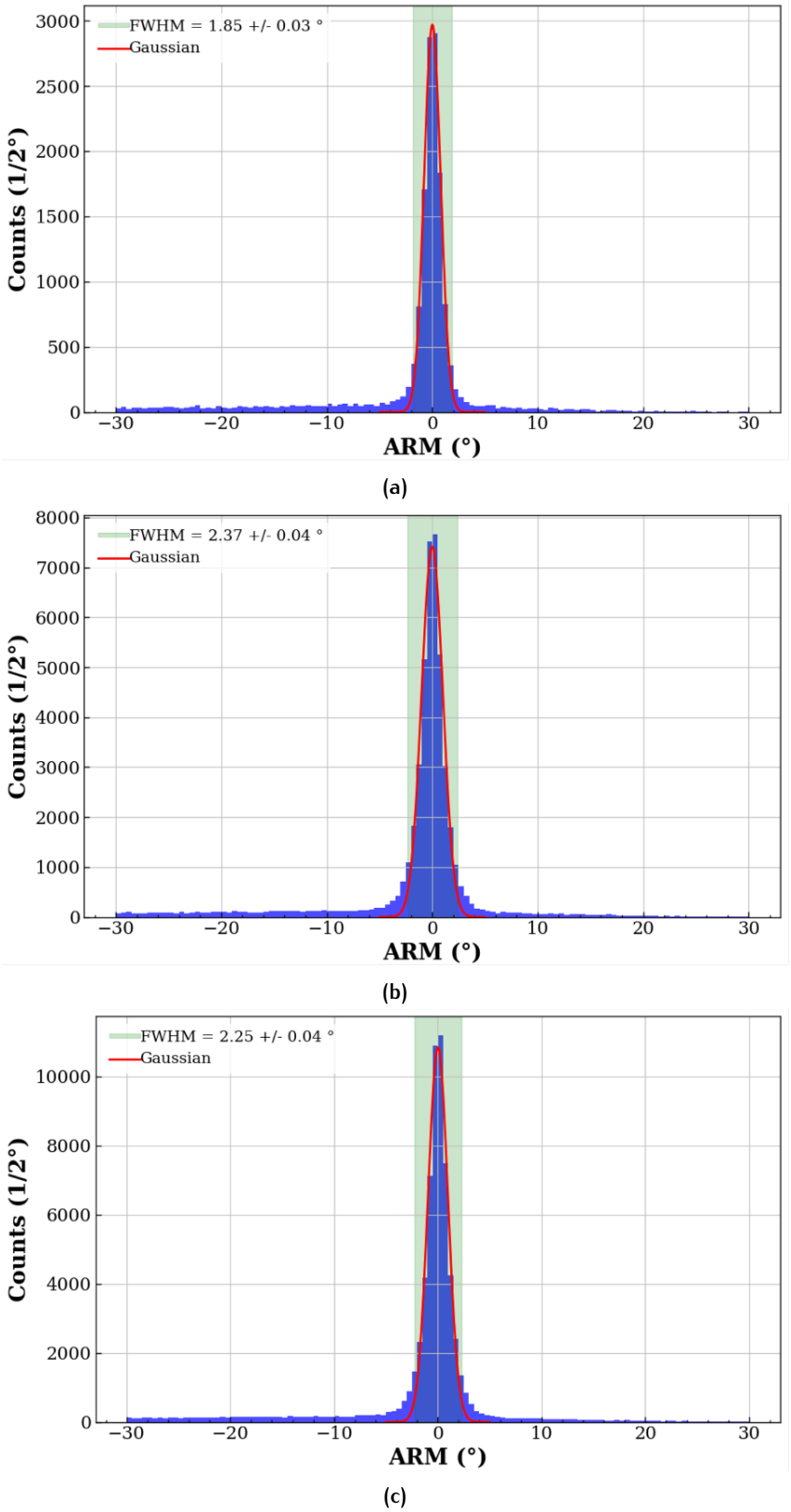

Figure 6.2.2: The ARM measurements simulated using a ^{137}Cs source placed 10 mm away from the centre of the detector face for the CC2 detector: (a) geometry 1, (b) geometry 2, and (c) geometry 3. The measurements were taken with the scatterer and absorber modules placed as 0.1 mm away from one another.

6.2.3 Influence of BSE on Image Reconstruction

Backscattering creates signals that mimic legitimate events, but they do not accurately represent the path of the original gamma ray. This misrepresentation introduces artefacts and noise in the final image, reducing sharpness and the overall ARM. To mitigate this issue, energy regions corresponding to high BSE must be excluded from analysis in experiments. This means applying energy thresholds to reject these events based on their energy deposition patterns.

In the case of a 661.7 keV gamma-ray source (^{137}Cs), simulations reveal that BSE in the scatterer were concentrated around a peak at 200.0 keV, as shown in Fig. 6.2.3 and Fig. 6.2.7 for the CC1 and CC3 geometries respectively. Figures 6.2.4, 6.2.5, and 6.2.6 show the energy distributions of the BSE for the CC2 design geometries 1, 2 and 3 respectively. Gamma rays depositing energy above this peak often undergo multiple Compton scatterings within one or both layers, which can obscure the original direction of the gamma ray. To counteract this, setting an energy threshold (e.g., excluding events with energy deposits above 170.0 keV in the scatterer) helps improve image quality by filtering out BSE and multi-scatter interactions that would otherwise introduce artefacts into the reconstructed image. These energy gate regions, established through simulations, ensure that the BSE photons, which degrade image resolution, were excluded, resulting in better experimental outcomes.

The BSE results for CC1 in Fig. 6.2.3 indicate that due to the greater distance between the scatterer and absorber layers, the impact of BSE was minimal. In this particular design, BSE show negligible contributions to image degradation, making energy gating unnecessary in practice. In contrast, the FSE and BSE energy distributions in CC3 and the CC2 geometries exhibit a significant contribution from BSE, as shown in the shaded green regions of each CC layer, within 3σ of the Gaussian peaks. These results highlight the importance of applying energy gates in the scatterer between $\sim$ 170.0–220.0 keV and 640.0–660.0 keV, and in the absorber layer between 440.0–500.0 keV, for a ^{137}Cs source. Implementing these energy gates in experiment would be an essential practise to maintain high image reconstruction quality by excluding BSE-related noise. In simulation, energy-gating on BSE is unnecessary because these events can be distinguished from CC events using the physics processes and other simulation parameters; however, in experimental data, where only energy, time, and position information are available, energy-gating on BSE is essential. However, since the results to follow are simulated results, energy-gating on BSE was not necessary but, rather, provide insight for future experiments.

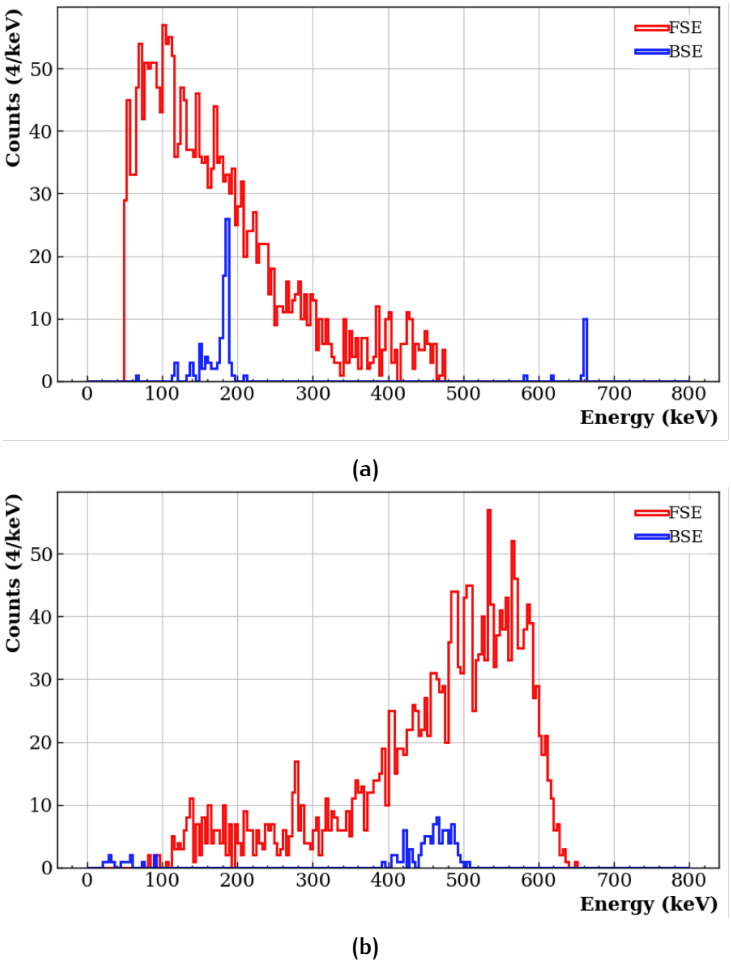

Figure 6.2.3: The simulated energy deposited in (a) the scatter layer, and (b) absorber layer of CC1 when gamma rays interact in both layers and deposit a total energy of 661.7 keV is shown. FSEs (red) and BSEs (blue) are displayed. Events correspond to single Compton scattering in each layer.

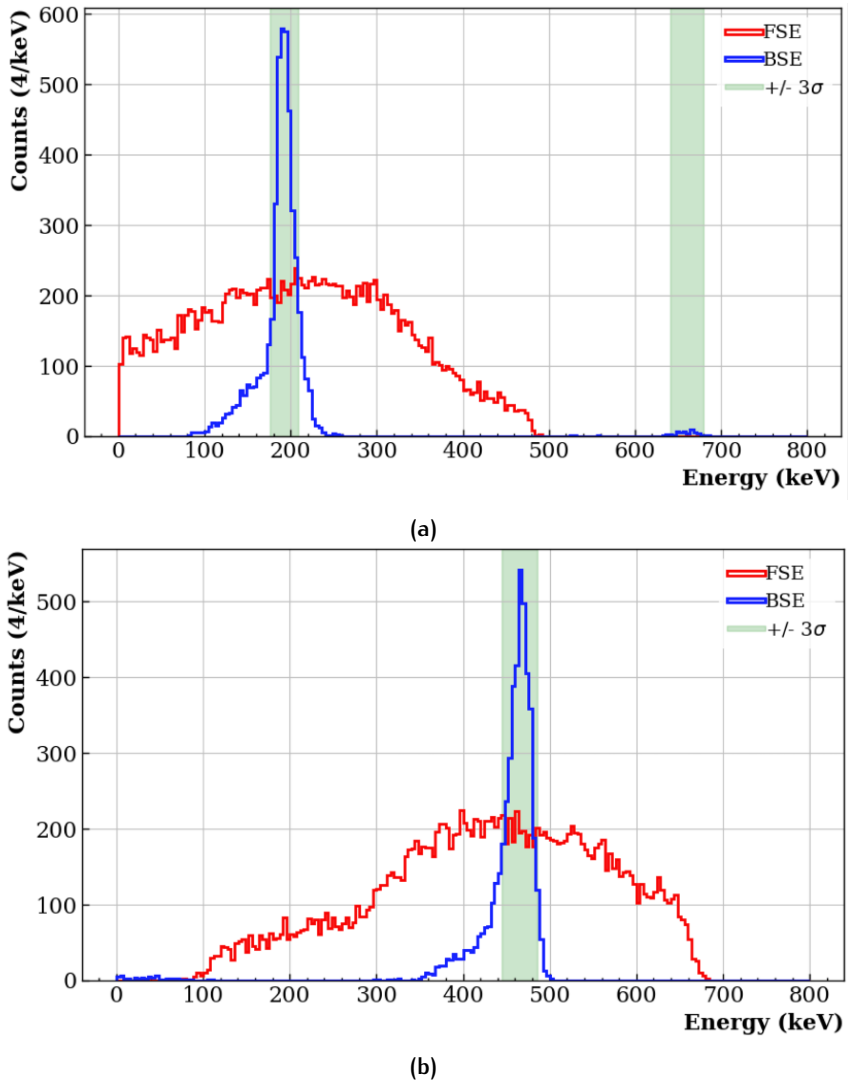

Figure 6.2.4: The simulated energy deposited in (a) the scatter layer, and (b) absorber layer of CC2 geometry 1 when gamma rays interact in both layers and deposit a total energy of 661.7 keV is shown. FSEs (red) and BSEs (blue) are displayed, and the regions of high BSE influence are shaded green. Events correspond to single Compton scattering in each layer.

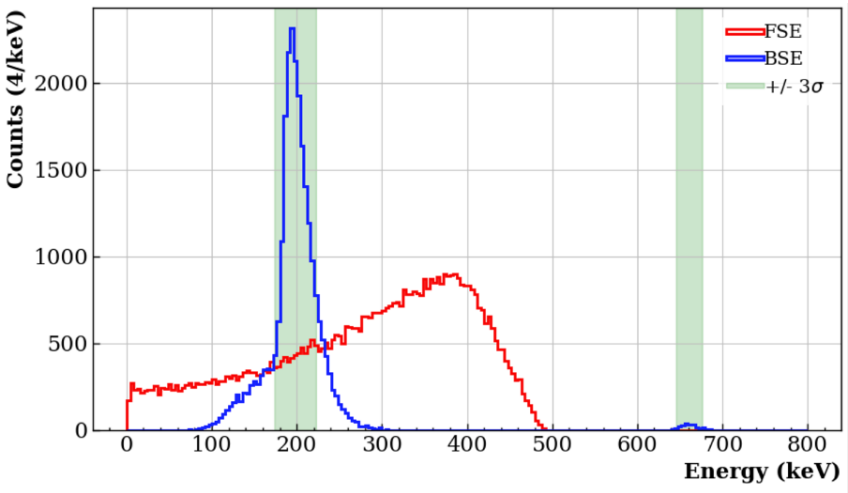

(a)

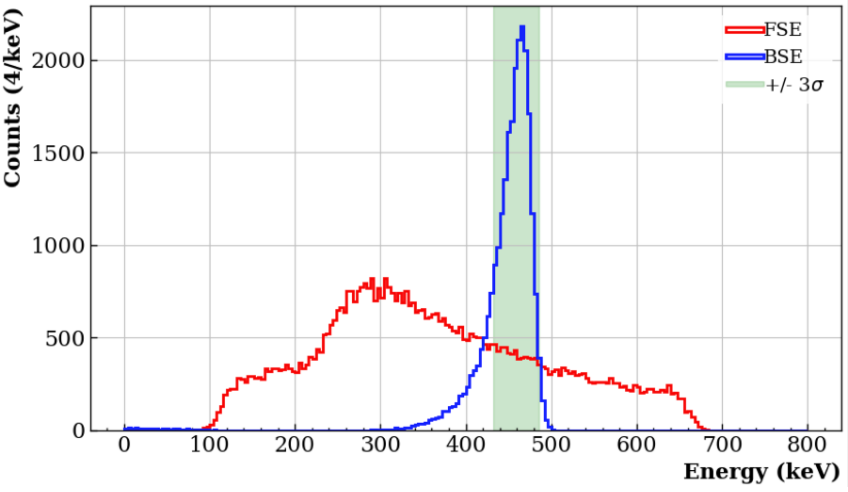

(b)

Figure 6.2.5: The simulated energy deposited in (a) the scatter layer, and (b) absorber layer of CC2 geometry 2 when gamma rays interact in both layers and deposit a total energy of 661.7 keV is shown. FSEs (red) and BSEs (blue) are displayed, and the regions of high BSE influence are shaded green. Events correspond to single Compton scattering in each layer.

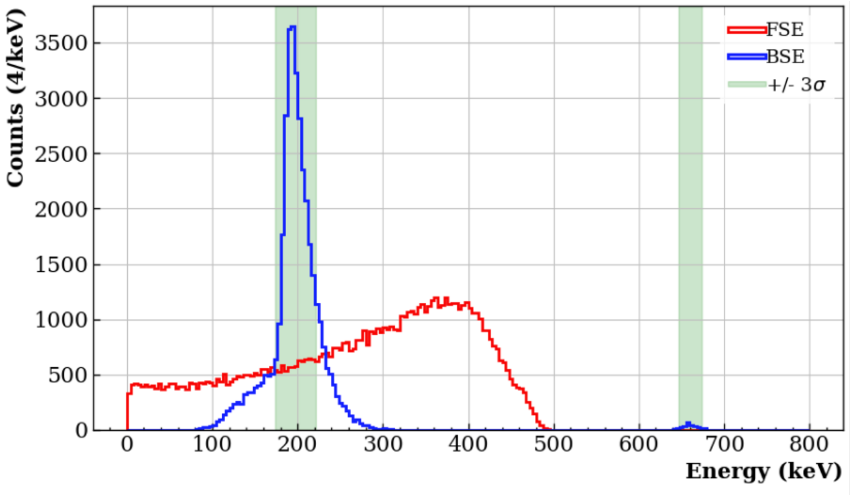

(a)

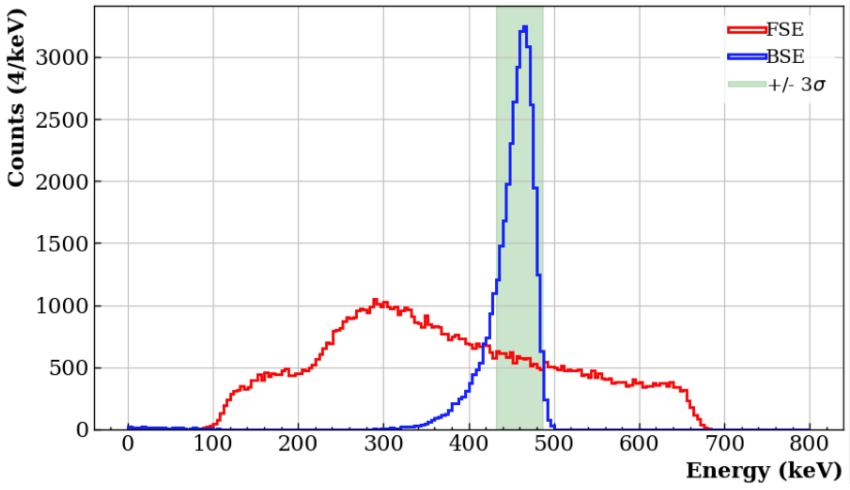

(b)

Figure 6.2.6: The simulated energy deposited in (a) the scatter layer, and (b) absorber layer of CC2 geometry 3 when gamma rays interact in both layers and deposit a total energy of 661.7 keV is shown. FSEs (red) and BSEs (blue) are displayed, and the regions of high BSE influence are shaded green. Events correspond to single Compton scattering in each layer.

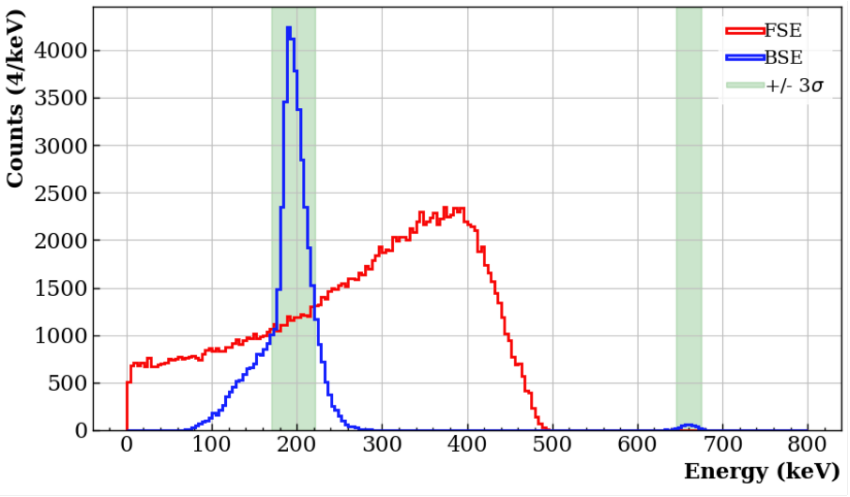

(a)

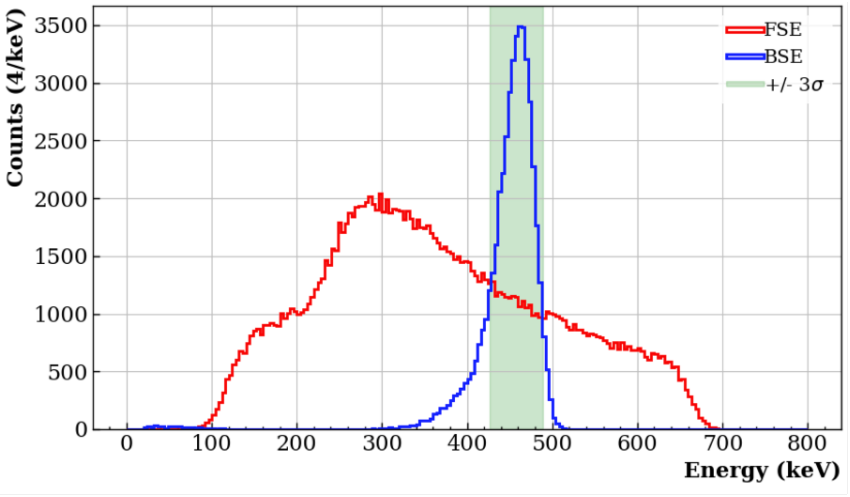

(b)

Figure 6.2.7: The simulated energy deposited in (a) the scatter layer, and (b) absorber layer of CC_3 when gamma rays interact in both layers and deposit a total energy of 661.7 keV is shown. FSEs (red) and BSEs (blue) are displayed, and the regions of high BSE influence are shaded green. Events correspond to single Compton scattering in each layer.

6.2.4 Image Reconstruction Comparison of ^{22}Na and ^{137}Cs Sources

Comparing the image reconstruction performance of a CC for different radioactive sources, such as ^{22}Na and ^{137}Cs, offers critical insights into the system's ability to handle varying photon energies and scattering scenarios. These two sources differ significantly in their gamma-ray emissions: ^{22}Na emits photons at 511.0 keV and 1274.5 keV, whereas ^{137}Cs primarily emits photons at 661.7 keV. These differences make them ideal candidates for evaluating the CCs performance across a spectrum of energies and assessing its capability to handle different image reconstruction challenges.

Higher-energy photons, such as the 1274.5 keV from ^{22}Na, tend to produce larger forward scatter angles, which can introduce image artefacts or blurring. This makes reconstructing accurate images more challenging, especially compared to the lower-energy photons of ^{137}Cs, which have less pronounced scattering angles. As such, the comparison helps in benchmarking the performance of the CC in terms of resolution, FEPE, and overall accuracy across varying energies.

In the results presented, Fig. 6.2.8 shows the results for ^{22}Na, and Fig. 6.2.9 shows the reconstruction for ^{137}Cs for CC1. Figures 6.2.10, 6.2.12 and 6.2.14 show the results of ^{22}Na source for CC2 geometries 1, 2 and 3 respectively. Figures 6.2.11, 6.2.13 and 6.2.15 show the results of ^{137}Cs source for CC2 geometries 1, 2 and 3 respectively. The single source measurements for ^{22}Na and ^{137}Cs are shown for CC3 in Figs. 6.2.16 and 6.2.17, respectively. The results shown in these figures demonstrate a consistent pattern across the CC systems: the image resolution (represented by the FWHM of the Gaussian fit) tends to be better for ^{137}Cs compared to ^{22}Na.

For example, in Fig. 6.2.9, the FWHM for ^{137}Cs was approximately 1 mm smaller than that of ^{22}Na in Fig 6.2.8. This was because ^{137}Cs only has a single prominent energy peak at 661.7 keV, simplifying the reconstruction process. In contrast, ^{22}Na, with two distinct energy peaks (511.0 keV and 1274.5 keV), adds complexity to the reconstruction, as the system must differentiate between these overlapping photons.

The performance of the different Compton camera designs is summarised in Table 6.2.5. While it was initially anticipated that CC1, with its Polaris detector, might perform worse due to geometric constraints, the superior energy resolution and high material density of CZT helped to mitigate these limitations. However, CC1 suffers from significantly fewer detected statistics compared to CC2 and CC3 designs, attributed to its geometry, which impacts its overall performance. In summary, the comparison of these two sources illustrates that ^{137}Cs generally provides better image reconstruction results due to its single energy peak. Meanwhile, the presence of multiple energies in ^{22}Na introduces additional challenges for the CC, leading to a slight reduction in image quality. CC2 geometry 1 achieved the best reconstruction ability with a FWHM of 3.36(1) mm for a ^{137}Cs source placed at (0,0,10) mm from the CC scatterer face.

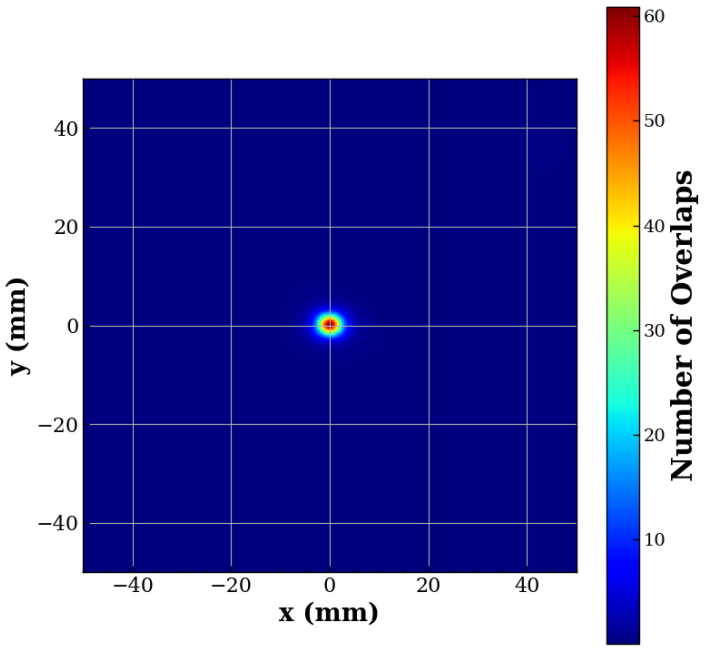

(a)

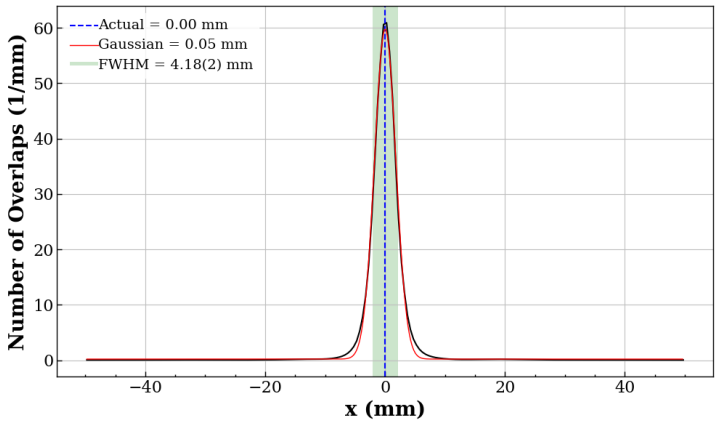

(b)

Figure 6.2.8: Reconstructed images of CC1 for the simulated gamma emission of a ^{22}Na source. The source was placed at (0,0,10) mm from the CC scatterer face, where (a) shows the x-y image slice at the maximum z intensity, and (b) shows the x profile of the distribution, where the dotted blue line represents the actual source location. The distribution was fitted with a Gaussian function (red), and the FWHM of the Gaussian is seen shaded in green and labelled with uncertainty.

CC Design	FWHM (mm), ^{137}Cs	FWHM (mm), ^{22}Na
CC1	3.20(1)	4.18(2)
CC2 Geometry 1	3.36(1)	4.04(1)
CC2 Geometry 2	3.51(1)	4.15(1)
CC2 Geometry 3	3.43(1)	4.26(1)
CC3	3.71(1)	3.71(1)

Table 6.2.5: Table showing the performance comparison of CC designs for a ^{137}Cs source placed at (0,0,10) mm from the CC scatterer face.

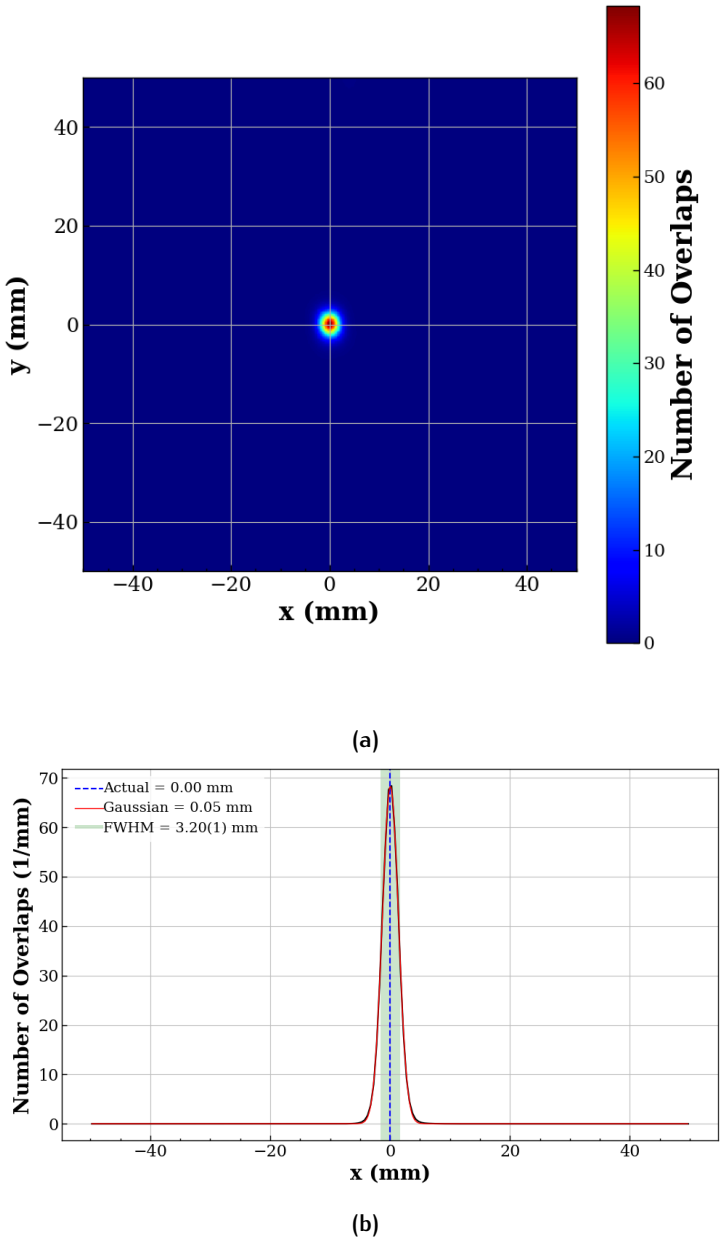

Figure 6.2.9: Reconstructed images of CC1 for the simulated gamma emission of a ^{137}Cs source. The source was placed at (0,0,10) mm from the CC scatterer face, where (a) shows the x-y image slice at the maximum z intensity, and (b) shows the x profile of the distribution, where the dotted blue line represents the actual source location. The distribution was fitted with a Gaussian function (red), and the FWHM of the Gaussian is seen shaded in green and labelled with uncertainty.

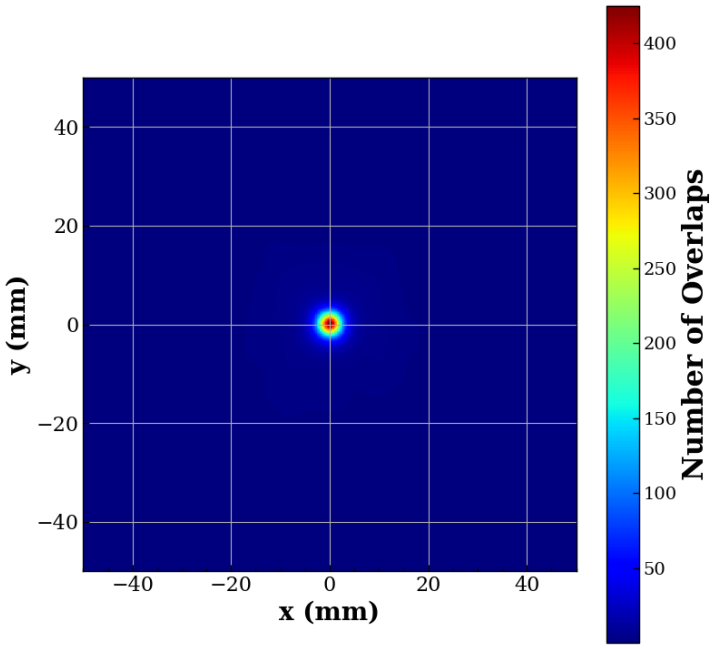

(a)

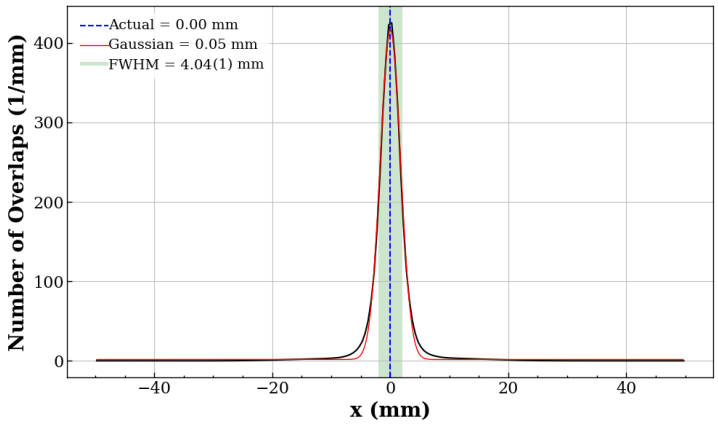

(b)

Figure 6.2.10: Reconstructed images of CC2 geometry 1 for the simulated gamma emission of a ^{22}Na source. The source was placed at (0,0,10) mm from the CC scatterer face, where (a) shows the x-y image slice at the maximum z intensity, and (b) shows the x profile of the distribution, where the dotted blue line represents the actual source location. The distribution was fitted with a Gaussian function (red), and the FWHM of the Gaussian is seen shaded in green and labelled with uncertainty.

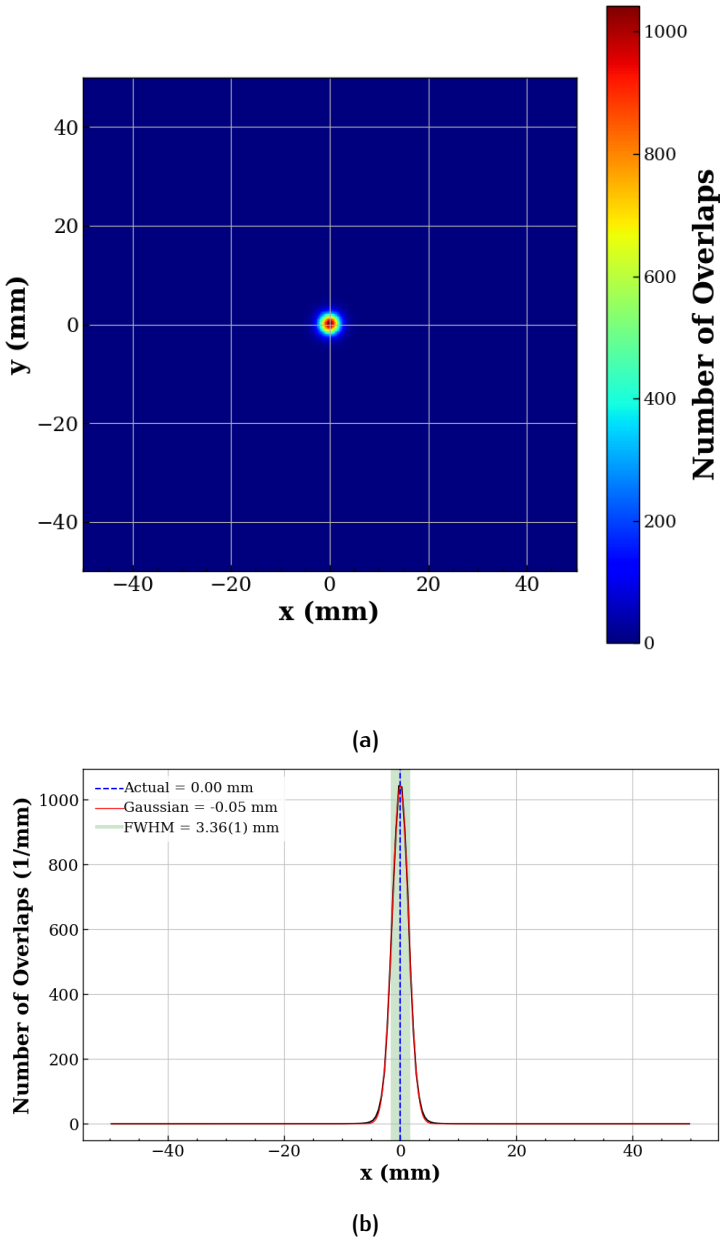

Figure 6.2.11: Reconstructed images of CC2 geometry 1 for the simulated gamma emission of a ^{137}Cs source. The source was placed at (0,0,10) mm from the CC scatterer face, where (a) shows the x-y image slice at the maximum z intensity, and (b) shows the x profile of the distribution, where the dotted blue line represents the actual source location. The distribution was fitted with a Gaussian function (red), and the FWHM of the Gaussian is seen shaded in green and labelled with uncertainty.

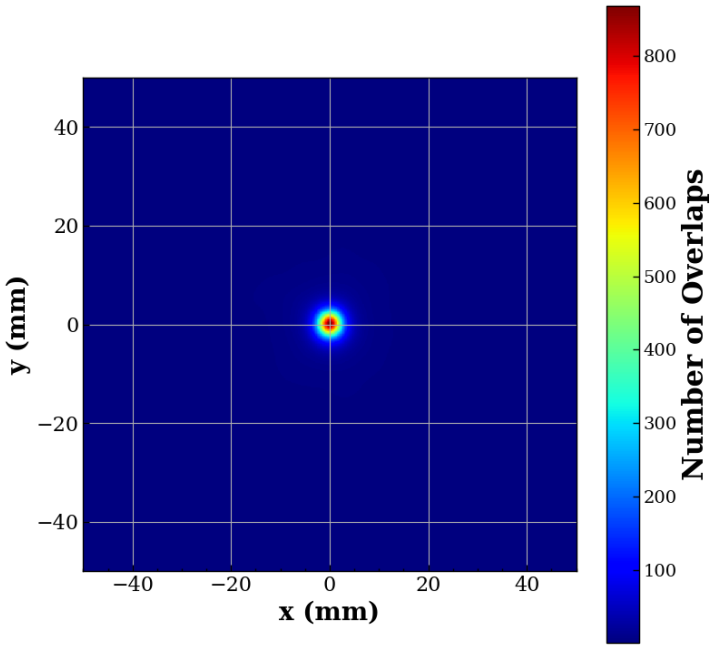

(a)

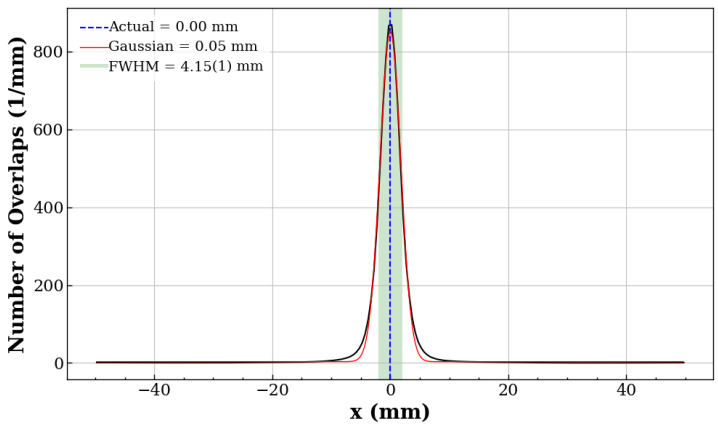

(b)

Figure 6.2.12: Reconstructed images of CC2 geometry 2 for the simulated gamma emission of a ^{22}Na source. The source was placed at (0,0,10) mm from the CC scatterer face, where (a) shows the x-y image slice at the maximum z intensity, and (b) shows the x profile of the distribution, where the dotted blue line represents the actual source location. The distribution was fitted with a Gaussian function (red), and the FWHM of the Gaussian is seen shaded in green and labelled with uncertainty.

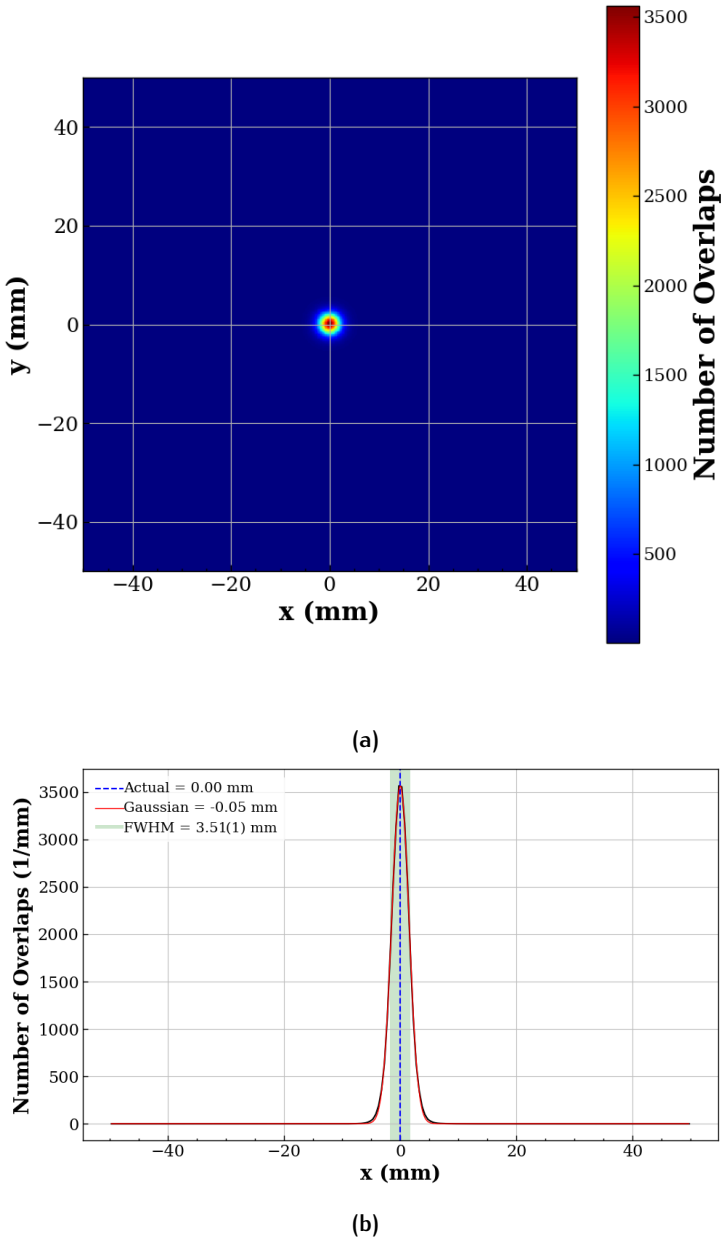

Figure 6.2.13: Reconstructed images of CC2 geometry 2 for the simulated gamma emission of a ^{137}Cs source. The source was placed at (0,0,10) mm from the CC scatterer face, where (a) shows the x-y image slice at the maximum z intensity, and (b) shows the x profile of the distribution, where the dotted blue line represents the actual source location. The distribution was fitted with a Gaussian function (red), and the FWHM of the Gaussian is seen shaded in green and labelled with uncertainty.

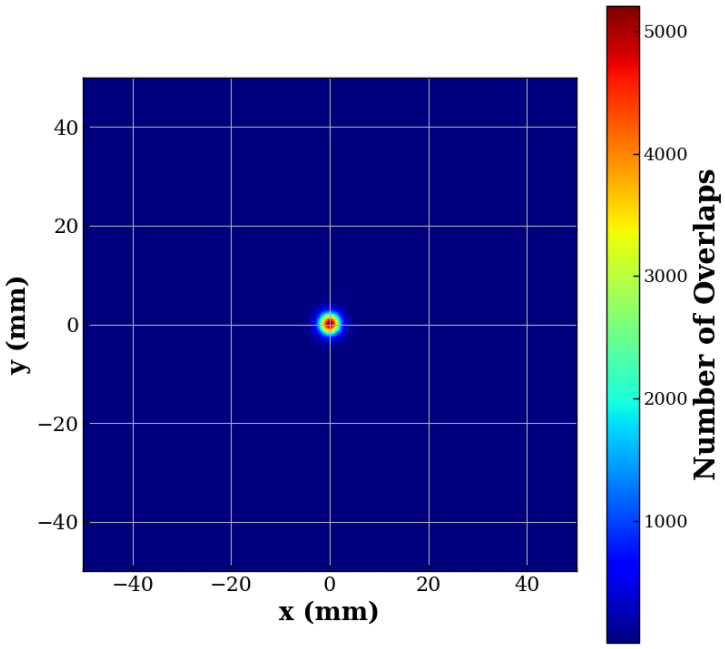

(a)

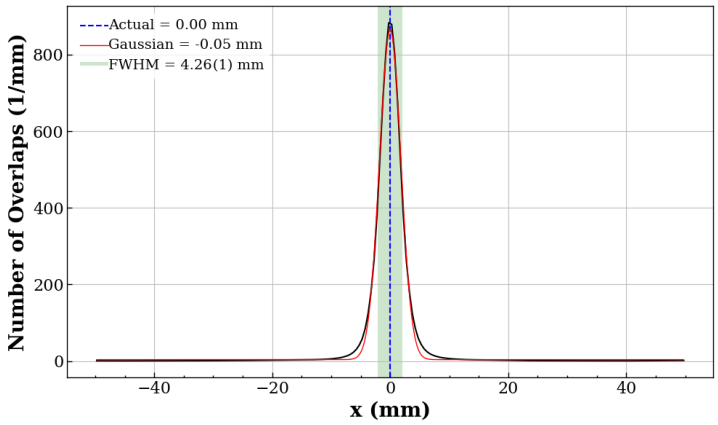

(b)

Figure 6.2.14: Reconstructed images of CC2 geometry 3 for the simulated gamma emission of a ^{22}Na source. The source was placed at (0,0,10) mm from the CC scatterer face, where (a) shows the x-y image slice at the maximum z intensity, and (b) shows the x profile of the distribution, where the dotted blue line represents the actual source location. The distribution was fitted with a Gaussian function (red), and the FWHM of the Gaussian is seen shaded in green and labelled with uncertainty.

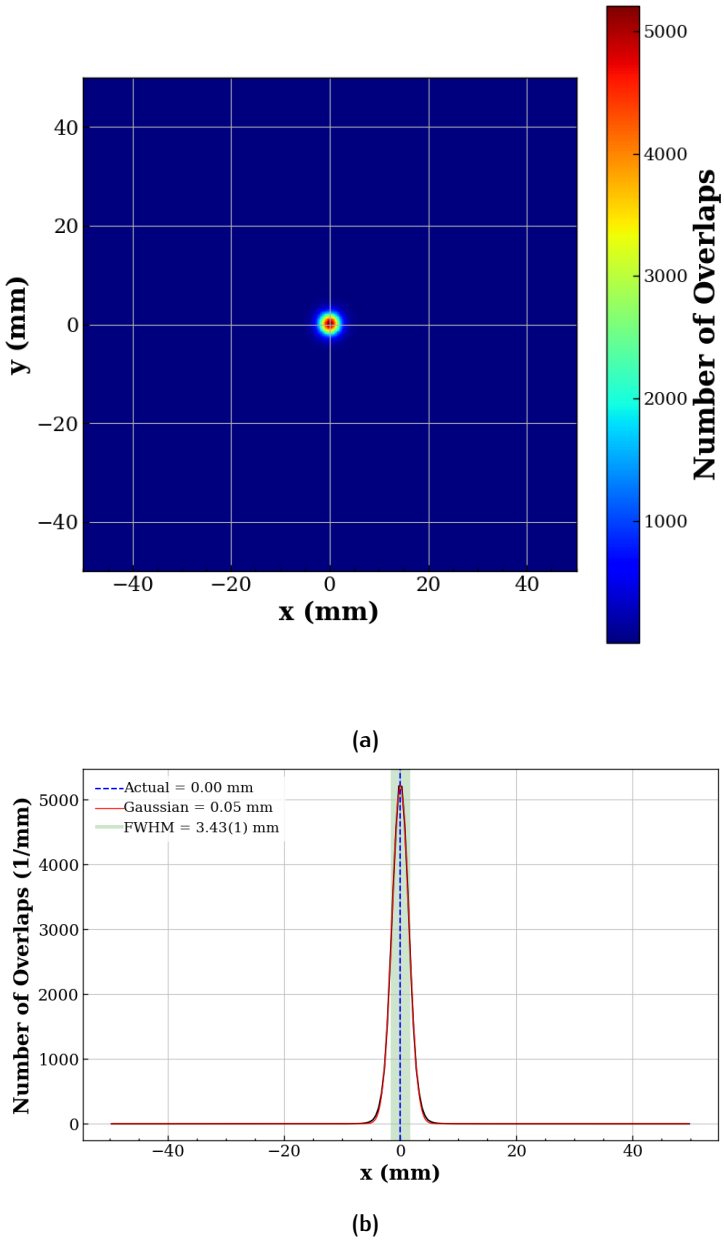

Figure 6.2.15: Reconstructed images of CC2 geometry 3 for the simulated gamma emission of a ^{137}Cs source. The source was placed at (0,0,10) mm from the CC scatterer face, where (a) shows the x-y image slice at the maximum z intensity, and (b) shows the x profile of the distribution, where the dotted blue line represents the actual source location. The distribution was fitted with a Gaussian function (red), and the FWHM of the Gaussian is seen shaded in green and labelled with uncertainty.

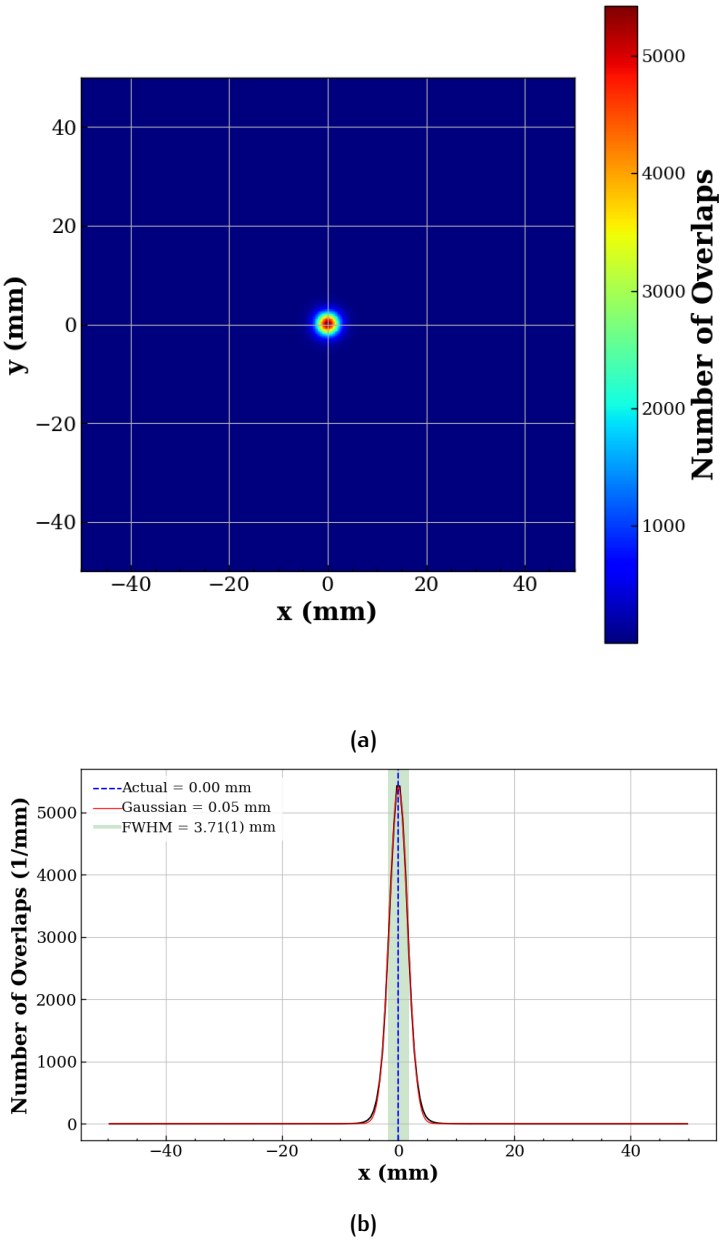

Figure 6.2.16: Reconstructed images of CC_3 for the simulated gamma emission of a ^{22}Na source. The source was placed at (0,0,10) mm from the CC scatterer face, where (a) shows the x-y image slice at the maximum z intensity, and (b) shows the x profile of the distribution, where the dotted blue line represents the actual source location. The distribution was fitted with a Gaussian function (red), and the FWHM of the Gaussian is seen shaded in green and labelled with uncertainty.

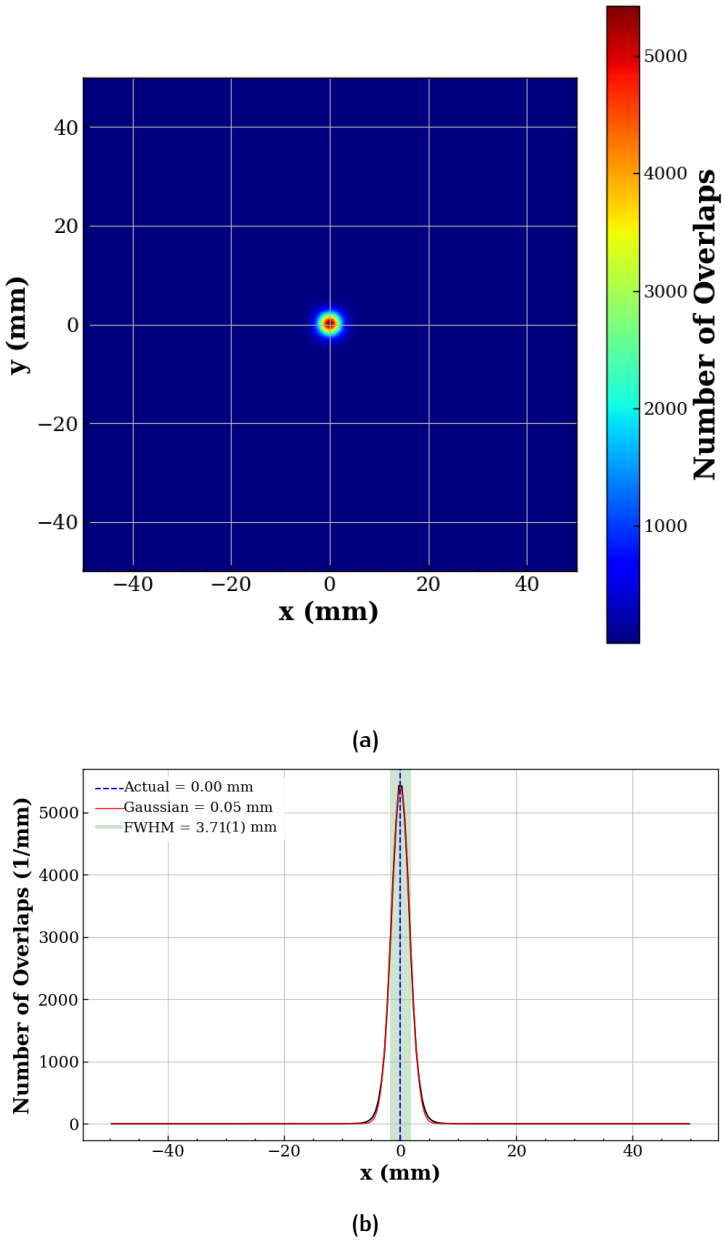

Figure 6.2.17: Reconstructed images of CC3 for the simulated gamma emission of a ^{137}Cs source. The source was placed at (0,0,10) mm from the CC scatterer face, where (a) shows the x-y image slice at the maximum z intensity, and (b) shows the x profile of the distribution, where the dotted blue line represents the actual source location. The distribution was fitted with a Gaussian function (red), and the FWHM of the Gaussian is seen shaded in green and labelled with uncertainty.

6.2.5 Image Reconstruction for Increased Source to Scatterer Distance

As the distance between the source and scatterer increases, the scattered photons spread out more before reaching the absorber. This spreading results in a broader and less distinct image, diminishing the spatial resolution and making the reconstructed image less clear. With a greater source-to-scatterer distance, fewer photons reach the scatterer due to the inverse-square law, which describes how FEPE decreases with distance. This reduction in photon flux leads to lower statistics and a poorer signal-to-noise ratio, further degrading image quality and increasing uncertainty in the reconstruction. As the distance increases, the number of detected photons may decrease, increasing the noise level relative to the signal, a factor that would need to be taken into account in experiment. This can further obscure details in the reconstructed image and make it more challenging to differentiate between signal and background noise.

To illustrate this, the CC image reconstruction performance was investigated for a ^{137}Cs source positioned at (0,0,100) mm from the scatterer face. This setup was compared with results from a source placed only (0,0,10) mm away, as detailed in Section 6.2.4, for which the results are seen in Table 6.2.6. Figure 6.2.18 presents the x-y reconstructed image matrix for CC1, along with the x profile extracted at maximum y-z intensity below. Due to the 88 mm separation between the CC layer crystals in CC1, increasing the distance to the detector led to notably low Compton cone statistics (<2 overlaps) and poor source localisation. The predicted source position was offset by 30.13 mm from the true location, with a FWHM of 3.35(59) mm. For CC3, the increase in source distance resulted in a 1 mm increase in the FWHM of the image reconstruction, as shown in Fig. 6.2.22. However, the source was still predicted to be at the correct position. Among CC2 designs, CC2 geometry 1 exhibited the least sensitivity to the increased distance, as illustrated in Fig. 6.2.19 when compared to Figs. 6.2.20 and 6.2.21. At the further distance, the FWHM remained below 4 mm, demonstrating its robustness to changes in source-to-scatterer distance. Each of the CC2 geometries performed well at an increased distance.

	FWHM (mm)	
CC Design	**(0,0,10) mm**	**(0,0,100) mm**
CC1	3.20(1)	3.35(59)
CC2 Geometry 1	3.36(1)	3.91(2)
CC2 Geometry 2	3.51(1)	4.27(1)
CC2 Geometry 3	3.43(1)	4.56(1)
CC3	3.71(1)	4.70(2)

Table 6.2.6: Table of the effect of increasing the source-to-scatterer distance for a ^{137}Cs source for each CC design.

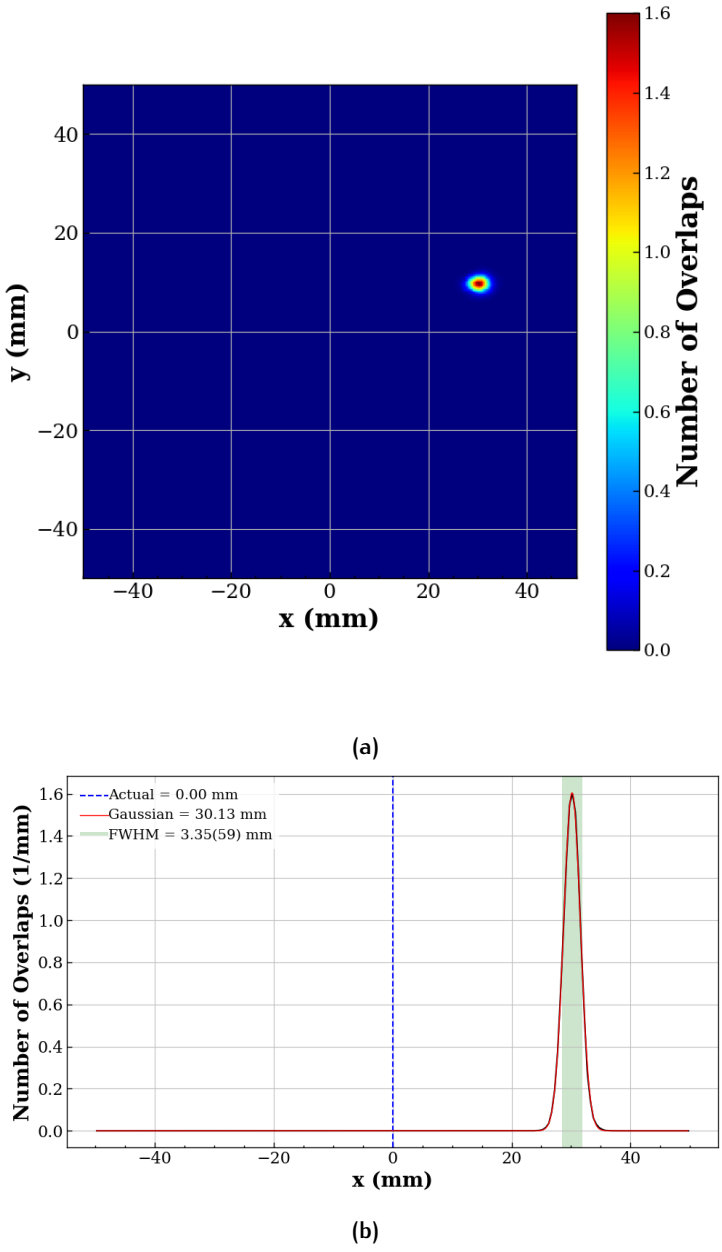

Figure 6.2.18: Reconstructed images of the simulated gamma emission of ^{137}Cs for CC1. The source was placed at (0,0,100) mm from the CC scatterer face, and the distance between the scatterer and absorber modules was <1 mm, where (a) shows the x-y image slice at the maximum z intensity, and (b) shows the x profile of the distribution, where the dotted blue line represents the actual source location. The distribution was fitted with a Gaussian function (red), and the FWHM of the Gaussian is seen shaded in green and labelled with uncertainty.

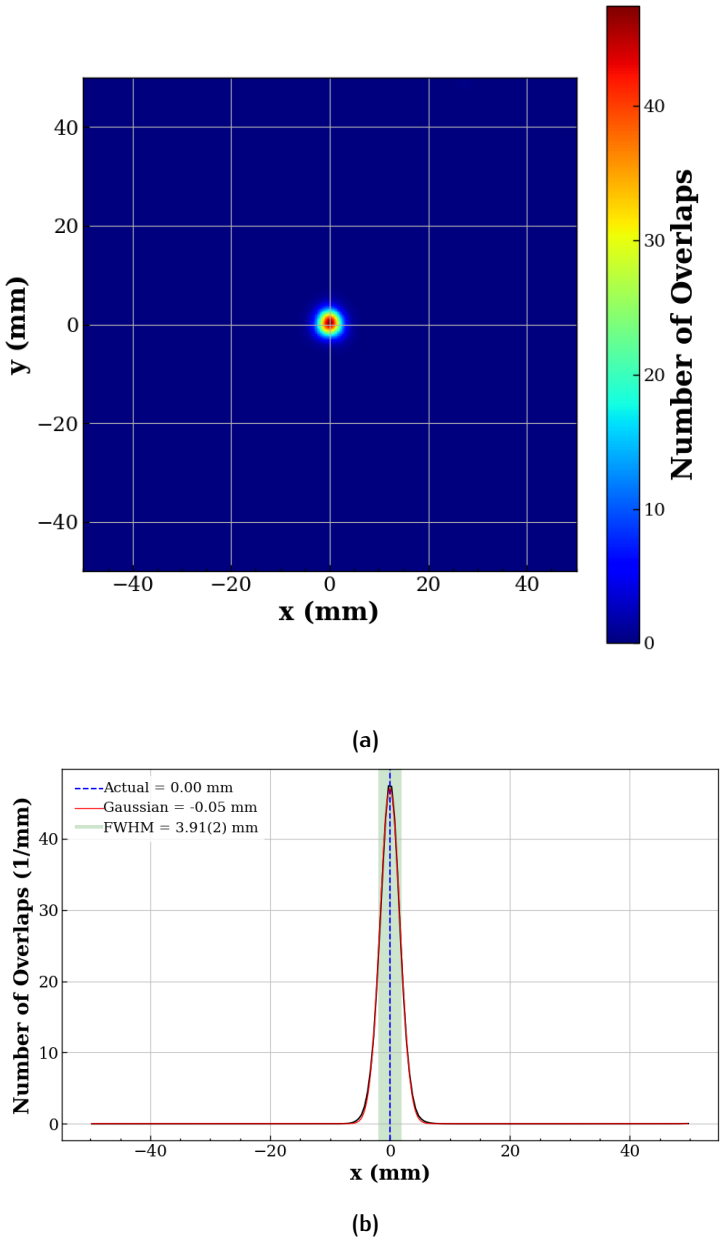

Figure 6.2.19: Reconstructed images of the simulated gamma emission of ^{137}Cs of CC2 geometry 1. The source was placed at (0,0,100) mm from the CC scatterer face, and the distance between the scatterer and absorber modules was <1 mm, where (a) shows the x-y image slice at the maximum z intensity, and (b) shows the x profile of the distribution, where the dotted blue line represents the actual source location. The distribution was fitted with a Gaussian function (red), and the FWHM of the Gaussian is seen shaded in green and labelled with uncertainty.

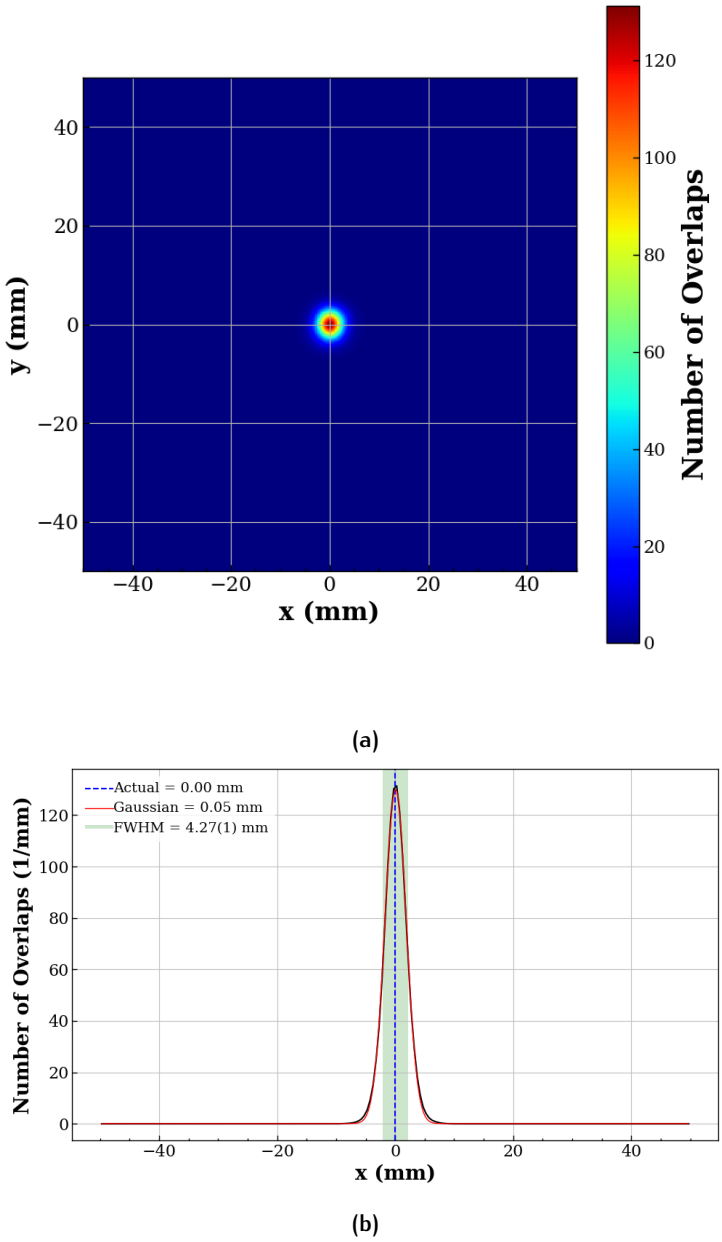

Figure 6.2.20: Reconstructed images of the simulated gamma emission of ^{137}Cs of CC2 geometry 2. The source was placed at (0,0,100) mm from the CC scatterer face, and the distance between the scatterer and absorber modules was <1 mm, where (a) shows the x-y image slice at the maximum z intensity, and (b) shows the x profile of the distribution, where the dotted blue line represents the actual source location. The distribution was fitted with a Gaussian function (red), and the FWHM of the Gaussian is seen shaded in green and labelled with uncertainty.

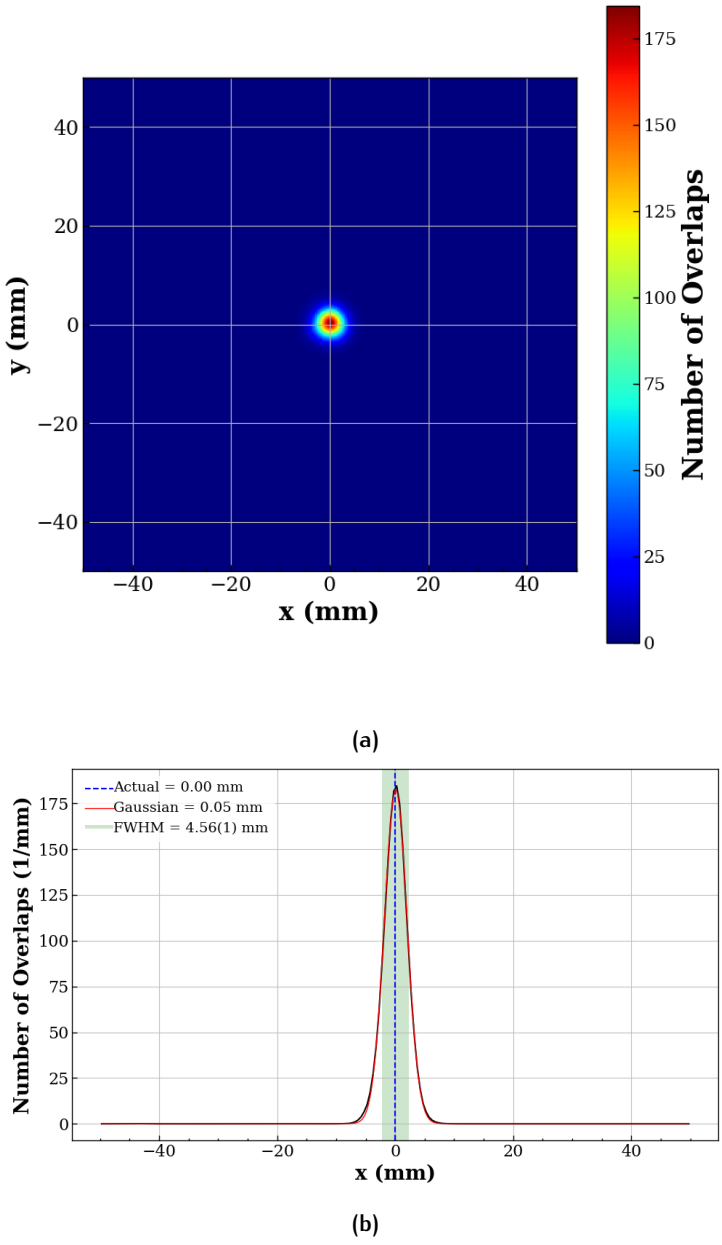

Figure 6.2.21: Reconstructed images of the simulated gamma emission of ^{137}Cs of CC2 geometry 3. The source was placed at (0,0,100) mm from the CC scatterer face, and the distance between the scatterer and absorber modules was <1 mm, where (a) shows the x-y image slice at the maximum z intensity, and (b) shows the x profile of the distribution, where the dotted blue line represents the actual source location. The distribution was fitted with a Gaussian function (red), and the FWHM of the Gaussian is seen shaded in green and labelled with uncertainty.

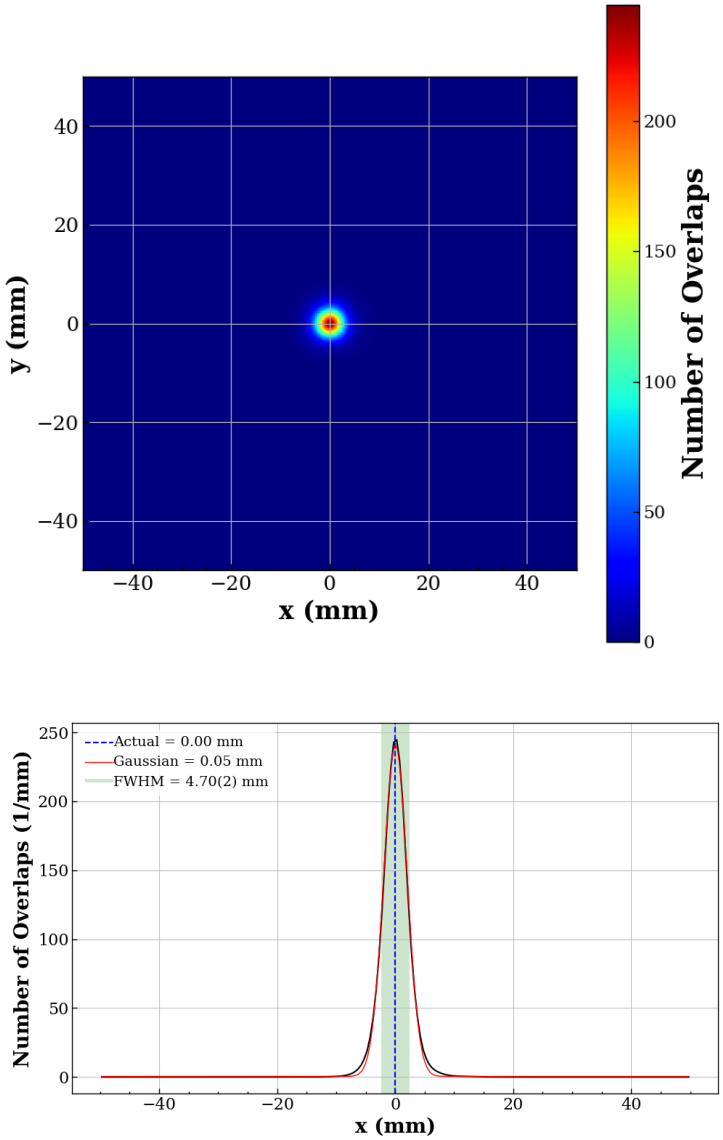

(a)

Figure 6.2.22: Reconstructed images of the simulated gamma emission of ^{137}Cs for CC3. The source was placed at (0,0,100) mm from the CC scatterer face, and the distance between the scatterer and absorber modules was <1 mm, where (a) shows the x-y image slice at the maximum z intensity, and (b) shows the x profile of the distribution, where the dotted blue line represents the actual source location. The distribution was fitted with a Gaussian function (red), and the FWHM of the Gaussian is seen shaded in green and labelled with uncertainty.

6.2.6 Image Reconstruction for Increased Scatterer to Absorber Distance

Increasing the distance between the scatterer and absorber in a CC can have a profound impact on image reconstruction quality. As scattered photons travel further to reach the absorber, they spread out over a larger area, leading to a broader and less distinct spatial resolution. This can introduce more noise into the system and complicate the FBP process, which relies on precise measurements of photon interactions to reconstruct accurate images. Typically, a larger scatterer-to-absorber distance can introduce geometric distortions, making it more challenging to produce high-resolution images.

The gamma emission from a ^{137}Cs source was simulated 10 mm away from the scatterer face. For CC1, seen in Fig. 6.2.23, the resulting image showed significant distortion, with the source reconstructed at (-48.8, -48.75) mm in the x-y plane instead of its true location at the origin position (0,0,0). Given that the scatterer and absorber were already 88 mm apart, this resulted in a total evaluation distance of 188 mm, leading to a significant source localisation uncertainty of ~ 50 mm. Such large deviations illustrate how increasing the distance between the camera components can cause degradation in image quality, particularly when the source was farther from the scatterer. Since the scatterer-absorber distance of CC1 was 88 mm to begin with, the results of Fig. 6.2.9 for a ^{137}Cs source at (0,0,10) mm from the scatterer face, and the nearest geometrical scatterer-absorber distance of 88 mm, can be compared to the results for the other CC systems as the 88 mm is more comparable to 10 mm than the 188 mm measurement above. For this measurement, the source was located 0.05 mm from its true position, with a FWHM of 3.20(1) mm.

The analysis of other systems, CC3 (Fig. 6.2.27) and CC2 (Fig. 6.2.24, 6.2.25, 6.2.26 for geometries 1, 2, and 3 respectively), revealed a trend, as listed in Table 6.2.7. Increasing the scatterer-to-absorber distance by 10 mm led to a slight improvement in image resolution across multiple configurations. For instance, in CC3 Fig. 6.2.27, the x-projection FWHM improved from 3.71(1) mm to 3.61(2) mm, and in CC2 geometry 1, the FWHM improved from 3.36(1) mm to 3.33(1) mm. Similarly, CC2 geometry 2 showed a slight improvement from 3.51(1) mm to 3.39(1) mm. These subtle gains in resolution, despite the increased distance, suggest that certain geometrical configurations can counterbalance the negative effects typically associated with increased distances.

One possible explanation for this improvement could be the reduction of edge effects and better delineation of the Compton cone projection. As the distance increases, the scattered photons may experience less interference from edge effects, allowing for more accurate projections onto the image plane. Additionally, the increased separation between scatterer and absorber may improve the system's ability to differentiate between photon interactions, leading to a clearer and more precise image reconstruction. Ultimately, while increasing the scatterer-to-absorber distance can introduce some challenges, such as reduced photon statistics and higher noise levels, the results demonstrate that careful optimisation of this distance can lead to improvements in image resolution, as seen in the comparison shown in Table 6.2.7. This finding underscores the importance of balancing geometry and photon dynamics to enhance the performance of CCs in experimental imaging.

	FWHM (mm)	
CC Design	**(0,0,0.1) mm**	**(0,0,10) mm**
CC1	3.20(1)	3.44(2)
CC2 Geometry 1	3.36(1)	3.33(1)
CC2 Geometry 2	3.51(1)	3.39(1)
CC2 Geometry 3	3.46(2)	3.49(1)
CC3	3.71(1)	3.61(2)

Table 6.2.7: Table of the effect of increasing the scatterer-absorber distance of the CC designs for a ^{137}Cs source placed at (0,0,10) mm from the CC scatterer face.

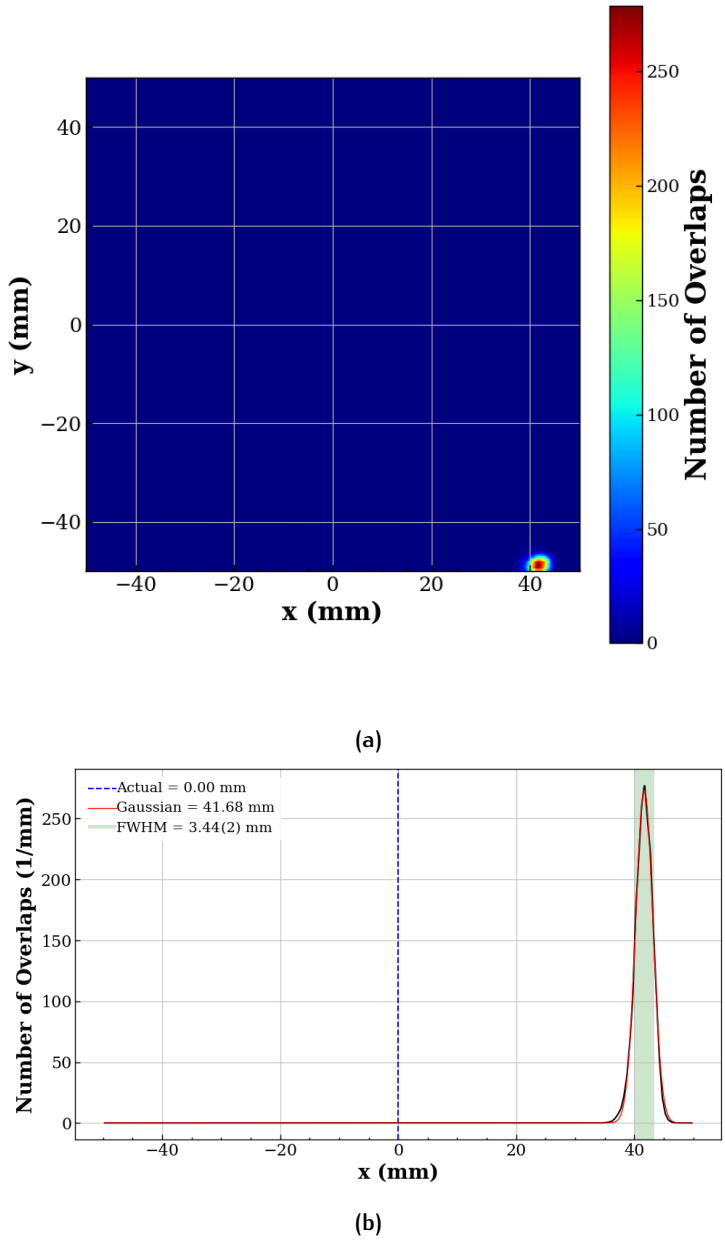

Figure 6.2.23: Reconstructed images of the simulated gamma emission of ^{137}Cs for CC1. The source was placed at (0,0,10) mm from the CC scatterer face, and the distance between the scatterer and absorber modules was 10 mm, where (a) shows the x-y image slice at the maximum z intensity, and (b) shows the x profile of the distribution, where the dotted blue line represents the actual source location. The distribution was fitted with a Gaussian function (red), and the FWHM of the Gaussian is seen shaded in green and labelled with uncertainty.

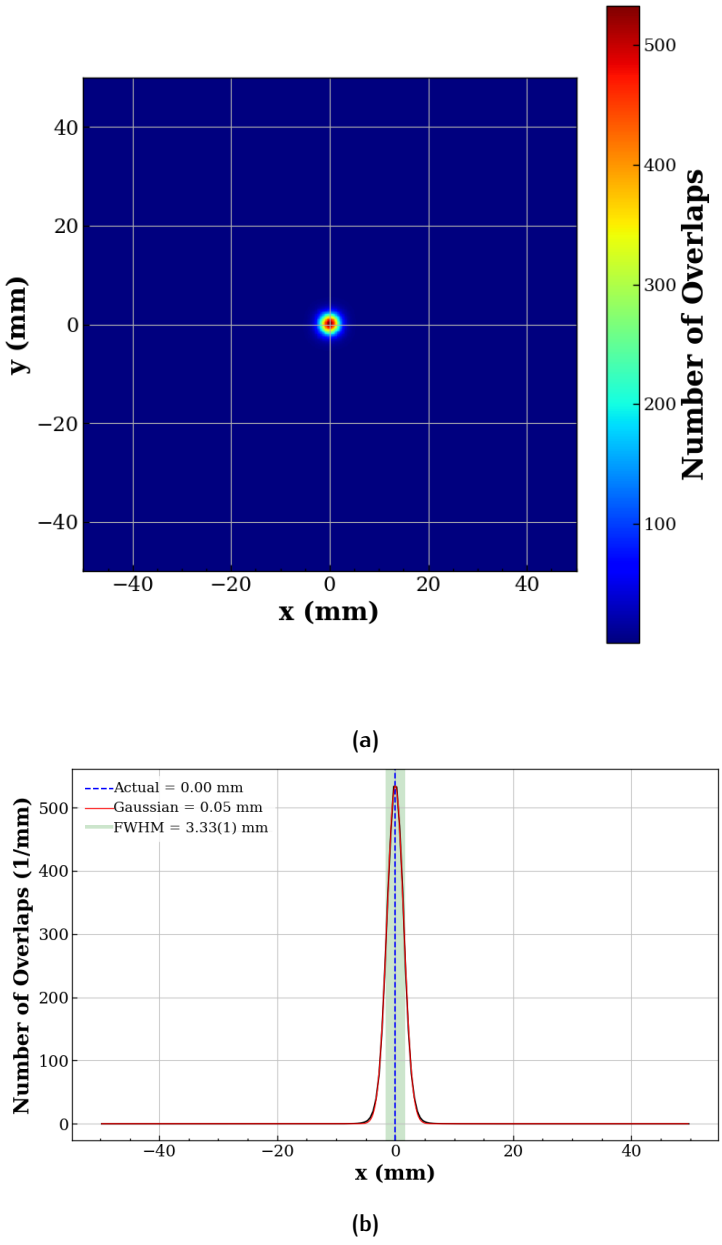

Figure 6.2.24: Reconstructed images of the simulated gamma emission of ^{137}Cs of CC2 geometry 1. The source was placed at (0,0,10) mm from the CC scatterer face, and the distance between the scatterer and absorber modules was 10 mm, where (a) shows the x-y image slice at the maximum z intensity, and (b) shows the x profile of the distribution, where the dotted blue line represents the actual source location. The distribution was fitted with a Gaussian function (red), and the FWHM of the Gaussian is seen shaded in green and labelled with uncertainty.

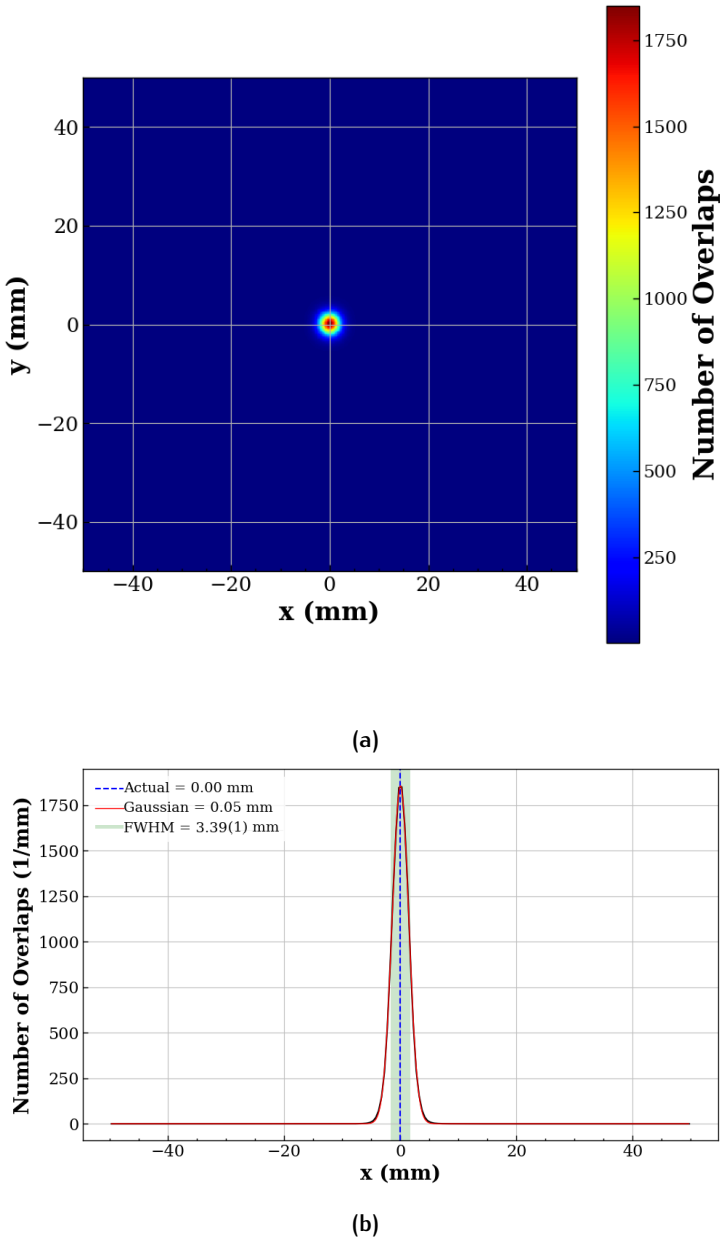

Figure 6.2.25: Reconstructed images of the simulated gamma emission of ^{137}Cs of CC2 geometry 2. The source was placed at (0,0,10) mm from the CC scatterer face, and the distance between the scatterer and absorber modules was 10 mm, where (a) shows the x-y image slice at the maximum z intensity, and (b) shows the x profile of the distribution, where the dotted blue line represents the actual source location. The distribution was fitted with a Gaussian function (red), and the FWHM of the Gaussian is seen shaded in green and labelled with uncertainty.

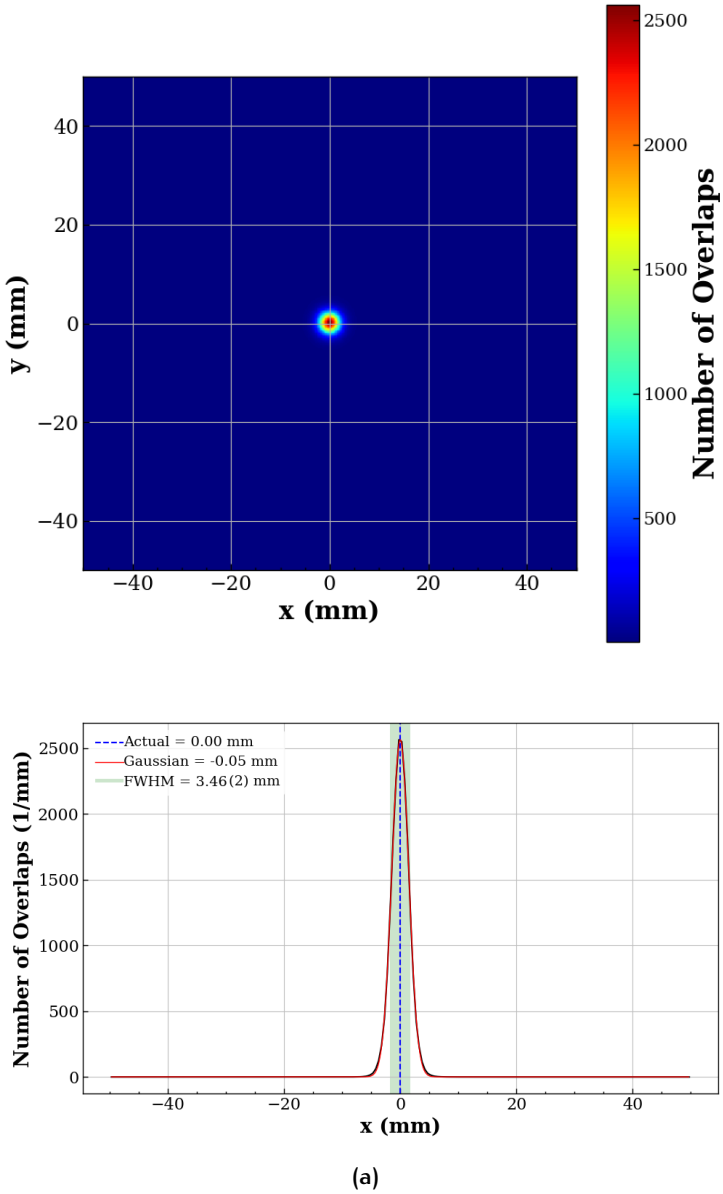

(a)

Figure 6.2.26: Reconstructed images of the simulated gamma emission of ^{137}Cs of CC2 geometry 3. The source was placed at (0,0,10) mm from the CC scatterer face, and the distance between the scatterer and absorber modules was 10 mm, where (a) shows the x-y image slice at the maximum z intensity, and (b) shows the x profile of the distribution, where the dotted blue line represents the actual source location. The distribution was fitted with a Gaussian function (red), and the FWHM of the Gaussian is seen shaded in green and labelled with uncertainty.

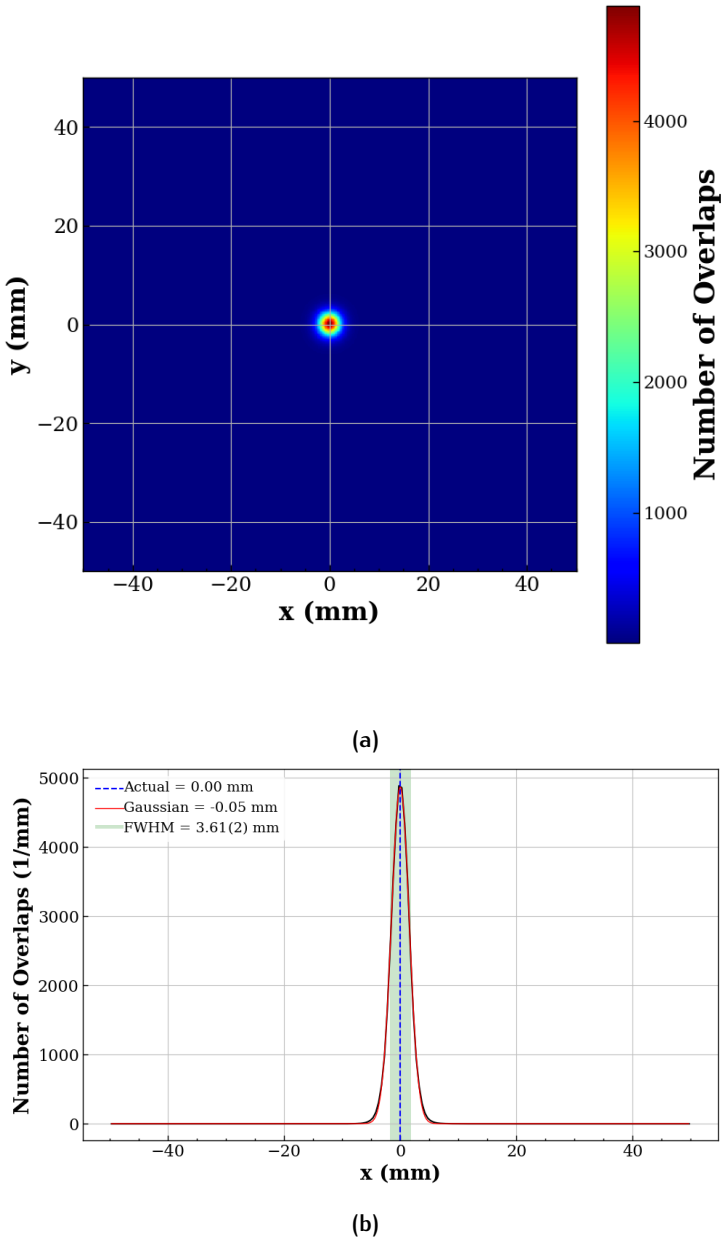

Figure 6.2.27: Reconstructed images of the simulated gamma emission of ^{137}Cs for CC3. The source was placed at (0,0,10) mm from the CC scatterer face, and the distance between the scatterer and absorber modules was 10 mm, where (a) shows the x-y image slice at the maximum z intensity, and (b) shows the x profile of the distribution, where the dotted blue line represents the actual source location. The distribution was fitted with a Gaussian function (red), and the FWHM of the Gaussian is seen shaded in green and labelled with uncertainty.

6.2.7 Image Reconstruction of Multiple Sources: ^{22}Na

In practical applications such as medical imaging, environmental monitoring, or nuclear security, multiple radiation sources may be present at the same time. Accurately distinguishing between these sources is crucial for correct diagnostics, detection, or threat assessment. To test the ability of the CC to differentiate between multiple sources, a simulation was conducted using two ^{22}Na sources placed at symmetric points relative to the scatterer face—specifically at coordinates (8,0,10) mm and (-8,0,10) mm. These placements allowed for the evaluation of how well the CC designs could spatially resolve two distinct sources that were positioned close together, a challenging task that simulates real-world complexities.

Figures 6.2.28 and 6.2.32 illustrate the results from the CC1 and CC3 designs, respectively. In both designs, each ^{22}Na source was given the same simulated activity, ensuring that the statistical weight assigned to each source was balanced. CC1 performed exceptionally well, accurately reconstructing the position of both sources with FWHM values of 4.24(114) mm and 4.12(108) mm for the sources at (8,0,10) mm and (-8,0,10) mm, respectively. This indicates that the CC1 design, which consists of a CZT Polaris-J detector as the scatterer and a 2″ × 2″ $LaBr_3$:Ce crystal as the absorber, was capable of resolving the two sources with high precision.

In contrast, the results from CC3, as shown in Figs. 6.2.32, were less consistent. While the source at (8,0,10) mm was reconstructed with a FWHM of 4.98(120) mm, the source at (-8,0,10) mm showed poorer resolution with a FWHM of 5.36(177) mm, and only 70% of the simulated statistics were associated with this second source. The larger FWHM and lower statistical confidence in the reconstruction of the second source suggest that CC3, which uses a larger 6×1 array $LaBr_3$:Ce MacroPixel scatterer combined with a 2″ × 2″ $LaBr_3$:Ce absorber, had more difficulty in resolving both sources equally. This asymmetry in performance indicates potential issues in the camera's sensitivity to sources placed at different positions.

The results from CC2, illustrated in Figs. 6.2.29, 6.2.30, and 6.2.31 for geometries 1, 2 and 3 respectively, show the performance of three different geometries for this design, which uses a 4×2 array $LaBr_3$:Ce DAs in each the scatterer and absorber. The results are summarised in Table 6.2.8. CC2 geometry 1 produced the best overall results, with both sources reconstructed. Each geometry rendered similar statistics, with ~ 300 overlaps seen in each image. However, across all geometries of CC2, as well as in the CC3 design, the source at (-8,0,10) mm consistently displayed poorer reconstruction than the source at (8,0,10) mm.

	FWHM (mm)	
CC Design	**(8,0,10) mm**	**(-8,0,10) mm**
CC1	4.24(114)	4.12(108)
CC2 Geometry 1	4.68(137)	4.55(115)
CC2 Geometry 2	4.85(156)	4.65(116)
CC2 Geometry 3	4.96(150)	4.89(119)
CC3	5.26(177)	4.98(120)

Table 6.2.8: Table of the results for two ^{22}Na sources, placed at (8,0,10) and (-8,0,10) mm from the CC scatterer face.

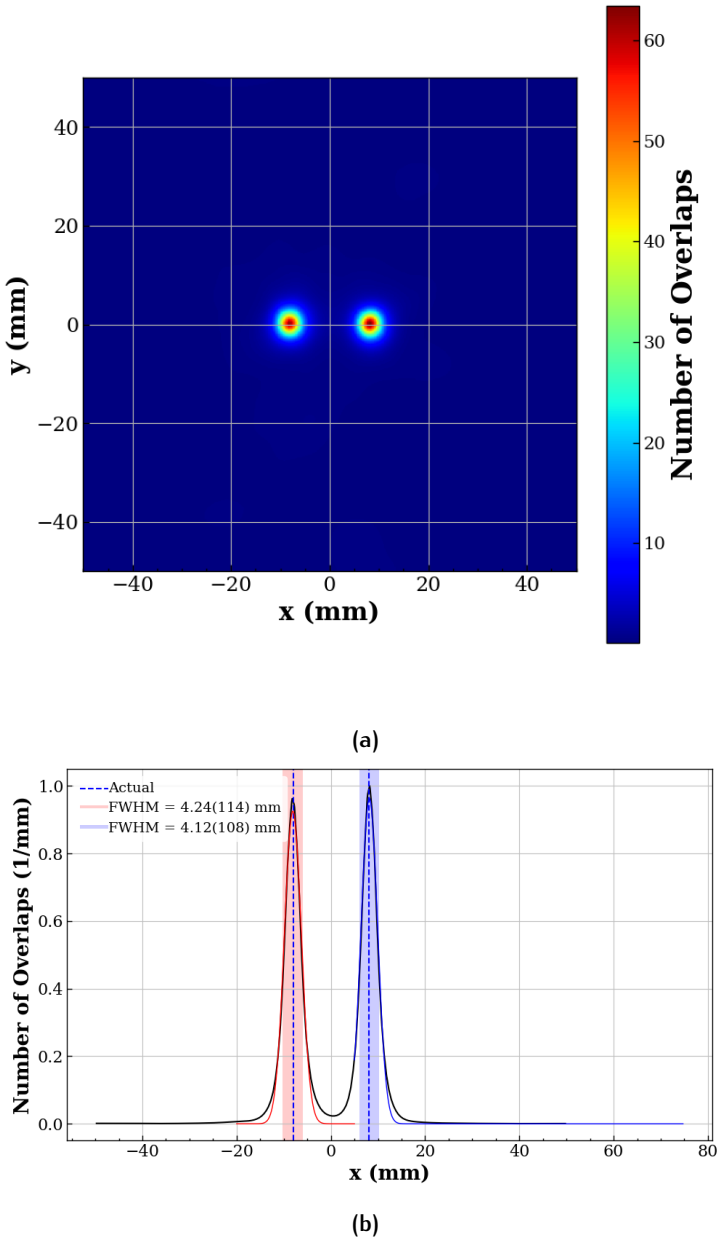

Figure 6.2.28: Reconstructed images of the simulated gamma emission of two ^{22}Na sources for CC1. The sources were placed at (8,0,10) and (-8,0,10) mm from the CC scatterer face, where (a) shows the x-y image slice at the maximum z intensity, and (b) shows the x profile of the distribution, where the dotted blue line represents the actual source location. The distributions were fitted with Gaussian functions (red and blue), and the FWHM of the fits are shaded in red and blue and labelled with uncertainty.

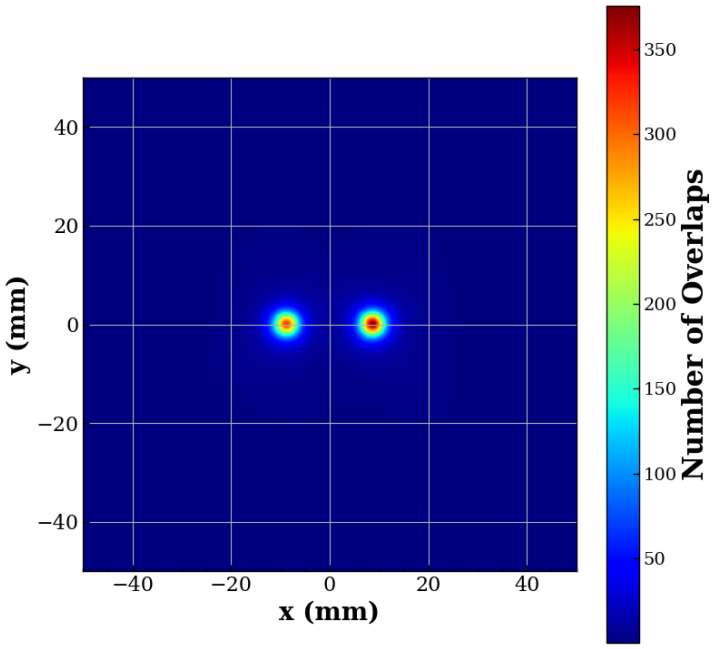

(a)

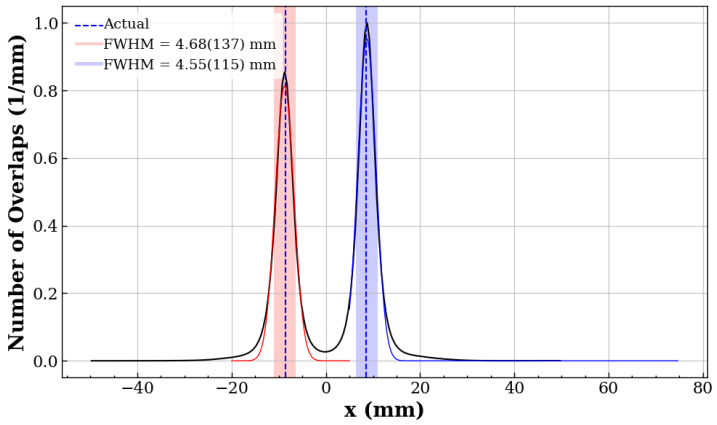

(b)

Figure 6.2.29: Reconstructed images of the simulated gamma emission of two ^{22}Na sources for CC2 geometry 1. The sources were placed at (8,0,10) and (-8,0,10) mm from the CC scatterer face, where (a) shows the x-y image slice at the maximum z intensity, and (b) shows the x profile of the distribution, where the dotted blue line represents the actual source location. The distributions were fitted with Gaussian functions (red and blue), and the FWHM of the fits are shaded in red and blue and labelled with uncertainty.

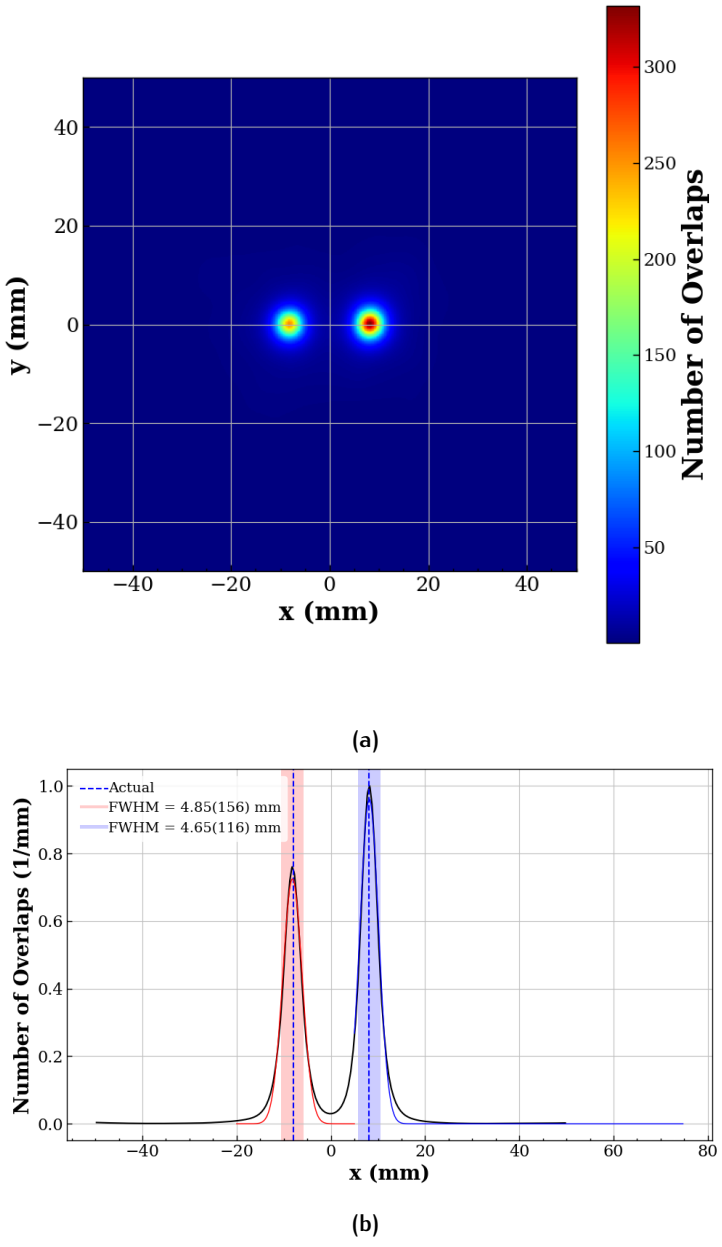

Figure 6.2.30: Reconstructed images of the simulated gamma emission of two ^{22}Na sources for CC2 geometry 2. The sources were placed at (8,0,10) and (-8,0,10) mm from the CC scatterer face, where (a) shows the x-y image slice at the maximum z intensity, and (b) shows the x profile of the distribution, where the dotted blue line represents the actual source location. The distributions were fitted with Gaussian functions (red and blue), and the FWHM of the fits are shaded in red and blue and labelled with uncertainty.

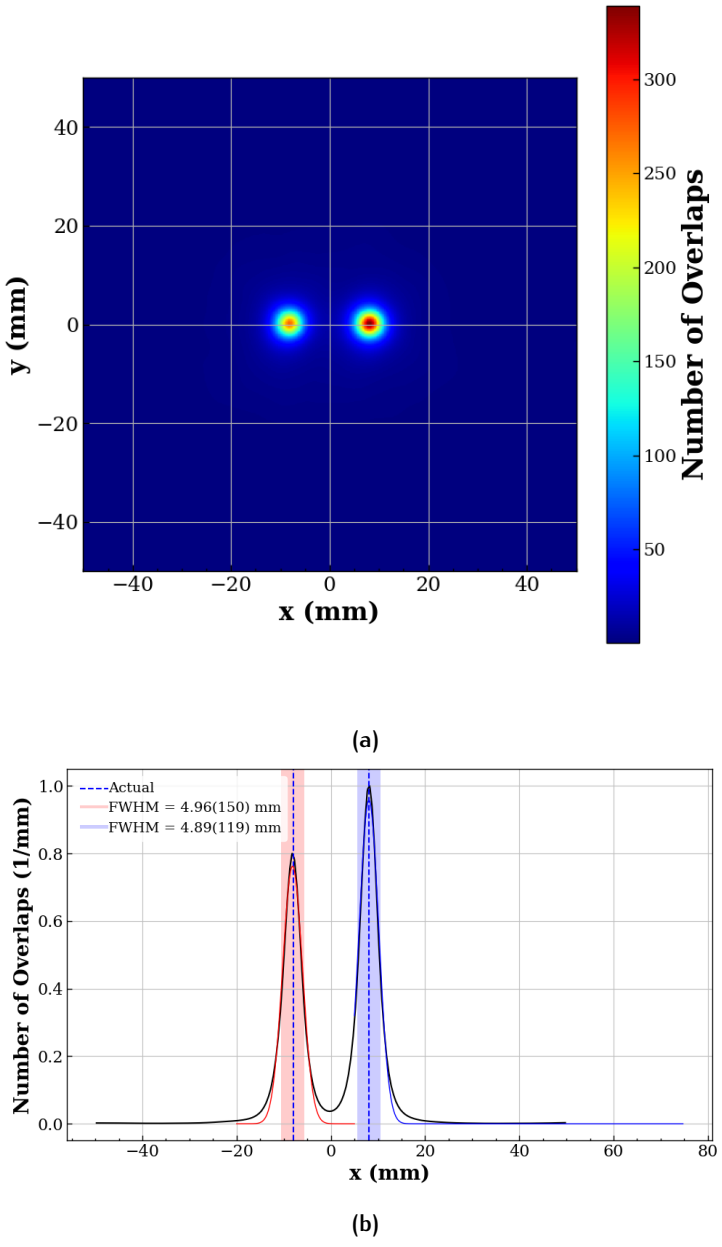

Figure 6.2.31: Reconstructed images of the simulated gamma emission of two ^{22}Na sources for CC2 geometry 3. The sources were placed at (8,0,10) and (-8,0,10) mm from the CC scatterer face, where (a) shows the x-y image slice at the maximum z intensity, and (b) shows the x profile of the distribution, where the dotted blue line represents the actual source location. The distributions were fitted with Gaussian functions (red and blue), and the FWHM of the fits are shaded in red and blue and labelled with uncertainty.

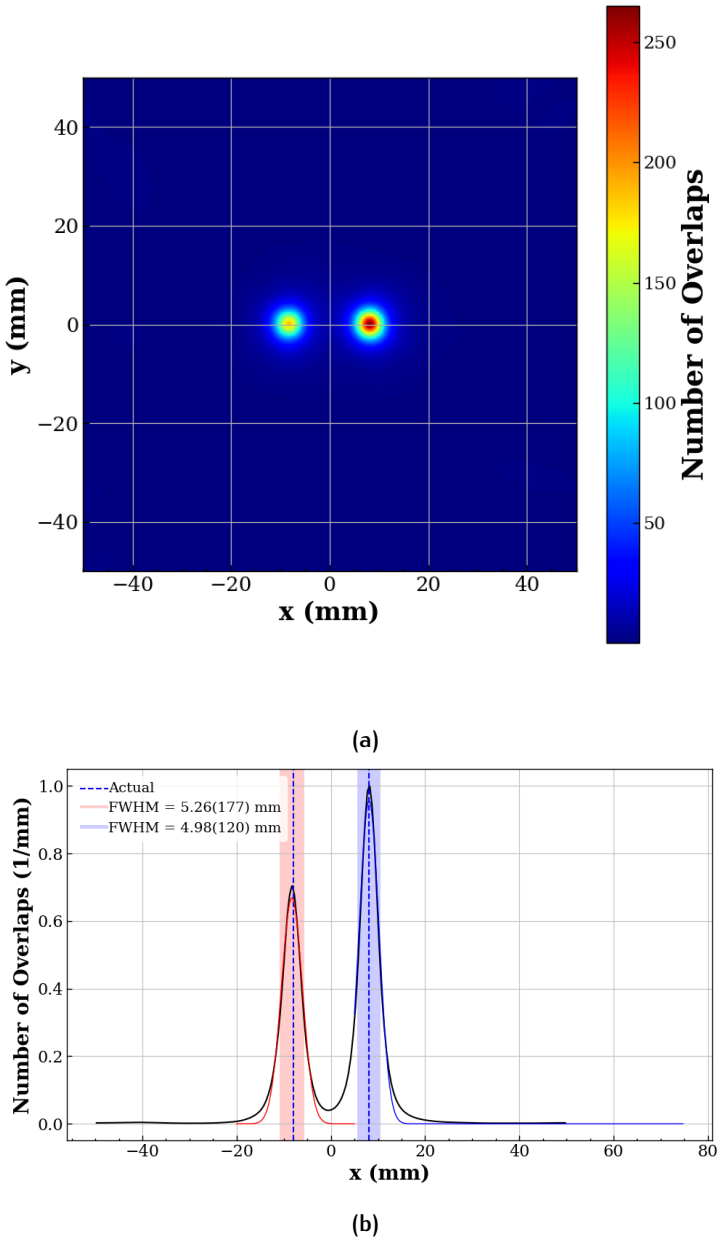

Figure 6.2.32: Reconstructed images of the simulated gamma emission of two ^{22}Na sources for CC3. The sources were placed at (8,0,10) and (-8,0,10) mm from the CC scatterer face, where (a) shows the x-y image slice at the maximum z intensity, and (b) shows the x profile of the distribution, where the dotted blue line represents the actual source location. The distributions were fitted with Gaussian functions (red and blue), and the FWHM of the fits are shaded in red and blue and labelled with uncertainty.

6.2.8 Image Reconstruction of Multiple Sources: ^{60}Co and a ^{22}Na Source

The ability of the CC designs to distinguish between two gamma-ray sources with different energies, ^{60}Co and ^{22}Na, placed symmetrically along the x-axis was studied. Each source was positioned 10 mm away from the scatterer surface, at coordinates (4, 0, 10) for ^{60}Co and (-4, 0, 10) for ^{22}Na. Despite both sources being simulated with identical activity, the reconstructed images exhibited differences in intensity, as shown in Fig. 6.2.33 and 6.2.37 for CC1 and CC3, and Figs. 6.2.34, 6.2.35, and 6.2.36 for the CC2 geometries 1, 2, and 3. The results are summarised in Table 6.2.9.

Several factors contribute to this variation in intensity between the two sources. ^{60}Co emits higher-energy gamma rays (1332.5 keV and 1173.2 keV), whereas ^{22}Na primarily emits gamma rays at 511.0 keV (annihilation radiation) and 1274.5 keV. These differences in energy impact how the gamma rays interact within the CC's scatterer and absorber.

Higher-energy gamma rays from ^{60}Co were more likely to undergo Compton scattering, which enhances the number of detectable Compton scatter events, seen in Table 6.2.9. This increased scattering leads to a more intense reconstructed image for ^{60}Co compared to the lower-energy 511.0 keV gamma rays from ^{22}Na. Additionally, 511.0 keV gamma rays have a higher probability of being absorbed via the photoelectric effect, which reduces the number of valid Compton scatter events for ^{22}Na, further lowering its image intensity.

Despite the differences in intensity, all CC designs successfully reconstructed both sources with high accuracy. However, CC1 (Fig. 6.2.33) and the geometry 1 configuration of CC2 (Fig. 6.2.34) demonstrated the best performance in reconstructing the intensity profile of the ^{22}Na source. These designs also achieved the most precise FWHM for the x-profile of the reconstructed image, indicating superior resolution in these configurations.

	FWHM (mm)	
CC Design	**(4,0,10) mm**	**(-4,0,10) mm**
CC1	3.51(178)	3.34(95)
CC2 Geometry 1	3.83(217)	3.60(100)
CC2 Geometry 2	4.03(254)	3.71(101)
CC2 Geometry 3	4.17(297)	3.78(102)
CC3	4.52(394)	3.91(105)

Table 6.2.9: Table of the results for two different sources: ^{60}Co placed at (4,0,10) and ^{22}Na at (-4,0,10) mm from the CC scatterer face.

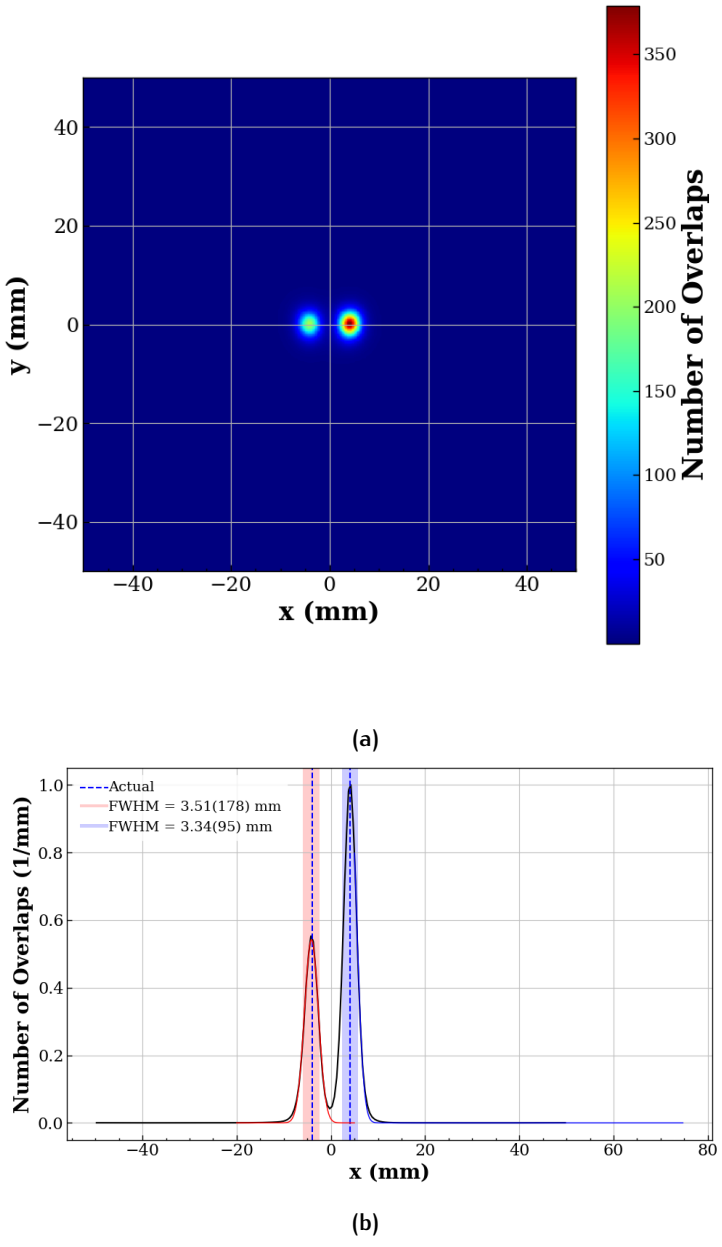

Figure 6.2.33: Reconstructed images of the simulated gamma emission of ^{60}Co and ^{22}Na sources placed at (4,0,10) and (-4,0,10) mm from the scatterer face for CC1. The plots show (a) the x-y image slice at the maximum z intensity, and (b) the x profile of the distribution, where the dotted blue lines represent the actual source locations. The distributions were fitted with Gaussian functions (red and blue), and the FWHM of the fits are shaded in red and blue and labelled with uncertainty.

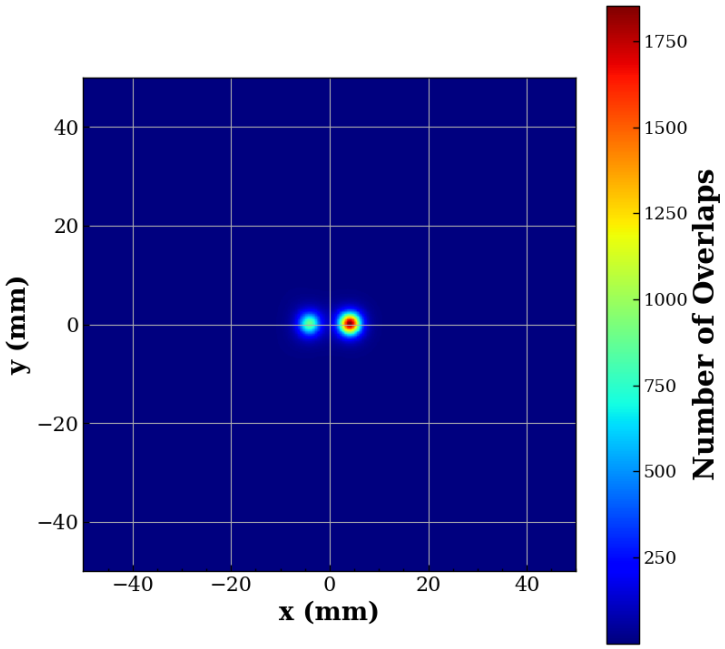

(a)

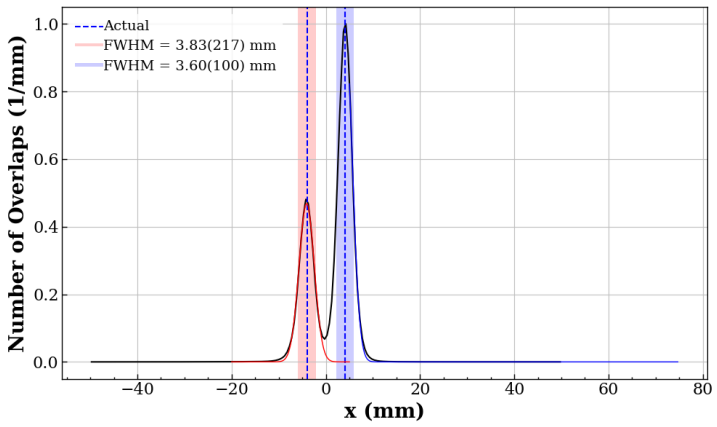

(b)

Figure 6.2.34: Reconstructed images of the simulated gamma emission of ^{60}Co and ^{22}Na sources placed at (4,0,10) and (-4,0,10) mm from the scatterer face for CC2 geometry 1. The plots show (a) the x-y image slice at the maximum z intensity, and (b) the x profile of the distribution, where the dotted blue lines represent the actual source locations. The distributions were fitted with Gaussian functions (red and blue), and the FWHM of the fits are shaded in red and blue and labelled with uncertainty.

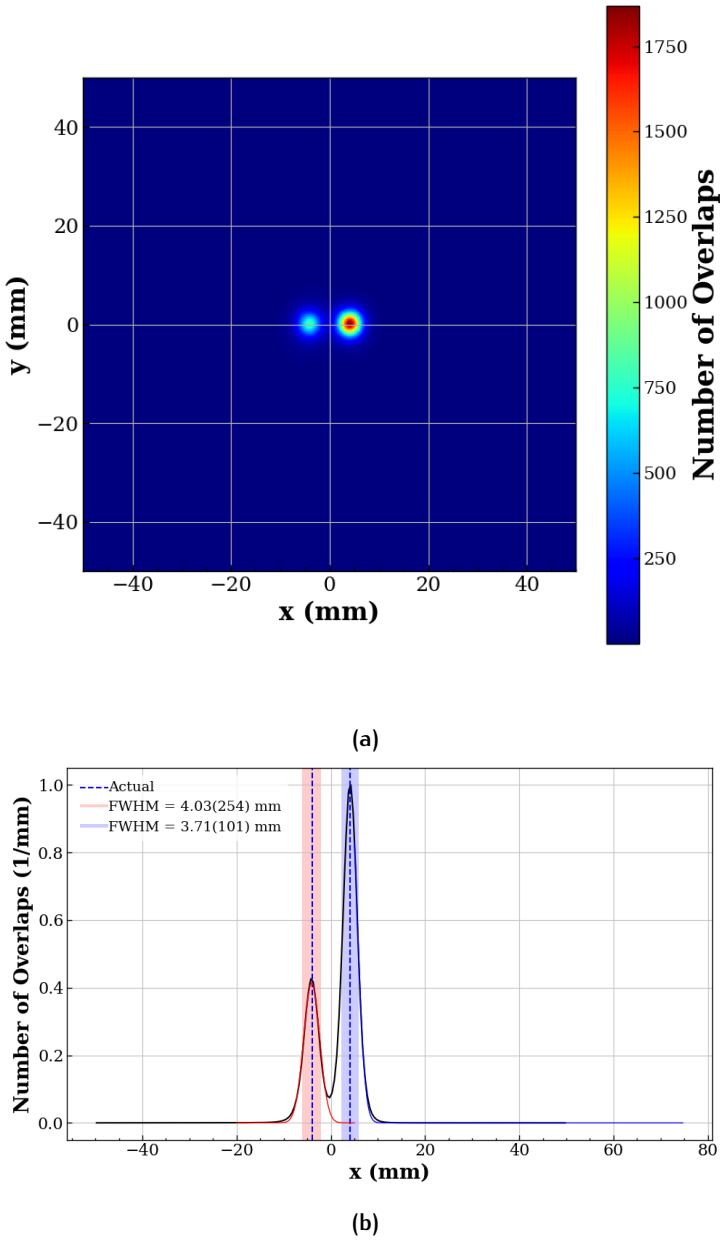

Figure 6.2.35: Reconstructed images of the simulated gamma emission of ^{60}Co and ^{22}Na sources placed at (4,0,10) and (-4,0,10) mm from the scatterer face for CC2 geometry 2. The plots show (a) the x-y image slice at the maximum z intensity, and (b) the x profile of the distribution, where the dotted blue lines represent the actual source locations. The distributions were fitted with Gaussian functions (red and blue), and the FWHM of the fits are shaded in red and blue and labelled with uncertainty.

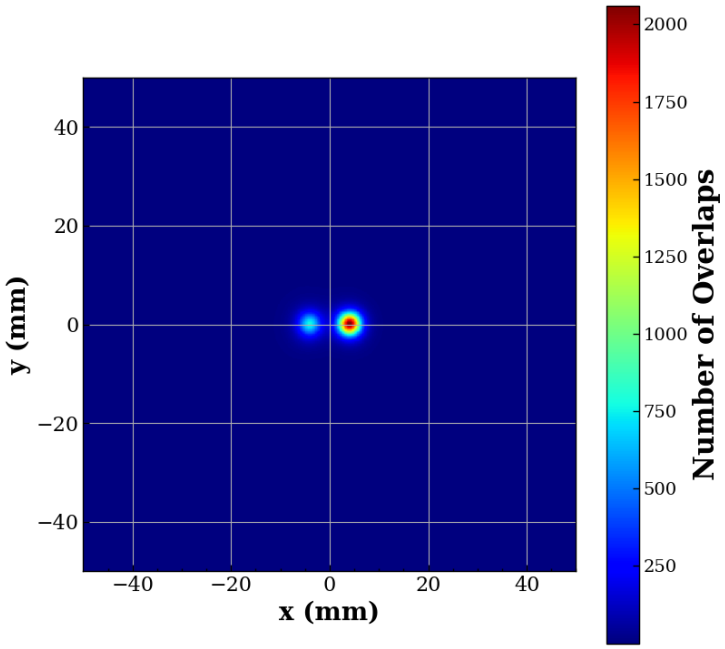

(a)

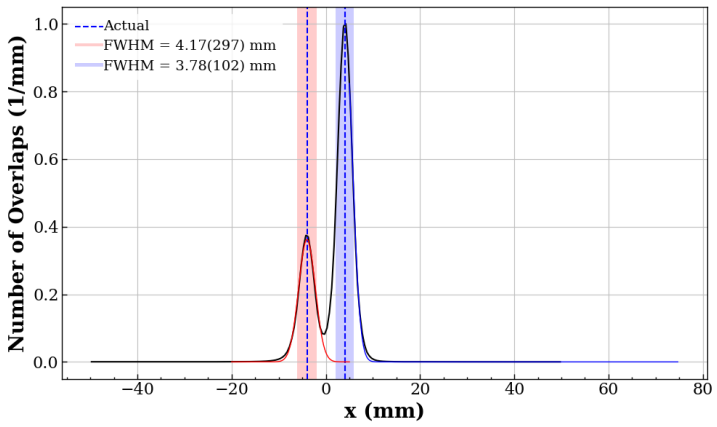

(b)

Figure 6.2.36: Reconstructed images of the simulated gamma emission of ^{60}Co and ^{22}Na sources placed at (4,0,10) and (-4,0,10) mm from the scatterer face for CC2 geometry 3. The plots show (a) the x-y image slice at the maximum z intensity, and (b) the x profile of the distribution, where the dotted blue lines represent the actual source locations. The distributions were fitted with Gaussian functions (red and blue), and the FWHM of the fits are shaded in red and blue and labelled with uncertainty.

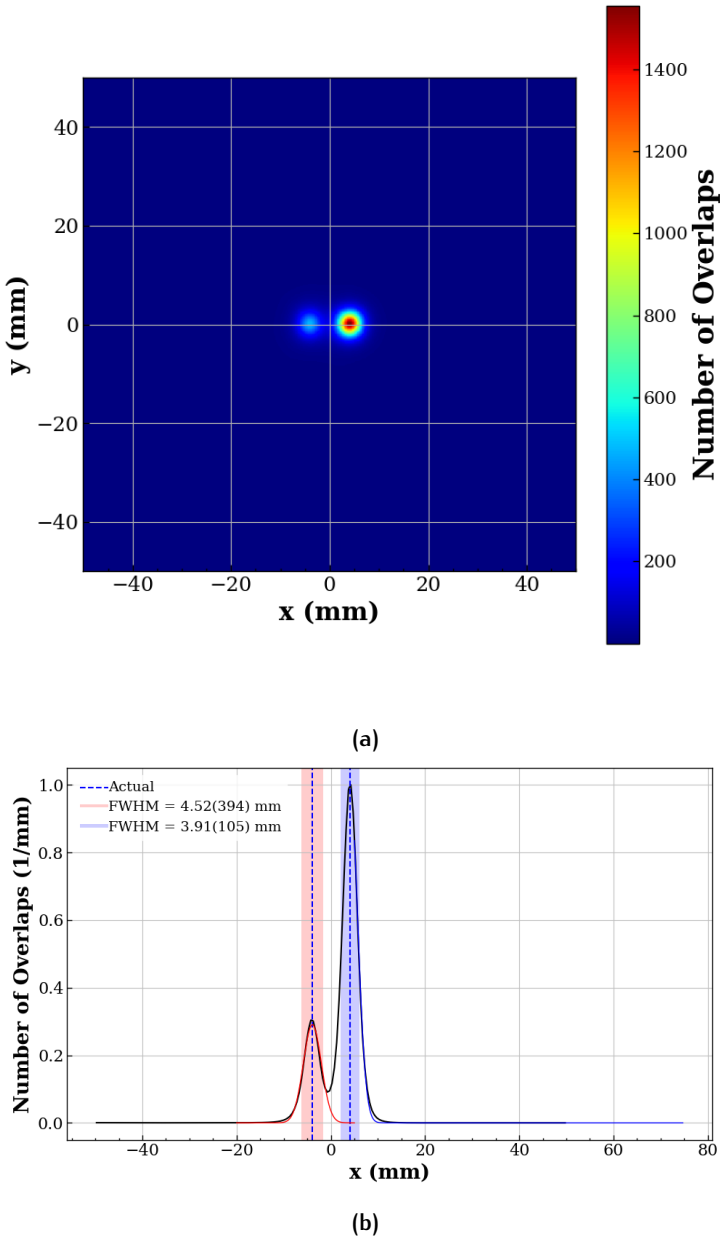

Figure 6.2.37: Reconstructed images of the simulated gamma emission of ^{60}Co and ^{22}Na sources placed at (4,0,10) and (-4,0,10) mm from the scatterer face for CC3. The plots show (a) the x-y image slice at the maximum z intensity, and (b) the x profile of the distribution, where the dotted blue lines represent the actual source locations. The distributions were fitted with Gaussian functions (red and blue), and the FWHM of the fits are shaded in red and blue and labelled with uncertainty.

6.2.9 Image Reconstruction of Multiple Sources: Closely Spaced ^{137}Cs Sources

The ability of the CC designs to distinguish between two closely spaced ^{137}Cs gamma-ray sources was studied by placing the sources symmetrically along the x-axis, 10 mm from the scatterer surface. The sources were positioned at coordinates (1, 0, 10) mm and (-1, 0, 10) mm, each designed as a cylinder with a height and diameter of 1 mm, effectively placing the sources 1 mm apart when accounting for their radii. Due to this close spacing, none of the CC designs were able to resolve the two sources as separate peaks, instead combining them into a single peak. This behaviour is demonstrated in Figs. 6.2.38 and 6.2.42 for CC1 and CC3 each, and in Figs. 6.2.39, 6.2.40, and 6.2.41 for the different geometries of CC2.

The FWHM values of the combined peak from the two sources were similar to the FWHM values from a single source placed at (0,0,10) mm, as shown in Table 6.2.10. The merging of two closely spaced sources should cause significant broadening of the peak in the x-profile, interpreting the source as being 2 to 3 times its true width. However, the FWHM values did not reflect such a large increase, while the uncertainties in the fits for the two-source peaks suggest a reasonable disagreement with the single-source measurements. Achieving sub-millimetre precision in such experimental setups would be challenging, especially with the current lack of segmentation in the individual CC2 DA modules. For a Compton Camera to be viable in PT, the ability to handle high count rates while maintaining sub-millimetre precision is crucial and would need to be measured in experiment in future work.

CC Configuration	$\mathbf{FWHM_z}$ (mm)	
	Single Source at (0,0,10)mm	**Multiple Source at (-1,0,10) and (1,0,10) mm**
CC1	3.20(1)	3.72(393) and 3.66(367)
CC2 geometry 1	3.36(1)	4.24(469) and 4.11(381)
CC2 geometry 2	3.51(1)	3.72(393) and 3.66(367)
CC2 geometry 3	3.43(1)	3.91(419) and 3.85(368)
CC3	3.71(1)	3.99(430) and 3.92(367)

Table 6.2.10: Comparison of the reconstructed FWHM values obtained from the simulations of one and two ^{137}Cs sources of the same geometry placed 10 mm from the detector scatterer faces.

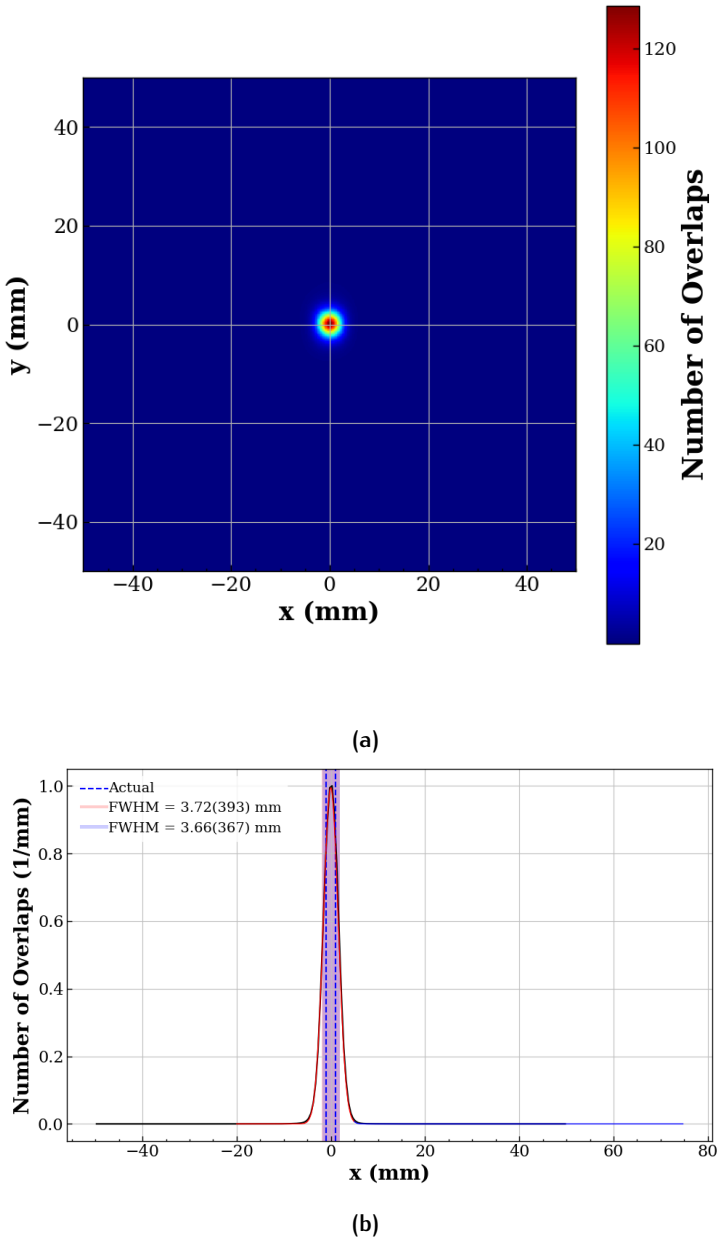

Figure 6.2.38: Reconstructed images of the simulated gamma emission of a ^{137}Cs source placed at (1,0,10) and (-1,0,10) mm from the scatterer face for CC1. The plots show (a) the x-y image slice at the maximum z intensity, and (b) the x profile of the distribution, where the dotted blue lines represent the actual source locations. The distributions were fitted with Gaussian functions (red and blue), and the FWHM of the fits are shaded in red and blue and labelled with uncertainty.

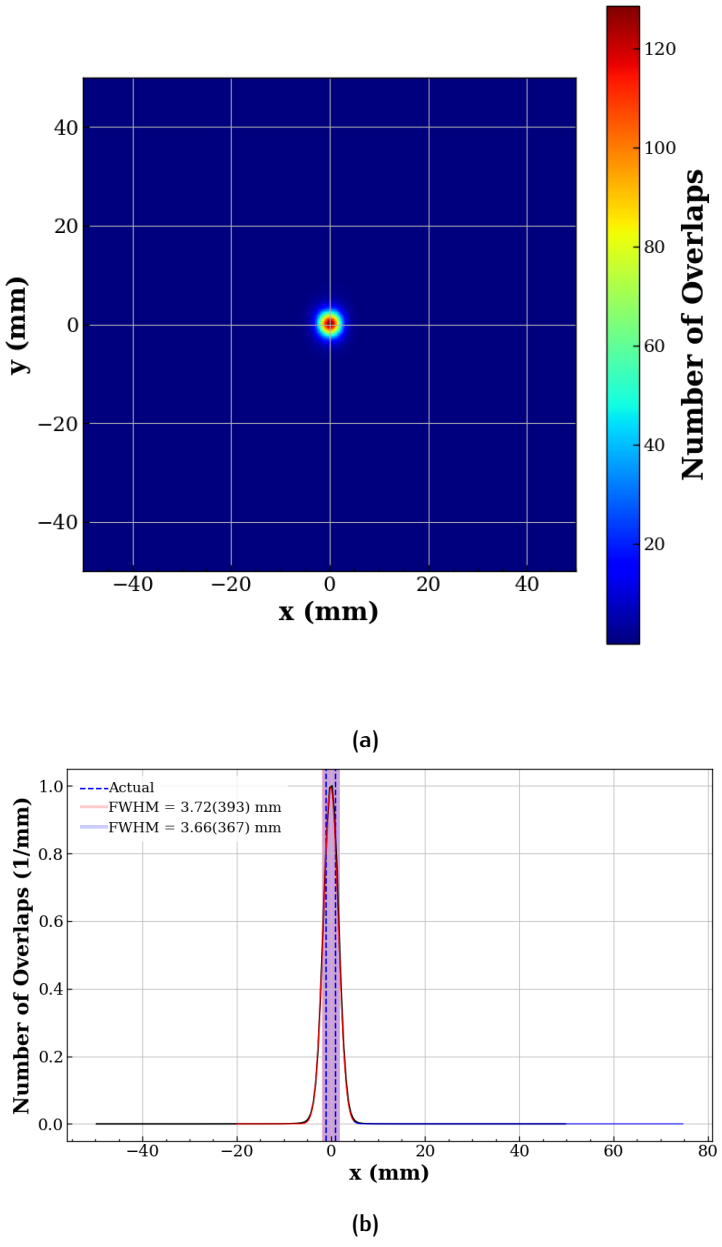

Figure 6.2.39: Reconstructed images of the simulated gamma emission of a ^{137}Cs source placed at (1,0,10) and (-1,0,10) mm from the scatterer face for CC2 geometry 1. The plots show (a) the x-y image slice at the maximum z intensity, and (b) the x profile of the distribution, where the dotted blue lines represent the actual source locations. The distributions were fitted with Gaussian functions (red and blue), and the FWHM of the fits are shaded in red and blue and labelled with uncertainty.

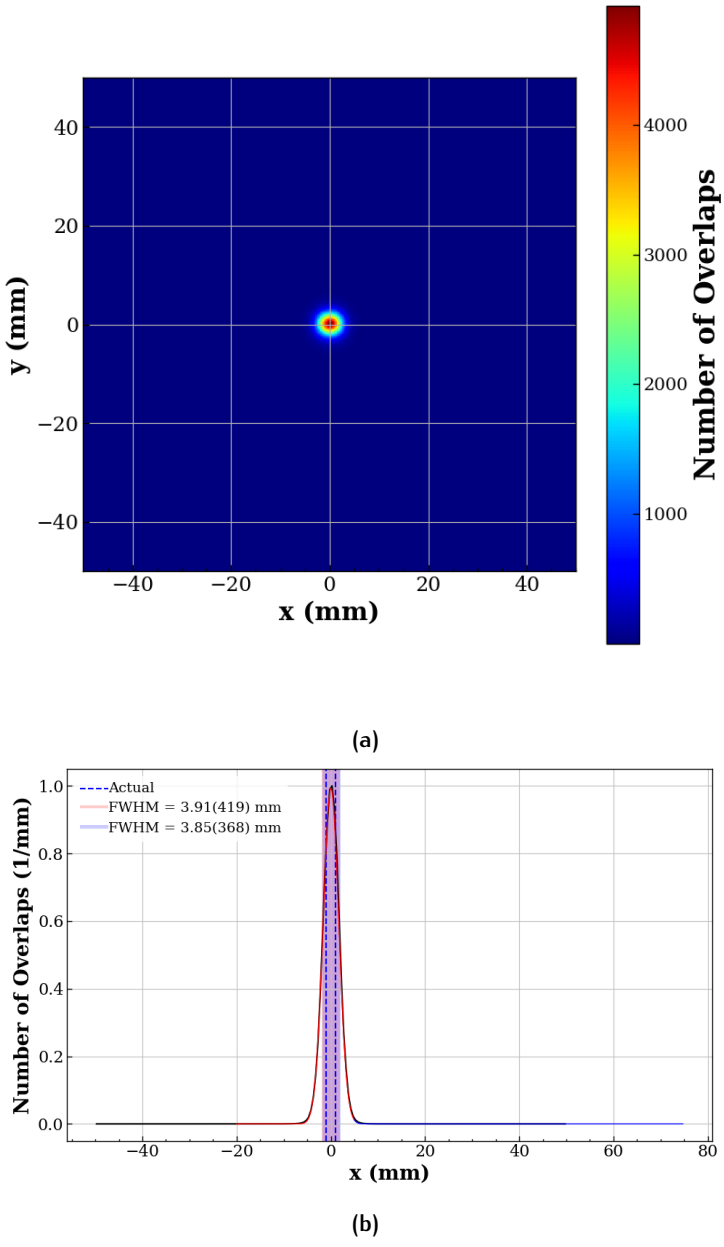

Figure 6.2.40: Reconstructed images of the simulated gamma emission of a ^{137}Cs source placed at (1,0,10) and (-1,0,10) mm from the scatterer face for CC2 geometry 2. The plots show (a) the x-y image slice at the maximum z intensity, and (b) the x profile of the distribution, where the dotted blue lines represent the actual source locations. The distributions were fitted with Gaussian functions (red and blue), and the FWHM of the fits are shaded in red and blue and labelled with uncertainty.

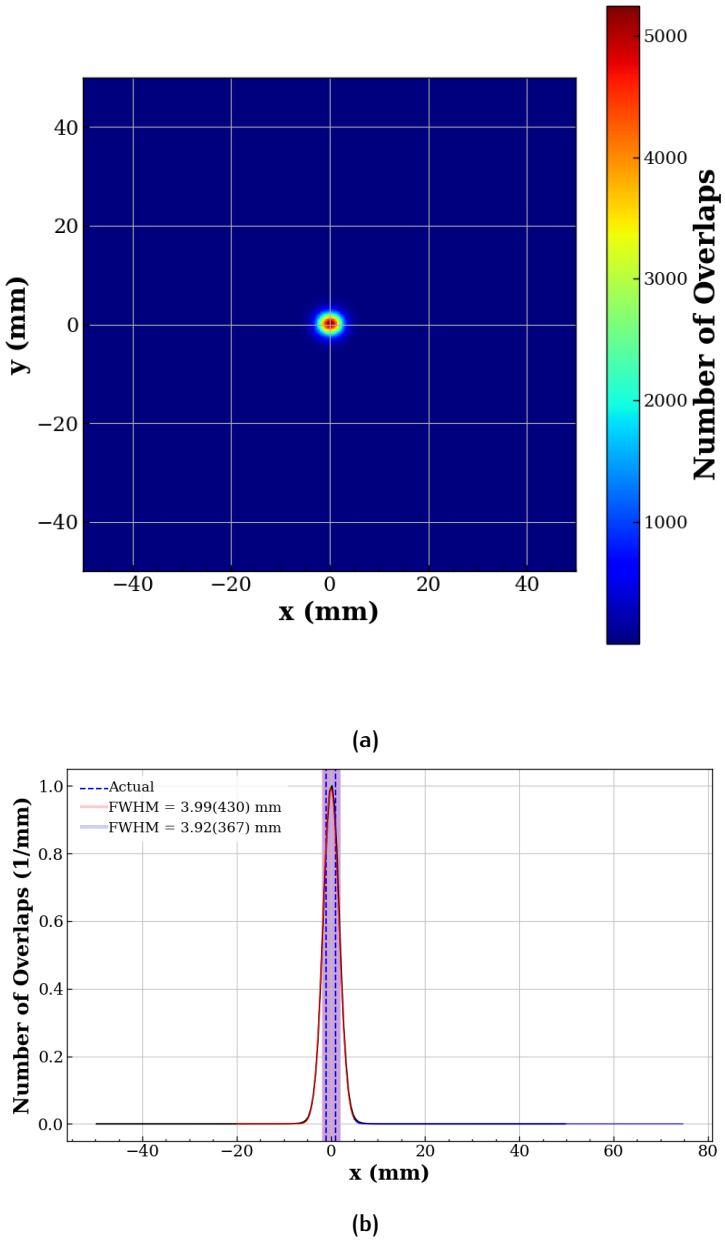

Figure 6.2.41: Reconstructed images of the simulated gamma emission of a ^{137}Cs source placed at (1,0,10) and (-1,0,10) mm from the scatterer face for CC2 geometry 3. The plots show (a) the x-y image slice at the maximum z intensity, and (b) the x profile of the distribution, where the dotted blue lines represent the actual source locations. The distributions were fitted with Gaussian functions (red and blue), and the FWHM of the fits are shaded in red and blue and labelled with uncertainty.

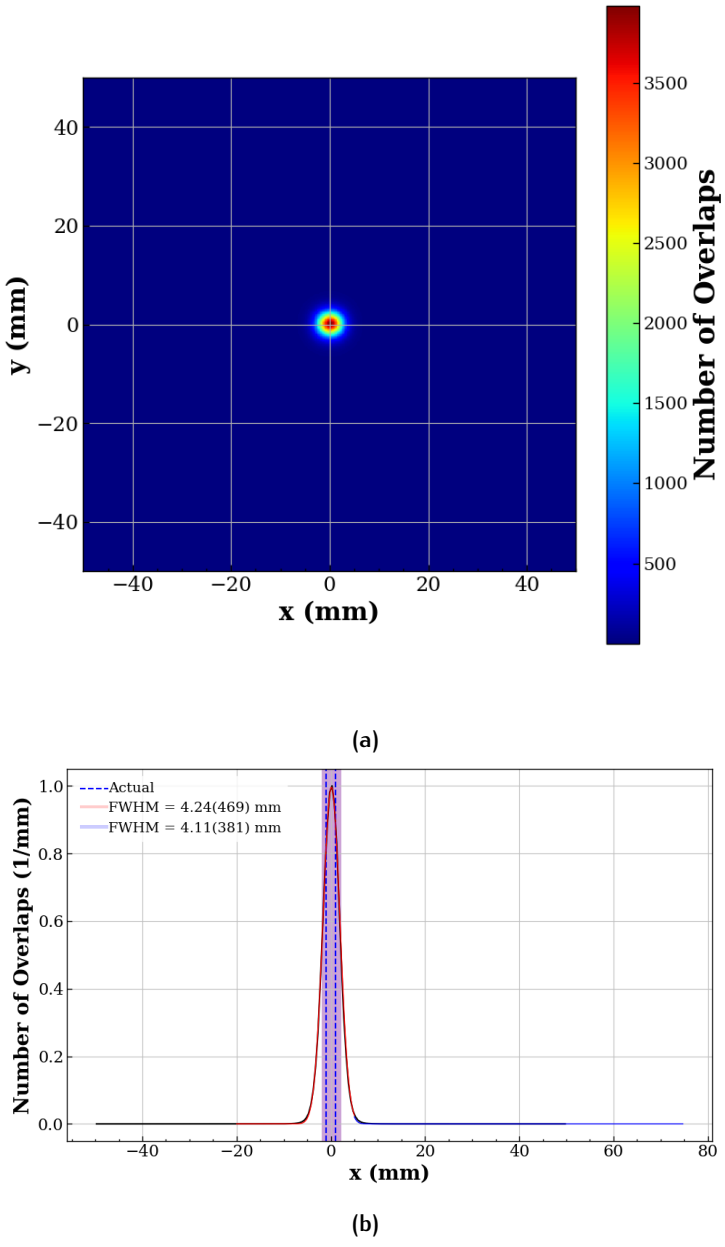

Figure 6.2.42: Reconstructed images of the simulated gamma emission of a ^{137}Cs source placed at (1,0,10) and (-1,0,10) mm from the scatterer face for CC3. The plots show (a) the x-y image slice at the maximum z intensity, and (b) the x profile of the distribution, where the dotted blue lines represent the actual source locations. The distributions were fitted with Gaussian functions (red and blue), and the FWHM of the fits are shaded in red and blue and labelled with uncertainty.

6.3 RESULTS OF EXPERIMENT

Experimental measurements were conducted for the CC1 design, making use of both beam and source measurements. The beam time was allocated early in the project, approximately two months into its initiation, providing an opportunity to assess the performance of the CC1 design. A 66.67 MeV proton beam, supplied by iThemba LABS in Cape Town, South Africa, was employed for these measurements. This beam, generated by the separated sector cyclotron, was structured in time with an interval of 300 ns and a selection rate of 1 in 5 pulses. This specific time structure was requested to facilitate the integration of the beam's RF signal with the DAQ system. This time structure allowed signals correlated with the proton beam's RF to be clearly identified and attributed to beam interactions with the target. As such, signals out of sync with the RF were gated as background, enabling effective discrimination between true beam-induced events and noise.

The Pixie-16 DAQ, operating at 500 MHz and detailed in Section 3.2.3.1, was used to interface with the $LaBr_3$:Ce detector absorber of CC1. It was configured to receive the RF signal from the cyclotron, in addition to the STM pulses from the Polaris scatterer, as discussed in Section 3.3.7.

The experimental setup of CC1, as described in Section 3.4, involved positioning the camera isocentric with respect to the beam and the water target along the z-axis. The water target was specifically designed to ensure complete stopping of the proton beam within its volume, allowing for the deposition of all its energy in the BP region. This setup enabled the detection of PG radiation correlated with the RF time of the beam. The investigations into the application of CC1 as a PG imaging device for medical purposes were primarily focused on event tracking and detector timing.

6.3.1 Sources of Background in Experiment

There was no significant source of background radiation in either the source or the beam experiment. The internal radioactivity of the $LaBr_3$:Ce detectors, discussed in detail in Section 3.2.2, did not contribute significantly to the background spectrum.

Figure 6.3.1(a) shows the full spectrum (red) of a ^{152}Eu source for a 10-minute measurement with the $2'' \times 2''$ $LaBr_3$:Ce detector, plotted with the background (black) obtained in the absence of sources for the same measurement duration. It can be seen that the internal radioactivity of the detector crystal is present in the background spectrum. Background subtraction for source measurements was straightforward, as the background was deducted from the counts of the full spectrum for the same measurement duration for measurements performed on the same day. This was seen as effective in omitting the internal radioactivity contribution and improving the peak structure of the 1408.0 keV ^{152}Eu emission line. Figure 6.3.1(b) shows the same source and background measurement for the Polaris detector. The background subtracted spectrum is shown in blue, with the background in black.

The cyclotron radio frequency guided background subtraction performed for the beam-time measurements is detailed in Section 3.4.1. This method was found to be effective for the low-energy background contribution originating from random out-of-sync emissions from the source and surrounding materials in the experiment vault, as well as eliminating the internal radioactivity contribution of the 2″ × 2″ $LaBr_3$:Ce detector used in beam-time experiment as the CC1 absorber.

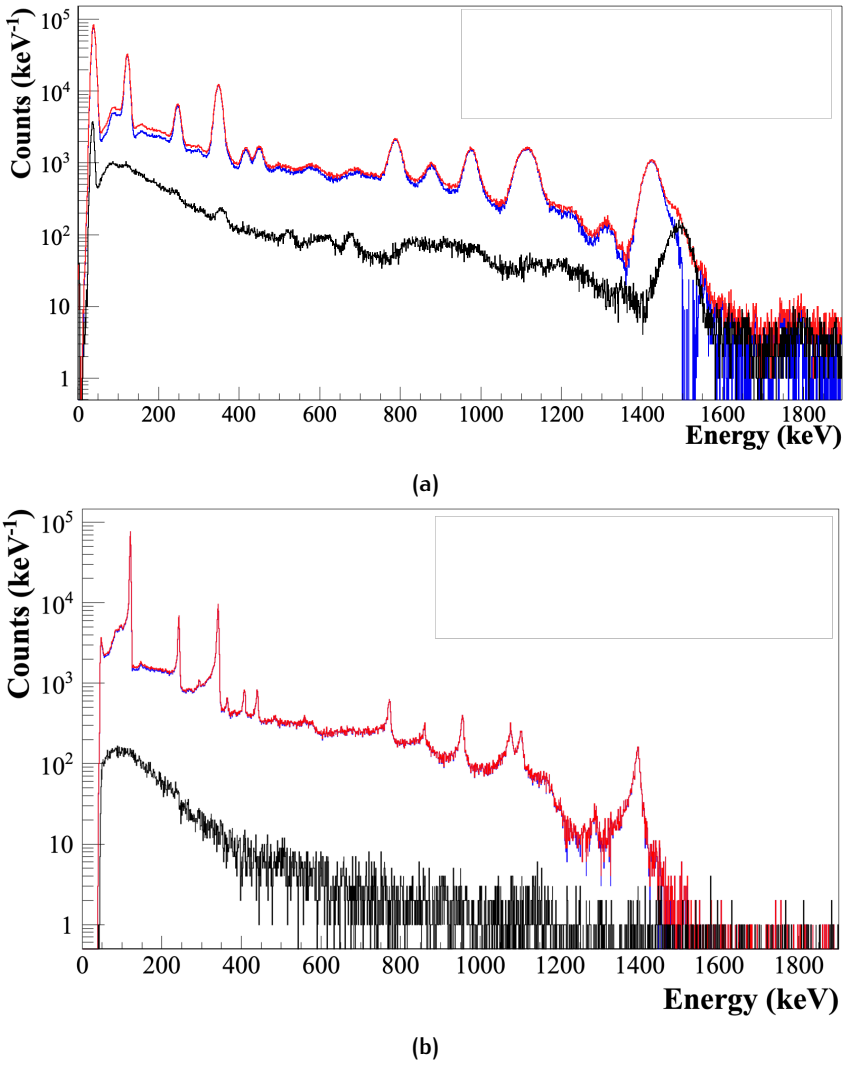

Figure 6.3.1: Measured gamma energy spectra of a ^{152}Eu source where the full energy spectrum is seen in red, background and detector intrinsic activity in black, and background subtracted spectrum in blue for each: (a) 2″ × 2″ $LaBr_3$:Ce detector and (b) Polaris detector.

6.3.2 CC1 Beam Measurements

Figure 6.3.2 shows the CC1 gamma-ray energy spectrum of the interaction of the proton beam with the water target, where the Polaris detector is plotted in red and the $LaBr_3$:Ce detector in black. The plot is separated into the lower 0.0–2000.0 keV energy region above and the 2000.0–7000.0 keV region below to improve the appearance of the peaks. Labelled in units of MeV are the PG emission lines and their single and double escape peaks, originating from the interaction of the 66.67 MeV proton beam with the water target. It can be seen that the

Polaris detector has a poor range (<3.0 MeV) caused by the efficiency dropping off because the detectors are thin, such that the PG emission lines were not visible in the spectrum of Polaris in the bottom plot. Due to the nature of how early beam-time was acquired for the project, the energy trapezoidal DDAS shaping parameters (discussed in Section 3.2.3.4) were not fully optimised, seen in the poor energy resolution in the $LaBr_3$:Ce detector energy spectrum.

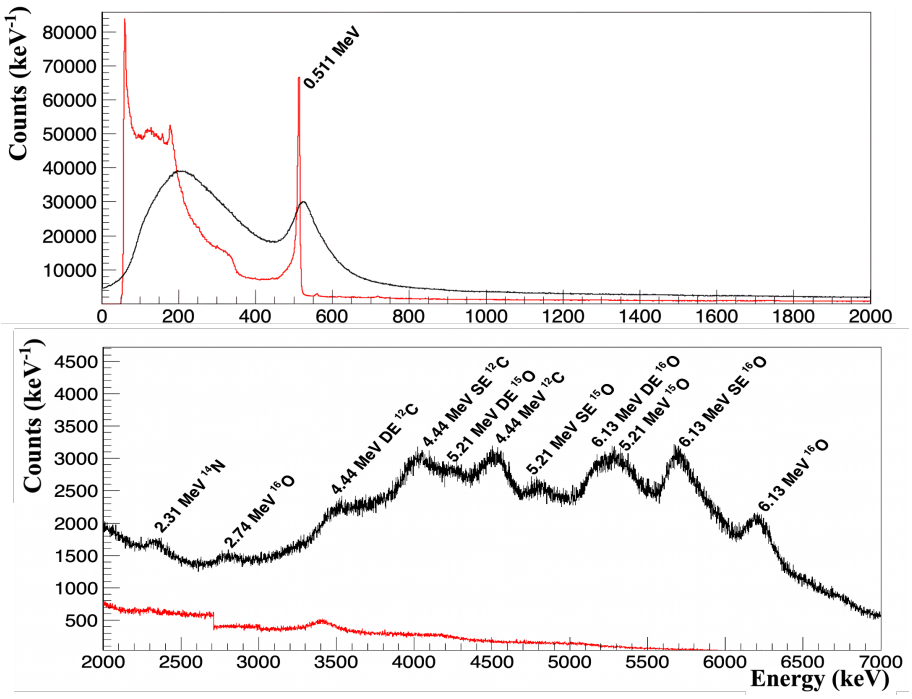

Figure 6.3.2: Background subtracted energy spectra from Polaris (red) and $LaBr_3$:Ce (black), where the low energy (0.0–2000.0 keV) region is seen above and the higher energy (2000.0–8000.0 keV) region is situated below for viewing clarity. Labelled in units of MeV are the PG emission lines and their single and double escape peaks, originating from the interaction of the 66.67 MeV proton beam with the water target.

6.3.3 Coincidence Measurement Event Time Window Investigation

The analysis of the beam-time data required a detailed understanding of the event time offset in the Polaris detector, which was introduced by the detector's processing electronics. When the detector recorded an energy deposition exceeding the threshold value, it entered a "triggered" state, during which no new events could be processed for up to 15 µs [60]. Due to the high event rates encountered during beam-time, it became apparent that time synchronisation using STM pulses alone was insufficient for confidently tracking double scatter events across the CC detectors. Attempts to resolve this by subtracting 15 µs from the Polaris event times and aligning them with the fast timing resolution of the $LaBr_3$:Ce detector did not demonstrate an improvement in timing accuracy.

Coincidence timing measurements were then necessitated, using a face-to-face configuration between the Polaris and $LaBr_3$:Ce detectors, as shown in Fig. 6.3.3, with a low-activity ^{22}Na source (13.80(138) kBq) placed between the detectors, 10 cm from each face. The measured energy spectra for each detector are seen plotted on the same axes in Fig. 6.3.4. A

10-minute measurement was performed, with the goal of identifying a consistent timing pattern in the Polaris detector by tracking the annihilation photons between the two detectors. This would allow for the determination of a predictable time offset between events, enabling the Polaris events to be shifted backward in time to facilitate accurate double scatter tracking in the CC.

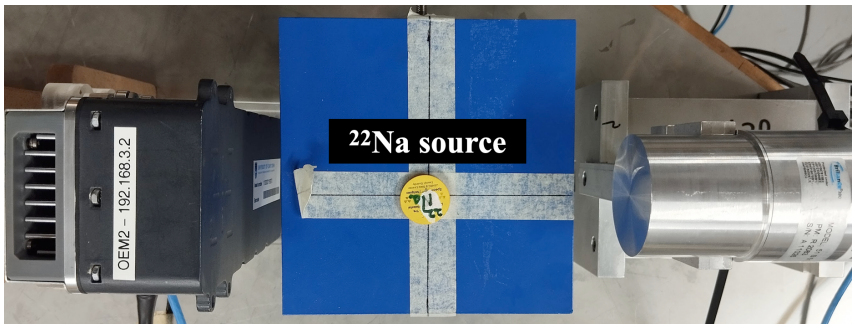

Figure 6.3.3: A photograph of the coincidence timing experimental setup of the Polaris and the 2″ × 2″ $LaBr_3$:Ce detector with a low activity 13.80(138) kBq ^{22}Na source placed (0,0,10) cm from each detector face.

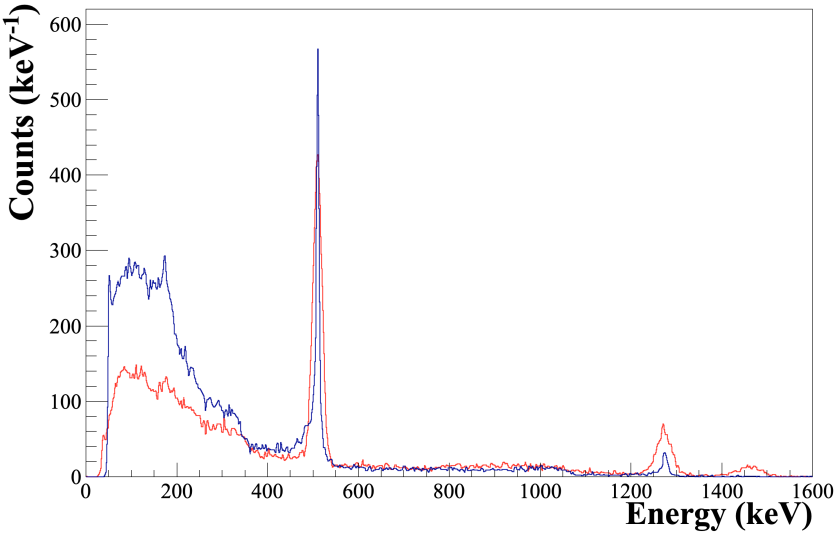

Figure 6.3.4: The energy spectra of a low activity ^{22}Na source shown for the Polaris detector (blue) and the $LaBr_3$:Ce detector (red) for a 10-minute measurement.

The analysis focused on identifying coincident annihilation photon events between the Polaris and $LaBr_3$:Ce detectors. The first step was to gate on single-scatter events in the Polaris detector, followed by energy gating to retain only those events within ± 76.65 keV of the 511.0 keV energy peak. This gating process was critical to ensure that only annihilation photons were analysed. Prior to applying the energy gate, the ratio of $LaBr_3$:Ce to Polaris events was 0.769. After filtering for events in the 511.0 keV region, this ratio increased significantly to a value of 2. This indicated that the energy gating successfully isolated the events of interest and emphasised that the $LaBr_3$:Ce experienced little to no DAQ dead-time compared to the Polaris detector, seen in there being twice as many events.

Next, the analysis focused on calculating the time difference between events in the two detectors. The goal was to find instances where a coincident event occurred, meaning that an event in the Polaris detector happened within a specific time window of an event in the

$LaBr_3$:Ce detector. It was assumed that the faster $LaBr_3$:Ce detector would trigger the coincidence event first, followed by the slower Polaris detector due to the inherent difference in processing times.

The likelihood of coincidence events between the Polaris detector and $LaBr_3$:Ce detector were calculated by analysing the temporal relationship between detected events. Initially, data from both detectors were filtered, sorted, and processed based on energy windows to isolate potential coincidence events around the 511.0 keV range. For each Polaris event, the time difference with preceding $LaBr_3$:Ce events were calculated and stored. These time differences were then grouped into predefined time windows, and the number of coincidences in each window were plotted, seen in Fig. 6.3.5. The time window with the highest number of coincidences was identified as situated between 50 and 60 µs, and the Polaris and $LaBr_3$:Ce event energies within this window were further analysed in Fig. 6.3.6. The analysis provided insights into time-correlated events, crucial for studying interactions between gamma rays in both detectors. By focusing on time windows with the most coincidences, this method aimed to isolate events that were likely to be in coincidence. Fig. 6.3.6 showed that there was a slightly higher concentration of coincidence events in the range of the 511.0 keV peak region. It is important to note that duplication of events did not occur in the alignment of coincidence events.

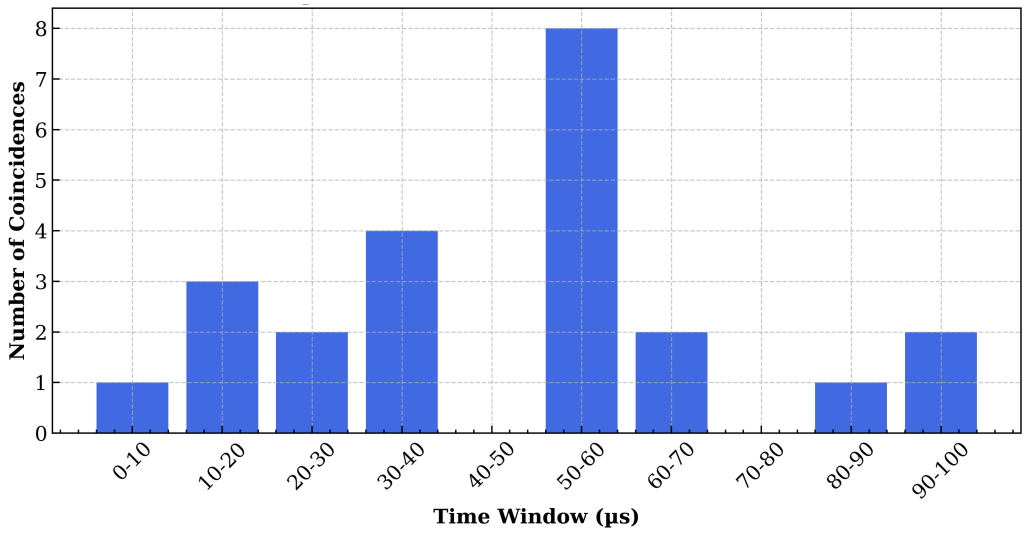

Figure 6.3.5: The time difference between energy-gated (± 5% of 511.0 keV) $LaBr_3$:Ce and Polaris events measured in a coincidence face-to-face geometry using a low activity ^{22}Na source. The time difference was calculated between a $LaBr_3$:Ce event and a Polaris event that occurred after it in time. The y-axis represents the probability of a coincidence within each of the time difference windows.

6.3.4 CC1 Source Measurement

Low activity ^{137}Cs (33.97(340) kBq) and ^{60}Co (22.72(227) kBq) sources were placed on top of one another, 10 cm away from the centre of the Polaris scatterer module crystal positions of CC1. The distance between the physical layers of CC1 was 1 mm, as near as possible, and a measurement was taken for a 10-minute period. The STM pulses were used to align

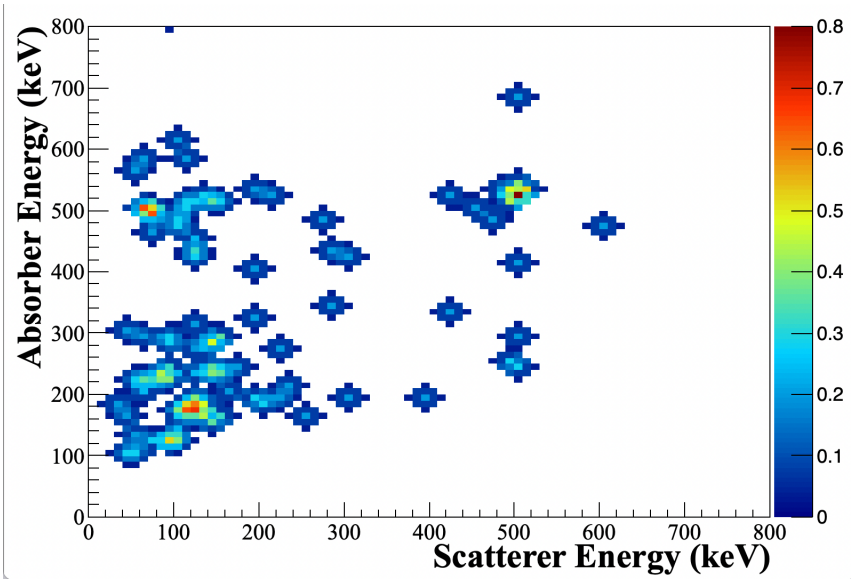

Figure 6.3.6: The 2D energy matrix of coincident events between Polaris and $LaBr_3$:Ce detectors measured using a low activity ^{22}Na source placed (0,0,10) mm. The scatterer and absorber axes represent the energy recorded in the Polaris and $LaBr_3$:Ce detectors, respectively, kept consistent with CC1. The coincidences were isolated by grouping $LaBr_3$:Ce events with a Polaris event that occurred 55(5) µs after it in time. No energy filtering was applied.

the timestamps of each DAQ, as described in Section 3.3.7. Further time synchronisation involved grouping $LaBr_3$:Ce events with a Polaris event that occurred 55(5) µs after it in time, determined in Section 6.3.3 as the most frequent time delay experienced by the Polaris DAQ. The CC1 results are shown, where Fig. 6.3.7(a) is the 2D energy matrix of coincident events between Polaris and $LaBr_3$:Ce detectors measured using ^{60}Co and ^{137}Cs sources placed (0,0,10) mm from the CC1 detector face. It was anticipated that with the correct event timing synchronisation applied, distinct diagonal CC events would emerge with a higher intensity than the surrounding events, as was demonstrated by Fig. 2.4.2. These events were expected to have this relationship in the CC due to how gamma rays from the source interact with the camera via Compton kinematics. The relationship between the scatterer energy and the absorber energy for a given gamma-ray energy depends on the scattering angle θ_1. When plotting the energies against each other, the points will fall along a line whose slope and intercept are determined by the gamma-ray energy and the scattering angle. Figure 6.3.7(a) should produce these diagonal lines at each of the strong PG emission lines: 661.7, 1173.2 and 1332.5 keV.

Further reason to believe that the event timing was not accurate was seen in Figure 6.3.7(b). In the plot of scatter angle (θ_1) versus energy deposited in the scatterer (E_1) for gamma-ray sources ^{60}Co and ^{137}Cs, distinct patterns should emerge. For ^{60}Co, two separate curves for each emission line should have appeared, each corresponding to one of the gamma-ray energies. These curves should have started from $E_1 = 0$ at $\theta_1 = 0°$ and increased, reaching higher E_1 values as θ_1 approached 180°, with the curve for the higher energy (1332.5 keV) lying above the one for the lower energy (1173.2 keV). The ^{137}Cs source, emitting a single gamma ray of 661.7 keV, should have displayed a single curve that was positioned lower on the E_1 axis compared to the curves for ^{60}Co, reflecting the lower gamma-ray energy. Overall,

the results of Fig. 6.3.7(b) revealed a shape inconsistent with the Compton scattering process, displaying no variations in vertical positioning based on gamma-ray energy.

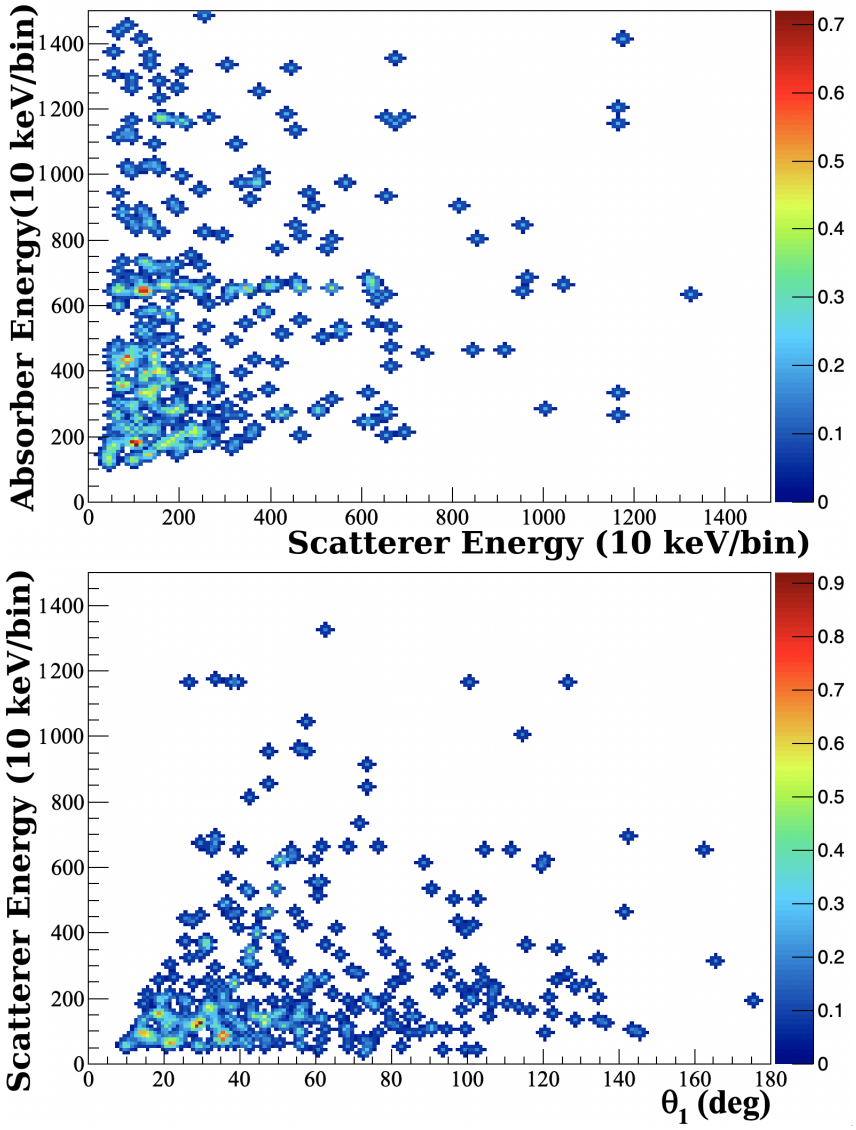

Figure 6.3.7: (a) The 2D energy matrix of coincident events between Polaris and $LaBr_3$:Ce detector events, measured using ^{60}Co and ^{137}Cs sources placed (0,0,10) mm from the CC1 detector face. The scatterer and absorber axes represent the energy recorded in the Polaris and $LaBr_3$:Ce detectors. The coincidences were isolated by grouping $LaBr_3$:Ce events with a Polaris event that occurred 55(5) μs after it in time, and (b) the relationship between the scattering angle (θ_1) and the scatterer module, calculated using the Compton scattering equation (Eq. 2.1.2)

The data was further refined by using the CLF to exclude non-physical scattering events in the data seen in Fig. 6.3.7, such as those not resulting from double or triple scatter gamma rays. The application of CLF helps to isolate and identify these "good" scatter events, which align with theoretical Compton scattering predictions by excluding θ_1 values that do not obey the physical principles, and gating on scatterer and absorber energies that obey the energy relationship of the equation. The Compton relation for the energy deposited in the initial scatter (E_1) as a function of the scatter angle (θ_1) can be derived from rearranging Eq. 2.1.2, resulting in:

$$E_1 = \frac{E_0\alpha(1-\cos\theta_1)}{1+\alpha(1-\cos\theta_1)}$$

where $\alpha = E_0/m_e c^2$.

This was performed to ensure that non-physical events were not obscuring CC behaviour in the data. Figure 6.3.8 shows the result of applying CLF to Fig. 6.3.7. It can be seen that the CLF seems to force the Compton scattering behaviour to emerge in the data.

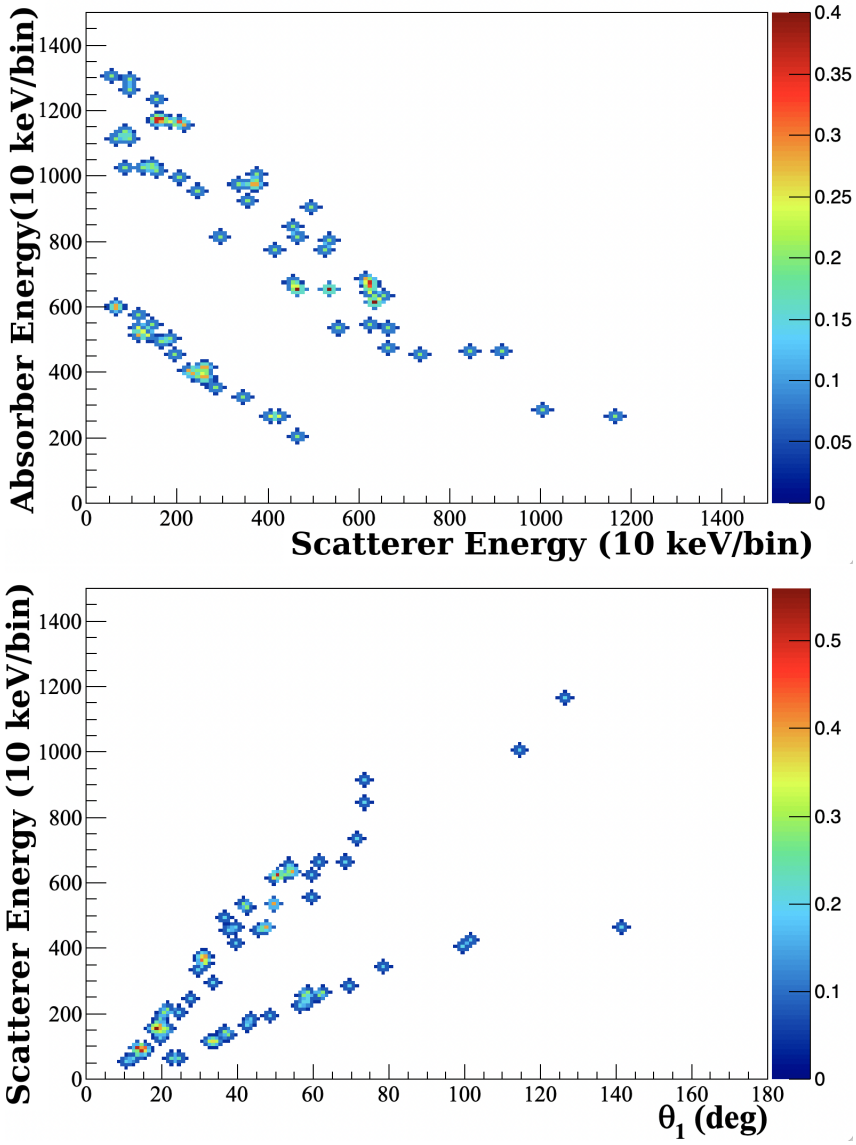

Figure 6.3.8: (a) The CLF 2D energy matrix of coincident events between Polaris and $LaBr_3$:Ce detectors measured using ^{60}Co and ^{137}Cs sources placed (0,0,10) mm from the CC1 detector face. The scatterer and absorber axes represent the energy recorded in the Polaris and $LaBr_3$:Ce detectors. The coincidences were isolated by grouping $LaBr_3$:Ce events with a Polaris event that occurred 55(5) µs after it in time, and (b) the relationship between the scattering angle (θ_1 and the scatterer module after CLF was applied, calculated using the Compton scattering equation (Eq. 2.1.2)

For completeness, the same time offset and filtering technique was applied to the beam-time data. The need for CLF in event discrimination was underscored in previous works such as [53], where a Polaris CZT CC was used to track gamma-ray interactions from a water target. The study demonstrated how advanced filtering techniques are crucial for refining imaging

results. Further findings were reported by [56], where a multi-stage Polaris CZT CC was used to track gamma rays from a water target.

In previous studies, gamma-ray emission lines from carbon and oxygen have been strongly linked with proton depth-dose distributions, making them highly valuable for PG applications [109, 53]. These emission lines, crucial for PG, arise from inelastic proton interactions with nuclei such as oxygen. However, in this analysis, the plot of E1 values against the calculated scattering angle, θ_1 (Fig. 6.3.9), revealed certain challenges. Figure 6.3.9 shows the identified key emission lines, where label 1 (5240.0 keV) represents a typical emission from inelastic proton scattering with ^{15}O nuclei, potentially involving higher-order escape peaks. Label 3 (4438.94 keV) corresponds to interactions with ^{12}C nuclei, while label 5 (2741.5 keV) indicates a ^{16}O prompt emission. These represent interactions with oxygen and carbon nuclei but lack the distinctive Compton scattering signatures necessary for precise imaging. The application of CLF (+/- 10%) around the 2741.5, 4438.94, and 5240.0 keV PG emission lines was performed in an attempt to identify valid scatter events consistent with theoretical Compton scattering predictions. Prior to CLF, the data points exhibited linear trends inconsistent with Compton scattering models, emphasising the need for accurate event classification. Figure 6.3.9 shows how the CLF forces the Compton scattering kinematics trend in the beam data; however, no distinct CC behaviour was distinguishable in the top plot (For reference, refer to Section 2.4.2, where the kinematic behaviour of the CLF was discussed). This was due to the high count rate ($\sim$ 4000/s) during beam irradiation, and the long DAQ processing time of the scatterer detector, making it challenging to track double scatter events. The high in-beam rates increased the likelihood of two or more different PGs undergoing simultaneous detection, creating noise that further mask the CL in the data.

Label 2 in Fig. 6.3.9 appears as a line beginning at $\sim 30^\circ$, crossing the 511 keV point around 60°, and gradually rising toward 90°. This line corresponds to events in which a PG Compton-scattered photon (E1) and a 511 keV gamma-ray (E_2) were detected simultaneously. Label 6 depicts the interaction of simultaneous 511.0 keV gamma rays (E_1 and E_2) from the water target. The line at a constant energy of $\sim$ 3400 keV is observed across all angles, seen as label 4. This line represents a pair production event involving a 4438.94 keV photon (E_1 = 4.44 - 1.022 MeV) detected simultaneously with another gamma-ray (E_2). These three labels involve interaction types which do not have the shape of the CL kinematics as they are not true coincident Compton scatters.

Overall, the extensive timing synchronisation, offset correction and filtering techniques applied could not correct for the variable timing problem introduced by the Polaris DAQ into the CC1 design. This prevented CC events from being tracked across the detector geometries. The results suggest that this CC design would not produce a feasible CC. The imaging challenges highlight the necessity for precise event classification, whether it's through timing adjustments in coincidence detection or energy-based filtering in proton imaging.

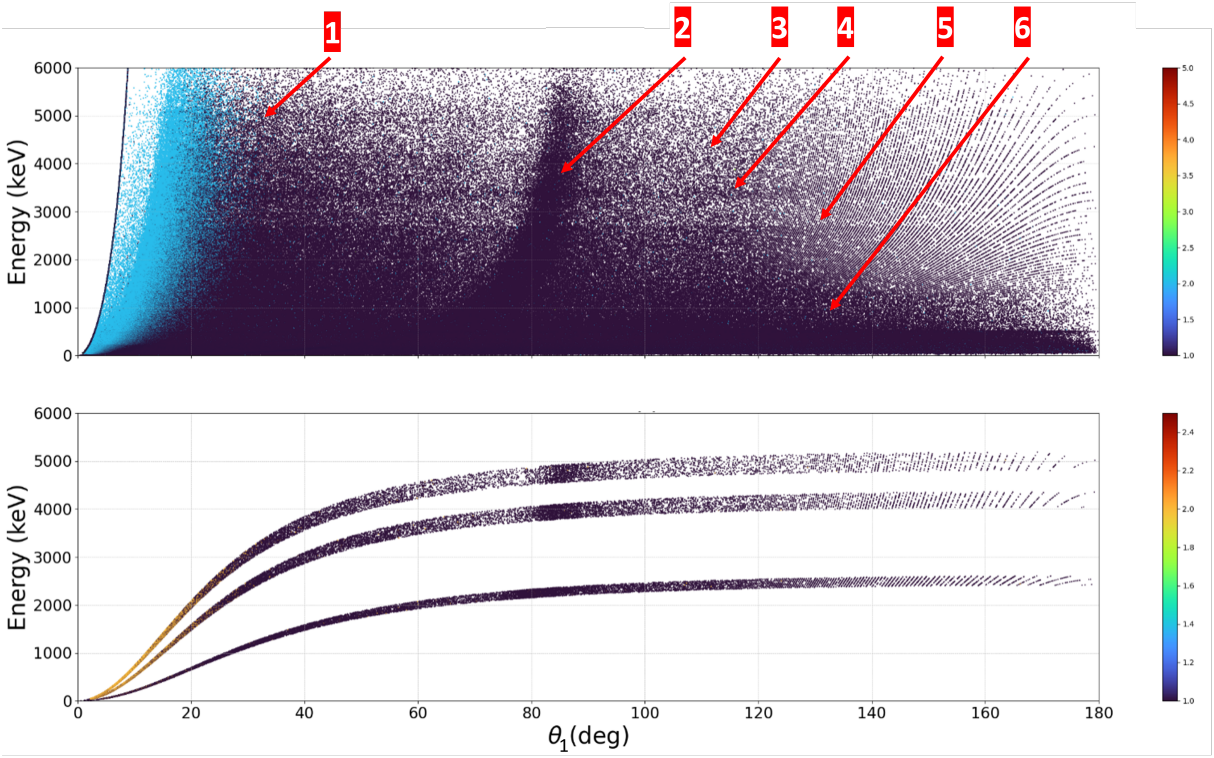

Figure 6.3.9: Top: Scatter plot of E1 values versus the calculated scattering angle θ_1 illustrating the characteristic emission lines associated with various interactions. Bottom: The application of CLF (+/- 10% around each PG emission line: 2741.5, 4438.94, and 5240.0 keV) assists in identifying valid scatter events consistent with theoretical Compton scattering predictions.

6.3.5 Final Timing Investigation

To refine the analysis, the coincidence data were examined by evaluating the time offset of the Polaris events. For each $LaBr_3$:Ce event, the time difference to the subsequent Polaris event was iterated, adjusting the Polaris event times by adding up to 300 µs in 10 µs increments. After each time adjustment, the coincidence events between the two detectors were re-assessed. A 2D matrix of energies recorded by both detectors was constructed for each time offset to visualize the presence of coincidences. The aim was to identify a strong peak around 511.0 keV in the matrix for both detectors, which would indicate successful coincidence detection following the correct time offset.

The 2D energy matrices are shown in Figure 6.3.10, with the scatterer and absorber axes corresponding to the CC1 geometry (Polaris and $LaBr_3$:Ce, respectively). As the time offsets were applied and visualised, it became evident that a 15 µs offset produced no 511.0 keV coincidences. Moreover, as the time offset increased, up to and beyond 35 µs, there was no significant improvement in detecting coincidence events. While more statistics were introduced with increasing time shifts, no distinct coincidence pattern emerged, making it impossible to

definitively identify true coincidences. This behaviour suggests why the 50.0–60.0 µs event offset correction returned no feasible CC results.

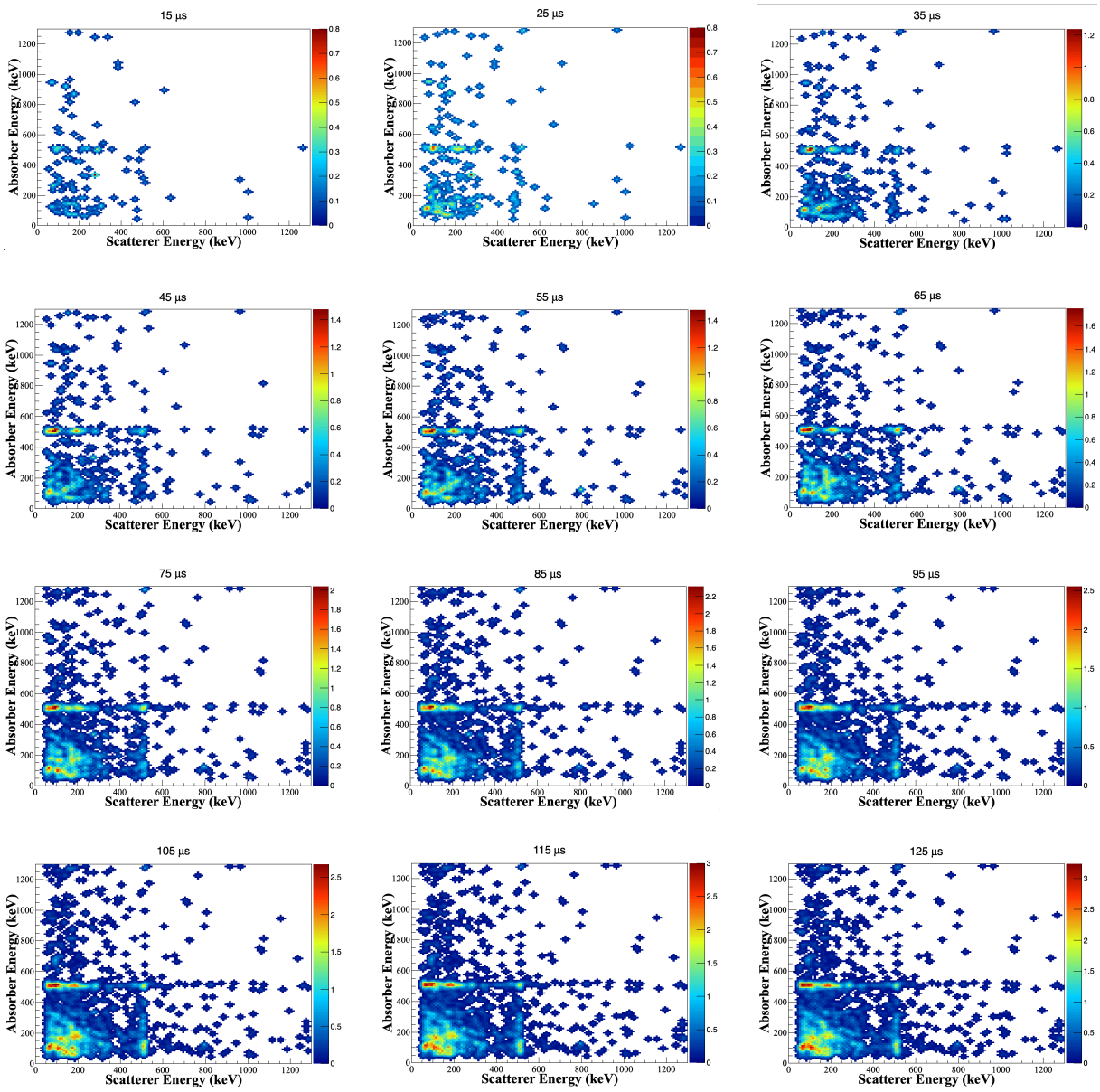

Figure 6.3.10: The 2D energy matrices of coincident events between Polaris and $LaBr_3$:Ce detectors as a function of varying time offsets (15–125 µs). The scatterer and absorber axes represent the energy recorded in the Polaris and $LaBr_3$:Ce detectors, respectively. Time shifts are applied to the Polaris events in increments as indicated in each matrix title. No distinct 511.0 keV coincidence peak was observed across the matrices, with changes in intensity attributed to statistical fluctuations rather than true coincidences.

7 INTERPRETATION OF RESULTS

In this study, the feasibility of three CC designs were investigated for potential application in medical imaging. The performance of these designs were assessed by simulating and experimentally measuring their responses to different gamma-ray sources. The CC1 design was also investigated using the PG response of a 66.67 MeV proton beam incident on a water target.

7.1 SUMMARY OF SIMULATION FINDINGS

This study implemented the use of comprehensive TOPAS simulations to verify the performance of various detector CC prototypes. Simulations were compared with experimental measurements to assess energy deposition and FEPE performance. The physics of the experiment was well reproduced by the simulated physics lists as all known peaks in the spectrum of ^{152}Eu were present in the simulated gamma-ray spectrum. However, discrepancies were noted for the Polaris detector due to charge build-up effects, which were not modeled in the simulation. This led to narrower simulated photopeaks in the simulated energy deposition spectrum of the ^{152}Eu source compared to the broader and tailed peaks observed experimentally, but which were not seen to affect the FEPE calculations. The FEPE simulations reflected the detector specifications accurately, showing agreement below 2σ with experimental results for the $2'' \times 2''$ $LaBr_3$:Ce, Polaris and $LaBr_3$:Ce DA detectors. The simulation FEPE results for the higher-energy 964.08 keV peak were consistent with experimental data, while the lower-energy 344.28 keV peak showed some differences due to threshold and pulse pile-up effects.

The simulation demonstrated satisfactory performance for most detectors, confirming the effectiveness of the TOPAS framework in replicating physical interactions and validating detector efficiency and energy deposition. Further work is suggested to address pulse shape analysis and corrections for detected imperfections. The simulated Sr_2:Eu FEPE response was unable to reproduce experimental measures for the 344.28 keV peak for source-to-detector distances of 10, 30, and 50 mm, and was not investigated further for use in a CC as the simulation did not model the pulse pile-up effects seen in experiment.

7.1.1 Comparison of the Simulated Performance of the Compton Cameras

7.1.1.1 *Compton Camera Efficiency*

The efficiency of a CC is defined as the ratio of the number of imageable Compton cones to the total number of emitted gamma rays. This efficiency is influenced by several factors, including the distance between the gamma-ray source and the detector, the FOV of the scatter layer, and the material properties of the detectors. Increasing the distance between the source and the scatterer leads to geometric attenuation and higher scattering probabilities, which generally reduces efficiency. The efficiency also depends on the size of the scatter layer and the material's density and thickness. The simulations, summarized in Table 6.2.1, revealed that CC3 achieved the highest efficiency, recording 8.57×10^{-5} and 2.49×10^{-6} cones/history at source-to-scatterer face distances of 10 mm and 100 mm, respectively. Despite its smaller size, CC2 geometry 3 demonstrated competitive performance, with efficiencies of 4.35×10^{-5} and 1.31×10^{-5} cones/history at the same distances. This design benefited from a larger scatterer surface area, enhancing photon capture. Conversely, CC1's lower efficiency was attributed to its smaller scatterer surface area and the large distance between the CC layers, enforced by the physical constraints of the Polaris detector box geometry, which decreases the likelihood of photon interactions. Notably, the efficiency decreases as the distance between the scatterer and absorber layers increases, with CC2 geometry 3 maintaining the highest efficiency across different distances among CC2 designs. This design is favoured over that of CC3, taking advantage of the SiPM readout in both the scatterer and absorber layers and modularity of the design.

The efficiency results also varied with different gamma-ray sources, seen in Table 6.2.3. The efficiency for ^{22}Na (emitting gamma rays at 511.0 keV and 1274.5 keV) was higher compared to ^{137}Cs (emitting at 661.7 keV) across all CC configurations. This was expected, as the lower energy photons of ^{22}Na were more likely to be absorbed fully by the detectors. CC2 geometry 3 consistently demonstrated superior efficiency for both sources among CC2 designs. CC3 again exhibited the highest efficiency, measuring 8.57×10^{-5} and 3.04×10^{-4} cones/history for ^{137}Cs and ^{22}Na, respectively, while CC1's efficiency was lower due to the inherent constraints of the design.

7.1.1.2 *ARM*

The ARM is a crucial metric for evaluating the performance of a CC, as it measures the precision in reconstructing the Compton scattering angle, θ_{CC}. Lower ARM values indicate more accurate source localisation, which is essential for applications requiring precise imaging. The ARM was assessed by analysing the FWHM of the ARM distribution.

Figures 6.2.1 and Table 6.2.4 revealed that ARM improves with increased distance between the scatterer and absorber layers. This was attributed to the larger distance allowing for more precise angle measurements, reducing uncertainty. However, there was a trade-off, as

increasing this distance can decrease efficiency, which was observed in the efficiency data for different distances.

CC2 geometry 1 achieved the highest ARM due to its thicker scatterer and absorber modules, which provide more material for gamma-ray interactions. Despite having lower FEPE, this design's enhanced accuracy in source localisation makes it advantageous in terms of ARM, highlighting the possibility that an ideal CC design would encompass a trade-off in parameter optimisation. On the other hand, CC1's ARM decreased with increased scatterer-absorber distance, indicating potential limits to the improvement offered by larger distances.

7.1.1.3 Influence of Backscattering Events on Image Reconstruction

BSE can introduce noise and artefacts into reconstructed images, which reduces sharpness and ARM. Simulations showed that for a ^{137}Cs source, BSE were concentrated around 200.0 keV, as illustrated in Figures 6.2.3–6.2.7. To mitigate these effects, energy thresholds would be applied to these regions of high contribution in experiment post-processing to filter out high BSE and to improve image outcomes. In the case of CC1, BSE had minimal impact due to the greater distance between the scatterer and absorber layers. However, CC3 and CC2 designs showed significant contributions from BSE, necessitating energy gating to improve image quality in experimental measures.

7.1.1.4 Image Reconstruction for Different Gamma-Ray Sources

The image reconstruction performance of ^{22}Na and ^{137}Cs sources was compared to assess how different gamma-ray energies affect image quality. The results indicated that ^{137}Cs, with a single prominent energy peak, provided better image resolution compared to ^{22}Na, which has two distinct peaks. Across various CC designs, the FWHM was smaller for ^{137}Cs, reflecting better image quality. For instance, CC1 had a FWHM of 3.20 mm, while CC2 and CC3 designs exhibited slightly larger values. Despite geometric constraints, CC1's superior energy resolution with CZT mitigated some of the limitations, though it still had fewer detected statistics compared to other designs. In summary, ^{137}Cs yielded better image reconstruction results due to its single energy peak. In contrast, the two energy peaks in the spectrum of ^{22}Na introduce additional challenges, leading to slightly reduced image quality. The findings underscore the importance of optimising detector designs and energy settings for improved performance in specific imaging applications.

7.1.1.5 *Impact of Distance on Image Reconstruction*

Source-to-Detector Distance Effects:
The 88 mm separation between the crystals in CC1 resulted in poor source localisation as the distance increased, with the predicted source position deviating by 30.13 mm from the true location, and a FWHM of 3.35(59) mm. In contrast, CC3 exhibited a 1 mm increase in FWHM with increased distance, but still accurately predicted the source position. CC2 geometry 1 showed robustness to increased distance. The FWHM remained below 4 mm, indicating minimal degradation in image quality with distance. This suggests that CC2's geometry 1 effectively mitigated the negative impacts of increased source-to-scatterer distance.

Impact of Scatterer-to-Absorber Distance:
For a ^{137}Cs source 10 mm from the scatterer, CC1's image reconstruction was significantly distorted, with a source localisation uncertainty of ~ 50 mm. CC3 and CC2 exhibited a slight improvement in resolution with increased distance, with FWHM values improving slightly (e.g., CC3 from 3.71(1) mm to 3.61(2) mm). This counter-intuitive result may be due to reduced edge effects and better delineation of the Compton cone projection. Increased distance between the scatterer and detector generally degrades image quality due to broader spatial resolution and geometric distortions. However, certain geometrical configurations (e.g., CC2) can maintain or even improve resolution under these conditions.

7.1.1.6 *Reconstruction of Multiple Sources*

^{22}Na Sources:
Simulation results with two ^{22}Na sources (at $(8, 0, 10)$ mm and $(-8, 0, 10)$ mm) tested the ability of different CC designs to resolve closely spaced sources. CC1 achieved excellent resolution, with FWHMs of 4.24(114) mm and 4.12(108) mm. In contrast, CC3 had more difficulty, with a larger FWHM and poorer statistical confidence for the second source. CC2 geometries performed well, with the best results from geometry 1.

^{60}Co and ^{22}Na Sources:
For a combination of ^{60}Co and ^{22}Na sources, the higher energy contribution of ^{60}Co decay resulted in more intense images due to increased Compton scattering and coincidence detections, whereas the lower energy and single photon emission of ^{22}Na led to a less intense image. Despite these intensity differences, CC1 and CC2 geometry 1 performed best in reconstructing both sources with high accuracy and resolution.

The results of the simulations highlighted two notable contenders for high-performance CC designs: CC2 geometry 1 and CC1. CC2 geometry 1 displayed exceptional ARM due to its thicker scatterer and absorber modules, making it highly accurate in source localisation, though it had slightly lower efficiency. CC1, while constrained by its smaller scatterer area and larger source-to-scatterer distance, showed superior image resolution for specific sources and scenarios, such as closely spaced ^{22}Na sources. Despite its geometric challenges, CC1's energy

resolution and detection capabilities made it a strong competitor, especially when attributed to its CZT material scatterer.

7.2 SUMMARY OF EXPERIMENTAL FINDINGS

The experiments performed for the CC1 design involved both beam and source measurements to evaluate its performance. Two months into the project, a 66.67 MeV proton beam from the separated sector cyclotron at iThemba LABS in Cape Town, South Africa was provided. This beam, structured with a 300.0 ns interval between pulses and a 1 in 5 pulse selection rate, was chosen to facilitate synchronisation with the DAQ for effective background subtraction.

Significant background radiation in both source and beam experiments primarily stemmed from the internal radioactivity of the $LaBr_3$:Ce detectors. This background, due to naturally occurring ^{138}La and impurity ^{227}Ac, notably affected the sensitivity for detecting gamma rays up to about 2.5 MeV. The ^{138}La decay, especially the peak around 1460.0 keV, was a prominent background contributor, obscuring photopeaks of interest. Comparisons between $2'' \times 2''$ and SiPM-coupled detectors highlighted that larger detectors exhibited higher background contributions due to increased crystal volume.

Background subtraction techniques proved highly effective in mitigating internal radioactivity in both source and beam measurements, allowing for improved peak clarity. The background subtraction performed for the beam measurements made use of the proton beam RF by correlating PG emissions that were in-sync and out-of-sync with the beam pulses, allowing for effective background subtraction, primarily in the low-energy region. This allowed for only PG statistics to be used in the CC event tracking, reducing the likelihood of non-physical double scatter contributions from the $LaBr_3$:Ce detector. The correction of the time-walk in both the source and beam measurements allowed for the use of the fast timing (measured in this study to have a time resolution with FWHM 218.08(11) ps) signal in conjunction with the slow energy signal (optimised in source measurements to have energy resolution of 4.073(85)% at 661.7 keV), maximising on the strengths of the $LaBr_3$:Ce detector capabilities and further reducing timing uncertainty in the detector.

7.2.1 Beam Measurements

The gamma-ray energy spectra from the CC1 design, showing interactions of the proton beam with the water target, revealed key insights. The Polaris detector exhibited poor dynamic range and lacked visibility of the PG emission lines. The early acquisition of beam-time data with unoptimised DDAS shaping parameters resulted in subpar energy resolution for the $LaBr_3$:Ce detector.

7.2.2 Coincidence Measurement and Timing Investigation

Detailed analysis of beam-time data revealed challenges in timing synchronisation due to the Polaris detector's processing onboard electronics, which introduced significant event time offsets. Attempts to correct this first involved the use of correlating DAQ clock times with the use of 2 s interval STM pulses, followed by adjusting Polaris event times by an offset determined from coincidence measurement, which did not significantly improve accuracy. Coincidence timing measurements using a ^{22}Na source in a face-to-face detector configuration aimed to identify consistent timing patterns, facilitating accurate double scatter tracking. The analysis of time differences between detectors identified a peak coincidence window between 50.0 and 60.0 µs, which aimed to provide a more accurate representation of coincidence events. Further investigations with low-activity ^{137}Cs and ^{60}Co sources revealed that this timing offset between Polaris and $LaBr_3$:Ce events was insufficient to produce the expected Compton behaviour. The sources were placed close to the Polaris scatterer module, with timing synchronisation achieved by grouping $LaBr_3$:Ce events with Polaris events occurring 55(5) µs later. The expected diagonal patterns in the 2D energy matrix, representing interactions of gamma rays with the CC1 detector, were not clearly visible. The lack of distinct patterns suggested inaccuracies in event timing.

Further filtering using the CLF technique aimed to isolate valid Compton scatter events from non-physical ones. The application of CLF improved alignment with theoretical Compton scattering predictions, although distinct Compton scattering behaviour was not observed. The results indicated that the CC1 design struggled with precise event tracking, underscoring the need for a better understanding of the Polaris processing electronics and how massive the timing delay introduced should be. To refine the analysis, time offsets were adjusted incrementally up to 300.0 µs to reassess coincidence events. Despite these efforts, the challenges with timing synchronisation persisted, highlighting the difficulties in achieving accurate tracking across detector geometries with this combination of detectors.

The ability to track events across a CC where one layer has 218.08(11) ps timing resolution and the other suffers possibly greater than 10.0–100.0 µs event delays provides a potentially insurmountable challenge as the confidence in the events, even once a timing offset was applied, was not promising.

The timing challenges encountered in CC1 design would not be encountered for CC2 and CC3 in experimental measures. A benefit of the experimental implementation of these designs lies in the detector instrumentation. The detectors would all be instrumented using the Pixie-16 500 MHz DAQ, ensuring fast timing capabilities and clock time synchronisation of the detectors. It is reasonably assumed from literature that the $LaBr_3$:Ce DA modules will demonstrate a time resolution in the order of ~ 300 ns, as it is consistent with the crystal type and SiPM coupling [110, 111, 112, 113].

7.3 SUMMARY OF FINDINGS

CC1 showed great promise in the results of the MC simulation. The inherent geometrical constraints of the design posed limitations to the CC efficiency; however, the simulated ARM (1.87(4) °) and image reconstruction FWHM values consistently demonstrated excellent performance across a variety of source and geometrical configurations. The limitations of the design became apparent in the form of timing delays introduced by the Polaris detector onboard electronics module. Efforts were undertaken to ensure event timing synchronicity between the Pixie-16 DAQ employed by the $LaBr_3$:Ce CC1 absorber and Polaris scatterer DAQ systems. RF-guided background subtraction was performed on the $LaBr_3$:Ce absorber events to remove events that were not correlated to the timing structure of the cyclotron beam. Background subtraction was also performed on source measurement data of both CC1 modules by removing the background measured during the same time duration, obtained under the same experimental conditions. The removal of background contamination allowed for greater CC event confidence. To ensure that the $LaBr_3$:Ce detector was operating optimally, the time-walk between the fast channel used for <300.0 ps timing resolution and the slow channel used for ~ 3% energy resolution was corrected for. Further, a ^{22}Na source coincidence timing investigation was undertaken to quantify the processing delay in the Polaris system once an event had been detected; however, a coincidence window that produced the expected CC behaviour was not isolated.

The tracking of double scatter events across the CC1 hybrid design was unsuccessful due to the timing challenges encountered. A further constraint in these timing measurements was encountered as one of the two Polaris-J detectors proposed for the project suffered an irreparable electronics failure. Had this detector been available, a double coincidence timing measurement would have been performed to measure a Polaris detector in coincidence with another Polaris detector and the $LaBr_3$:Ce detector with the aim of gaining deeper insight into quantifying the delay to allow for image reconstruction to be performed from the valuable source and beam-time data obtained. For these reasons, the CC system was not found to be clinically viable.

Among the other CC designs investigated, geometry 1 of CC1 showed great performance in simulation, as mentioned above. The benefits of this CC design include the low-voltage power supply (30 V) bias and the modularity of the DA modules that make up the CC layers. The modular design provides a unique flexibility in its scalability. This configuration allows for the continuous expansion of the detection system by adding more detector units, thus increasing the position sensitivity, efficiency, and overall resolution of the system. As more detectors are integrated, the camera's ability to accurately track and image gamma radiation improves. This flexibility enables the camera to be customised for various applications, ranging from small-scale setups for focused imaging tasks to larger arrays for high-resolution imaging in medical or environmental monitoring. For optimal in vivo range verification, it is necessary to gather sufficient data during the delivery of a small portion (e.g., $\leqslant$ 20%) of the dose for each treatment field in a daily session, necessitating a high efficiency in the CC design [5]. This data should enable precise localisation of the beam range within a margin of 1.0–2.0

mm. [5]. In a clinical setting, imaging needs to be fast enough to be practical. This means the CC should achieve a high rate of valid cones per second, typically corresponding to a FEPE that can handle the emitted gamma rays without needing prolonged acquisition times. The results of the MC simulation and experiment suggest that the CC2 geometry 1 design would be a suitable candidate for further investigation in terms of clinical viability.

It is worth noting that the simulated image reconstruction using the Octane EM method produced FWHM and ARM values that were highly ideal due to the nature of position resolution scoring in the simulation. Benchmarking of the simulation results for CC2 geometry 1 against current literature suggests that the values were better than what would be experimentally achievable. In a CC study performed by [10], an array of 22 $\times$ 22 GAGG crystals coupled to an MPPC SiPM array was used as the scatterer module and a monolithic $LaBr_3$:Ce detector coupled to 64-channel PMT was used as the absorber. The obtained ARM value for a ^{60}Co source was 6° from simulated data and nearly double for images from experimental data. Recent PG imaging systems can detect differences of about 2 mm for low-energy proton beams (<50.0 MeV) and ~ 3 mm for higher-energy beams (120.0—-150.0 MeV). Most research has been conducted using homogeneous phantoms, with accuracy varying based on the number of primary particles [114, 115]. The simulations performed give valuable insight into the CC performance and can be endlessly adapted to incorporate more information as it becomes known. Further instrumentation of the design will involve the coupling of more SiPM to the geometry to introduce greater position sensitivity and pixelation, as discussed in 8.1.

8 CONCLUSIONS

This work has evaluated the performance of three CC designs (CC1, CC2, and CC3) making use of different detector configurations and geometries to enhance gamma-ray imaging capabilities. The primary objectives were to assess detection efficiency, energy resolution, timing accuracy, and image reconstruction performance through both MC simulations and experimental validations to gain understanding into the feasibility of using these CC detection systems in a PT treatment scenario.

The simulation results demonstrate that CC2 geometry 1 emerged as the most promising design based on simulation and very limited experimental performance. This configuration showed superior ARM and efficient gamma-ray detection, although it exhibited slightly lower efficiency compared to other designs. The CC2 geometry 1's modular design and low-voltage operation offer flexibility and scalability, making it suitable for high-resolution imaging applications.

The MC simulations, conducted using TOPAS MC toolkit, accurately reflected the performance of the detector systems, particularly for the $LaBr_3$:Ce detectors and the Polaris detector. The simulations provided valuable insights into detector performance, though some discrepancies, particularly for high and low-energy peaks in the performance of the Sr_2:Eu and Polaris detectors, highlighted the need for further refinement in pulse pile-up and charge build-up modeling.

The study found that increasing the distance between the scatterer and absorber layers improved ARM but often at the expense of detection efficiency. CC2 geometry 1 balanced these parameters effectively, maintaining a high ARM while offering robust performance across various source-to-detector distances. In contrast, the CC1 simulations demonstrated excellent image resolution in specific scenarios, such as closely spaced ^{22}Na sources, despite its geometrical constraints and timing synchronisation challenges.

The Polaris detector, used in the CC1 design as the scatterer, exhibited significant timing synchronisation challenges. This issue stemmed from the limitations in the detector's electronics, which affected the precision with which double scatter events could be tracked. In a CC system, accurate timing synchronisation between the scatterer and absorber detectors is crucial for determining the correct interaction positions and energy deposition of gamma rays. The Polaris detector's electronics struggled with this synchronisation, leading to difficulties in distinguishing double scatter events. This timing issue resulted in an ability to accurately reconstruct the gamma-ray source locations, as the system's resolution was compromised by the misalignment in timing data. The problem was evident in both source and beam measurements.

8.1 OUTLOOK

8.1.1 Improvement of Simulation

The simulation will model pulse pile-up effects in the Sr_2:Eu detector by simulating the temporal behaviour of events, the detector's signal response, and simulating digital integration of summed overlapping pulses. Pulse pile-up occurred in the experiment, causing two or more signals to overlap in time due to long shaping times in the electronics. This was not modelled for in simulation, resulting in a discrepancy between simulated and measured detector efficiency. Without such adjustments, the simulation could give a falsely optimistic picture of the detector's ability to resolve closely spaced photopeaks, potentially leading to inaccurate conclusions when comparing the efficiency, resolution, or overall performance between the simulated and real detector systems.

8.1.2 Compton Camera Position Sensitivity

Future work to introduce position sensitivity in the CC1 and CC2 designs for experimental measures would involve the coupling of recently acquired Broadcom AFBR-S4N44P164M 4×4 SiPM array to the face of the DA modules [116, 45]. Work is underway to instrument the SiPMs for independent read-out of the four SiPM quadrants, with the overarching aim of ensuring that the detector designs remain compact. The modularity of the DA design allows the stacking of DA modules to the scatterer and absorber layers to improve CC sensitivity.

The feasibility of adapting the 17×17 mm face of the aluminium detector casing can be explored to see if any small sections could be modified to include optically transparent materials (e.g., glass, acrylic) as an optical window to directly couple the SiPM array to the transparent section. The limitation of this method is that it would require modifying the pre-assembled housing, which might not be possible depending on the assembly's design constraints and the hygroscopic nature of the $LaBr_3$:Ce and SrI_2:Eu crystals within.

A different approach would involve the use of an optical coupling method, similar to how optical grease is often used between scintillators and photodetectors. A thin light guide sheet (e.g., room-temperature-vulcanising material) could be placed between the aluminium casing and the SiPM array to allow the transmission of scintillation photons that escape the casing. The light guide would transfer photons from the scintillator within the casing to the SiPM array. The light guide should be as thin and optically efficient as possible to minimise signal loss and allow for reasonable photon collection through the aluminium wall. This could necessitate the need to create a custom housing that aligns the SiPM array tightly against the detector casing to ensure optimal photon transfer. A limitation of this method is that aluminium is not highly transparent to scintillation light, so this method might suffer from significant signal attenuation.

These two proposed methods to add position sensitivity to the DA detectors would allow for position measurements in the x and y directions due to the introduction of the Broadcom SiPM. By using the Broadcom SiPM array on one side of the $14 \times 14 \times 25.4$ mm DA in conjunction with the DA pre-assembled single readout SiPM array on the opposite side, timing to estimate the DOI of gamma rays within the 25.4 mm depth could be employed. When a gamma ray interacts within the scintillator, the scintillation light is emitted and travels to both SiPM arrays on opposite sides. The time difference in the arrival of the light signals at the two arrays can be used to infer how deep in the 25.4 mm dimension the interaction occurred. By measuring the time difference between the light reaching the two SiPM arrays, an estimate of the DOI based on the speed of light in the scintillator material can be determined. The equation to represent this calculation is as follows:

Assuming v_{light} is the speed of light in the scintillator material:

$$DOI = \frac{d}{2} \pm \frac{\Delta t \times v_{light}}{2}$$

where: d is the total thickness of the scintillator (25.4 mm), and Δt is the time difference between the signals from the two SiPM arrays.

The precision of the DOI measurement will depend on how precisely the time difference can be determined. Time resolution in the range of tens to hundreds of picoseconds is possible for the $LaBr_3$:Ce detectors, which could allow for reasonable DOI resolution in the detector. The timing jitter of the SiPMs and associated readout electronics would need to be ensured to be at a minimum.

Timing-based DOI measurements can enhance the overall spatial resolution of the CC by adding the third dimension (depth) to the interaction position. This is critical for reducing parallax errors in Compton imaging. Accurate DOI information allows for better reconstruction of the gamma-ray interaction point, improving the quality of the reconstructed image and reducing ambiguity in source localisation. The amount of scintillation light produced, and its collection efficiency also play a role in ensuring that the timing information is accurate. Lower light yields may reduce the signal-to-noise ratio, affecting timing accuracy, emphasising the need for the optimal SiPM-DA coupling method.

Recent work was performed to introduce position sensitivity to $2'' \times 2''$ and $3'' \times 3''$ $LaBr_3$:Ce detectors by Liprandi et al. and Agnolin et al. using two different methods [10, 113]. The first method by the Liprandi et al. group investigated the use of a monolithic $3'' \times 3''$ $LaBr_3$:Ce) scintillator coupled to a 64-channel multianode PMT (Hamamatsu H8500C) to determine the position resolution of gamma-ray interactions [10]. A CC arrangement was developed with the $LaBr_3$:Ce scintillator acting as an absorber and a pixelated GAGG scintillator array, read by a SiPM-based multi-pixel photon counter, as the scatterer. Tests with ^{137}Cs and ^{60}Co point sources showed that shifts of 2 mm in source positions could be resolved with a spatial resolution of 1 mm for the scatterer and less than 3 mm for the absorber. Reconstructed images showed good agreement between experimental data and MC simulations, though experimental data displayed higher noise due to unmodeled optical photon propagation in simulations. The monolithic absorber's spatial resolution improved with higher ener-

gies, yielding better performance for the entire CC system. Ultimately, the work demonstrates successful image reconstruction accuracy, resolving 2 mm shifts in source positions and highlighting potential applications in nuclear medicine, such as gamma-PET imaging and range monitoring in hadron therapy. The coupling of the $2'' \times 2''$ detector used in this study to a multi-anode PMT is a proposed direction that could be taken to introduce position sensitivity to the detector as a CC absorber.

The second method of introducing position sensitivity in the $2'' \times 2''$ $LaBr_3$:Ce detector would involve the coupling of SiPM arrays to the optical window of the detector by removing the PMT. Work performed by the Milano group on the GAMMA CC revealed that this approach shows considerable promise across a wide energy range [113]. The group coupled a $3'' \times 3''$ $LaBr_3$:Ce:Sr crystal coupled to an array of 144 SiPMs. The detector used an Adaptive Gain Control system to automatically select the optimal gain for each SiPM channel, allowing it to maintain excellent resolution across the entire energy range from 80.0 keV to 16.0 MeV with state-of-the-art energy resolution. Its pixelated nature allowed for position reconstruction and Doppler broadening correction, as well as per-SiPM analyses of gamma-ray interactions.

BIBLIOGRAPHY

[1] T. M. Inc., "TOPAS: A Tool for Particle Simulation." http://www.topasmc.org/, 2022.

[2] World Health Organisation, "Cancer." https://www.who.int/health-topics/cancer#tab=tab_1, 2022.

[3] M. Shams, S. Abdallah, L. Alsadoun, Y. H. Hamid, R. Gasim, and A. Hassan, *Oncological Horizons: The Synergy of Medical and Surgical Innovations in Cancer Treatment*, Cureus **15** no. 11, (2023).

[4] Wilson, R R, *Radiological Use of Fast Protons*, Radiology **47** no. 5, (1946) 487–491.

[5] Polf, J C and Parodi, K, *Imaging Particle Beams for Cancer Treatment*, Physics Today **68** no. 10, (2015) 28–33.

[6] Paganetti, H, *Range Uncertainties in Proton Therapy and the Role of Monte Carlo Simulations*, Physics in Medicine and Biology **57** no. 11, (2012) R99–R117.

[7] Knopf, A and Lomax, A, *In Vivo Proton Range Verification: A Review*, Physics in Medicine and Biology **58** (2013) 131–160.

[8] J. Kasper, K. Rusiecka, R. Hetzel, M. K. Kozani, R. Lalik, A. Magiera, A. Stahl, and A. Wrońska, *The SiFi-CC Project – Feasibility Study of a Scintillation-fiber-based Compton Camera for Proton Therapy Monitoring*, Physica Medica **76** (2020) 317–325.

[9] L. Barrientos, M. Borja-Lloret, J. V. Casaña, F. Hueso-González, A. Ros, J. Roser, C. Senra, C. Solaz, R. Viegas, and G. Llosá, *System Characterization and Performance Studies with MACACO III Compton Camera*, Radiation Physics and Chemistry **208** (2023) 110922.

[10] S. Liprandi, S. Takyu, M. Safari, T. Binder, G. Dedes, K. Kamada, M. Kawula, A. Mohammadi, F. Nishikido, I. I. Valencia-Lozano, et al., *Compton Camera Arrangement With a Monolithic $LaBr_3$:(Ce) Scintillator and Pixelated GAGG Detector for Medical Imaging*, IEEE Transactions on Radiation and Plasma Medical Sciences **7** no. 7, (2023) 764–774.

[11] T. Watanabe, R. Enomoto, H. Muraishi, H. Katagiri, M. Kagaya, M. Fukushi, D. Kano, W. Satoh, T. Takeda, M. M. Tanaka, et al., *Development of an Omnidirectional Gamma-ray Imaging Compton Camera for Low-radiation-level Environmental Monitoring*, Japanese Journal of Applied Physics **57** no. 2, (2017) 026401.

[12] H. Katagiri, W. Satoh, R. Enomoto, R. Wakamatsu, T. Watanabe, H. Muraishi, M. Kagaya, S. Tanaka, K. Wada, M. Tanaka, et al., *Development of an All-sky Gamma-ray Compton Camera Based on Scintillators for High-dose Environments*, Journal of Nuclear Science and Technology **55** no. 10, (2018) 1172–1179.

[13] H. Muraishi, R. Enomoto, H. Katagiri, M. Kagaya, T. Watanabe, N. Narita, and D. Kano, *Visualization of Low-level Gamma Radiation Sources Using a Low-cost, High-sensitivity, Omnidirectional Compton Camera*, JoVE (Journal of Visualized Experiments) **155** (2020) e60463.

[14] R. Hofstadter, *The Detection of Gamma-rays with Thallium-activated Sodium Iodide Crystals*, Physical Review **75** no. 5, (1949) 796.

[15] K. Kamada, Y. Shoji, V. V. Kochurikhin, S. Okumura, S. Yamamoto, A. Nagura, J. Y. Yeom, S. Kurosawa, Y. Yokota, Y. Ohashi, et al., *Growth and Scintillation Properties of 3 in. Diameter Ce Doped $Gd_3Ga_3Al_2O_{12}$ Scintillation Single Crystal*, Journal of Crystal Growth **452** (2016) 81–84.

[16] A. Kishimoto, J. Kataoka, T. Nishiyama, T. Fujita, K. Takeuchi, H. Okochi, H. Ogata, H. Kuroshima, S. Ohsuka, S. Nakamura, et al., *Performance and Field Tests of a Handheld Compton Camera Using 3-D Position-sensitive Scintillators Coupled to Multi-pixel Photon Counter Arrays*, Journal of Instrumentation **9** no. 11, (2014) P11025.

[17] K. Takeuchi, J. Kataoka, T. Nishiyama, T. Fujita, A. Kishimoto, S. Ohsuka, S. Nakamura, S. Adachi, M. Hirayanagi, T. Uchiyama, et al., *"Stereo Compton Cameras" for the 3-D Localization of Radioisotopes*, Nuclear Instruments and Methods in Physics Research Section A: Accelerators, Spectrometers, Detectors and Associated Equipment **765** (2014) 187–191.

[18] K. Ogane, M. Uenomachi, K. Shimazoe, M. Takahashi, H. Takahashi, Y. Seto, and T. Momose, *Simultaneous Measurements of Single Gamma Ray of ^{131}I and Annihilation Radiation of ^{18}F with Compton PET Hybrid Camera*, Applied Radiation and Isotopes **176** (2021) 109864.

[19] T. Takahashi, J. Kawarabayashi, H. Tomita, T. Iguchi, and E. Takada, *Development of Omnidirectional Gamma-imager with Stacked Scintillators*, pp. , 1–4, IEEE. 2013.

[20] H. Katagiri, N. Narita, R. Enomoto, H. Muraishi, D. Kano, T. Watanabe, R. Wakamatsu, M. Kagaya, and M. M. Tanaka, *Development of an Omnidirectional Compton Camera Using CaF_2(Eu) Scintillators to Visualize Gamma Rays with Energy Below 250 keV for Radioactive Environmental Monitoring in Nuclear Medicine Facilities*, Nuclear Instruments and Methods in Physics Research Section A: Accelerators, Spectrometers, Detectors and Associated Equipment **996** (2021) 165133.

[21] L. Barrientos, M. Borja-Lloret, A. Etxebeste, E. Muñoz, J. F. Oliver, A. Ros, J. Roser, C. Senra, R. Viegas, and G. Llosá, *Performance Evaluation of MACACO II Compton Camera*, Medical Physics **48** no. 3, (2021) 1293–1300.

[22] M. McCleskey, W. Kaye, D. S. Mackin, S. Beddar, Z. He, and J. C. Polf, *Evaluation of a Multistage CdZnTe Compton Camera for Prompt Gamma Imaging for Proton Therapy*, Nuclear Instruments and Methods in Physics Research Section A: Accelerators, Spectrometers, Detectors and Associated Equipment **785** (2015) 163–169.

[23] A. E. Bolotnikov, G. S. Camarda, G. De Geronimo, J. Fried, D. Hodges, A. Hossain, K. Kim, G. Mahler, L. O. Giraldo, E. Vernon, et al., *A 4× 4 Array Module of Position-sensitive Virtual Frisch-grid CdZnTe Detectors for Gamma-ray Imaging Spectrometers*, Nuclear Instruments and Methods in Physics Research Section A: Accelerators, Spectrometers, Detectors and Associated Equipment **954** (2020) 161036.

[24] G. F. Knoll, *Radiation Detection and Measurement*. John Wiley and Sons Ltd, 2010. https://www.osti.gov/biblio/6642801.

[25] Sempere Roldan, P, *Quality Control and Preparation of the PWO Crystals for the Electromagnetic Calorimeter of CMS*. PhD thesis, Santiago de Compostela University, 2011. https://cds.cern.ch/record/1388922?ln=en.

[26] Martin, J E and Wen, C, *Physics for Radiation Protection—A Handbook 2nd Edition*, Medical Physics **33** no. 12, (2006) 4773–4773.

[27] O. Klein and Y. Nishina, *The Scattering of Light by Free Electrons according to Dirac's New Relativistic Dynamics*, Nature **122** no. 3072, (1928) 398–399.

[28] Gilmore, G, *Practical Gamma-Ray Spectroscopy*. John Wiley and Sons Ltd, 2008.

[29] https://physics.nist.gov/cgi-bin/Xcom/xcom2?Method=Comp&Output2=Hand, Accessed 2025-6-02. XCOM NIST.

[30] Paganetti, H, *Proton Beam Therapy*. IOP Publishing, 2017.

[31] Jones, D, *Radiation Oncology: A Physicist's-Eye View Radiation Oncology, Michael Goitein, Springer, New York*, Physics Today **61** no. 12, (2008) 55–56.

[32] K. S. Krane, *Introductory Nuclear Physics*. Wiley, 3 ed., 1991.

[33] Vitti, E T and Parsons, J L, *The Radiobiological Effects of Proton Beam Therapy: Impact on DNA Damage and Repair*, Cancers **11** no. 7, (2019).

[34] Tommasino, F and Durante, M, *Proton Radiobiology*, Cancers **7** no. 1, (2015) 353–381.

[35] Alpen, E L, *Interaction of Radiation with Matter*, Radiation Biophysics (1998) 50–77.

[36] Paganetti, H, *Proton Relative Biological Effectiveness – Uncertainties and Opportunities*, International Journal of Particle Therapy **5** no. 1, (2018) 2–14.

[37] L. G. Jacobsohn, K. B. Sprinkle, S. A. Roberts, C. J. Kucera, T. L. James, E. G. Yukihara, T. A. DeVol, and J. Ballato, *Fluoride Nanoscintillators*, Journal of Nanomaterials **2011** no. 1, (2011) 523638.

[38] P. A. Rodnyi, *Physical Processes in Inorganic Scintillators*. CRC Press, 2020.

[39] S. C. Curran and J. D. Craggs, *Counting Tubes: Theory and Applications*. Academic Press, 1949. https://books.google.co.za/books/about/Counting_Tubes.html?id=dNk5AQAAIAAJ&redir_esc=y.

[40] Z. Y. Sadygov, M. Suleimanov, and T. Y. Bokova, *Supersensitive Avalanche Silicon Drift Photodetector*, arXiv Preprint hep-ex/9909017 (1999).

[41] Z. Sadygov, A. Sadigov, and S. Khorev, *Silicon Photomultipliers: Status and Prospects*, Physics of Particles and Nuclei Letters **17** (2020) 160–176.

[42] G. Golmore, *Electronics for Gamma-ray Spectrometry*. John Wiley and Sons Ltd, 2008.

[43] H. Photonics, *Photomultiplier Tubes: Basics and Applications 4ed*. Hamamatsu Photonics, 2021. https://www.hamamatsu.com/content/dam/hamamatsu-photonics/sites/documents/99_SALES_LIBRARY/etd/PMT_handbook_v4E.pdf.

[44] https://www.onsemi.com/pub/Collateral/AND9770-D.PDF., Accessed: 2024-09-09. Onsemi Website.

[45] CapeScint. https://capescint.com/product-category/detector-assemblies/.

[46] C. Piemonte and A. Gola, *Overview on the Main Parameters and Technology of Modern Silicon Photomultipliers*, Nuclear Instruments and Methods in Physics Research Section A: Accelerators, Spectrometers, Detectors and Associated Equipment **926** (2019) 2–15.

[47] P. Eckert, H. Schultz-Coulon, W. Shen, R. Stamen, and A. Tadday, *Characterisation Studies of Silicon Photomultipliers*, Nuclear Instruments and Methods in Physics Research Section A: Accelerators, Spectrometers, Detectors and Associated Equipment **620** no. 2-3, (2010) 217–226.

[48] B. Dolgoshein, V. Balagura, P. Buzhan, M. Danilov, L. Filatov, E. Garutti, M. Groll, A. Ilyin, V. Kantserov, V. Kaplin, et al., *Status Report on Silicon Photomultiplier Development and its Applications*, Nuclear Instruments and Methods in Physics Research Section A: Accelerators, Spectrometers, Detectors and Associated Equipment **563** no. 2, (2006) 368–376.

[49] J. Kataoka, A. Kishimoto, T. Nishiyama, T. Fujita, K. Takeuchi, T. Kato, T. Nakamori, S. Ohsuka, S. Nakamura, M. Hirayanagi, et al., *Handy Compton Camera Using 3D Position-Sensitive Scintillators Coupled with Large-Area Monolithic MPPC Arrays*, Nuclear Instruments and Methods in Physics Research Section A: Accelerators, Spectrometers, Detectors and Associated Equipment **732** (2013) 403–407.

[50] G. Daniel, O. Limousin, D. Maier, A. Meuris, and F. Carrel, *Compton Imaging Reconstruction Methods: A Comparative Performance Study of Direct Back-projection, SOE, a New Bayesian Algorithm and a New Compton Inversion Method Applied to Real Data with Caliste,* in *EPJ Web of Conferences*, p. , 06006, EDP Sciences. 2020.

[51] M. Galloway, A. Zoglauer, E. E. Boggs, and M. Amman, *A Combined Compton and Coded-aperture Telescope for Medium-energy Gamma-ray Astrophysics*, Astronomy & Astrophysics **614** (2018) A93.

[52] A. Caffrey, L. J. Harkness-Brennan, H. Alshammari, A. J. Boston, H. C. Boston, O. Griffiths, D. S. Judson, S. Kalantan, B. Le Crom, P. J. Nolan, et al., *Gamma-ray Imaging Performance of the GRI+ Compton Camera*, Journal of Instrumentation **16** no. 09, (2021) P09015.

[53] E. Draeger, S. Peterson, D. Mackin, H. Chen, S. Beddar, and J. C. Polf, *Feasibility Studies of a New Event Selection Method to Improve Spatial Resolution of Compton Imaging for Medical Applications*, IEEE Transactions on Radiation and Plasma Medical Sciences **1** no. 4, (2017) 358–367.

[54] J. M. Verburg, K. Riley, T. Bortfeld, and J. Seco, *Energy- and Time-resolved Detection of Prompt Gamma-rays for Proton Range Verification*, Physics in Medicine & Biology **58** no. 20, (2013).

[55] N. Hyslop, *Sub-Millimetre Positron-Emission Particle Tracking Using a CdZnTe Semiconductor Array*, Master's thesis, University of Cape Town, 2021. http://hdl.handle.net/11427/35825.

[56] E. Draeger, D. Mackin, S. Peterson, H. Chen, S. Avery, S. Beddar, and J. Polf, *3D Prompt Gamma Imaging for Proton Beam Range Verification*, Physics in Medicine & Biology **63** (2018).

[57] L. Msebi, V. W. Ingeberg, P. Jones, J. F. Sharpey-Schafer, A. A. Avaa, T. D. Bucher, C. P. Brits, M. V. Chisapi, D. J. C. Kenfack, E. A. Lawrie, et al., *A Fast-Timing Array of 2" x 2" $LaBr_3$:Ce Detectors for Lifetime Measurements of Excited Nuclear States*, Nuclear Instruments and Methods in Physics Research Section A: Accelerators, Spectrometers, Detectors and Associated Equipment **1026** (2022) 166195.

[58] Z. He, W. Li, G. F. Knoll, D. K. Wehe, J. Berry, and C. M. Stahle, *3-D Position Sensitive CdZnTe Gamma-ray Spectrometers*, Nuclear Instruments and Methods in Physics Research Section A: Accelerators, Spectrometers, Detectors and Associated Equipment **422** no. 1, (1999) 173–178.

[59] F. Zhang and Z. He, *New Readout Electronics for 3-D Position-Sensitive CdZnTe/HgI_2 Detector Arrays*, IEEE Transactions on Nuclear Science **53** no. 5, (2006) 3021–3027.

[60] P. Maggi, S. Peterson, R. Panthi, D. Mackin, H. Yang, Z. He, S. Beddar, and J. Polf, *Computational Model for Detector Timing Effects in Compton-camera Based Prompt-gamma Imaging for Proton Radiotherapy*, Physics in Medicine & Biology **65** no. 12, (2020) 125004.

[61] D. Xu, *Gamma-ray Imaging and Polarization Measurement Using 3-D Position-Sensitive CdZnTe Detectors*. PhD thesis, The University of Michigan, 2006. http://gateway.proquest.com/openurl?url_ver=Z39.88-2004&rft_val_fmt=info:ofi/fmt:kev:mtx:dissertation&res_dat=xri:pqm&rft_dat=xri:pqdiss:3238119.

[62] P. Dorenbos, J. de Hass, and C. W. E. Van Eijk, *Gamma Ray Spectroscopy With a 19 × 19 mm^3 $LaBr_3$:Ce 5% Ce^3+ Scintillator*, IEEE Transactions on Nuclear Science **51** (2004).

[63] I. Holl, E. Lorenz, and G. Mageras, *A Measurement of the Light Yield of Common Inorganic Scintillators*, IEEE Transactions on Nuclear Science **35** no. 1, (1988).

[64] B. Morosin, *Crystal Structures of Anhydrous Rare-Earth Chlorides*, The Journal of Chemical Physics **49** no. 7, (1968).

[65] C. M. Rozsa, P. R. Menge, and M. R. Mayhugh, *Performance Summary: Brillance Scintillators $LaCl_3$ and $LaBr_3$*, Scintillation Products Tech. Note (2007). https://gammadata.se/wp-content/uploads/2024/01/SGC-BrilLanCe-Scintillators-Performance-Summary2-v2.pdf.

[66] L. Solutions. https://luxiumsolutions.com/radiation-detection-scintillators/crystal-scintillators/lanthanum-bromide-labr3.

[67] K. Alzimami, E. Abuelhia, Z. Podolyak, A. Ioannou, and N. Spyrou, *Characterization of $LaBr_3$:Ce and $LaCl_3$:Ce Scintillators for Gamma-ray Spectroscopy*, Journal of Radioanalytical and Nuclear Chemistry **278** (2008) 755–759.

[68] H. Cheng, B. Sun, L. Zhu, T. Li, G. Li, C. Li, X. Wu, and Y. Zheng, *Intrinsic Background Radiation of $LaBr_3$:(Ce) Detector Via Coincidence Measurements and Simulations*, Nuclear Science and Techniques **31** no. 10, (2020) 99.

[69] National Nuclear Data Center, "Information Extracted from the NuDat Database." https://www.nndc.bnl.gov/nudat/, Accessed: 2024-09-09.

[70] X. LLC, *Pixie-16 User Manual*. XIA LLC, 2019. https://docs.frib.msu.edu/daq/newsite/pixie16/Pixie16_UserManual.pdf. Accessed: 12-03-2024.

[71] M. Ellis, pp. , 197–24. Springer International Publishing, 2018.

[72] V. T. Jordanov, G. F. Knoll, A. C. Huber, and J. A. Pantazis, *Digital Techniques for Real-Time Pulse Shaping in Radiation Measurements*, Nuclear Instruments and Methods in Physics Research Section A: Accelerators, Spectrometers, Detectors and Associated Equipment **353** no. 1-3, (1994) 261–264.

[73] iThemba LABS, *Annual Report March 2013*, tech. rep., iThemba LABS, National Research Foundation, Somerset West, South Africa, 2013. https://tlabs.ac.za/wp-content/uploads/pdf/annual_reports/Annual_Report_2013_small.pdf.

[74] B. Rene and R. Fons, *ROOT — An Object Oriented Data Analysis Framework*, Nuclear Instruments and Methods in Physics Research Section A: Accelerators, Spectrometers, Detectors and Associated Equipment **389** no. 1, (1997) 81–86.

[75] Radware. https://radware.phy.ornl.gov/main.html.

[76] A. Giaz, L. Pellegri, S. Riboldi, F. Camera, N. Blasi, C. Boiano, A. Bracco, S. Brambilla, S. Ceruti, S. Coelli, et al., *Characterization of Large Volume 3.5 "× 8" $LaBr_3$:Ce Detectors*, Nuclear Instruments and Methods in Physics Research Section A: Accelerators, Spectrometers, Detectors and Associated Equipment **729** (2013) 910–921.

[77] R. Pani, M. N. Cinti, R. Scafè, R. Pellegrini, F. Vittorini, P. Bennati, S. Ridolfi, S. L. Meo, M. Mattioli, G. Baldazzi, et al., *Energy Resolution Measurements of $LaBr_3$:Ce Scintillating Crystals With an Ultra-High Quantum Efficiency Photomultiplier Tube*, Nuclear Instruments and Methods in Physics Research Section A: Accelerators, Spectrometers, Detectors and Associated Equipment **610** no. 1, (2009) 41–44.

[78] D. Weisshaar, M. S. Wallace, P. Adrich, D. Bazin, C. M. Campbell, J. M. Cook, S. Ettenauer, A. Gade, T. Glasmacher, S. McDaniel, et al., *$LaBr_3$:Ce Scintillators for In-Beam Gamma-ray Spectroscopy With Fast Beams of Rare Isotopes*, Nuclear Instruments and Methods in Physics Research Section A: Accelerators, Spectrometers, Detectors and Associated Equipment **594** no. 1, (2008) 56–60.

[79] M. Ciemała, D. Balabanski, M. Csatlós, J. M. Daugas, G. Georgiev, J. Gulyás, M. Kmiecik, A. Krasznahorkay, S. Lalkovski, A. Lefebvre-Schuhl, et al., *Measurements of High-Energy γ-Rays With $LaBr_3$:Ce Detectors*, Nuclear Instruments and Methods in Physics Research Section A: Accelerators, Spectrometers, Detectors and Associated Equipment **608** no. 1, (2009) 76–79.

[80] J. Lee, *Optimization of 500 MHz Pixie Module for Fast Time Measurement*, tech. rep., ISOLDE Decay Station, CERN, 2023. http://cds.cern.ch/record/2868002.

[81] Onsemi, "J-Series High PDE and Timing Resolution, TSV Package." https://www.onsemi.com/pdf/datasheet/microj-series-d.pdf, 2024.

[82] H. Robert, *Europium Activated Strontium Iodide Scintillators*, 1968. US Patent 3,373,279.

[83] C. M. Wilson, E. V. Van Loef, J. Glodo, N. Cherepy, G. Hull, S. Payne, W. Choong, W. Moses, and K. S. Shah, *Strontium Iodide Scintillators for High Energy Resolution Gamma Ray Spectroscopy,* in *Hard X-ray, Gamma-Ray, and Neutron Detector Physics*, pp. , 334–340, SPIE. 2008.

[84] D. H. Gahane, N. S. Kokode, P. L. Muthal, S. M. Dhopte, and S. V. Moharil, *Luminescence of Eu^{2+} in Some Iodides*, Optical Materials **32** no. 1, (2009) 18–21.

[85] E. V. van Loef, C. M. Wilson, N. J. Cherepy, G. Hull, S. A. Payne, W. Choong, W. W. Moses, and K. S. Shah, *Crystal Growth and Scintillation Properties of Strontium Iodide Scintillators*, IEEE Transactions on Nuclear Science **56** no. 3, (2009) 869–872.

[86] N. J. Cherepy, G. Hull, A. D. Drobshoff, S. A. Payne, E. Van Loef, C. M. Wilson, K. S. Shah, U. N. Roy, A. Burger, L. A. Boatner, et al., *Strontium and Barium Iodide High Light Yield Scintillators*, Applied Physics Letters **92** no. 8, (2008).

[87] M. Dhibar, G. Anil K, S. Singh, and S. Gadkari, *Growth and Characterization of SrI_2:Eu Scintillators*, in *DAE-BRNS Symposium on Nuclear Physics. V. 59*. 2014.

[88] M. Takabe, A. Kishimoto, J. Kataoka, S. Sakuragi, and Y. Yamasaki, *Performance Evaluation of Newly Developed SrI_2(Eu) Scintillator*, Nuclear Instruments and Methods in Physics Research Section A: Accelerators, Spectrometers, Detectors and Associated Equipment **831** (2016) 260–264.

[89] M. Moszynski, M. Kapusta, M. Balcerzyk, M. Szawlowski, D. Wolski, I. Wegrzecka, and M. Wegrzecki, *Comparative Study of Avalanche Photodiodes with Different Structures in Scintillation Detection*, IEEE Transactions on Nuclear Science **48** no. 4, (2001) 1205–1210.

[90] S. Bae, J. W. Hwang, S. Ahn, S. M. Cha, K. I. Hahn, D. Kim, Y. H. Kim, C. Park, X. P. López, and C. Kim, *Study on the Application of SiPM to γ Ray and Charged Particle*

Measurement Using Scintillation Crystals, Nuclear Instruments and Methods in Physics Research Section B: Beam Interactions with Materials and Atoms **541** (2023) 45–47.

[91] D. W. O. Rogers, *Monte Carlo Techniques in Radiotherapy*, Physics in Canada **58** no. 2, (2002) 63–70. https://people.physics.carleton.ca/~drogers/pubs/papers/MC_inRadiotherapy_PiCanada58_2002_63_70.pdf.

[92] J. Perl, J. Shin, J. Schümann, B. Faddegon, and H. Paganetti, *TOPAS: An Innovative Proton Monte Carlo Platform for Research and Clinical Applications*, Medical Physics **39** no. 11, (2012) 6818–6837.

[93] B. Faddegon, J. Ramos-Méndez, J. Schuemann, A. McNamara, J. Shin, J. Perl, and H. Paganetti, *The TOPAS Tool for Particle Simulation, A Monte Carlo Simulation Tool for Physics, Biology and Clinical Research*, Physica Medica **72** (2020) 114–121.

[94] S. Agostinelli, J. Allison, K. Amako, J. Apostolakis, H. Araujo, P. Arce, M. Asai, D. Axen, S. Banerjee, G. J. N. I. Barrand, et al., *GEANT4—A Simulation Toolkit*, Nuclear Instruments and Methods in Physics Research Section A: Accelerators, Spectrometers, Detectors and Associated Equipment **506** no. 3, (2003) 250–303.

[95] J. Allison, K. Amako, J. Apostolakis, P. Arce Dubois, M. Asai, T. Aso, A. Bagulya, et al., *Recent Developments in Geant4*, Nuclear Instruments and Methods in Physics Research Section A: Accelerators, Spectrometers, Detectors and Associated Equipment **835** (2016) 186–225.

[96] G. Xiaofeng, X. Qingpei, T. Dongfeng, W. Yi, H. Fanhua, Z. Yingzeng, C. Chengsheng, and L. Na, *Simulation Study of the Backward-scattering Effect in Compton Imager*, Applied Radiation and Isotopes **124** (2017) 93–99.

[97] S. J. Wilderman, W. L. Rogers, G. F. Knoll, and J. C. Engdahl, *Fast Algorithm for List Mode Back-projection of Compton Scatter Camera Data*, IEEE Transactions on Nuclear Science **45** no. 3, (1998) 957–962.

[98] D. Xu, Z. He, C. E. Lehner, and F. Zhang, *4π Compton Imaging With Single 3D Position-Sensitive CdZnTe Detector,* in *Hard X-Ray and Gamma-Ray Detector Physics VI*, pp. , 144–155, SPIE. 2004.

[99] W. Xian-Chao, Y. Bin, L. Lei, and H. Guo-En, *Cone-Beam Local Reconstruction Based on a Radon Inversion Transformation*, Chinese Physics B **21** (2012) 118702.

[100] V. Maxim, *Enhancement of Compton Camera Images Reconstructed by Inversion of a Conical Radon Transform*, Inverse Problems **35** no. 1, (2018) 014001.

[101] J. Radon, *Über die Bestimmung von Funktionen durch ihre Integralwerte Längs gewisser Mannigfaltigkeiten*, Berichte Über die Verhandlungen der Königlich-Sächsischen Gesellschaft der Wissenschaften zu Leipzig, Mathematisch-Physische Klasse **69** (1917) 262–277.

[102] A. Haefner, D. Gunter, R. Barnowski, and K. Vetter, *A Filtered Back-Projection Algorithm for 4π Compton Camera Data*, IEEE Transactions on Nuclear Science **62** no. 4, (2015) 1911–1917.

[103] A. Buades, B. Coll, and J. M. Morel, *A Non-Local Algorithm for Image Denoising*, in *2005 IEEE Computer Society Conference on Computer Vision and Pattern Recognition (CVPR'05)*, pp. , 60–65. 2005.

[104] A. E. Bolotnikov, G. S. Camarda, Y. Cui, G. Yang, A. Hossain, K. Kim, and R. B. James, *Characterization and Evaluation of Extended Defects in CZT Crystals for Gamma-Ray Detectors*, Journal of Crystal Growth **379** (2013) 46–56.

[105] J. E. Barney, M. Kroupa, and C. A. Maldonado, *Study of Charge Trapping in CZT Detectors*, tech. rep., Los Alamos National Lab.(LANL), 2022.

[106] S. N. Pike, S. E. Boggs, J. Beechert, J. Roberts, A. Y. Shih, J. A. Tomsick, and A. Zoglauer, *Characterizing and Correcting Electron and Hole Trapping in Germanium Cross-strip Detectors*, Nuclear Instruments and Methods in Physics Research Section A: Accelerators, Spectrometers, Detectors and Associated Equipment **1056** (2023) 168562.

[107] S. L. Molodtsov and A. F. Gurbich, *Simulation of the Pulse Pile-up Effect on the Pulse-height Spectrum*, Nuclear Instruments and Methods in Physics Research Section B: Beam Interactions with Materials and Atoms **267** no. 20, (2009) 3484–3487.

[108] K. Taguchi, C. Polster, W. P. Segars, N. Aygun, and K. Stierstorfer, *Model-based Pulse Pileup and Charge Sharing Compensation for Photon Counting Detectors: A Simulation Study*, Medical Physics **49** no. 8, (2022) 5038–5051.

[109] E. Hilaire, D. Sarrut, F. Peyrin, and V. Maxim, *Proton Therapy Monitoring by Compton Imaging: Influence of the Large Energy Spectrum of the Prompt-γ Radiation*, Physics in Medicine & Biology **61** no. 8, (2016) 3127.

[110] J. Schmall, R. Wiener, S. Surti, A. Ferri, A. Gola, A. Tarolli, C. Piemonte, and J. S. Karp, *Timing and Energy Resolution of New Near-UV SiPMs Coupled to $LaBr_3$:Ce for TOF-PET*, IEEE Transactions on Nuclear Science **61** no. 5, (2014) 2426–2432.

[111] W. M. Steinberger, M. L. Ruch, A. Di-Fulvio, S. D. Clarke, and S. A. Pozzi, *Timing Performance of Organic Scintillators Coupled to Silicon Photomultipliers*, Nuclear Instruments and Methods in Physics Research Section A: Accelerators, Spectrometers, Detectors and Associated Equipment **922** (2019) 185–192.

[112] J. Delgado, F. Pino, S. Moretto, D. Corti, A. Griggio, L. Pancheri, and D. Fabris, *Performance Comparison of Different SiPM Arrays Coupled to Neutron-γ Scintillators*, in *EPJ Web of Conferences*, p. , 10008, EDP Sciences. 2023.

[113] M. Agnolin, D. Di Vita, G. Borghi, M. Carminati, F. Camera, O. Wieland, B. Million, A. Giaz, C. Mihai, A. Turturica, et al., *A γ-Ray Detector Based on a 3" $LaBr_3$:Ce:Sr Crystal With SiPM Readout for 80 keV–16 MeV Energy Range With Position Sensitivity for Doppler Correction*, IEEE Transactions on Nuclear Science (2023).

[114] I. V. Lozano, G. Dedes, S. Peterson, D. Mackin, A. Zoglauer, S. Beddar, S. Avery, J. Polf, and K. Parodi, *Comparison of Reconstructed Prompt Gamma Emissions Using Maximum Likelihood Estimation and Origin Ensemble Algorithms for a Compton Camera System Tailored to Proton Range Monitoring*, Zeitschrift für Medizinische Physik **33** no. 2, (2023) 124–134.

[115] E. Munoz, A. Ros, M. Borja-Lloret, J. Barrio, P. Dendooven, J. F. Oliver, I. Ozoemelam, J. Roser, and G. Llosá, *Proton Range Verification With MACACO II Compton Camera Enhanced By a Neural Network for Event Selection*, Scientific Reports **11** no. 1, (2021) 9325.

[116] B. Inc., "AFBR-S4N44P164M 4×4 NUV-MT Silicon Photomultiplier Array." https://www.broadcom.com/products/optical-sensors/silicon-photomultiplier-sipm/afbr-s4n44p164m, 2021.